Transactions of the ASME

Journal of Engineering for Power

Published Quarterly by The American Society of Mechanical Engineers
VOLUME 103 • NUMBER 3 • JULY 1981

481 **A Study of Viscous and Nonadiabatic Flow in Radial Turbines**
I. Khalil and W. Tabakoff

490 **Wake Behavior in the Presence of Free Stream Turbulence**
S. Pal and R. Raj

499 **A Correlation for Air Velocities in Cylindrical Prechambers of Diesel Engines**
B. A. Ajakaiye and J. C. Dent

505 **A Mathematical Model for the Stirling Engine Cycle**
E. W. Beans

511 **Application of the Semi-Loof Thin Shell Element to the Analysis of Aircraft Engine Structures (81-GT-104)**
M. S. Elkelish, A. Elsawaf, and M. Barsoum

514 **Airblast Atomization of Alternative Liquid Petroleum Fuels under High Pressure Conditions**
A. K. Jasuja

519 **Conserving Energy in Saudi Arabia**
A. R. Petruzzo

522 **Long Arc Shrouding—A Reliability Improvement for Untuned Steam Turbine Blading (78-JPGC/Pwr-12)**
R. J. Ortolano, J. A. La Rosa, and W. p. Welch

532 **A Furnace Wall Ash Monitoring System for Coal Fired Boilers (80-WA/Fu-1)**
A. K. Chambers, J. R. Wynnyckyi, and E. Rhodes

539 **A Detailed Transient Model of an OTEC Evaporator**
M. C. Chapman and G. T. Heydt

545 **A Mathematical Model for Heat Transfer in Combustion Chambers of Steam Generators**
M. G. Gulič and D. D. Gvozdenac

552 **An Assessment of Deposition in PFBC Power Plant Turbines (80-WA/CD-1)**
R. A. Wenglarz

561 **Water Tempered Cleaning Medium for Sootblowers**
J. D. Shenker, A. R. White, and B. D. Ziels

566 **Separation Efficiency of a Cyclone Separator with a Turbulence-Suppressing Rotating Insert (80-IPC/Pwr-11)**
R. Razgaitis and D. A. Guenther

572 **The Thermodynamic Performance of Two Combined Cycle Power Plants Intergrated with Two Coal Gasification Systems**
F. L. Stasa and F. Osterle

582 **Performance of a Multiphase Boiling MHD Generator**
H. B. Urbach, J. G. Purnell, and D. T. Knauss

587 **The Effect of Bevel Angle on Safety Valve Vent-Pipe Systems**
Chung-Hsiung Li

589 **NO_x Removal Process by Injection of NH_3 and H_2O_2 in Gas Turbine Exhaust Gas**
Y. Hishinuma, A. Akimoto, S. Azuhata, F. Nakajima, S. Matsuda, Y. Uchiyama, R. Oshima, and M. Kato

594 **Once-Through Cooling Potential of the Middle and Lower Mississippi River During Low Flow Conditions**
A. R. Giaquinta

602 **Discussion of a previously published paper by**
R. A. Graziani, M. F. Blair, J. R. Taylor, and R. E. Mayle

602 **Discussion of a previously published paper by**
J. W. Vogan and A. R. Stetson

603 **Discussion of a previously published paper by**
E. C. Hansen, G. K. Serovy, and P. M. Sockol

ANNOUNCEMENTS

538 **Mandatory excess page charges for Transactions**

565 **Call for papers: Pressure Vessel Safety and Reliability Conference**

593 **Change of address form for subscribers**

Inside back cover **Information for Authors**

Journal of Engineering for Power (ISSN 0022-0825) is edited and published quarterly at the offices of The American Society of Mechanical Engineers, United Engineering Center, 345 E. 47th St., New York, N. Y. 10017. ASME-TWX No. 710-581-5267, New York. Second Class postage paid at New York, N.Y., and at additional mailing offices.

CHANGES OF ADDRESS must be received at Society headquarters seven weeks before they are to be effective. Please send old label and new address.

PRICES: To members, $30.00, annually; to nonmembers, $60.00. Single copies, $20.00 each. Add $5.00 for postage to countries outside the United States and Canada.

INDEXED by the Engineering Index, Inc.

I. Khalil[1]
W. Tabakoff
Professor.

Department of
Aerospace Engineering
and Applied Mechanics,
University of Cincinnati,
Cincinnati, OH 45221

A Study of the Viscous and Nonadiabatic Flow in Radial Turbines

A method for analyzing the viscous nonadiabatic flow within turbomachine rotors is presented. The field analysis is based upon the numerical integration of the incompressible Navier-Stokes equations together with the energy equation over the rotors blade-to-blade stream channels. The numerical code used to solve the governing equations employs a nonorthogonal boundary fitted coordinate system that suits the most complicated blade geometries. Effects of turbulence are modeled with two equations; one expressing the development of the turbulence kinetic energy and the other its dissipation rate. The method of analysis is applied to a radial inflow turbine. The solution obtained indicates the severity of the complex interaction mechanism that occurs between different flow regimes (i.e., boundary layers, recirculating eddies, separation zones, etc.). Comparison with nonviscous flow solutions tend to justify strongly the inadequacy of using the latter with standard boundary layer techniques to obtain viscous flow details within turbomachine rotors. Capabilities and limitations of the present method of analysis are discussed.

Introduction

A focal point of research in turbomachinery flow problems has been the development of suitable solution methods to the flow field inside these machines. During the past few years extensive progress has been made in the application of different solution techniques [1–4]. Nevertheless, general flow solutions within turbomachine passages presently remain mostly beyond the scope of prevailing methods.

These limitations, especially of the numerical methods, have long been known to be acute due to the complicated nature of the flow problem. The blade rows impose velocity as well as vorticity fields on the flow. The inviscid effects in these fields are dominant, yet the viscous effects are not small enough to be neglected. Because such flows can only be described using the full viscous equations of motion, the limitations of the prevailing methods may therefore be attributed to at least three major obstacles. The first is the excessive computer time needed for the solution of the equations of motion. The second is the difficulties and uncertainties associated with the treatment of certain boundary conditions. The third is the lack of accurate and general methods for describing turbulent transport phenomena that include effects of blades surface curvature and the presence of appreciable separation and reattachment zones in the flow field.

In an earlier paper [5], the authors of this article reported a method suitable for analyzing the viscous incompressible flow in turbomachines that partially overcomes the first two obstacles. In principle, the approach adopted emphasized the feasibility of obtaining viscous flow details within turbomachine passages by appropriatley combining several blade-to-blade viscous flow solutions. Each of these solutions were obtained through the numerical integration of the full Navier-Stokes equations over a predetermined computational surface that extends between the blades. The set of computational surfaces required for the analysis (see Fig. 1) were themselves generated from the solution of Euler equations in the manner suggested by Wu [1]. Results that had been obtained by applying this method of analysis to flows within straight radial bladed impellers were promising. This was evidenced by the fair agreement achieved between predicted and experimental data [5].

A more ambitious goal was recently introduced to extend the above analysis to deal with nonadiabatic incompressible viscous flows inside turbomachines having arbitrary blade geometries. In particular, the approach which has been established is modified and utilized in conjunction with:

1. a two equation turbulence model
2. a coordinate transformation package [6] that employs a nonorthogonal boundary-fitted coordinate system to suit the most complicated blade geometries

The differential equations describing the behavior of viscous flow in turbomachine passages are briefly reviewed in this article with pertinent references made to the questions of their solution efficiency and accuracy in describing different boundary conditions. The numerical procedures developed on this basis are discussed and illustrated by results obtained for the flow in a cooled radial inflow turbine.

Mathematical Formulation

Governing Differential Equations. The development of the mathematical model for the present problem starts with the Reynolds equations for the mean turbulent motion of flow within the turbine. These equations are written in a generalized form as follows [5].

Conservation of Mass

---

[1] Presently with Cummins Engine Company, Columbus, Indiana.

Contributed by the Gas Turbine Division for publication in the JOURNAL OF ENGINEERING FOR POWER. Manuscript received at ASME Headquarters January 3, 1980.

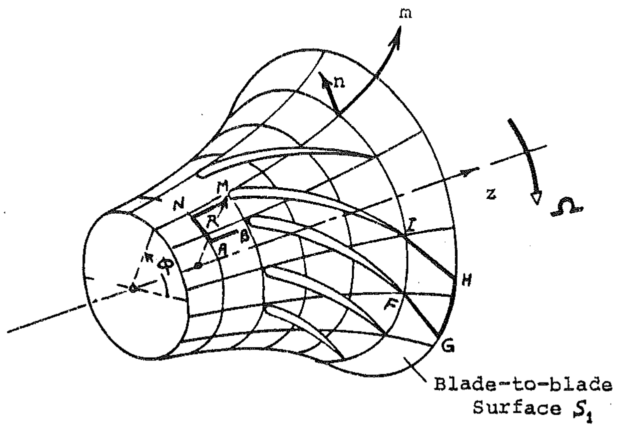

Fig. 1(*a*) Blade row intersection with a surface

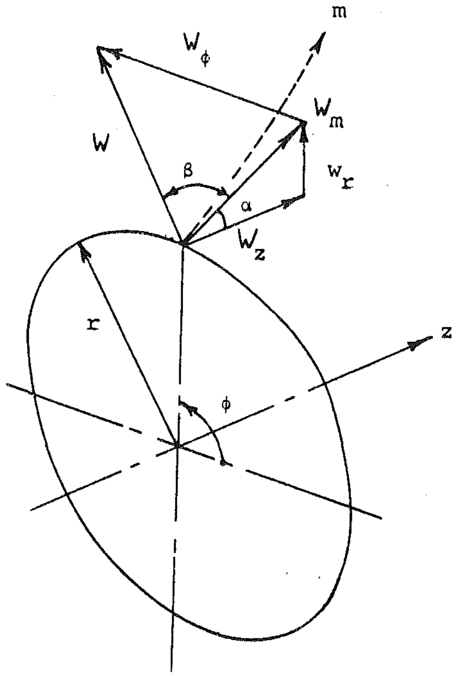

Fig. 1(*b*) Coordinate system and velocity components

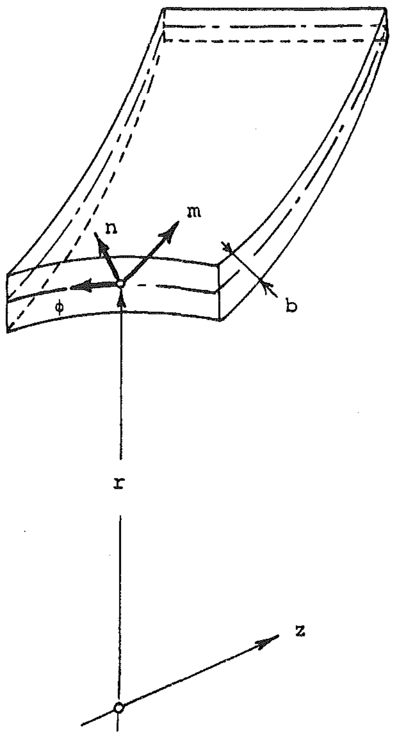

Fig. 1(*c*) Details of surface coordinate system with finite thickness sheet

Fig. 1 Blade-to-blade surface S_1

$$\nabla\cdot(\rho\overline{W}) = 0 \qquad (1)$$

Conservation of Momentum

$$\rho(\overline{W}\cdot\nabla\overline{W} + 2\overline{\Omega}\times\overline{W} - \Omega^2\overline{R}) = -\nabla p - \nabla\times[\mu_e(\overline{\nabla}\times\overline{W})] + \frac{4}{3}\nabla(\mu_e\nabla\cdot\overline{W}) \qquad (2)$$

Conservation of Energy

$$\rho(\overline{W}\cdot\nabla h) = \frac{\partial p}{\partial t} + (\overline{W}\cdot\nabla)p + D + \nabla\cdot(K\nabla T) \qquad (3)$$

In the above p, ρ, T and h denote the static pressure, density, temperature and enthalpy respectively. While, $\overline{W}$ represents the relative velocity vector at any point whose location is defined by the relative position vector $\overline{R}$ in a rotating frame of reference (Fig. 1). The speed of rotation of this frame of reference is equal to the angular velocity of the turbine ($\overline{\Omega}$). The effective turbulent viscosity, μ_e, in the above equations is assumed to describe the effects of Reynolds stresses and is determined from a two equation turbulence model.

As pointed out in the introduction, the flow equations are solved on several blade-to-blade surfaces. The geometry of each surface can be conveniently described in terms of the coordinates (m, ϕ, n) as shown in Fig. 1. To reduce the complexity of handling the computations along such surface, it is found more convenient [5] to introduce

Nomenclature

b = normal stream annulus thickness, m
C_1, C_2, = constants in the turbulence model
C_p = specific heat at constant pressure, J/(Kg) (K)
D = dissipation function, equation (3)
E = kinetic energy of turbulence, J/Kg
G_0, G_1, G_2, G_3 = denoting source terms in the flow governing equations
h = static enthalpy, J/Kg
H = total enthalpy, J/Kg, see equation (6)
m = meridional distance, m
$\dot{M}$ = mass flow per blade flow through stream annulus, Kg/s
p = static pressure, N/m^2
Pr = effective turbulent Prandtl number
$\dot{q}_w$ = heat flux, J/Kg
R = position vector, see Fig. 1
r = radius from axis of rotation, m
Re = Reynolds number
Sc_E = Schmidt number for kinetic energy of turbulence
Sc_ϵ = Schmidt number of dissipation of kinetic energy of turbulence
$\overline{V}$ = absolute velocity vector, m/s
V = magnitude of $\overline{V}$, m/s
$\overline{W}$ = relative velocity vector, m/s
W = magnitude of $\overline{W}$, m/s
W_m = meridional component of the relative velocity vector
W_ϕ = tangential component of the relative velocity vector
z = axial coordinate, m
Z = number of blades
α = angle between the meridional coordinate and the axis, rad., see Fig. 1
ϵ = dissipation of kinetic energy of turbulence
Ω = rotational speed, rad/s
ϕ = relative angular coordinate, rad, see Fig. 1
ψ = stream function
ω = vorticity, m/s

Subscript

ℓ = laminar

a stream function and the mean vorticity of the turbulent flow as new dependent variables. The flow governing equations (1–3) when recasted in terms of these variables and transformed to the (m, ϕ, n) coordinate system give the following system of equations [5].

Stream Function Equation

$$\omega = -\frac{1}{r}\left[\frac{\partial}{\partial m}\left(\frac{\dot{M} r}{b\rho}\frac{\partial \psi}{\partial m}\right) + \frac{\partial}{\partial \phi}\left(\frac{\dot{M}}{b\rho r}\frac{\partial \psi}{\partial \phi}\right)\right] \tag{4}$$

In this equation ω denotes the mean vorticity and ψ is the stream function defined according to the following relations

$$W_m = \frac{\dot{M}}{b}\frac{1}{\rho r}\frac{\partial \psi}{\partial \phi} \quad \text{and} \quad W_\phi = -\frac{\dot{M}}{b}\frac{1}{\rho}\frac{\partial \psi}{\partial m} \tag{4a}$$

where W_m, W_ϕ are the components of the mean relative velocity vector $\overline{W}$ in the meridional, tangential directions and $\dot{M}$ is the mass flow passing through the volume bounded by the surface S_1 and the filament thickness b, shown in Fig. 1. The definition of ψ as given by equation (4*a*) identically satisfies the continuity equation (1). In the process of eliminating the pressure by taking the curl of the momentum equation (2), while using equations (4) and (4*a*), the following equation is obtained:

Vorticity Transport Equation

$$\frac{\partial}{\partial m}\left(\frac{\dot{M}}{b}\frac{\partial \psi}{\partial \phi}\omega\right) - \frac{\partial}{\partial \phi}\left(\frac{\dot{M}}{b}\frac{\partial \psi}{\partial m}\omega\right) - \frac{\partial}{\partial m}\left[r\frac{\partial}{\partial m}(\mu_e \omega)\right] - \frac{\partial}{\partial \phi}\left[\frac{1}{r}\frac{\partial}{\partial \phi}(\mu_e \omega)\right] + G_1 = 0 \tag{5}$$

The source term G_1 in the above equation represents the generation or decay of vorticity due to the effects of rotation and variable viscosity, it is given by:

$$G_1 = 2\Omega\left[\frac{\partial}{\partial m}\left(\frac{\dot{M}}{b}\sin\alpha\frac{\partial \psi}{\partial \phi}\right) - \frac{\partial}{\partial \phi}\left(\frac{\dot{M}}{b}\sin\alpha\frac{\partial \psi}{\partial m}\right)\right] + G_0 + \frac{\partial \rho}{\partial m}\frac{\partial W^2/2}{\partial \phi} - \frac{\partial \rho}{\partial \phi}\frac{\partial W^2/2}{\partial m} + \Omega^2 r \sin\alpha\frac{\partial \rho}{\partial \phi}. \tag{5a}$$

Energy Equation

It is found more appropriate for a turbomachine rotor to express the energy equation in terms of the total enthalpy (H) of the flow. The total enthalpy for a turbulent flow is expressed as follows:

$$H = h + \frac{W^2}{2} + \Omega W_\phi r + \frac{\Omega^2 r^2}{2} + E \tag{6}$$

where E is the kinetic energy of turbulence. Thus, the energy equation (3) when transformed to the (m, ϕ, n) coordinate system, results in [7]:

$$\begin{aligned}\frac{\dot{M}}{b}\left[\frac{\partial}{\partial m}\left(H\frac{\partial \psi}{\partial \phi}\right) - \frac{\partial}{\partial \phi}\left(H\frac{\partial \psi}{\partial m}\right)\right] - \frac{\partial}{\partial m}\left(\frac{\mu_e}{\mathrm{Pr}} r\frac{\partial H}{\partial m}\right) - \frac{1}{r}\frac{\partial}{\partial \phi}\left(\frac{\mu_e}{\mathrm{Pr}}\frac{\partial H}{\partial \phi}\right) \\ + \frac{\partial}{\partial m}\left\{\mu_e r\left[\frac{1}{\mathrm{Pr}}\frac{\partial W^2/2}{\partial m} - \left(\frac{1}{\mathrm{S}_{CE}} - \frac{1}{\mathrm{Pr}}\right)\frac{\partial E}{\partial m}\right]\right\} \\ + \frac{\partial}{\partial \phi}\left\{\frac{\mu_e}{r}\left[\frac{1}{\mathrm{Pr}}\frac{\partial W^2/2}{\partial m} - \left(\frac{1}{\mathrm{S}_{CE}} - \frac{1}{Pr}\right)\frac{\partial E}{\partial \phi}\right]\right\} \\ - W_\phi\frac{\partial}{\partial m}(\mu_e \omega) + \frac{W_m}{r}\frac{\partial}{\partial \phi}(\mu_e \omega) - \mathrm{Dr} + G_2 = 0\end{aligned} \tag{7}$$

where

$$\begin{aligned}G_2 = -\Omega\frac{\dot{M}}{b}\left\{\frac{\partial}{\partial m}\left[(W_\phi r + r^2\Omega)\frac{\partial \psi}{\partial \phi}\right] - \frac{\partial}{\partial \phi}\left[(W_\phi r + r^2\Omega)\frac{\partial \psi}{\partial m}\right]\right\} \\ + \Omega\left\{\frac{\partial}{\partial m}\left[\frac{\mu_e}{\mathrm{Pr}} r\frac{\partial}{\partial m}\left(W_\phi r + \frac{\Omega r^2}{2}\right)\right] + \frac{1}{r}\frac{\partial}{\partial \phi}\left[\frac{\mu_e}{\mathrm{Pr}}\frac{\partial}{\partial \phi}\left(W_\phi r + \frac{\Omega r^2}{2}\right)\right]\right\}\end{aligned} \tag{7a}$$

Turbulence Model. The mean flow equations introduced earlier as equations (4, 5) and (7) involve more unknowns than appropriate to the equations. This well known problem of closure is a characteristic of all nonlinear stochastic systems. The majority of investigators in the area of turbulent flow have been concerned with this problem. Their most prominent and practical attempts were the development of various second order two equation turbulence models. Commonly, the two equation models employ the kinetic energy of turbulence as one variable. The second variable used by different researchers [8] is a dissipation function, a length scale, or a dissipation rate.

The two equation model proposed in reference [9] for the kinetic energy of turbulence E, and its volumetric rate of dissipation ϵ is used in the present work. Previous experience [10] indicates that this model provides accurate prediction of various flow regimes within turbomachine passages, in addition to being less complex and more general. The equations governing the transport of E and ϵ have a general form which includes convection, production, diffusion and dissipation terms. These can be written in terms of the (m, ϕ, n) system of coordinates as follows [7]:

Turbulent Kinetic Energy Equations

$$\frac{\dot{M}}{b}\left[\frac{\partial}{\partial m}\left(E\frac{\partial \psi}{\partial \phi}\right) - \frac{\partial}{\partial \phi}\left(E\frac{\partial \psi}{\partial m}\right)\right] - \frac{\partial}{\partial m}\left(\frac{\mu_e}{\mathrm{S}_{CE}} r\frac{\partial E}{\partial m}\right) - \frac{\partial}{\partial \phi}\left(\frac{\mu_e}{\mathrm{S}_{CE}}\frac{\partial E}{r\partial \phi}\right) - rD + \rho\epsilon r = 0 \tag{8}$$

Dissipation Rate Equation

$$\frac{\dot{M}}{b}\left[\frac{\partial}{\partial m}\left(\epsilon\frac{\partial \psi}{\partial \phi}\right) - \frac{\partial}{\partial \phi}\left(\epsilon\frac{\partial \psi}{\partial m}\right)\right] - \frac{\partial}{\partial m}\left(\frac{\mu_e}{\mathrm{S}_{C\epsilon}} r\frac{\partial \epsilon}{\partial m}\right) - \frac{\partial}{\partial \phi}\left(\frac{\mu_e}{\mathrm{S}_{C\epsilon}}\frac{1}{r}\frac{\partial \epsilon}{\partial \phi}\right) - \overline{C}_1\frac{\epsilon}{E} rD + \overline{C}_2\frac{\epsilon^2}{E}\rho r = 0 \tag{9}$$

where the expression for the effective viscosity μ_e is given by

$$\mu_e = \mu_\ell + C_D\frac{\rho E^2}{\epsilon} \tag{9a}$$

The numerical values of the constants in equations (8) and (9) used in the present work are those recommended by reference [9].

$$C_D = 0.09, \quad \overline{C}_1 = 1.44, \quad \overline{C}_2 = 1.92, \quad \mathrm{S}_{CE} = 1.0, \quad \mathrm{S}_{C\epsilon} = 1.3.$$

It should be emphasized at this point that additional production of turbulence energy due to rotational effects as well as effects of surface curvature has been neglected in the present form of turbulence model. Modification to include these effects continues to be a subject of recent research.

Equations (4, 5, 7, 8) and (9) are the equations to be solved for ω, ψ, H, E and ϵ to study the turbine flow problem. One can observe that these equations constitute a system of coupled elliptic partial differential equations, involving second order derivatives. From the nature of the problem, none of the terms are negligible in the governing equations. The convective terms introduce nonlinearity and also instability if the proper differences are not taken into account. Once a solution for these variables has been obtained, the velocity distribution can be determined from equation (4*a*). The pressure distribution can then be evaluated using equation (2) as shown in reference [5].

In order to solve the elliptic equations, it is necessary to define a selected region in the physical domain with boundary conditions specified for all the flow variables, ω, ψ, H, E and ϵ. The computational domain used in the present study is shown in Fig. 2(*a*). The domain contains the blade row and segments of the surface, S_1, extending upstream and downstream of the row. Due to the circumferential periodicity in turbomachine passages, the selected domain needs to encompass only that fraction of the flow annulus containing a single blade-to-blade passage. The shape and location of the periodic boundaries (AB, NM, IH and FG) may be defined arbitrarily as long as their spacing corresponds to the blade pitch $2\pi/Z$. The upstream and downstream boundaries (AN, GH) are located sufficiently far from the blade so that tangential variation along them are ignored. The flow properties are consequently considered to be uniform along the boundaries AN and GH.

Boundary Conditions.

Inlet Boundary AN. Irrotational and prescribed uniform flow conditions are imposed along this boundary. Therefore,

$$\frac{\partial\psi}{\partial m} = -\frac{1}{r}\frac{\partial\psi}{\partial\phi}\tan\beta_{\text{inlet}}, \frac{\partial\psi}{\partial\phi} = \frac{1}{2\pi/z},$$

$$\omega = -[2\Omega\sin\alpha]_{\text{inlet}}, H = H_{\text{inlet}}. \tag{10}$$

The value of the inlet kinetic energy of turbulence, E_{inlet}, is specified to be 0.05 percent of the square of inlet velocity.

The dissipation rate is deduced from the turbulence length scale [9]:

$$\epsilon = E_{\text{inlet}}^{3/2}\, C_D^{3/4}/\ell$$

where ℓ is taken to be 0.006 m for the case studied in the present work.

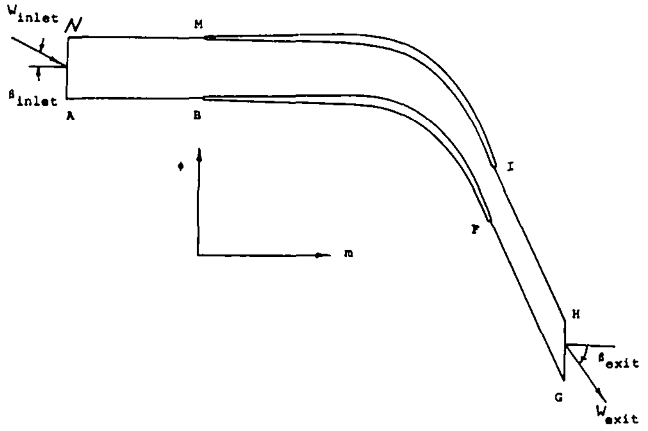

Fig. 2(a) Computational domain in the physical space

Periodic Boundaries AB, NM and FG, IH. The periodicity condition is enforced along these boundaries. This implies that all fluid properties as well as their ϕ derivatives, except for the stream function ψ, have equal values at every two corresponding points along AB, NM. Regarding the stream function the value of ψ's are made to differ on the two boundaries AB, NM by a constant that is proportional to the mass flow rate $\dot{M}$. Similarly, the same conditions are imposed along FG and IH.

Blade Surfaces MI and BF. A special approach is needed to compute the flow variables near the blade surfaces for the following reasons. In the central region of the flow, the gradients of flow properties are usually not very steep, and a moderately fine finite difference grid yields accurate solutions. However, close to the blade surfaces, the variations in flow properties are much steeper, thus requiring an extremely fine grid for accurate computation. This implies that the total storage requirement in the computer will be rather large. Moreover, the present form of turbulence model as given by equations (8) and (9) is valid only for fully turbulent flows. Modifications are required to make it applicable near laminar sublayer regions where the turbulence Reynolds number is low. To overcome these difficulties, an approach based on the use of wall functions [9] will be employed in the present study. In this approach, all the finite-difference grid nodes (except for those representing the blade surface) are located in the fully turbulent region. It is then assumed that a logarithmic velocity profile exists between the blade surface and the first grid point ($w + 1$) located in the turbulent region. This can be expressed as follows:

$$W_{w+1} = \frac{\dot{M}}{b\rho}\frac{\partial\psi}{\partial N}\bigg|_{w+1}$$

$$= C_D^{1/4}\, E_{w+1}^{1/2}\,\frac{1}{K}\,\ell\text{n}[e\,\Delta N\,\rho C_D^{1/4}\, E_{w+1}^{1/2}/\mu_\ell] \tag{11}$$

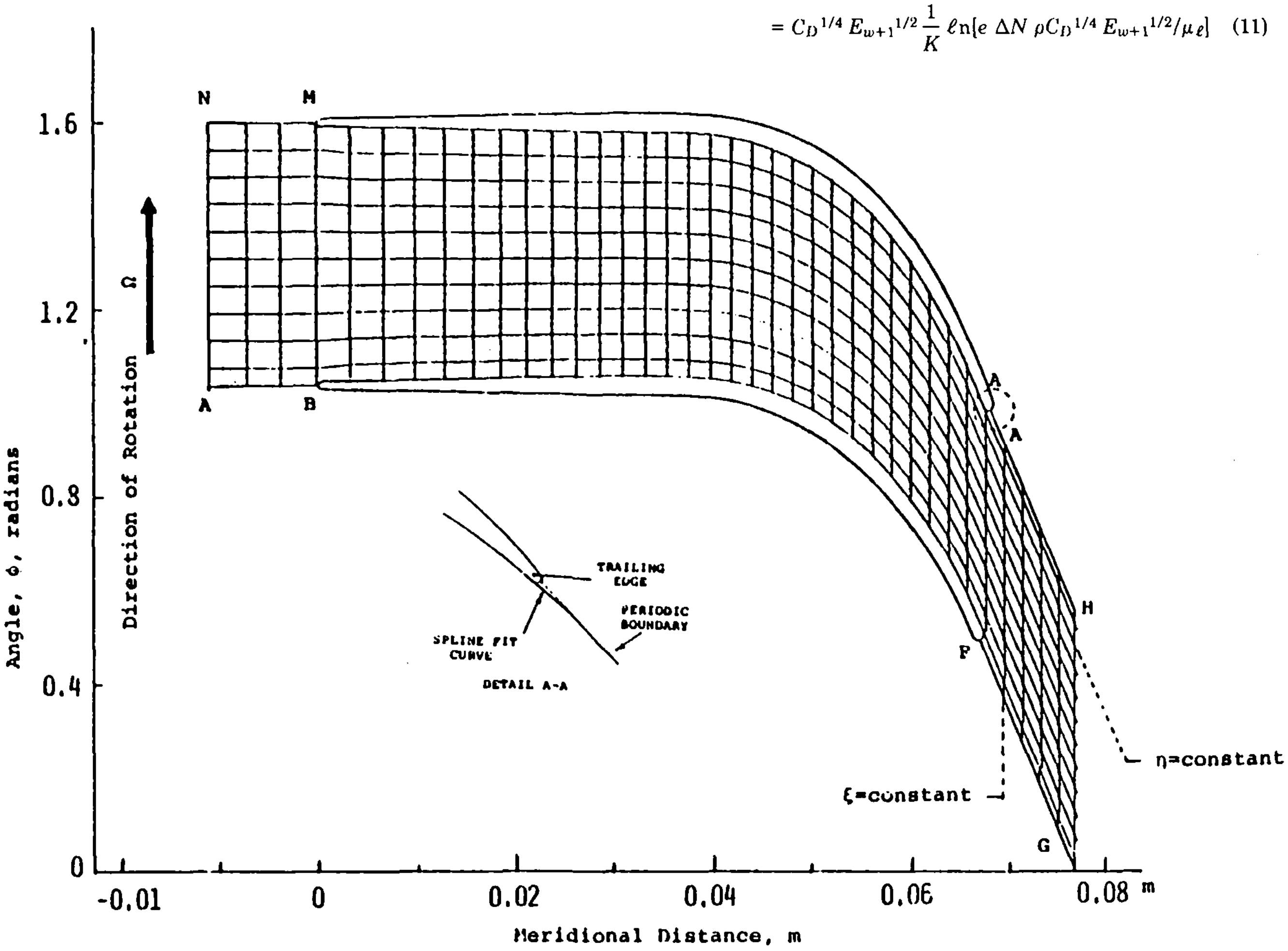

Fig. 2(b) Boundary fitted coordinate system

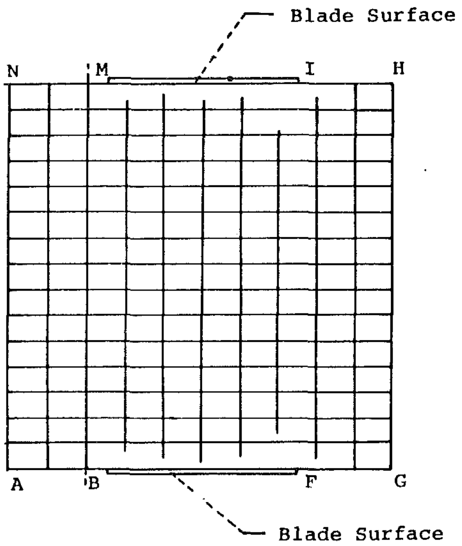

Fig. 2(*c*) The transformed domain

The flux of heat to the blade surface, based on the assumption of the log-law velocity variation [9] is given by:

$$\frac{(T_{w+1} - T_w)C_p\,\rho C_D{}^{1/4} E_{w+1}{}^{1/2}}{\dot{q}_w} = \frac{\mathrm{Pr}}{K}\,\ell n\left[\frac{e\,\Delta N\,\rho C_{\mathrm{D}}{}^{1/4}\,E_{w+1}{}^{1/2}}{\mu_\ell}\right] + 9\left(\frac{\mathrm{Pr}_\ell}{\mathrm{Pr}} - 1\right)\left(\frac{\mathrm{Pr}_\ell}{\mathrm{Pr}}\right)^{-1/4} \tag{11a}$$

where T_{w+1}, T_w are the time averaged temperatures of the flow at the point $(w + 1)$ and the blade surface, respectively; and $\dot{q}_w$ designates the heat flux to the blade surface. The value of the energy-dissipation rate at the internal grid node ϵ_{w+1} is determined from the requirement that the length scale varies linearly with the distance, ΔN, from the blade surfaces [9],

$$\epsilon_{w+1} = \frac{C_D{}^{3/4}\,E_{w+1}{}^{3/2}}{K\Delta N} \tag{11b}$$

The value of the energy of turbulence E_{w+1} is calculated from the governing equation (8) using the same procedures outlined in reference [11].

It is important to note that equation (11) provides boundary conditions for velocities, but none for ω. Therefore, the necessary boundary condition for the vorticity equation (5) is derived from the above boundary condition on the derivative of ψ, together with the stream function equation (4) relating ψ to ω.

Downstream Boundary GH. The conditions of zero gradients in the meridional direction are imposed along this boundary for H, E and ϵ, i.e.

$$\frac{\partial H}{\partial m} = \frac{\partial E}{\partial m} = \frac{\partial \epsilon}{\partial m} = 0 \tag{12a}$$

For the vorticity ω, the absolute value is taken to be zero, thus

$$\omega = -[2\Omega\,\sin\alpha]_{\mathrm{exit}} \tag{12b}$$

For the stream function ψ, the downstream flow velocities, which may be used to determine ψ derivatives along GH, and that guarantee a unique solution to the problem are unknown a priori. Therefore, a supplementary condition based on the conservation of angular momentum principle is employed in the present work to yield the required unique solution. The details of the procedure can be found in reference [5].

Coordinate Transformation. The solution of equations (4–9) subjected to the appropriate boundary conditions discussed earlier is carried out numerically. In order to reduce the complexity of handling the numerics near the curved boundaries of the blade surface a coordinate transformation of the (m, ϕ, n) system to a contracted boundary fitted coordinate is required. The overall effect of this transformation is to produce a square field in which the blade surfaces become straight and parallel. Basically, two transformations are used in the present study to implement the generation of the boundary fitted coordinates for the blade-to-blade domain of Fig. 2(*b*). The first one is obtained by defining a stretched meridional coordinate, x, given by:

$$dx = \frac{dm}{r} \tag{13a}$$

The second transformation [6] generates the boundary fitted coordinates ξ and η through the numerical solution of the following equations for $x(\xi, \eta)$ and $\phi(\xi, \eta)$.

$$\delta\frac{\partial^2 x}{\partial\xi^2} - 2\beta\frac{\partial^2 x}{\partial\xi\partial\eta} + \gamma\frac{\partial^2 x}{\partial\eta^2} = Q(\xi, \eta)$$

$$\delta\frac{\partial^2 \phi}{\partial\xi^2} - 2\beta\frac{\partial^2 \phi}{\partial\xi\partial\eta} + \gamma\frac{\partial^2 \phi}{\partial\eta^2} = P(\xi, \eta) \tag{13b}$$

where

$$\delta = \left(\frac{\partial x}{\partial\eta}\right)^2 + \left(\frac{\partial\phi}{\partial\eta}\right)^2, \quad \beta = \frac{\partial x}{\partial\eta}\frac{\partial x}{\partial\xi} + \frac{\partial\phi}{\partial\xi}\frac{\partial\phi}{\partial\eta},$$

$$\gamma = \left(\frac{\partial x}{\partial\xi}\right)^2 + \left(\frac{\partial\phi}{\partial\xi}\right)^2. \tag{13c}$$

The functions Q and P in the above equations are appropriately chosen to provide control over the spacing of the coordinate lines in the field.

Mapping the region of interest in Fig. 2(*b*) in terms of the new boundary-fitted system of coordinates (ξ, η) yields a fixed square field in the final transformed domain as shown in Fig. 2(*c*). Thus, it is possible to carry out all flow calculations on the fixed square field, using uniform grid with no interpolation required regardless of the blades shape in the physical space.

The transformation of the flow governing equations (4–9) from the physical space to the transformed domain gives:

Stream Function Equation

$$\delta\frac{\partial}{\partial\xi}\left(\frac{\dot{M}}{b\rho}\frac{\partial\psi}{\partial\xi}\right) - \beta\frac{\partial}{\partial\xi}\left(\frac{\dot{M}}{b\rho}\frac{\partial\psi}{\partial\eta}\right) - \beta\frac{\partial}{\partial\eta}\left(\frac{\dot{M}}{b\rho}\frac{\partial\psi}{\partial\xi}\right) + \gamma\frac{\partial}{\partial\eta}\left(\frac{\dot{M}}{b\rho}\frac{\partial\psi}{\partial\eta}\right) + \frac{\dot{M}}{b\rho}\left(\sigma\frac{\partial\psi}{\partial\eta} + \tau\frac{\partial\psi}{\partial\zeta}\right) = -\,\omega\, r^2 J^2 \tag{14}$$

Vorticity Transport Equation

$$\frac{\partial}{\partial\xi}\left(\frac{\dot{M}}{b}\frac{\partial\psi}{\partial\eta}\,\omega\right) - \frac{\partial}{\partial\eta}\left(\frac{\dot{M}}{b}\frac{\partial\psi}{\partial\xi}\,\omega\right) - \frac{1}{J}\left[\delta\frac{\partial^2}{\partial\xi^2}(\mu_e\omega) - 2\beta\frac{\partial^2}{\partial\xi\partial\eta}(\mu_e\omega) + \gamma\frac{\partial^2}{\partial\eta^2}(\mu_e\omega) + \sigma\frac{\partial}{\partial\eta}(\mu_e\omega) + \tau\frac{\partial}{\partial\xi}(\mu_e\omega)\right] + G_3 = 0 \tag{15}$$

Energy Equation

$$\frac{\dot{M}}{b}\left[\frac{\partial}{\partial\xi}\left(H\frac{\partial\psi}{\partial\eta}\right) - \frac{\partial}{\partial\eta}\left(H\frac{\partial\psi}{\partial\xi}\right)\right] - \frac{1}{J}\left[\delta\frac{\partial}{\partial\xi}\left(\frac{\mu_e}{\mathrm{Pr}}\frac{\partial H}{\partial\xi}\right) - \beta\frac{\partial}{\partial\xi}\left(\frac{\mu_e}{\mathrm{Pr}}\frac{\partial H}{\partial\eta}\right) - \beta\frac{\partial}{\partial\eta}\left(\frac{\mu_e}{\mathrm{Pr}}\frac{\partial H}{\partial\xi}\right) + \gamma\frac{\partial}{\partial\eta}\left(\frac{\mu_e}{\mathrm{Pr}}\frac{\partial H}{\partial\eta}\right) + \frac{\mu_e}{\mathrm{Pr}}\left(\sigma\frac{\partial H}{\partial\eta} + \tau\frac{\partial H}{\partial\xi}\right)\right] - \frac{D}{J} + G_4 = 0 \tag{16}$$

Turbulent Kinetic Energy Equation

$$\frac{\dot{M}}{b}\left[\frac{\partial}{\partial\xi}\left(E\frac{\partial\psi}{\partial\eta}\right) - \frac{\partial}{\partial\eta}\left(E\frac{\partial\psi}{\partial\xi}\right)\right] - \frac{1}{J}\left[\delta\frac{\partial}{\partial\xi}\left(\frac{\mu_e}{\mathrm{S}_{CE}}\frac{\partial E}{\partial\xi}\right) - \beta\frac{\partial}{\partial\xi}\left(\frac{\mu_e}{\mathrm{S}_{CE}}\frac{\partial E}{\partial\eta}\right) - \beta\frac{\partial}{\partial\eta}\left(\frac{\mu_e}{\mathrm{S}_{CE}}\frac{\partial E}{\partial\xi}\right) + \gamma\frac{\partial}{\partial\eta}\left(\frac{\mu_e}{\mathrm{S}_{CE}}\frac{\partial E}{\partial\eta}\right) + \frac{\mu_e}{\mathrm{S}_{CE}}\left(\sigma\frac{\partial E}{\partial\eta} + \tau\frac{\partial E}{\partial\eta}\right)\right] - \frac{D}{J} + J\rho\, r^2\epsilon = 0 \tag{17}$$

Dissipation Rate Equation

$$\frac{\dot{M}}{b}\left[\frac{\partial}{\partial\xi}\left(\epsilon\frac{\partial\psi}{\partial\eta}\right)-\frac{\partial}{\partial\eta}\left(\epsilon\frac{\partial\psi}{\partial\xi}\right)\right]-\frac{1}{J}\left[\delta\frac{\partial}{\partial\xi}\left(\frac{\mu_e}{S_{C\epsilon}}\frac{\partial\epsilon}{\partial\xi}\right)\right.$$
$$-\beta\frac{\partial}{\partial\xi}\left(\frac{\mu_e}{S_{C\epsilon}}\frac{\partial\epsilon}{\partial\eta}\right)-\beta\frac{\partial}{\partial\eta}\left(\frac{\mu_e}{S_{C\epsilon}}\frac{\partial\epsilon}{\partial\xi}\right)+\gamma\frac{\partial}{\partial\eta}\left(\frac{\mu_e}{S_{C\epsilon}}\frac{\partial\epsilon}{\partial\eta}\right)$$
$$+\frac{\mu_e}{S_{C\epsilon}}\left(\sigma\frac{\partial\epsilon}{\partial\eta}+\tau\frac{\partial\epsilon}{\partial\eta}\right)-\overline{C}_1\frac{\epsilon}{E}\frac{D}{J}+\overline{C}_{2\rho}\frac{\epsilon^2}{E}J\,r^2=0 \quad (18)$$

where the exact expressions for the transformation parameters J, σ, τ as well as the source terms G_3 and G_4 in the above equations are given in reference [7].

The system of equations (14–18) are somewhat more complicated by the extra terms added by the transformation. The disadvantage of having these terms, however, is far outweighed by the computational advantages of the simple square flow region. In general, one can demonstrate that the transformed flow equations are still elliptic in spite of the appearance of the cross derivative terms $\partial/\partial\xi\ \partial/\partial\eta$. The solution of these equations in the (ξ, η) domain provides the required distribution of the flow variables ψ, ω, H, E and ϵ in physical space. In order to solve these equations numerically, a suitable finite difference method is required. The computational method used in the present work is based on an alternating direction implicit (ADI) procedure. Some important aspects of the method as well as the details of the techniques used for differencing the equations for high Reynolds number flow are shown in reference [16]. In the following only the procedures used for advancing the solution towards a converged state is outlined.

Solution Procedure

In solving the system of coupled nonlinear equations (14–18) using the ADI scheme, there are alternate methods for handling the coupling between these equations during the solution procedure. For example, if these equations are solved sequentially rather than simultaneously, the coupling has to be restored through repeated iterations. On the other hand, if the equations are solved simultaneously, the recursion relation used to obtain a solution for one variable, say ω, must contain the other variables, ψ, E, ϵ, etc. In either case, the nonlinear terms in the differential equations are linearized or quasi-linearized at any given stage of the calculations. The nonlinearities in the original equations must be restored thereafter through repeated iterations. Not all iterative schemes, however, converge to a solution and experience proves that the solution of a system of coupled nonlinear equations converges for laminar flows, but diverges for turbulent flows. The problem of instability appears to arise from the coupling between the mean velocity profile and the effective viscosity profile. Reference [12] suggests the use of a successive convergence technique to retard and dampen this coupling to insure convergence under any set of boundary conditions.

The successive convergence technique is implemented in the present work by decoupling the E and ϵ equations ((17) and (18)) from the remaining equations and solving them sequentially rather than simultaneously with the ω and ψ equations ((14) and (15)). The details of the procedure are as follows. The stream function and the vorticity equations are first solved simultaneously using the coupled ADI scheme proposed by Davis [13] with a frozen viscosity field. Once a convergence solution has been obtained the kinetic energy of turbulence and the dissipation rate equations are then solved sequentially (again using an ADI scheme) to obtain a new round of frozen viscosity field which will be used in a next cycle of convergent solution for ψ, ω. The step described immediately above is executed several times until a convergence criteria is satisfied. When the calculations have reached this stage, the energy equation (16) is then solved.

The computer program used to carry out the actual calculations is a modified version of the one used previously [5]. In general, the program requires as an input the configuration of the computational surface S_1, the blades geometry, the inlet flow conditions, and the rotational speed of the machine. In the results presented here, the configuration of the S_1 surface is generated using the meridional flow analysis of reference [14]. Recalling that all flow calculations are carried out in the unit square of the transformed domain, therefore the blade input geometry is supplied to the program in the form of the transformation parameters δ, β, γ and J. In order to keep the computer time within reasonable limits (usually less than 8 minutes on an AMDAHL 470) the unit square region has been divided into 30 step sizes in η direction and 40 in the ζ direction. These grid nodes were found to be sufficiently fine to suppress grid-size influence.

Discussion of Results

To check the correctness of the developed program and the accuracy of the present method of analysis, a sample numerical test case is considered first. The chosen test case is similar to that investigated experimentally by Johnston [15]. In the experimental work, measurements of the mean velocity profiles were obtained in a channel, of constant width $2D$, that rotates about an axis normal to the flow direction. The channel was long enough so that the mean flow at the measuring station, which is located at $x/D = 68$, was nearly fully developed. The channel depth, $2L$, between end walls was large enough such that the flow in its central third (where the measurements were taken) was unaffected by end walls and corner secondary flows.

Computations using the present method of analysis are carried out based on the above cited flow data. Figure 3 shows the comparison of the experimentally measured and numerically predicted velocity profiles for the channel flow under different operating conditions. Johnston used two dimensionless parameters, namely the Reynolds number, Re, and the rotation number, R_0, to describe these conditions. The Reynolds number is based on the mean flow velocity, $\overline{W}_m$, at the channel inlet and the channel width, $2D$, [$\mathrm{Re} = (2D\,\overline{W}_m\rho/\mu_e)_{\mathrm{inlet}}$]. While the rotation number is based on the rotation speed, Ω, the mean flow velocity, $\overline{W}_m$, and the channel width $2D$, [$R_0 = (2D\Omega/\overline{W}_m)_{\mathrm{inlet}}$]. Figure 3($a$) gives a comparison of the computed and measured velocity profiles at zero rotation and Reynolds number = 11,500. It can be seen

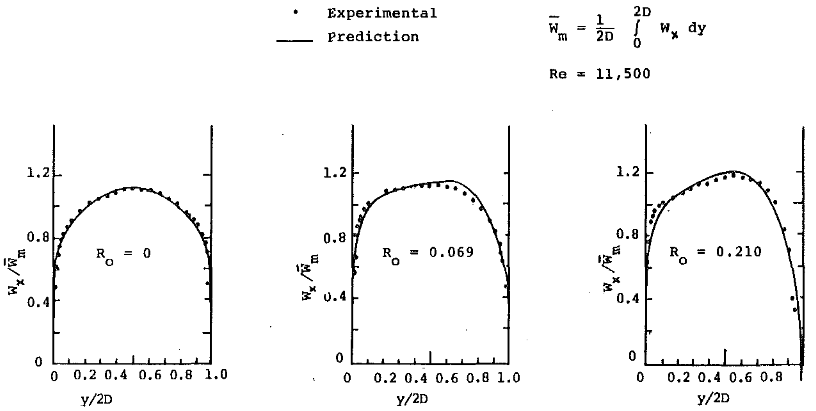

Fig. 3(*a*) **Fig. 3(*b*)** **Fig. 3(*c*)**

Fig. 3 Comparison of predictions and measurements of the velocity profiles in a rotating duct

from this figure that both velocity profiles are symmetrical about the channel center-line. As the rotation speed increases, it is observed that for both prediction and experiment, the velocity maximum shifts towards the pressure side of the channel (Fig. 3(*b*)). This maximum is increased as the rotation speed increases (Fig. 3(*c*)). The pressure gradient that is required to balance the Corioli's acceleration, resulting from the rotational effects, is quite evident from the slope of the velocity profiles in Figs. 3(*b*) and 3(*c*). The essentially good agreement between the computed results[2] and the experimental data, in all three figures, ensures the accuracy of the present method of analysis.

With the validity of the analysis established, results were then obtained for the flow in a cooled radial inflow turbine rotor. A full description of the rotor geometry is given in Fig. 4. The following operating conditions for the turbine are used in the present analysis:

Turbine inlet total temperature, $T_t = 1083$ K

Turbine inlet density, $\rho = 1.0060$ Kg/m^3

Rotational speed, $\Omega = 38{,}500$ rpm

Inlet flow angle, $\beta_{\text{in}} = 62.5$ deg

Exit flow angle, $\beta_{\text{exit}} = 63$ deg

Meridional component of the relative velocity at rotor inlet, $W_m = 66.2$ m/s

Flow Reynolds number at rotor inlet,

$$\text{Re}\left(\equiv \frac{\rho W_m r_{\text{tip}}}{\mu_e}\right) = 3.34 \times 10^5$$

Prandtl number, Pr = 0.8.

The flow through the turbine is considered to be incompressible and the blade surfaces are cooled and kept at a uniform temperature of 550 K.

In the following, the flow patterns on a blade-to-blade surface which is located midway the hub and shroud, as shown in Fig. 4, are only considered. The boundary fitted coordinates employed in the solution are those shown in Fig. 3. The results are presented in Figs. 5–10 as contour plots for the distribution of the stream function, the velocity, the kinetic energy of turbulence, the static pressure, as well as the temperature within the blade passages.

The stream function contour plots are given in Fig. 5. The flow contours depicted reflect the appearance of a recirculating eddy near the pressure surface of the blades. The flow rate within the eddy amounts to about 2.5 percent of the flow rate through the turbine (as indicated by the designation of the streamlines). This low flow rate implies low relative velocities within the eddy, as will be discussed shortly. The manner in which the streamline ($\psi = 1$) leaves the blade surface indicates a separation bubble is formed over the aft portion of the blade suction surface. This behavior seems to be caused by the inability of flow to accommodate the large blade deflection angle in this region.

The distribution of relative velocity, W, across the blade-to-blade passage, nondimensionalized with respect to the blade tip speed, Ωr_{tip}, is shown in Fig. 6. The contours show a core of high relative velocity centered at a point located at approximately 15 percent of the passage width from the blade suction surface. A region of distinct velocity deficiency is also observed in the upper half of the passage extending to about 70 percent of the blade chord and is most pronounced near the blade pressure surface. This region coincides with the location of the recirculatory eddy shown in Fig. 5. The data in Fig. 6 also indicate that the flow experiences a high acceleration rate near the blade pressure surface as it approaches the passage exit. This behavior is similar to that of flow approaching a turning duct and is expected.

In order to gain some insight into the development of the boundary layer over the blade surfaces, the velocity profiles, across the rotor passage, at different meridional locations are introduced in Fig. 7. The locations are selected to correspond to the meridional distances 1.0, 4.0 and 6.0 cms, respectively. The profiles of Fig. 7(*a*) and 7(*b*) show reversed flow regions existing near the blade pressure surface and steep gradients in the velocity near the suction surface. There is a noticeable change in the velocity profiles at subsequent downstream stations. A jet type of profile exists near the turbine exit as illustrated in Fig. 7(*c*). The complex flow pattern observed generally in Figs. 5 and 7 indicate the significant extent of the complex interaction mechanism that occurs between the different flow regimes (i.e., boundary layers, recirculating eddies and separation regions, etc.) within the rotor channel. As a consequence of such interaction, no clear distinction can be made between the boundary layer regions and the inviscid core. This result emphasizes the inaccuracies involved in using a nonviscous flow solution, such as the one shown in Fig. 7 (with dotted lines), to generate boundary layer characteristic parameters for flows in turbomachine rotors.

Figure 8 shows the distribution of the kinetic energy of turbulence between the blades. The turbulence intensities are plotted using the nondimensional quantity, $E' = E/\Omega^2 r_{\text{tip}}^2$. Near the passage inlet and up to 60 percent of the blade chord peak turbulence intensities are observed to occur in the mixing region of the recirculating eddy noted in Fig. 5. The flow energy dissipated in this process of recirculation is responsible for the velocity defficiency encountered near the blade

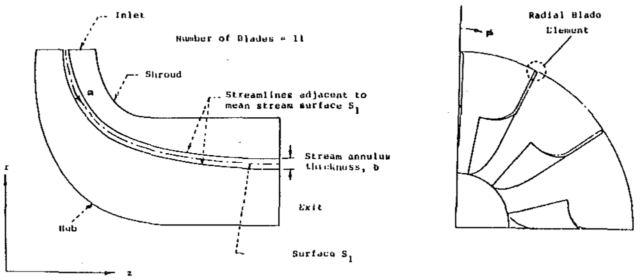

Fig. 4(*a*) Meridional view **Fig. 4(*b*) Blade-to-blade view (schematic)**

Fig. 4 Hub-shroud profile with surface S_1, used for blade-to-blade analysis

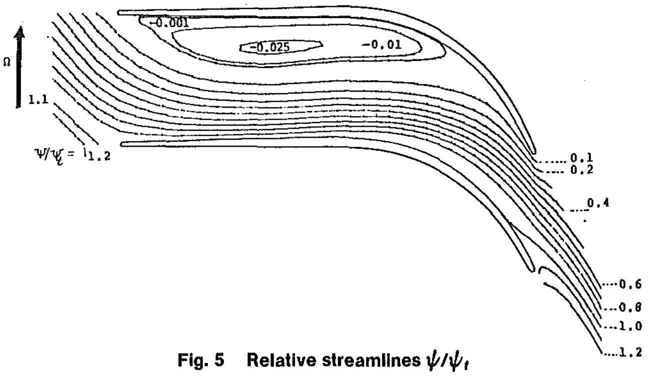

Fig. 5 Relative streamlines ψ/ψ_t

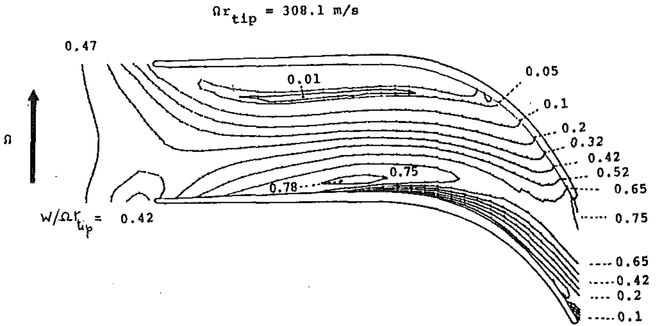

Fig. 6 Relative velocity distribution ($W/\Omega r_{\text{tip}}$)

---

[2] No effort has been made to modify the turbulence constants in equations (8) and (9) to account for rotational effects. This modification may be necessary if one wishes to obtain excellent agreement between theory and experiments.

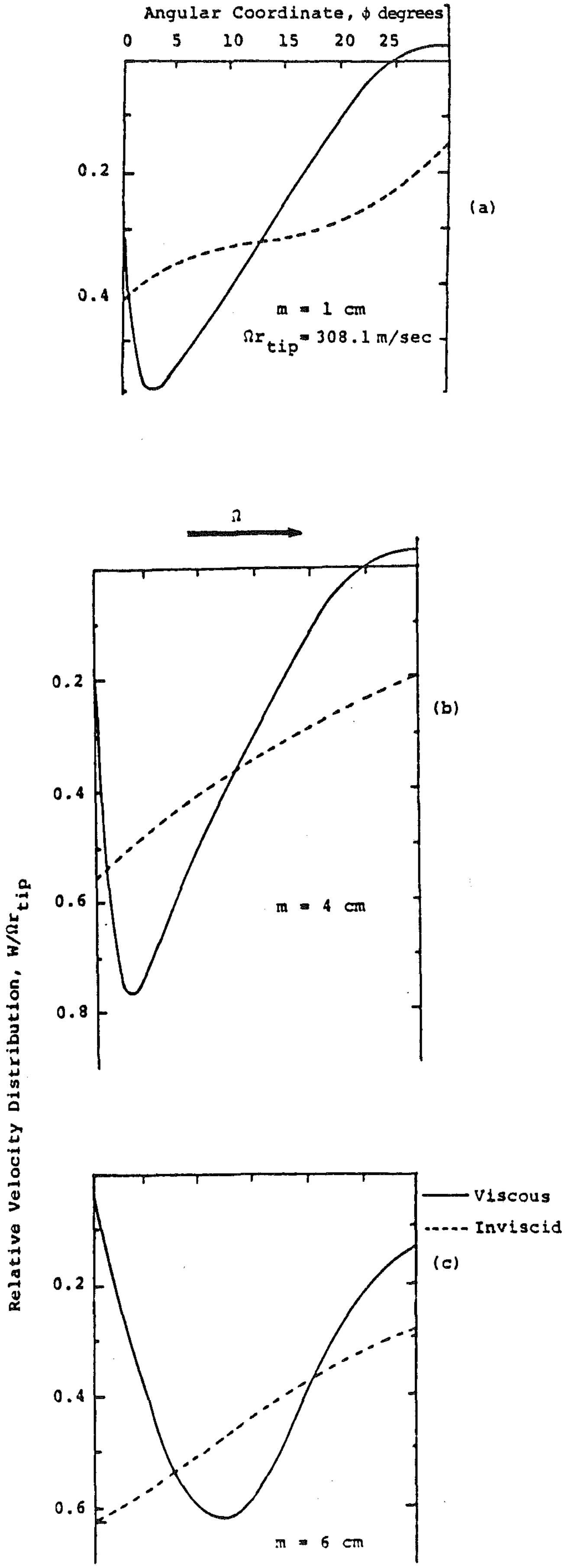

Fig. 7 Nondimensional velocity distribution at different meridional locations

pressure surface as shown in Fig. 5. On the whole, it could be recognized that the turbulence intensities are generally higher than those encountered in a stationary passage. The maximum intensities are seen to occur near the blade surfaces and especially at the passage exit. The relatively high values of kinetic energy of turbulence shown in the figure away from the blade surfaces reflect the extent of turbulent mixing even near the mid passage. The classical assumption that the viscous and turbulence effects are confined to very thin regions near the blade surfaces is evidently inaccurate when dealing with flow in turbomachinery. It is with the present type of analysis that involves the solution of the full field equations in addition to a suitable closure model for turbulence that a realistic flow prediction can be made. It should be emphasized, however, that the kinetic energy of turbulence results presented here must be viewed as qualitative. This is attributable to the fact that the additional production of turbulence energy by the rotational effects as well as the effects of blade curvature has been neglected in the present form of the turbulence model.

The static pressure distribution within the rotor channel nondimensionalized with respect to the square of blade tip speed, $\Omega^2 r^2{}_{\text{tip}}$, is shown in Fig. 9. It is observed that nearly uniform static pressures exist at the rotor inlet (the isobars run in a direction parallel to the direction of rotation). The drop in static pressures as the flow proceeds towards the rotor exit is evident. The pressure drop is seen to be high near the rotor tip. This behavior is expected since large pressure gradients ought to exist in this region to counterbalance the effects of centrifugal forces set up by the radius change. Generally, high blade loading is observed to occur near the rotor inlet and up to the 50 percent chord point where the core of high relative velocity exists as noted in Fig. 6. The contours also indicate that the blades unload near the turbine exit. This loss of loading results principally from the simultaneous effects of the formation of the separation bubble over the suction surface and the increase of velocities along the pressure surface.

Finally, the static temperature distribution within the blade-to-blade passage, nondimensionalized with respect to the inlet total temperature is given in Fig. 10. Inspection of the contours plot indicates that the steepest gradients in temperature profiles occur near the blade suction surface at the channel inlet and near the pressure surface at the channel exit. This behavior is plausible, for the velocities in these regions are high (see Fig. 6). Conversely, it is observed that the thermal layers tend to thicken on the suction surface at the trailing edge and also near the pressure surface where the recirculating zone exists. Since the rate of heat transfer to the blades is proportional to the temperature gradients near the surface, therefore, one can conclude from Fig. 10 that the maximum rate of heat transfer occurs near the blades leading edge and also along the blade suction surface up to a point located at approximately 30 percent of the blade chord. This result has important impact on the process of designing the cooling passages for new impellers, particularly when the design procedure is based on specifying the blade temperature distribution. The present results suggest that in order to keep the blades cooled at constant temperature, it is necessary to place a large number of cooling passages near the blades leading edge and also along the blade suction surfaces in the vicinity of rotor inlet.

Conclusions

A method has been developed which is suitable for analyzing the viscous nonadiabatic flow within turbomachine passages. The field analysis was based upon the numerical integration of the full incompressible Navier-Stokes equations over a predetermined set of blade-to-blade computational surfaces. The method employs a nonorthogonal body-fitted coordinate system to account for the most complicated blade geometries. Effects of turbulence were modelled using a two-equation turbulence model. The numerical integration of the governing equations was performed using an alternating direction implicit method with careful treatment of the various boundary conditions.

Significant viscous flow results were obtained by applying the method of analysis to a radial inflow turbine. The predicted flow patterns indicated the severity of the complex interaction mechanism

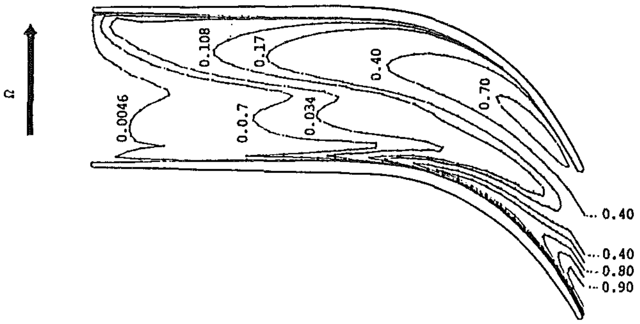

Fig. 8 Kinetic energy turbulence distribution $[E/\Omega^2 r^2_{tip}) \times 10^2]$

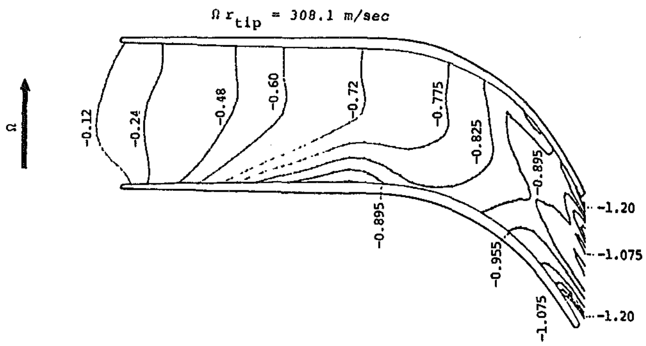

Fig. 9 Static pressure distribution $[(p - p_{inlet})\, \rho/2g\Omega^2 r^2_{tip}]$

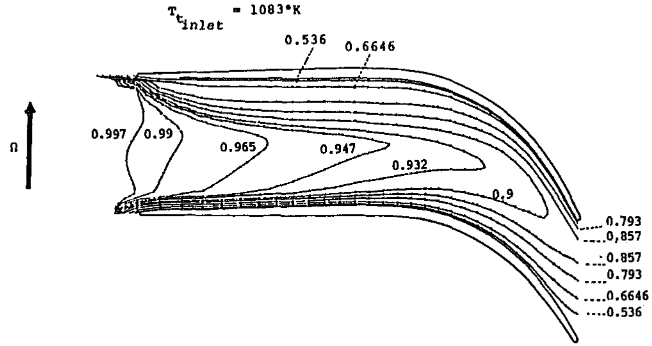

Fig. 10 Temperature distribution $(T/T_{r\,inlet})$

that occurs between the different flow regimes (i.e., boundary layers, recirculating eddies, separation zones, etc.). This result emphasized clearly the inaccuracies involved in using a nonviscous flow solution with classical boundary layer techniques to obtain viscous flow details within turbomachine rotors. Heat transfer results pointed out that in order to keep the rotor blades cooled at uniform temperatures, it was necessary to place a large number of cooling passages near the blades leading edge and also along the blade suction surfaces in the vicinity of the rotor inlet.

Acknowledgment

This research work was sponsored by NASA Contract No. NAS3-21609, NASA Lewis Research Center, Cleveland, Ohio.

References

1 Wu, C. H., "A General Theory of Three-Dimensional Flow in Subsonic and Supersonic Turbomachines of Axial, Radial and Mixed-Flow Types," National Advisory Committee for Aeronautics, TN 2604, 1952.

2 Dodge, P. R., "A Numerical Method for 2-D and 3-D Viscous Flow," AIAA Paper No. 76-425, 1976.

3 Ribaut, M., "On the Calculation of Three-Dimensional Divergent and Rotational Flow in Turbomachines," *Journal of Fluids Engineering*, Vol. 99, Series 1, No. 1, pp. 187–196.

4 Sturge, D. P., "Compressible Flow in a Centrifugal Impeller with Separation, A Two-Dimensional Calculation Method," ASME Paper No. 77-WA/FE-8, 1977.

5 Khalil, I. and Tabakoff, W., Hamed., A., "Viscous Flow Analysis in Mixed Flow Rotors," ASME JOURNAL OF ENGINEERING FOR POWER, Vol. 102, No. 3, pp. 193–201.

6 Thompson, J. F., Thanes, F. C. and Wayne, C., "Automatic Numerical Generation of Body-Fitted Curvilinear Coordinate System for Field Containing Any Number of Arbitrary Two-Dimensional Bodies," *Journal of Computational Physics*, Vol. 15, 1974, pp. 299–319.

7 Khalil, I. and Tabakoff, W., "A Calculation Procedure for Viscous Flow in Turbomachines—Vol. I," NASA CR 159635, July 1979. (Vol. II is in preparation.)

8 Wilcox, D. C. and Chambers, T. L., "Critical Examination of Two-Equations Turbulence Closure Models," AIAA Paper No. 76-352, 1976.

9 Launder, B. E., and Spalding, D. B., "The Numerical Computations of Turbulent Flows," *Computer Methods in Applied Mechanics and Engineering*, Vol. 3, 1974, pp. 269–289.

10 Quemord, C. and Michel, R., "Definition and Application of Means for Predicting Shear Turbulent Flows in Turbomachines," ASME Paper No. 76-GT-67, 1976.

11 Gosman, A. D. and Spalding, D. B., "Transfer of Heat in Rotating Systems," ASME Paper No. 76-GT-25, 1976.

12 Hai, S. M., "Numerical Solution of Nonlinear Elliptic Partial Differential Equations by Successively Converging Techniques," *Numerical/Laboratory Computers Methods in Fluid Mechanics*, ASME, New York.

13 Davis, R. T., "Numerical Solutions of the Navier-Stokes Equations for Symmetric Laminar Incompressible Flow Past a Parabola," *Journal of Fluid Mechanics*, Vol. 51, Part 3, 1972, pp. 417–433.

14 Katsanis, T., "Use of Arbitrary Quasi-Orthogonals for Calculating Flow Distribution in the Meridional Plane of a Turbomachine," NASA TND-2546, Dec. 1964.

15 Johnston, J. and Hallen, R., "Effect of Spanwise Rotation on the Structure of Two-Dimensional Fully Developed Turbulent Channel Flow," *Journal of Fluid Mechanics*, Vol. 56, Part 3, 1972, pp. 533–557.

16 Khalil, I. M., "A Study of the Viscous Flow in Turbomachines," Ph.D. Thesis, University of Cinncinati, Ohio, 1978.

S. Pal[1]
Project Engineer,
Research Engineering—Turbomachinery,
Sundstrand Aviation Operations,
Rockford, Ill. 61101
Assoc. Mem. ASME

R. Raj
Consultant,
Curtiss-Wright Corporation,
Mem. ASME

Turbomachinery Laboratory,
Department of Mechanical Engineering,
The City College of The City University of
New York, New York, N. Y. 10031

Wake Behavior in the Presence of Free Stream Turbulence

The effect of free stream turbulence on the characteristics of a turbulent wake developed from the trailing edge of a thin and smooth flat plate was studied analytically and experimentally. The experimental measurements were taken in a low speed wind tunnel using cross-wire anemometry. Two levels of free stream turbulence were obtained at the leading edge of the flat plate using grids with square bars ($T \sim 5.23$ percent) and circular rods ($T \sim 7.23$ percent). The grids were kept at distance of 273 mm from the leading edge of the flat plate. Experimental results are presented on the mean velocity profile, wake centerline velocity, half wake width, displacement thickness, and shape factor. It is shown that the free stream turbulence increases the wake recovery and growth rates. The semi-empirical correlations are developed to predict the foregoing behavior. The analytical investigation also lead to the establishment of the two turbulence parameters. These parameters simulate the effect of free stream turbulence on the wake velocity (U_0) and length (L_0) scales.

1 Introduction

In many practical situations, wake evolves in the presence of free stream turbulence. One such situation exists in multistage turbomachinery. In multistage turbomachinery the wake of a blade following the first row of blades always evolves under the influence of the turbulence present in the wake of the previous row of blades. The nature of this free stream turbulence depends upon the spacing between stator-rotor and rotor-stator, stage loading, and rotation [1].

An extensive search of the literature on general two and three-dimensional wakes is reported by Raj [2]. The review shows that, with the exception of few remarks made in the report by Eagleson, et al. [3], which indicate that the wake recovery rate increases with the increase in turbulence level, there is practically no study to date describing the effect of free stream turbulence on wake behavior. However, very interesting and revealing studies are reported on the effect of free stream turbulence on boundary layer and heat transfer [4–17]. These studies provide considerable useful information which can be used to model the wake development in the presence of free stream turbulence. It is concluded in these investigations that free stream turbulence increases the boundary layer thickness, flattens the velocity profile, increases the skin friction, reduces the shape factor, reduces the Reynolds Number for transition from laminar to turbulent flow, and increases the heat transfer. This general behavior of the effect of free stream turbulence on various parameters is summarized in Table 1.

In this paper, correlations based on analytical and experimental considerations are developed to predict the characteristics of the plane wake in the presence of the free stream turbulence. Experimental data on plane wake are presented for inlet turbulence levels of 0.4, 5.23 and 7.23 percent. It is shown that the wake behavior changes in the presence of free stream turbulence and this change is dependent upon the magnitude of the free stream turbulence level.

2 Theoretical Considerations

Consider Navier-Stokes equations in a two-dimensional Cartesian coordinate system. Applying the condition of incompressibility, stationarity, and boundary layer approximation, and neglecting the viscous diffusion and normal stress terms which are usually small relative to the other terms in the equation, the continuity and the Navier-Stokes equations take the following form:

$$\frac{\partial \overline{U}}{\partial x} + \frac{\partial \overline{V}}{\partial y} = 0 \qquad (1)$$

$$\overline{U}\frac{\partial \overline{U}}{\partial x} + \overline{V}\frac{\partial \overline{U}}{\partial y} + \frac{\partial}{\partial y}(\overline{uv}) = \overline{U}_e \frac{\partial \overline{U}e}{\partial x} \qquad (2)$$

It is known from past investigations that the wake flow evolution can be determined solely by the local velocity (U_0) and length (L_0) scales [19]. Experimental results described later confirm that a self-similarity in the wake mean velocity profile is also maintained even in the presence of free stream turbulence. Therefore, it is expected that the presence of the free stream turbulence will affect only the velocity and length scales. If multiples of ϕ_1, with U_0 and ϕ_2 with L_0 represent the effect of free stream turbulence on the local velocity and length scales then ϕ_1 will reduce the velocity scale, while ϕ_2 will increase the length scale with increase in free stream turbulence level. Such a trend has been observed in practically all the existing investigations [4–17] on boundary layers in the presence of free stream turbulence since the boundary layer thickens and the velocity profile flattens in the presence of free stream turbulence. Note that an increase in velocity scale in a boundary layer due to free stream turbulence (flattening of velocity profile) is equivalent to decrease in wake velocity scale (wake velocity defect at the wake centerline). Taking into consideration these observations and applying arguments similar to the one given in Tennekes and Lumley [19], it is not difficult to see that, in the presence of free stream turbulence, the wake velocity profile can be expressed as follows.

$$\frac{\overline{U}_e - \overline{U}}{U_0\phi_1} = f\left(\frac{y}{L_0\phi_2}\right) \qquad (3)$$

---

[1] Formerly of the Turbomachinery Laboratory, Department of Mechanical Engineering, CCNY, New York, NY.

Contributed by the Gas Turbine Division for publication in the JOURNAL OF ENGINEERING FOR POWER. Manuscript received at ASME Headquarters January 9, 1980.

Table 1 Summary of the effect of free stream turbulence on various parameters based on review [18]

No.	Parameter/Region	Turbulence Level	Variation in Parameter	General	References
1	Boundary Layer	7%	45%	Thickens	7, 11, 14, 17
2	Mean Velocity Profile	7%	10%	Flattens	5, 6, 7, 11, 17
3	Turbulent Shear Stress	No. Inf.	No. Inf.	Increases	5, 6
4	Wall Shear Stress	5%	30%	Increases	4, 5, 6, 8, 14
5	Heat Transfer	5%	30%	Increases	14, 16
6	Transition Region	No. Inf.	No. Inf.	Shifts Forward	12, 13
7	Skin Friction Coefficient	0.2%	1.0%	Increases	7, 17
8	Displacement Thickness	No. Inf.	No. Inf.	Increases	4
9	Momentum Thickness	No. Inf.	No. Inf.	Increases	4
10	Transition Reynolds No.	No. Inf.	No. Inf.	Rapidly Reduces	12, 17
11	Shape Factor	0.2%	0.5%	Decreases	7, 8
12	Production of Turbulent Kinetic Energy	No. Inf.	No. Inf.	Increases	5, 6
13	Law of the Wake in Outer Region	No. Inf.	No. Inf.	Modifies	4, 5, 6, 17
14	Law of the Wall	No. Inf.	No. Inf.	Changes	4
				Unchanged for Small Free Stream Turbulence	17
15	Mixing Length	No. Inf.	No. Inf.	Increases	8, 14
16	Eddy Viscosity	No. Inf.	No. Inf.	Increases	8

where $\overline{U}_e$ is the wake edge velocity, $\overline{U}$ is the velocity in the wake, U_0 and L_0 are velocity and length scales, respectively, and ϕ_1 and ϕ_2 are turbulence parameters affecting velocity and length scales, respectively. The form of the parameters ϕ_1 and ϕ_2 will be determined from the following analysis.

Replace $\overline{uv}$ in equation (2) with the eddy viscosity model

$$-\overline{uv} = \nu_T \frac{\partial \overline{U}}{\partial y} \tag{4}$$

Substituting (3) and (4) in (2) and eliminating $\overline{V}$ in the resulting equation by the use of the continuity equation (1), we obtain the following equation:

$$\begin{aligned}\frac{L_0\phi_2}{U_0\phi_1}\frac{d}{dx}(U_0\phi_1)[f^2] - \frac{L_0\phi_2}{U_0{}^2\phi_1{}^2}\frac{d}{dx}(\overline{U}_eU_0\phi_1)[f] \\ + \frac{1}{U_0\phi_1}\frac{d}{dx}(\overline{U}_eL_0\phi_2)[\eta f'] - \frac{d}{dx}(L_0\phi_2)\eta ff' \\ - \frac{1}{U_0\phi_1}\frac{d}{dx}(U_0L_0\phi_1\phi_2)f'\int f d\eta + \frac{\nu_T}{U_0L_0\phi_1\phi_2}f'' = 0\end{aligned} \tag{5}$$

The condition of self-similarity in mean velocity profile is satisfied, only if coefficients of f, f^2, $\eta f'$, $\eta ff'$, $f'\int f d\eta$ and f'' are constant. This condition will provide a set of equations such that

$$\frac{L_0\phi_2}{U_0\phi_1}\frac{d}{dx}(U_0\phi_1), \frac{L_0\phi_2}{U_0{}^2\phi_1{}^2}\frac{d}{dx}(\overline{U}_eU_0\phi_1),$$

$$\frac{d}{dx}(L_0\phi_2) \quad \text{and} \quad \frac{1}{U_0\phi_1}\frac{d}{dx}(\overline{U}_eL_0\phi_2)$$

are constants and

$$U_0L_0\phi_1\phi_2 \;\alpha\; \nu_T \tag{6}$$

The similarity condition on momentum integral of equation (2) provides that $U_0L_0\phi_1\phi_2$ is identically constant for a nonpressure gradient and is nearly true for the case of pressure gradient [20].

Let,

$$U_0L_0\phi_1\phi_2 = K_1 \tag{7}$$

and consider the case when $x/c \simeq 0.1$. The first and third terms in correlations (6) become small compared to the other terms because wake centerline velocity recovers to about 60 percent. Hence similarity is attained if

$$\frac{L_0\phi_2}{U_0{}^2\phi_1{}^2}\frac{d}{dx}(\overline{U}_eU_0\phi_1) = K_2,$$

and

$$\frac{1}{U_0\phi_1}\frac{d}{dx}(\overline{U}_eL_0\phi_2) = K_3 \tag{8}$$

where K_2 and K_3 are constants.

Substituting (7) in (8), we get

$$\frac{1}{U_0{}^3\phi_1{}^3}\frac{d}{dx}(\overline{U}_eU_0\phi_1) = \frac{K_2}{K_1} = K_4 \tag{9}$$

Nomenclature

a = constant (equation (19))
b = constant (equation (19))
b_1 = bar width
c = chord of the flat plate
C_d = drag coefficient in the presence of freestream turbulence
C_{d_0} = drag coefficient in the absence of free stream turbulence
d = diameter of the grid rod
f = velocity profile function
H = shape factor
K_1 to K_9 = similarity constants (equations (7–12))
K_{10}, K_{11} = constants (equations (19, 20))
L_0 = length scale (half wake width) (Fig. 1)
M = grid spacing
m = constant representing pressure gradient effect
n = constant dependent upon free stream turbulence level
R = Reynolds Number ($\overline{U}_1c/\nu$)
T = turbulence level $\sqrt{\overline{u}^2}/\overline{U}_1$
$\overline{U}$, $\overline{V}$ = mean velocity components along axial and lateral directions, respectively
$\overline{U}_1$ = inlet velocity
U_0 = velocity scale ($\overline{U}_e - \overline{U}_c$), (Fig. 1)
$\overline{U}_c$ = mean velocity at the wake centerline (Fig. 1)
$\overline{U}_e$ = outer edge velocity
$-\rho\overline{uv}$ = Reynolds stress
x, y, z = axial, lateral and radial axes, respectively (Fig. 1)
x_0 = virtual origin (equations (17, 18))
x_ℓ = distance from the leading edge of the flat plate
α = constant (equation (13))
β = constant (equation (14))
δ_1 = displacement thickness
ρ = density
η = similarity variable ($y/L_0\phi_2$)
ν = kinematic viscosity
ν_T = eddy viscosity
θ = momentum thickness
ϕ_1 = turbulence parameter (equations (3, 17))
ϕ_2 = turbulence parameter (equations (3, 17))

Subscripts

c = centerline values
e = edge values
ℓ = leading edge
t = trailing edge values
∞ = free stream values

Superscript

— = mean values

and

$$\frac{1}{U_0^2\phi_1^2}\frac{d}{dx}\left(\frac{\bar{U}_e}{U_0\phi_1}\right)=\frac{K_3}{K_1}=K_5 \tag{10}$$

where K_4 and K_5 are constants.

Adding (9) and (10), we get

$$\frac{1}{U_0^2\phi_1^2}\frac{d\bar{U}_e}{dx}=\frac{K_4+K_5}{2}=K_6 \tag{11}$$

Let $\bar{U}_e = K_7x^{-m}$, this type of functional choice is dictated by the similarity considerations [21], then from (11) we get

$$U_0\phi_1 = K_8x^{-(m+1)/2} \tag{12}$$

and

$$L_0\phi_2 = K_9x^{(m+1)/2}$$

where

$$K_8=\frac{-mK_7}{K_6} \quad \text{and} \quad K_9=\frac{K_1K_6}{-mK_7}$$

However ϕ_1 and ϕ_2 are not constant and are functions of x and T, where T is the free stream turbulence. Since the right hand side of (12) is a monotonic function, it is expected that the left hand side will also be monotonic in character. Therefore, an appropriate choice of ϕ_1 is given by the following correlation.

$$\phi_1 \sim x^n$$

where

$$n \sim F(T,x) \sim G(T)$$

if T is a weakly dependent function of x. For values of $T < 1$, a Taylor series expansion of G in T suggests that

$$G(T) = T$$

therefore

$$n \sim T$$

For convenience taking the constant of proportionality as $\alpha/2$, we can easily rewrite the correlation for ϕ_1 as follows.

$$\phi_1 \sim x^{\alpha T/2} \tag{13}$$

If ϕ_1, is known, apparently the behavior of ϕ_2 will be inverse of ϕ_1 and will be of the form,

$$\phi_2 \sim x^{-\beta T/2} \tag{14}$$

using (13) and (14), equation (12) can be rewritten as follows:

$$U_0 \sim x^{-(m+1+\alpha T)/2} \tag{15}$$

and

$$L_0 \sim x^{(m+1+\beta T)/2} \tag{16}$$

The coefficient of proportionality in (13) and (14) can be obtained from the following boundary conditions when

$$T = 0, \phi_1 \quad \text{and} \quad \phi_2 = 1$$

Therefore, the constants of proportionality in (13) and (14) are of order one. Since the chord length of the plate c has been taken as the nondimensionalizing length (this is a usual practice in the area of turbomachinery) and wake origin is assumed from distance x_0/c ahead of trailing edge, (13) and (14) can be rewritten as follows.

$$\phi_1=\left(\frac{x}{c}+\frac{x_0}{c}\right)^{\alpha T/2} \tag{17}$$

and

$$\phi_2=\left(\frac{x}{c}+\frac{x_0}{c}\right)^{-\beta T/2}$$

Equating momentum loss through coefficient of drag, it can be shown that the constant of proportionality in (15) is a function (to a first order) of the coefficient of drag ($C_d^{1/2}$) of the flat plate in free stream turbulence.

Therefore, the decay of the wake defect in the presence of the free stream turbulence and pressure gradient in a general form may be expressed as follows.

$$1-\frac{\bar{U}_c}{\bar{U}_e}=KC_d^{1/2}\left(\frac{x}{c}+\frac{x_0}{c}\right)^{-(1+\alpha T-m)/2} \tag{18}$$

where C_d is the coefficient of drag with free stream (equation (21)).

It can be shown from dimensional reasons that K in equation (18) is a constant depending upon the turbulence parameter ϕ_2 at the trailing edge of flat plate and will be of the form of

$$K=\frac{K_{10}}{a+b\phi_{2t}} \tag{19}$$

The values of K_{10}, a and b, were found to be 2.7, 0.76 and 1, respectively. For nonfree stream turbulence case and for thick trailing edges, the value of K was found to be 1.25 [20]. K, x_0/c and α for the present case were found to be 1.534, 0.021 and 4, respectively.

Similarly, the growth of the wake half width can be represented by the following correlation.

$$\frac{L_0-L_{0t}}{c}=K_{11}C_d^{1/2}\left(\frac{x}{c}\right)^{(1+\beta T+m)/2} \tag{20}$$

where L_{0t} is the half wake width at the trialing edge. K_{11} and β for the present investigation were found to be 1.05 and 8.27, respectively.

It is clear from equations (18) and (20), that, when m is very small ($m \simeq 0$) and the free stream turbulence level is low ($T \simeq 0$), these equations correspond to the case of a flat plate and cylinder wake when placed in a uniform stream.

3 Experimental Equipment, Method and Instrumentation

The measurements of the mean quantities were carried out in a wake region developed from the trailing edge of a flat plate at various axial and lateral locations (Fig. 1) with and without free stream turbulence.

An open circuit wind tunnel was used in the experimentation. The test section cross section of the wind tunnel is 45.72 × 45.72 cm^2. Provisions exist for the attachment of any length test section with the same cross section. The test model consisted of a flat plate (Fig. 1) made of precision ground, nondistorting stainless steel, 45.72 × 14.92 × 0.238 cm^3. The flat plate was mounted firmly in the wind tunnel in the x–z plane (Fig. 1), such that the wake produced from its trailing edge varied in the x–y plane. The levelling of the flat plate was checked at the start of the measurements.

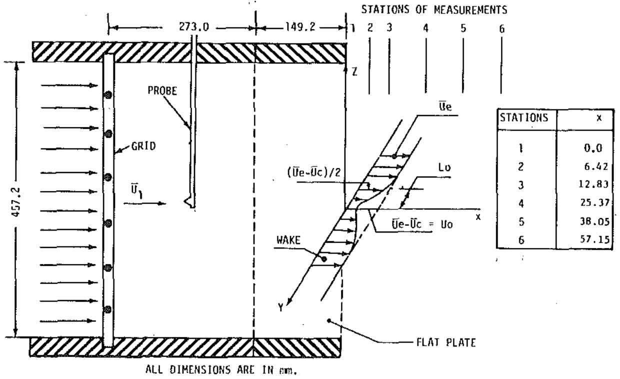

Fig. 1 Schematic of the experimental set up

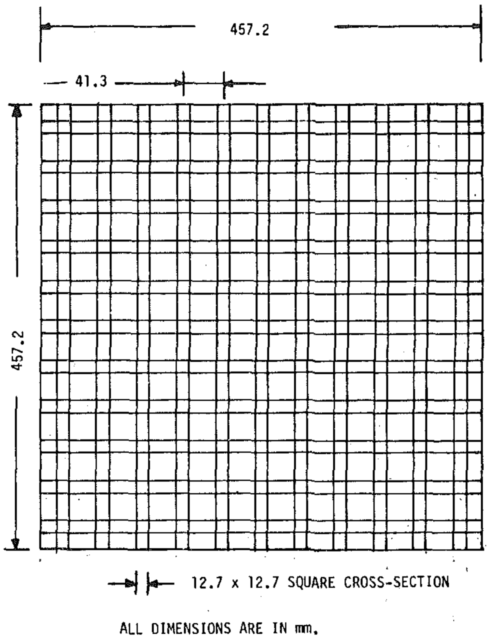

Fig. 2(*a*) Schematic of the square bars grid used to generate turbulence

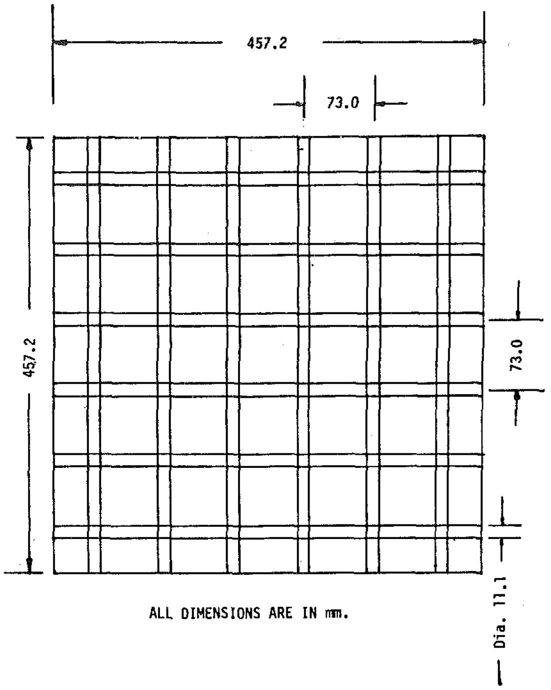

Fig. 2(*b*) Schematic of the circular rods grid used to generate turbulence

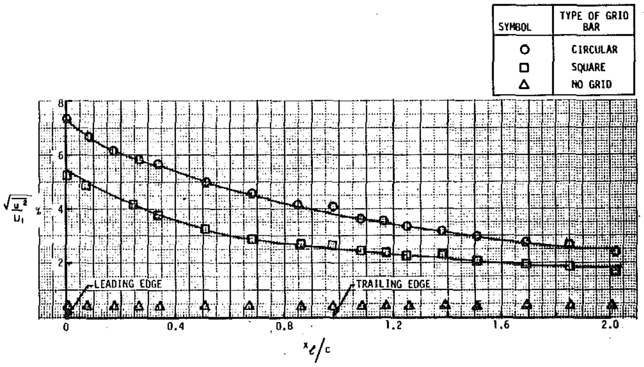

Fig. 3 Variation of the free stream turbulence intensity with downstream distance

The free stream turbulence was generated with the help of two grids (Figs. 2, (*a*) and (*b*)). Grid I consisted of a combination of square bars placed horizontally and vertically and has the dimensions M/b_1 = 3.25, b_1 = 1.27 cm, where M is the spacing between the two consecutive grid bars and b_1 is the dimension of each bar having square cross-section. This grid produced a free stream turbulence level of 5.23 percent. Grid II has the dimensions M/d = 6.57, d = 1.11 cm, where d is the diameter of the grid cylinder. This grid produced a free stream turbulence level of 7.23 percent.

The traversing mechanism was used to vary the location of the probe in the axial and transverse directions. Clamps were used to hold the mechanism firmly on the rails to damp the vibrations.

Two sensors hot-wire probe with nearly equal resistance (within 0.15 percent), having length to diameter ratio of 300, was used to measure the mean and the turbulence quantities. The mean quantities measured using the wedge probe along with two pressure transducers, one used to align the probe, the other used to measure the total and static pressures. These quantities were found to be in good agreement with those obtained from the cross-wire. Output from the sum and difference unit was fed to the rms voltmeter which was connected to a digital voltmeter through a channel selector.

The flow Reynolds Number based on the inlet average velocity and chord length was 2.56 × 10^5, 2.07 × 10^5 and 2.45 × 10^5 at a turbulence level of 0.4, 5.23 and 7.23 percent. The corresponding average mean velocities were 26.62, 21.52 and 25.46 m/s.

4 Experimental Results and Comparison with Predictions

The data are presented in the dimensionless form using c and $\overline{U}_e$ as dimensional parameters; c being the chord length of the flat plate and $\overline{U}_e$ the local mean velocity at the outer edge of the wake.

4.1 Free Stream Turbulence Level. The variation of the free stream turbulence level (T) with downstream distance beginning with the leading edge of the flat plate is shown in Fig. 3. It is clear from Fig. 3 that T is a weakly dependent function of x/c behind the trailing edge of the flat plate. This is one of the assumptions made in the development of the analytical model. The free stream turbulence level at the leading edge was found to be 0.4 percent for no grid, 5.23 percent with square bars grid and 7.23 percent with circular rods grid. However, at the trailing edge of the flat plate, the point of beginning of the wake, the free stream turbulence level was found to be 0.4 percent for no grid, 2.56 percent with square bars grid and 4 percent with circular rods grid.

4.2 Mean Velocity Profile. Mean velocity profiles at six axial stations and for three inlet free stream turbulence levels are shown plotted in Figs. 4 (*a*, *b*) and (*c*). It is clear from these figures that the presence of free stream turbulence did not disturb the symmetry of the profiles. An important observation was made while collecting the data near the wake edge. It was found that the instrument readout was more stable near the wake edges for the cases of data presented in Figs. 4 (*b*) and 4 (*c*) compared to the case of data presented in Fig. 4 (*a*). This was probably due to the fact that the presence of free stream turbulence reduces intermittency at the wake edges.

4.3 Wake Recovery Rate. The variation of the wake centerline velocity with downstream distance for the three free stream turbulence levels is presented in Fig. 5 (*a*). It is clear from this plot that an increase in the free stream turbulence level increases the wake recovery rate. A logarithmic plot of data presented in Fig. 5 (*a*) is shown in Fig. 5 (*b*). The change in the slope of the lines in Fig. 5 (*b*) represents the change in the velocity power law. For a change in free stream turbulence level from 0 to 4 percent the velocity power index changed from −0.50 to −0.58. Based on this change in velocity power index the value of α in equation (18) suggests a value of 4. For a free stream turbulence level of the order of 15 percent, which is the case in the multistage turbomachines, the velocity power index will be of the order of −0.8 for the no pressure gradient case and is significantly

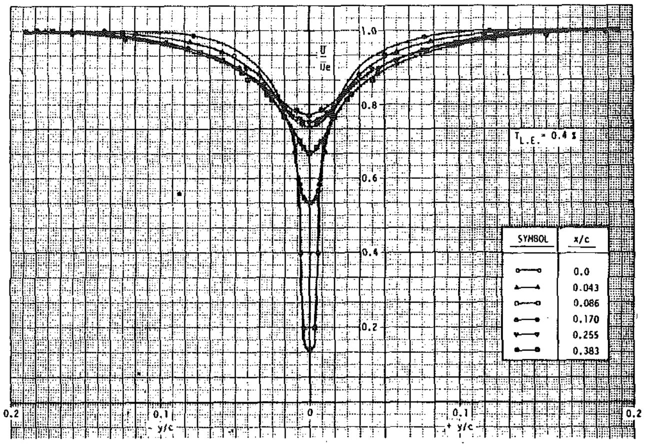

Fig. 4(*a*) Mean velocity profile with downstream distance ($T_{L.E} = 0.004$)

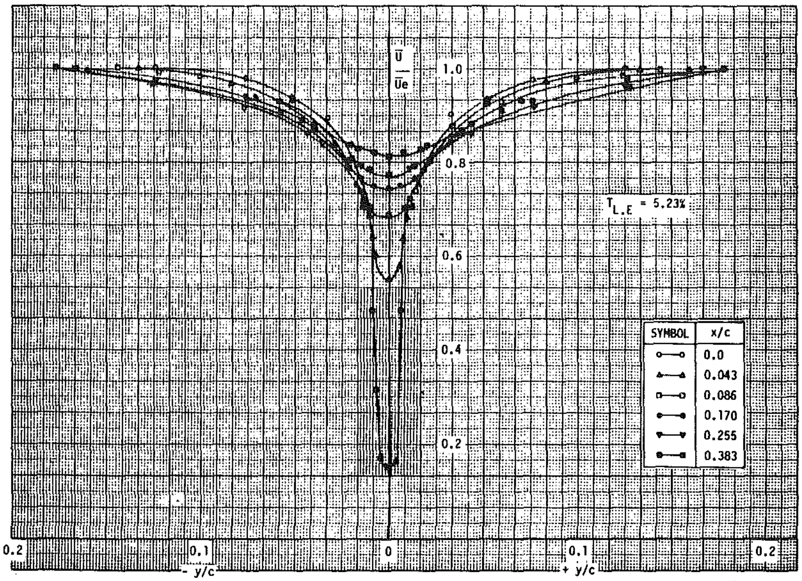

Fig. 4(*b*) Mean velocity profile with downstream distance ($T_{L.E} = 0.0523$)

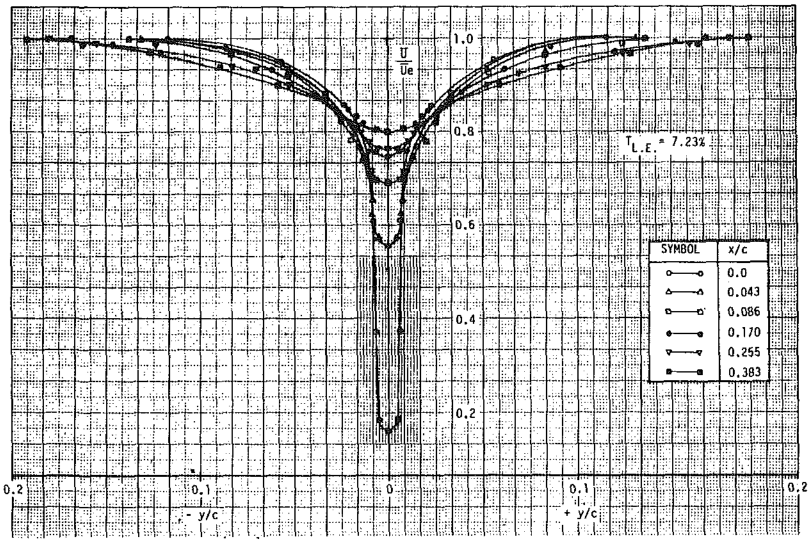

Fig. 4(*c*) Mean velocity profile with downstream distance ($T_{L.E} = 0.0723$)

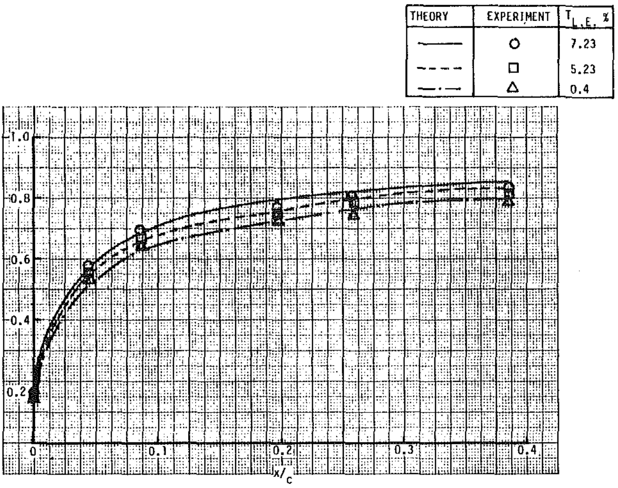

Fig. 5(*a*) Variation of wake centerline velocity with downstream distance

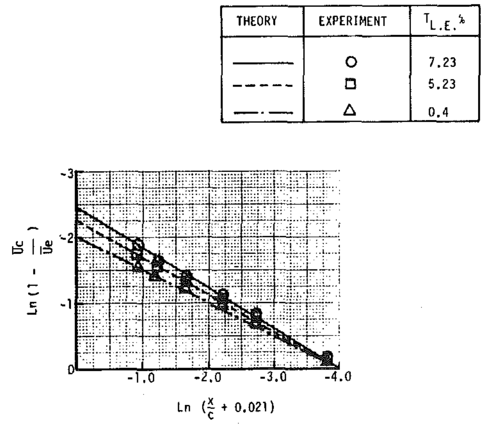

Fig. 5(*b*) Logarithmic variation of wake centerline velocity with downstream distance

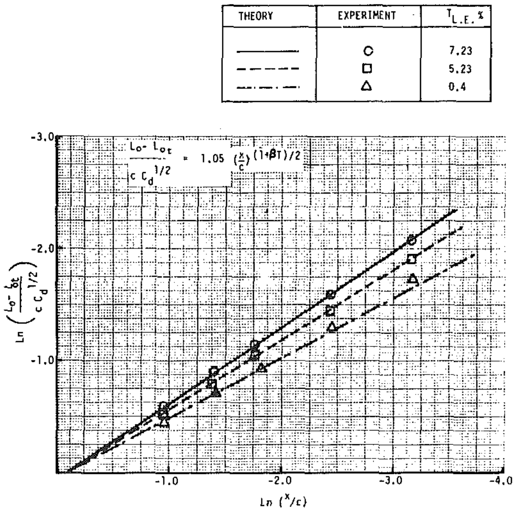

Fig. 6 Logarithmic variation of length scale with downstream distance

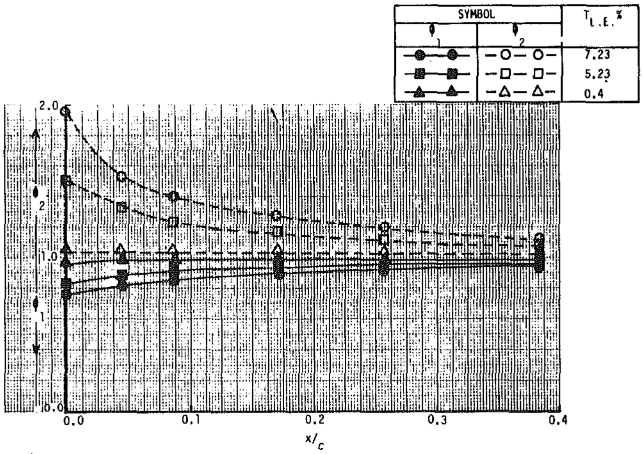

Fig. 7 Variation of turbulence parameters with downstream distance

larger than the ordinary power law of −0.5 for no free stream and no pressure gradient case. Note, therefore, that the above change in velocity power index is purely due to the effect of free stream turbulence. Earlier observation by Eagleson, et al. [3] on flat plate wake data indicates that a presence of free stream turbulence of the order of 10 percent changes the velocity power index to the order of −1.00 and is consistent with the trends predicted by the present theory. The previous investigation on cascade wake by Raj [2] incorporated the effect of pressure gradient and the present model is a more general version accounting for both the pressure gradient and the free stream turbulence effect on wake development. The constant K in equation (18) was found to depend upon the value of ϕ_2 at the trailing edge and is given by the following correlation.

$$K = \frac{2.70}{\phi_{2t} + 0.76}$$

For a zero free stream turbulence case $\phi_{2t} = 1$ and K becomes equal to 1.534, which is of the order of magnitude of 1.25 reported in reference [2]. The discrepancy in the value of K is due to the fact that the correlations developed in the present investigation are based on the flat plate data while the correlations given in references [2, 20] are based on isolated airfoil and cascade of airfoils data. The trailing edge thickness in both the cases is different. The value of x_0/c in the present investigation was found to be 0.021. The coefficient of drag in the absence of free stream turbulence was found to be 0.0064. The coefficient of drag with free stream turbulence was obtained from the modified form of a correlation given in reference [11] and is as follows.

$$C_d = C_{d0}(1 + 4.8T) \tag{21}$$

A few important observations can be made from Fig. 5 about the wake centerline velocity.

1 The effect of free stream turbulence on wake centerline is predominant only in the near wake region, $x/c < 0.3$.

2 The wake centerline velocity recovers to about 65 percent for $x/c < 0.1$.

3 The wake velocity power index is strongly dependent upon the free stream turbulence level.

4 The constant of proportionality in equation (18) is dependent upon trailing edge conditions.

4.4 Length Scale (Half Wake Width). The effect of free stream turbulence on the variation of wake length scale in the downstream direction is shown in Fig. 6. It is clear that the free stream turbulence increases the length scale in the downstream direction. The increase in the length scale of the wake is adequately given by the following correlation.

$$\frac{L_0 - L_{0t}}{c\,C_d{}^{1/2}} = 1.05\left(\frac{x}{c}\right)^{(1+\beta T)/2}$$

where L_{0t} is the value of the length scale at the trailing edge of the flat plate. The value of β obtained from the experimental data is 8.27. The predictions of the growth law for the length scale of the wake with downstream distance in the presence of free stream turbulence are in good agreement with the data obtained experimentally (Fig. 6). It is interesting to note that the increase in exponent of the length scale is nearly twice the value of exponent for the recovery of the wake centerline velocity. This is due to the fact that free stream turbulence acts strongly at the wake edge than at the wake centerline. The higher is the free stream turbulence, the quicker is the growth of the wake.

4.5 Turbulence Parameters. The parameters ϕ_1 and ϕ_2 are known as turbulence parameters. They are given by the following equations derived earlier in Section 2.

$$\phi_1 = \left[\frac{x}{c} + \frac{x_0}{c}\right]^{\alpha T/2}$$

$$\phi_2 = \left[\frac{x}{c} + \frac{x_0}{c}\right]^{-\beta T/2}$$

It was observed in Sections 4.3 and 4.4 that α was found to be 4, β was found to be 8.27 and x_0/c was found to be 0.021 from the present investigation. The plots of ϕ_1 and ϕ_2 are shown in Fig. 7. As mentioned in Section 2, these parameters represent the effect of free stream turbulence on velocity and length scales, respectively. The behavior of ϕ_1 and ϕ_2 is inverse to each other. While ϕ_1 reduces the velocity scale, ϕ_2 increases the length scale with increase in free stream turbulence. However, both the parameters approach unity for zero free stream turbulence level or for far downstream distances where the free stream turbulence is substantially dissipated. The plots of these parameters also indicate that the maximum effect of free stream turbulence is felt only up to $x/c < 0.2$ and this effect is negligible beyond $x/c > 1$.

4.6 Similarity. In Figs. 8 (a, b) and (c) an effort is made to reduce the velocity profiles given in Figs. 4 (a, b) and (c) to a single curve. For this purpose, $L_0\,\phi_2$ is used as the length scale while $U_0\phi_1$ is used as the velocity scale. L_0 is the distance from the wake centerline to a point in the lateral direction where the velocity defect is 50 percent of the velocity scale $U_0 = \overline{U}_e - \overline{U}_c$. It is clear from Figs. 8 (a, b) and (c) that the similarity in the mean velocity profile is maintained to a good extent and the similarity profiles are well described and lie between the functions $[1-(\eta/2)^{1.5}]^2$ and $e^{-\eta^2/2}$ where $\eta = y/L_0\phi_2$. Compared to the case of no free stream turbulence, a very little scatter of data points is observed at the wake edge. This is due to reduction in intermittency at the wake edges in the presence of stream turbulence. The ratio $U_0L_0\phi_1\phi_2/\overline{U}_ec$ is found to be nearly constant at all the axial locations beyond $x/c > 0.05$ (Fig. 9). This confirms the similarity assumptions made in Section 2. However, for $x/c < 0.05$ a slight scatter in the value $U_0L_0\phi_1\phi_2/\overline{U}_ec$ is observed.

4.7 Displacement Thickness, Momentum Thickness, Shape Factor and Energy Thickness. The variation of shape factor (H), with downstream distance from the trailing edge of the flat plate is shown in Fig. 10. The displacement thickness (δ_1),

$$\delta_1 = \int_{-\infty}^{+\infty}\left(1-\frac{\overline{U}}{\overline{U}_e}\right)dy$$

after substitution of equation (3) can be rewritten as

$$\frac{\delta_1}{c} = \frac{U_0L_0\phi_1\phi_2}{\overline{U}_ec}\int_{-\infty}^{+\infty} f d\eta \qquad (22)$$

It is also shown in Section 4.6 that the similarity profile f can be well described by the function

$$f = e^{-\eta^2/2}$$

Therefore, (22) becomes

$$\frac{\delta_1}{c} = \frac{U_0L_0\phi_1\phi_2}{\overline{U}_ec}(2\pi)^{1/2} \qquad (23)$$

since $U_0L_0\phi_1\phi_2 = K_1$ from equation (7). Therefore δ_1, should be constant for a given level of free stream turbulence. A plot of $U_0L_0\phi_1\phi_2/\overline{U}_ec$ (Fig. 9) when multiplied with $(2\pi)^{1/2}$ gives the results for displacement thickness. However, note that the larger the free stream turbulence, the higher the value of δ_1, as is evident from Fig. 9.

The momentum thickness on the other hand, should increase slightly near the trailing edge and farther downstream ($x/c \sim 0.38$) becomes constant. Since

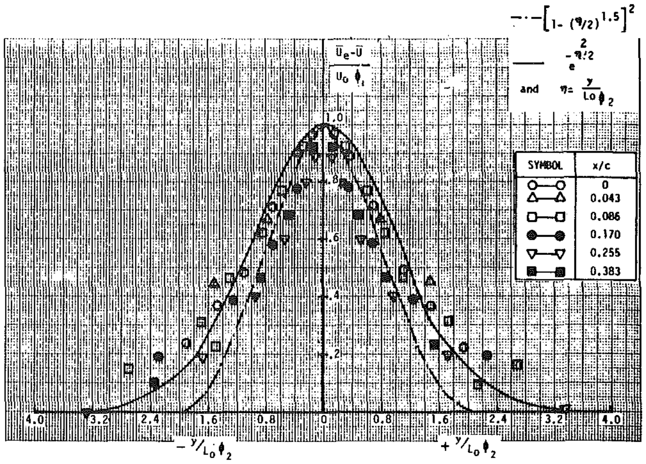

Fig. 8(a) Similarity of mean velocity profile ($T_{L.E} = 0.004$)

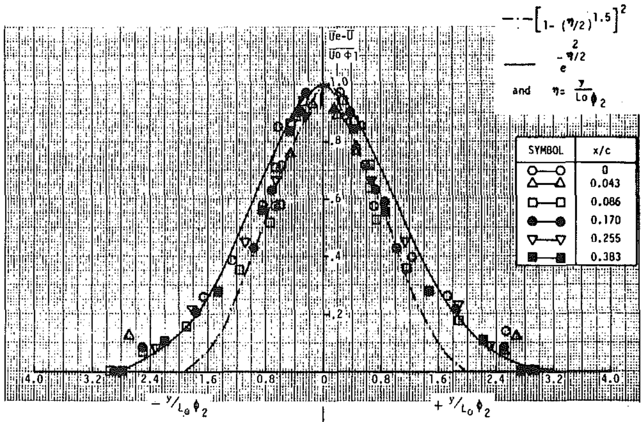

Fig. 8(b) Similarity of mean velocity profile ($T_{L.E} = 0.0523$)

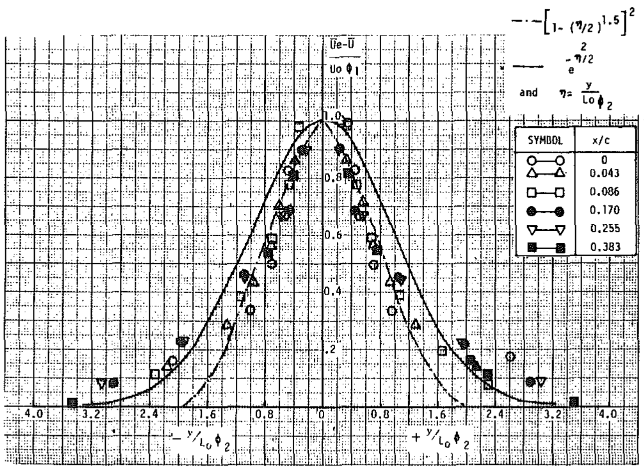

Fig. 8(c) Similarity of mean velocity profile ($T_{L.E} = 0.0723$)

$$\theta = \int_{-\infty}^{+\infty}\frac{\overline{U}}{\overline{U}_e}\left(1-\frac{\overline{U}}{\overline{U}_e}\right)dy$$

after substitution of equation (3) becomes

$$\theta = \frac{U_0L_0\phi_1\phi_2}{\overline{U}_e}\left(\int_{-\infty}^{+\infty} f d\eta - \frac{U_0\phi_1}{\overline{U}_e}\int_{-\infty}^{+\infty} f^2 d\eta\right)$$

writing

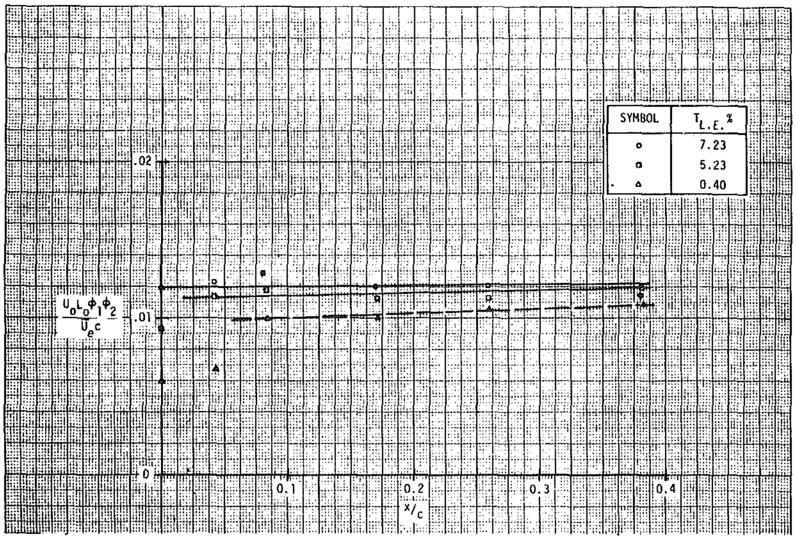

Fig. 9 Variation of $U_0 L_0 \phi_1 \phi_2 / \overline{U}_e c$ with downstream distance

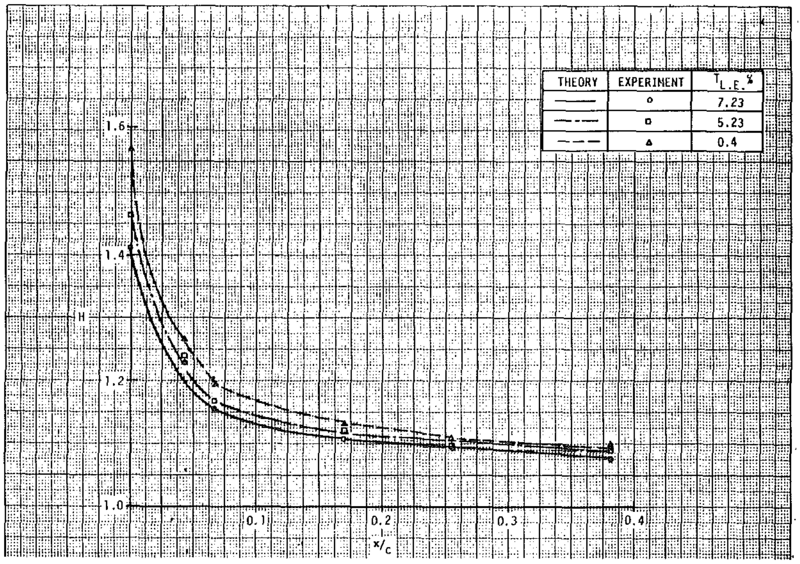

Fig. 10 Variation of shape factor with downstream distance

$$I_1 = \int_{-\infty}^{+\infty} f d\eta \quad \text{and} \quad I_2 = \int_{-\infty}^{+\infty} f^2 d\eta \tag{24}$$

$$\frac{\theta}{c} = \frac{K_1}{\overline{U}_e c}\left[I_1 - \left(\frac{U_0 \phi_1}{\overline{U}_e}\right) I_2\right]$$

Since for a given similarity velocity profile f, I_1 and I_2 are constant and $U_0\phi_1$ decrease with downstream distance, therefore θ/c increases with downstream distance. However, farther downstream ($x/c > 0.38$) the term $U_0\phi_1/\overline{U}_e \ll 1$ therefore

$$\frac{\theta}{c} \cong \frac{K_1}{\overline{U}_e c} \cong \frac{\delta_1}{c}.$$

Note here also that the larger the free stream turbulence, the larger the increase in momentum thickness. At the trailing edge, a free stream turbulence level of 2.56 and 4 percent will increase the momentum thickness of 9.56 and 15.92 percent, respectively, compared to the turbulence level of 0.4 percent.

The shape factor, H, is obtained from equations (23) and (24), $H = \delta_1/\theta$ and can be rewritten by the following equation

$$\frac{1 - \dfrac{1}{H}}{1 - \dfrac{1}{H_t}} = \frac{\phi_1}{\phi_{1t}}\left(1 + \frac{x/c}{x_0/c}\right)^{-1/2(1+\alpha T)} \tag{25}$$

where ϕ_{1t} and H_t are values of ϕ_1 and H at the trailing edge. The theoretical curve (equation (25)) is plotted together with the experimentally obtained results (Fig. 10) and is found to be quite satisfactory. It is clear from the data and equation (25) that free stream turbulence reduces the value of shape factor.

A discussion on energy thickness and other related parameters is described in reference [22].

5 Conclusions

The theoretical and experimental investigation of the free stream turbulence on the wake behavior leads to the following conclusions:

1 Mean velocity profiles are observed to be nearly symmetrical in the presence of free stream turbulence.

2 Similarity in the mean velocity profiles is maintained to a good extent when the profiles are normalized with respect to analytically derived turbulence dependent parameters ϕ_1 and ϕ_2.

3 The higher the free stream turbulence, the greater is the recovery of the wake centerline velocity. The decay law for the centerline velocity defect due to free stream turbulence is well described by equation (18).

4 The higher the free stream turbulence, the greater is the increase in length scale. The growth law of length scale with downstream dis-

tance due to free stream turbulence is well described by equation (20).

5 The behavior of the turbulence parameters ϕ_1 and ϕ_2 is inverse in character and they tend to unity for far wake ($x/c > 1.0$).

6 The displacement thickness of the wake increases with the increase in free stream turbulence level and can be predicted by equation (22). A similar trend is observed for the momentum thickness and is predicted by equation (24).

7 Increase in free stream turbulence reduces the shape factor and the shape factor approaches unity towards the far wake regions. The higher the turbulence level, the greater is the decrease in shape factor as observed from the decay law given by equation (25).

Acknowledgment

The authors wish to thank Professor J. L. Lumley for valuable comments on the theoretical developments. During the course of this investigation the first author was supported by the FRAP-CUNY award and the second author by the NSF. Eng. 76-09611. The authors also thank the Curtiss-Wright Corporation for their help in the preparation of the manuscript and the figures.

References

1 Raj, R. and Lumley, J. L., "A Theoretical Investigation on the Structure of Fan Wakes," *Journal of Fluids Engineering,* Vol. 100, Mar. 1978, p. 113.

2 Raj, R., "On the Investigation of Cascade and Turbomachinery Rotor Wake Characteristics," Ph.D. Thesis, Department of Aerospace Engineering, The Pennsylvania State University, Nov. 1974.

3 Eagleson, P. S., Huval, C. J. and Perkins, F. E., "Turbulence in the Early Wake of a Fixed Flat Plate," MIT Hydrodynamic Lab., TR. No. 46, Feb. 1961.

4 Kline, S. J., Lisin, A. V., and Waitman, B. A., "Preliminary Experimental Investigation of Effect of Free Stream Turbulence on Turbulent Boundary Layer Growth," NASA, TND-368, 1969.

5 Charnay, G., Compte-Bellot, G., and Mathieu, J., "Development of a Turbulent Boundary Layer on a Flat Plate in an External Turbulent Flow," AGARD-CP-93, Paper No. 27, 1971.

6 Huffman, G. D., Zimmerman, D. R., and Bennet, W. A., "The Effect of Free Stream Turbulence Level on Turbulent Boundary Layer Behavior," AGARD No. 164, Paper I-5, 1972.

7 Robertson, J. M., and Holt, C. F., "Stream Turbulence Effects on Turbulent Boundary Layer," *Proceedings of ASCE,* Vol. 98, No. HY6, 1972, p. 1095.

8 Tsuji, Y., and Iida, S., "Influence of Free Stream Turbulence on Mean Velocities of Turbulent Boundary Layer Without Pressure Gradient," *Transactions of Japan Society of Aerospace Space Science,* Vol. 15, No. 29, 1972, p. 105.

9 Evans, R. L., and Horlock, J. H., "Calculation of the Development of Turbulent Boundary Layers With a Turbulent Free Stream," Trans. ASME, 1974, p. 348.

10 Bradshaw, P., "Effect of Free Stream Turbulence on Turbulent Shear Layers," I.C. Aero. Report, 74-10, 1974.

11 Green, G. E., "On the Influence of Free Stream Turbulence on a Turbulent Boundary Layer as it Relates to Wind Tunnel Testing at Subsonic Speeds," AGARD Report No. 602, 1973.

12 Hall, D. J., and Gibbings, J. C., "Influence of Free Stream Turbulence and Pressure Gradient Upon Boundary Layer Transition," *Journal of Mechanical Engineering Science,* Vol. 14, No. 2, 1972.

13 Dryden, H. L., *Transition from Laminar to Turbulent Flow, Turbulent Flows and Heat Transfer,* Edited by C. C. Lin, Princeton University Press, Princeton, 1959, p. 3.

14 McDonald, H., and Kreskovsky, J. P., "Effect of Free Stream Turbulence on Turbulent Boundary Layer," *International Journal of Heat and Mass Transfer,* Vol. 17, 1974, p. 705.

15 Junkhan, G. H., and Serovy, G. K., "Effect of Free Stream Turbulence and Pressure Gradient on Flat Plate Boundary Layer Velocity Profiles and on Heat Transfer," ASME *Journal of Heat Transfer,* 1967, p. 169.

16 Kestin, J., "The Effect of Free Stream Turbulence on Heat Transfer Rates," *Advances in Heat Transfer,* Edited by T. F. Irvine and H. P. Hartnett, Vol. 3, 1966, p. 1.

17 Michel, R., "Effects of Flow Turbulence and Noise on Aerodynamic Phenomena and Wind Tunnel Results," AGARD Report No. 615, 1974.

18 Pal, S., and Raj, R., "Wake Boundary Layer Interaction in Turbomachinery," working paper.

19 Tennekes, H., and Lumley, J., *A First Course in Turbulence,* MIT Press 1974.

20 Raj, R., and Lakshminarayana, B., "Characteristics of the Wake Behind a Cascade of Airfoils," *Journal of Fluid Mechanics,* Vol. 61, 1973, p. 707.

21 Schlicting, H., *Boundary Layer Theory,* McGraw-Hill, 1955, p. 116.

22 Pal, S., "Wake Boundary Layer Interactor in Turbomachinery," Ph.D. Thesis, Department of Mechanical Engineering, CCNY, 1980.

B. A. Ajakaiye
Lecturer,
University of Ife,
Department of Chemical Engineering,
Ile-Ife, Nigeria
Mem. ASME

J. C. Dent
Reader,
University of Technology,
Department of Mechanical Engineering,
Loughborough,
England

A Correlation for Air Velocities in Cylindrical Prechambers of Diesel Engines

Theoretical analysis and measurements of air velocities in cylindrical prechambers of the indirect injection type Diesel engine are reported. Comparisons are made between the theoretical analysis and the measurements for two cylindrical prechambers tested in the present study and the results of previous investigators [4–6]. A correlation is derived to link air velocity in the cylindrical prechamber and known engine parameters. The results show that there is poor and inconsistent agreement between theory and experiment in some of the cases considered. Reasons are suggested to explain these inconsistencies. The derived correlation could serve as an additional tool for the engine designer in predicting air motion and hence combustion and heat transfer in the prechamber of indirect injection diesel engine.

1 Introduction

It is desirable to fully understand the air motion in both the direct injection and the indirect injection diesel engines. The air motion directly influences the mixing of the fuel and air and, thus, the subsequent combustion process. The combustion process, in turn, determines the composition of exhaust products. In addition, the air motion has a direct influence on the convective heat transfer in the diesel engine.

There have been many more theoretical and experimental investigations of air motion in the direct injection diesel engine than in the indirect injection engine. There is still a need to better understand air motion in the prechamber of the indirect injection diesel.

This paper presents a study of air motion in cylindrical prechambers; the conclusion is the derivation of a correlation between swirl velocities and engine parameters.

The correlation of experimental data is a well tried technique which has not been extended to the investigation of the gas motion in the prechamber of an indirect injection diesel engine. It is noted that there are few published studies of the measurement of air velocity patterns in the prechamber of diesel engine. There is also little work toward making a direct comparison of the computations of a mathematical model with experimental measurements. This may be a main reason why the technique of correlation has not been used to provide estimates of air velocities in different prechambers thus avoiding the necessity of making experimental measurements in each case.

The empirical correlation proposed in this paper was developed as a result of a combined theoretical and experimental investigation discussed in detail in [7]. It is considered that the correlation relationship obtained could be used to obtain estimates of air velocity in the prechamber for design calculations.

2 Previous Theoretical Analyses of Air Motion in the Prechamber

The two methods that have been applied to the computation of mean air velocities in the prechamber are (1) conservation of angular momentum [1] and (2) conservation of kinetic energy [2]. These two analyses employed the two common assumptions that the total trapped mass in the engine remains constant during the compression and expansion strokes and that the pressure and temperature in the engine is uniform at each crank angle. In addition Alcock [1] assumed that the throat was tangential to the prechamber periphery and that the gas mass in the prechamber rotated as a solid body. He also neglected the effects of wall friction. The momentum due to the gas jet from the throat is conserved within the prechamber and at the end of the compression stroke the angular velocity of the gas in the prechamber w_p, is given by:

$$w_p = k \frac{V_p N}{A_{th}} \frac{R_p}{{R_I}^2} \frac{\left\{\frac{{f^2}_1(\Theta)}{{f_2}^3(\Theta)}\right\} d\Theta}{\left\{\frac{f_1(\Theta)}{{f_2}^2(\Theta)}\right\} d\Theta} \tag{1}$$

Knight [2] allowed for the loss of energy by wall friction by using pipe friction coefficients. The kinetic energy quantities were calculated under the following headings:

1 induction induced air motion
2 fuel—injection induced air motion
3 piston induced air motion (squish energy)
4 energy induced by transfering gas to and from the prechamber
5 kinetic energy loss from prechamber due to outflow of gas during expansion
6 energy loss due to surface friction at the walls

The mean kinetic energy in each chamber at any crank angle is obtained by summing the increments (1–6) above so that

$$E_p = \sum_{i}^{vi} \left({}^{\Theta}\int_0 E \right) \tag{2}$$

and the mean velocity, U_p, in the chamber is given as

$$U_p = \frac{2E_P}{m_p} \tag{3}$$

Contributed by the Gas Turbine Division for publication in the JOURNAL OF ENGINEERING FOR POWER. Manuscript received at ASME Headquarters January 18, 1980.

Comparison of the two methods of conservation of angular momentum and conservation of kinetic energy in the prechamber suggests that application of the principle of conservation of angular momentum for air motion in the prechamber is more realistic than the application of the principle of conservation of kinetic energy especially for the case when the throat is tangential to the periphery of the prechamber. The kinetic energy solution is totally insensitive to the inclination of the throat. This is a serious drawback since the throat inclination relative to the prechamber curved wall must have a decisive effect on the magnitude and distribution of the mean gas velocity in the prechamber.

Jankov [3] combined the two principles of conservation of energy and of momentum. He applied the conservation of energy principle separately to the main cylinder and the prechamber. The piston work and the heat transfer across the engine walls were considered and the unsteady flow energy equation used. It will be noted that Jankov's analysis allowed for the pressure ratio across the prechamber throat. The principle of conservation of angular momentum was applied to air motion within the prechamber.

3 Previous Experimental Investigations

There are not many published reports of velocity measurement in the prechamber of internal combustion engines. This has been mainly due to the difficulties of measurements.

Most of the published studies have been qualitative. It is now generally accepted that when the throat is tangential to the curvature of the prechamber wall, the air motion is like a forced vortex.

Only a few investigators have published quantitative measurements of velocities in prechambers. Nakajima [6] used high speed photography and obtained velocity patterns at particular crank angles. Hassan [4] used a hot wire anemometer to make measurements in a cylindrical prechamber. Hassan made the velocity measurement in one radial position at one engine speed only.

Horvatin [5] also used hot wires to make velocity measurements in the cylindrical pre-chamber of a diesel engine. He found that for a uniform throat tangential to the prechamber, the air motion is a solid vortex in the sixty deg "before top dead center" (BTDC) up to "top dead center" (TDC). He also found that swirl velocity increases with engines speed though the increase is less than linear. Horvatin's evidence supports other investigators' finding that air motion in the prechamber resembles a forced vortex around the TDC of the compression stroke.

4 Present Study

The initial objective was to develop a mathematical model capable of predicting air velocities in the prechamber of an internal combustion engine. The two methods of analysis outlined by Alcock [1] and by Jankov [3] were combined. Solutions of the throat velocities showed that Alcock's method of considering directly the mass transport from the main cylinder to the prechamber in terms of relative volumes was preferable to the more complicated energy analysis of Jankov. A fuller discussion of the throat velocity analysis is given in [7].

4.1 Angular Momentum Equations for Air Motion in the Prechamber. The analysis of the air motion in the prechamber is simplified by making the following assumptions:

1 There is no overlap of the inlet and exhaust valves.

2 The total trapped mass remains constant throughout the compression and expansion strokes.

3 The trapped air mass is considered to behave like an ideal gas. The compression and expansion are taken to be polytropic with an index of 1.33.

4 A uniform shape of prechamber is assumed (e.g., cylindrical or spherical).

5 The gas in the prechamber rotates as a solid body.

6 The connecting passage is tangential to the prechamber curved surface.

The assumption of conservation of angular momentum in the prechamber means that at any instant the resultant external torque on the gas in the prechamber equals the rate of change of angular momentum of the gas mass plus the net rate of flow of angular momentum across the prechamber boundary. In this case, the resultant *external torque is the torque due to friction at the wall. The net flow* of angular momentum is due to the flow of gas through the throat. Therefore, the principle of conservation of angular momentum yields, for the compression stroke,

$$\frac{d}{dt}(Iw)_p - \frac{dm_p}{dt} U_{th} R_1 = F_T \qquad (4)$$

and for the expansion stroke:

$$\frac{d}{dt}(Iw)_p + \frac{dm_p}{dt} w_p R_p{}^2 = -F_T \qquad (5)$$

Equations (4) and (5) can be solved step by step to give the swirl velocity in the prechamber at any instant during the compression and expansion periods.

4.2 The Experimental Program. A three-wire probe, with the wires set mutually perpendicular, was manufactured and used to measure the velocity vector in the prechamber. The details of construction and the calibration of the three-wire probe may be found in [7]. An error assessment based on calibration data obtained in wind tunnel tests predicted measurement errors of −5 to +15 percent in the velocity magnitude.

The test engine was a Ruston and Hornby WB four-stroke air-cooled single cylinder engine with a side valve arrangement and a flat-topped piston. The engine's geometric specifications are given in Table 1. The cylinder head was specially fabricated in order to achieve the idealized cylindrical shape of the prechamber and to make the circular throat tangential to the curved periphery of the prechamber at their intersection. The main features of the prechamber arrangement is shown in Fig. 1. The side valve arrangement results in recesses both around the valves and in the cylinder head to accomodate the valve lift. It is therefore inevitable that there was a large clearance volume; for this reason, the maximum compression ratio that could be investigated was 12:1 for a realistic prechamber volume of 8.0 cm^3.

Nomenclature

a = constant in equation (8)
A = cross-sectional area of main cylinder
A_{th} = cross-sectional area of throat
b = constant in equation (8)
b_1 = thickness of prechamber
D = diameter of main cylinder
D_p = diameter of prechamber
D_{th} = diameter of throat
E_p = kinetic energy in prechamber
$f_1(\Theta)$ = function of piston travel
$f_2(\Theta)$ = function of piston velocity
F_T = friction torque
HA = horizontal angle
I_p = moment of inertia of air mass in prechamber
k = constant in equation (1)
m_p = mass of gas in prechamber
N = engine speed
$R_1 = (D_p - D_{th})/2$
R_I = radius of gyration of air mass in prechamber
R_p = radius of prechamber
Re_m = Reynolds number in main cylinder
Re_p' = Reynolds number in prechamber
S = piston stroke
t = time
U = absolute gas velocity
U_p = mean velocity in prechamber
U_{swirl} = solid swirl velocity in prechamber
U_{th} = air velocity in throat
VA = vertical angle
V_p = volume of prechamber
w_p = angular velocity in prechamber
ATDC = after top dead center
BTDC = before top dead center
ESBRV = equivalent solid body rotational velocity
TDC = top dead center
Θ = crank angle from TDC of induction stroke
μ_i = instantaneous dynamic viscosity
π = ratio of circle circumference to diameter
ρ_i = instantaneous density
σ = ratio of prechamber volume to total volume at TDC

Table 1 Geometric specifications of prechamber engines discussed in present study

	Present Cylindrical Prechambers				
	25mm dia	51mm dia	Hassan [4]	Horvatin [5]	Nakajima [6]
Bore, *D* mm	76.2	76.2	76.2	115.0	68.0
Stroke, *S* mm	82.5	82.5	82.5	140.0	68.0
Con-Rod Length Crank Radius	4.0	4.0	4.0	5.0	
Compression Ratio	12:1	7.8:1	8.1	15.5:1	7:1
Prechamber Diameter, mm	25.5	51.0	51.0	54.0	33.0
Prechamber Thickness, mm	15.0	15.0	9.5	33.2	23.4
Throat Area, Bore Area, %	1.00	1.00	1.55	2.50	1.00

A micrometer screw arrangement was used to enable the traversing of the probe across the prechamber. There were three measuring positions (labelled A, B and C in Fig. 1) spaced around the circumference of the prechamber. Provision was made so that the probe could be rotated on its axis. It was hoped that measurement errors would be minimized if the measurements of mean velocity made with the probe set at three different orientations were averaged.

Two cylindrical prechambers were investigated. One had a diameter of 25mm and the other, 51mm. Both had a thickness of 15mm. There were four radial measuring locations in the smaller prechamber and seven locations in the bigger prechamber. The range of engine speeds investigated was limited to 600–1100 rpm by the existing motoring arrangements.

The three velocity signals from the the three wires of the probe were recorded simultaneously in analogue form on magnetic tape using a RACAL 4 tape recorder. The gas pressure was measured using a KISTLER capacitive pressure transducer (Type 601H). The gas temperature was calculated from the measured pressure using a polytropic index of 1.33. The recorded analogue signals were digitized on a Hewlett Packard (Model 5451A) Analogue to Digital converter. The digital data was then processed on an ICL computer to give the velocity vector magnitudes and angles at intervals of about 5 deg crank throughout the engine cycle.

5 Experimental Results

The mean velocity vectors were referred to geometric planes of the cylindrical prechambers investigated. The reference planes and reference angles for the case of solid body rotation are shown in Fig. 2. The departure from solid body rotation of the gas in the prechamber was indicated by comparison of measured vector angles with the reference values.

The individual results for all the probe position and radial locations are too numerous to present here. A selection of results are reported in [7].

An examination of all the measurements showed that the air motion in the two cylindrical prechambers investigated was not entirely solid-body rotation. A typical set of results are shown in Fig. 3(*a*, *b*, *c*). It is noted that the difference between the reference angles and the measured vector angles does not always fall within the predicted measurement error of 5–25 deg. In addition, the difference in vector angles for three circumferential measuring positions A, B, C makes it impossible to make a direct comparison of the velocity magnitudes. Therefore, it was decided to resolve the absolute velocity vectors in the direction of solid-body rotation. If all vectors are thus resolved, a direct comparison of the resolved components can be made. This course of action was also justified in view of the fact that the mathematical model was based on the assumption of solid-body rotation of the gas mass in the prechamber.

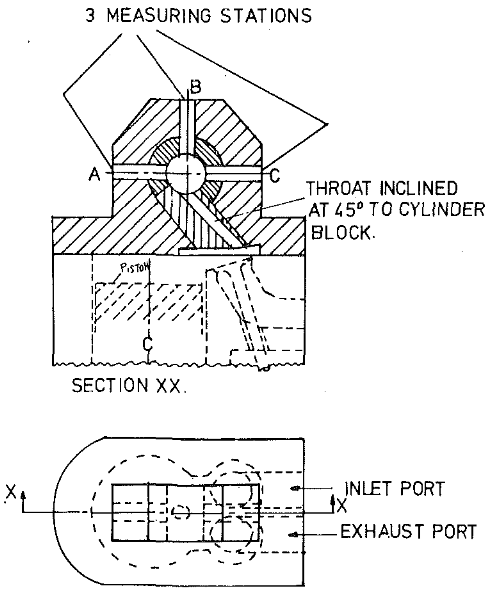

Fig. 1 Illustrative sketch of prechamber

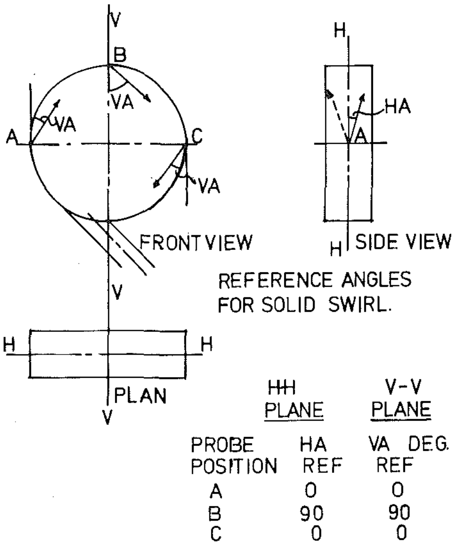

Fig. 2 Reference planes in cylindrical prechamber

5.2 Comparison of the Mathematical Model with Experimental Data. It is recalled that the mathematical model was based on the assumption of solid-body rotation of the gas in the cylindrical prechamber. It was found that there are variations in the radial profiles for the measuring positions A, B and C. In order to determine a consistent mean velocity profile to compare with the mathematical model it was decided to calculate an equivalent solid body velocity in the way suggested by Tindal, et al. [10]. The average swirl velocity of all three measuring positions was taken to give one value for each radial measuring location at each crank angle. This results in one radial profile of velocity for each crank angle. The equivalent solid body velocity was determined by equating the angular momentum represented by the area under each radial profile to the area under a straight line passing through the origin (center) of the prechamber. This equivalent solid body velocity is then compared with the results of the mathematical model. These comparisons are shown in Figs. 4–8 for the two cylindrical prechambers of the present study and for some previously published studies by Hassan [4], Horvatin [5] and Nakajima, et al. [6]. It should be noted that it has not been possible to calculate ESBRV for the data of Hassan, Horvatin and Nakajima, et al. The experimental data shown in Figs. 9–11 were single wire measurement near the prechamber wall. Also, the ESBRV profiles shown

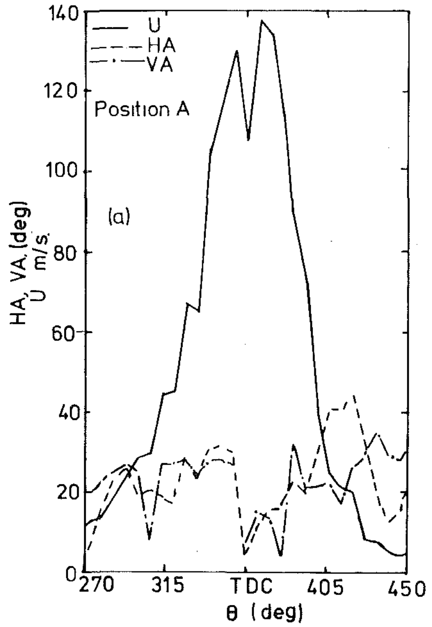

Fig. 3(*a*) Absolute velocity vector in 25 mm dia

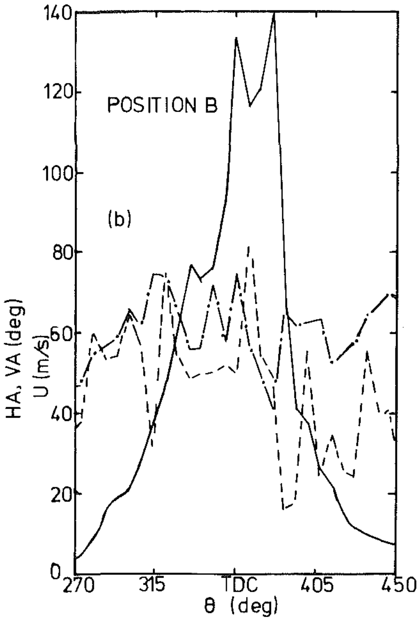

Fig. 3(*b*) cylindrical prechamber (1100 rpm, Location 1)

in Figs. 4–8 are for the radial location nearest to the prechamber wall.

It will be seen that the agreement between the mathematical model and the experimental results is poor especially in the period 60 deg BTDC to 60 deg ATDC which is of prime importance in the cycle of an internal combustion engine. It is also noted that the discrepancy between model and experiment is not consistently in one direction. The model predicts velocities that are lower than experimental results by up to 50 percent for the 25 mm prechamber in the present study whereas the model results are higher than the experimental results of Nakajima, et al. [6] by up to 100 percent.

These very large discrepancies may be due to the following:

1 There was no available data for a flow coefficient that may be applied to the particular case of a throat discharging into a prechamber.

2 Little is known of the mechanism of mixing of the jet from the throat with the gas already in the prechamber.

3 Some disturbance is caused to the flow in the prechamber due to the size of the probe and its being tranversed radially into the prechamber.

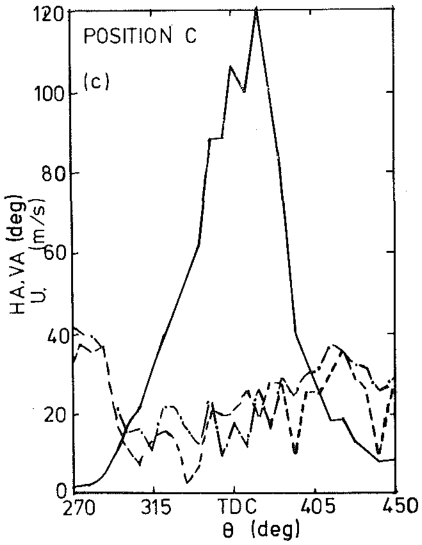

Fig. 3(*c*) Stations A. B. C

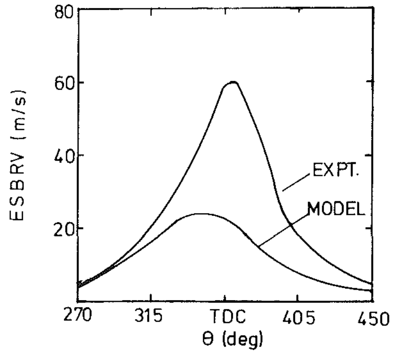

Fig. 4 Comparison of ESBRV with mathematical model (ϕ 25 mm, 600rpm)

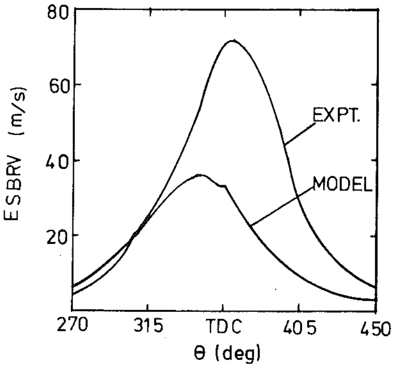

Fig. 5 Comparison of ESBRV with mathematical model (ϕ25 mm, 900rpm)

4 The assumption of a uniform solid swirl in the mathematical model may be too optimistic.

From these observations it was concluded that a simple model of air motion in a prechamber based on the assumption of solid-body rotation of the gas in the prechamber cannot accurately predict the mean gas velocity in the prechamber.

6 Experimental Data

The experimental data employed in the development of the correlation included the results of the authors' investigation reported in [7] and previously published data by other authors [4, 5, 6].

The mean velocity vectors, obtained by the present authors, were

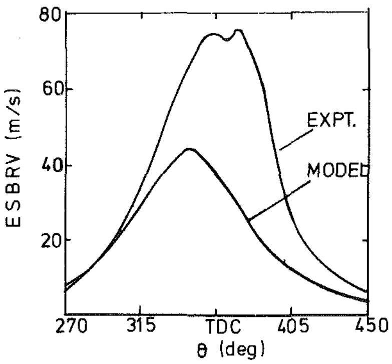

Fig. 6 Comparison of ESBRV with mathematical model (ϕ25mm, 1100rpm)

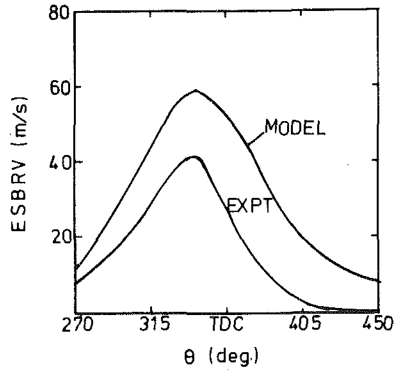

Fig. 7 Comparison of ESBRV with mathematical model (ϕ51mm, 600rpm)

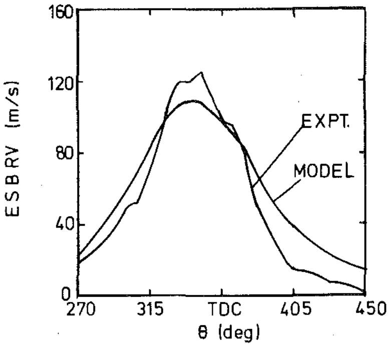

Fig. 8 Comparison of ESBRV with mathematical model (ϕ51mm, 1100rpm)

referred to geometric planes of the cylindrical prechambers investigated. The individual results for all the probe positions and radial locations are too numerous to present here. A selection of the results are reported in [7].

An examination of all the measurements showed that the air motion in the two cylindrical prechambers investigated was not entirely solid-body rotation. In addition, the differences in the velocity vector angles for the three circumferential measuring positions, A, B, and C make it impossible to make a direct comparison of the absolute velocity magnitudes. Therefore it was decided to resolve the absolute velocity vectors in the direction of solid-body rotation. If all the vectors are thus resolved, a direct comparison of the resolved components (swirl velocities) can be made.

The mean of the swirl velocities at measuring positions A, B, and C were taken and the velocity values for the probe location 1 (measuring point nearest the prechamber wall) were those utilized in the correlation analysis.

7 The Correlation

Because of the absence of any previous investigation along these lines, a method of "trial and error" was adopted. We attempted to find a relationship between a prechamber Reynold's number and a main cylinder Reynolds number based on the engine speed.

The experience gained during the theoretical investigation reported in [7] helped in isolating the most significant of the engine parameters.

For the main cylinder the two dimensions of interest are the bore diameter, D, and piston stroke, S. It is noted that the mean piston speed is proportional to the product of engine speed and piston stroke. If the mean piston speed is chosen as the characteristic velocity in the main cylinder Reynolds number then the obvious dimension to be taken as the characteristic length is the bore diameter. For the cy-

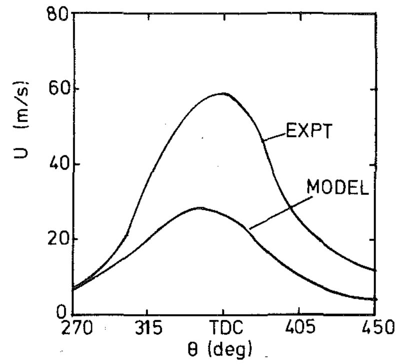

Fig. 9 Comparison of Hassan's [4] data with mathematical model

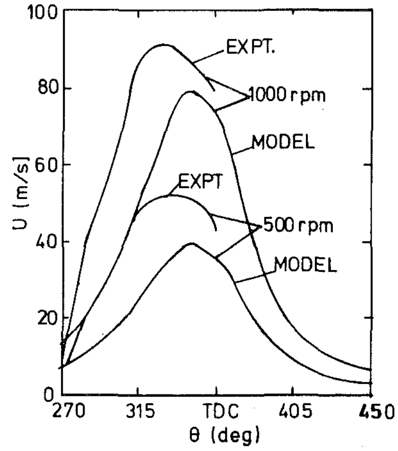

Fig. 10 Comparison of Horvatin's [5] data with mathematical model

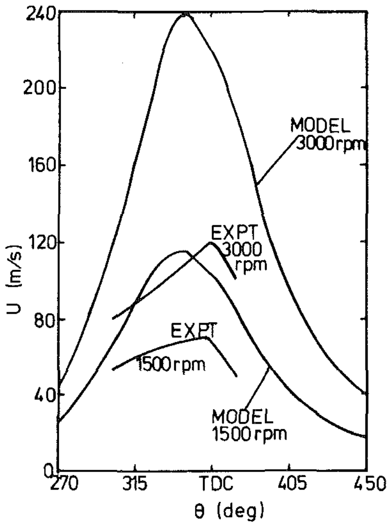

Fig. 11 Comparison of Nakajima's [6] data with mathematical model

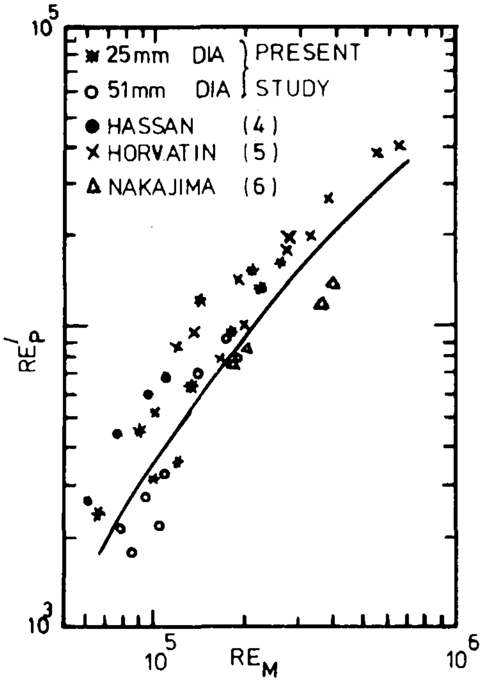

Fig. 12 Correlation for air velocity in prechamber

lindrical prechamber the important dimensions are the diameter D_p and the thickness b_1. If the characteristic velocity chosen for the prechamber Reynolds number is the swirl velocity, U_{swirl}, at the periphery of the prechamber, then it may be argued that the effect of the prechamber diameter is included in U_{swirl}. The thickness of the prechamber, b_1, could then be taken as the characteristic length.

It was recognized that the prechamber and the main cylinder properties must be related by the size of the throat connecting them. The theoretical model had shown that a reduction in the ratio of throat cross-sectional area to piston area (A_{th}/A) leads to an increase in the throat velocity and, hence, to an increase in the mean velocity of the gas in the prechamber. It had also been shown that an increase in the ratio of prechamber volume to the total volume at TDC results in a proportional increase in the prechamber gas velocity. The above examination of the engine geometric parameters formed the basis of the derivation of the correlation outlined below.

A Reynolds number, Re_m, was defined for the main cylinder as

$$\mathrm{Re}_m = \frac{\rho_i \left(\frac{2\pi NS}{60}\right) * D}{\mu_i} \qquad (6)$$

It is noted that the term in brackets is the mean piston speed and that the characteristic length is the cylinder bore diameter. A Reynolds number, Re'_p, was defined for the prechamber as:

$$\mathrm{Re}'_p = \frac{\rho_i * U_{\mathrm{swirl}} * b_1}{\mu_i} - \left(\frac{A_{th}}{A}\right) * \left(\frac{1}{\sigma}\right) \qquad (7)$$

Here it will be noted that the term $\left(\frac{A_{th}}{A}\right)$ the ratio of throat cross-sectional area to the cylinder cross-section, represents the sudden contraction in the flow between the cylinder and the prechamber. The term containing σ takes into account the proportion of total trapped mass present in the prechamber as the piston comes up to TDC. The characteristic length, b_1, has been chosen because, in the cylindrical prechamber, the throat is situated symetrically on the thickness of the prechamber. It had been pointed out that the prechamber diameter is indirectly involved in the swirl velocity U_{swirl}.

Instances of U_{swirl} were selected in the period 45 deg BTDC to TDC. This period was selected because it is the most relevant part of the cycle with regard to the mixing of injected fuel and air. The data for the five cylindrical prechambers discussed previously were included.

Figure 12 shows a log – log plot of the prechamber's Reynolds number, Re'_p, versus the main cylinder Reynolds number Re_m. A curve was fitted to the data by a means of a least square polynomial procedure which searched continuously until the highest degree of polynomial with a least squares fit was found. The resulting correlation was a straight line of the form

$$\mathrm{Re}'_p = a + b\,\mathrm{Re}_m \qquad (8)$$

where

a and b are constants.
In the present case:
$a = -1881$
$b = 0.556$

There are two major points of criticism to note in Fig. 12: (1) the scatter in the data and (2) the limited ranges of Re_m and Re'_p. The problem of the limited range could only be solved if there were more published studies of the measurement of air velocity in various prechambers. Because of the scatter in the data, this correlation in the present form of equation (8) can only be used within the ranges of Reynolds numbers for which it has been obtained.

Conclusions

The following conclusions can be drawn from the above results and discussions.

1 The assumption of solid swirl in the prechamber is an oversimplification.

2 There are significant discrepancies between the mathematical model and experimental results.

3 The two main reasons for the discrepancies are the disturbance to the flow caused by the probe and uncertainties about the throat flow coefficients.

4 A correlation exists between a mean forced vortex air velocity in cylindrical prechamber and other known engine parameters.

5 The derived correlation needs to be tested with the experimental data of many more investigators.

6 If the correlation is verified it could be a quick way of obtaining estimates of gas velocity in cylindrical prechambers.

References

1 Alcock, J. F., "Air Swirl in Oil Engines," *Proceedings of the Institution of Mechanical Engineers*, Vol. 128, 1934, pp. 123-193.

2 Knight, B. E., "The Problem of Predicting Heat Transfer in Diesel Engines," *Proceedings of the Institution of Mechanical Engineers*, Pt. 3C, Vol. 179, 1964-65, pp. 99-112.

3 Jankov, R., "Flow and Mixture Formation in Swirl Prechamber Diesel Engines," *Automobil-Industrie*, Vol. 17, No 2, 1972, pp. 57-73.

4 Hassan, H., "Unsteady Heat Transfer in a Motored Internal Combustion Engine," Ph.D. Thesis, University of Technology, Loughborough, 1968.

5 Horvatin, M., "Beitrag Zur Awendung Des Hitzdraht-Anemometers Fur Stromungs Und Turbulenzmessungen in Verbrennungsmotoren," Dr. Ing. Thesis, Technical University, Munich, 1971.

6 Nakajima, K., Kajiya, S., and Nagao, F., "An Experimental Investigation of the Air Swirl Motion and Combustion in the Swirl Chamber of Diesel Engines," *Bulletin of JSAE*, 1969, pp. 195-209.

7 Ajakaiye, B. A., "Air Motion in an Indirect Injection Diesel Engines," Ph.D. Thesis, University of Technology, Loughborough, 1976.

8 Hassan, H., and Dent, J. C., "Correction for Temperature Loading and High Gas Pressure Effects for the Constant Temperature Hot Wire Anemometer," *Journal of Physics, D. (Applied Physics)* Vol. 2, 1969, pp. 85-92.

9 Dent, J. C., and Derham, J. A., "Air Motion in a Four-Stroke Direct Injection Diesel Engine," *Proceedings of the Institution of Mechanical Engineers*, Vol. 188, 1974, pp. 269-280.

10 Tindal, M. J., Williams, T. J., and El Khafaji, A. H. A., "Gas Flow Measurements in Engine Cylinders," *SAE Transactions*, Paper 740719.

A Mathematical Model for the Stirling Engine Cycle

E. W. Beans
College of Engineering,
The University of Toledo,
Toledo, OH 43606

A mathematical model for the Stirling engine cycle is presented. This model differs from the Schmidt Cycle in that an adiabatic dead space is assumed and that the enthalpy exchange between various volumes is accounted for. The model, in general, predicts performance which is lower than the Schmidt Cycle. The model results in a thermal efficiency which is a function of all design parameters rather than temperature only. A comparison between the p-v diagram from the mathematical model and a measured diagram is in good agreement.

Introduction

A useful mathematical model for analyzing the Stirling engine is the Schmidt Cycle. The Schmidt Cycle was developed by G. Schmidt in 1871 [1]. The Schmidt Cycle is presented in English in references [2] and [3]. The utility of the Schmidt Cycle is that the model consists of a number of closed form equations, which are readily solvable. Hence, the effect of the various design parameters can easily be examined.

The Schmidt Cycle analysis is based on two assumptions which appear to be thermodynamically incorrect. The subject of this paper is to present the thermodynamically correct assumptions and the mathematical model based on these assumptions. The mathematical model is similar to the Schmidt Cycle. The model consists of a set of closed form equations which must be solved simultaneously for each design case. The set can easily be programed for a computer.

Development of Mathematical model

The mathematical model is based on a number of assumptions which were also made for Schmidt Cycle [2]. These common assumptions are:

1. The volume variations in the model are sinusoidal.
2. The instantaneous pressure is uniform throughout the model.
3. The working fluid is a perfect gas, $pv = RT$ and $cp =$ const.
4. The mass of the working fluid within the model is constant.
5. The temperatures of the working fluid is the expansion and compression space are constant.
6. The volume and the average temperature of the dead space are constant.

The mathematical model like the Schmidt Cycle is divided into three volumes: expansion, V_e, dead, V_d, and compression, V_c. The equations which describe the variation in these volumes from assumptions 1 and 6 are:

$$V_e = (V_E/2)(1 + \cos \phi) \tag{1}$$

$$V_c = (\kappa V_e/2)[1 + \cos (\phi - \alpha)] \tag{2}$$

$$V_d = \lambda V_E \tag{3}$$

where V_E is maximum volume of the expansion space and α is the phase angle between the compression and expansion volumes.

From Assumptions 2–5, one can express the total mass in the model in terms of the instantaneous pressure p and the crankangle ϕ. Since the total mass is known from the initial conditions, the pressure can be expressed as a function of the crankangle and system constants.

$$p = K/[B(1 + \delta \cos (\phi - \beta)] \tag{4}$$

The above equation can be integrated over the one cycle to determine the mean pressure p_m. A more convenient form of equation (4) is

$$(p/p_m) = \sqrt{1 - \delta^2}/[1 + \delta \cos (\phi - \beta)] \tag{5}$$

where

$$\beta = \tan^{-1}[\sin \alpha/(\theta/\kappa + \cos \alpha)] \tag{6}$$

$$\delta = \sqrt{1 + (\kappa/\theta)^2 + 2(\kappa/\theta) \cos\alpha}/[1 + \kappa/\theta + 2\lambda(T_e/T_d)] \tag{7}$$

The term θ is the ratio of the compression volume temperature T_c to the expansion volume temperature T_e. The term T_d is the mass average temperature in the dead volume for an adiabatic system. Up to this point, the mathematical model is identical to the Schmidt Cycle analysis.

The mass within the expansion volume at any angle can be obtained from Assumption 3 and equations (1) and (5)

$$m_e = \frac{pV_e}{RT_e} = \frac{p_m V_E \sqrt{1 - \delta^2}\,(1 + \cos \phi)}{2RT_e[1 + \delta \cos (\phi - \beta)]} \tag{8}$$

Differentiating equation (8) with respect to ϕ and setting the result equal to zero, one can establish the conditions for maximum and minimum mass in the expansion volume

$$\delta(\sin (\phi_e - \beta) - \sin \beta) = \sin \phi_e \tag{9}$$

The term ϕ_e is defined as the crankangle which satisfies equation (9). One can see from equations (8) and (9) that the minimum mass in the expansion volume is zero when $\phi_e = \phi_{\min} = 180$ deg. Equation (9) must be solved for ϕ_e for the maximum mass condition. The mass transferred in and out of the expansion space over a cycle is

$$\Delta m_e = \frac{p_m V_E}{2RT_e} \frac{\sqrt{1 - \delta^2}\,(1 + \cos \phi_e)}{[1 + \delta \cos (\phi_e - \beta)]} \tag{10}$$

By a similar procedure, the conditions for maximum and minimum

---

Contributed by the Gas Turbine Division for publication in the JOURNAL OF ENGINEERING FOR POWER. Manuscript received at ASME Headquarters January 18, 1980.

mass in the compression space can be determined. The equation for this condition is

$$\delta[\sin(\phi_c - \beta) - \sin(\beta - \alpha)] = \sin(\phi_e - \alpha) \tag{11}$$

The mass within the compression space at any crankangle is

$$m_c = \frac{pV_c}{RT_e} = \frac{\kappa V_E p_m}{2\theta RT_e} \frac{\sqrt{1-\delta^2}\,[1 + \cos(\phi - \alpha)]}{[1 + \delta\cos(\phi - \beta)]} \tag{12}$$

Again, one can see from equation (11) and (12) that zero mass in the compression space occurs when $\phi_c = \phi_{\min} = 180 + \alpha$. Equation (11) must be solved to find ϕ_c for the maximum mass condition. The change in mass within the compression space, Δm_c, is obtained substituting ϕ_c into equation (12).

The process within the dead space is taken to be adiabatic. If this is not true, the heat transfer to the dead space must be accounted for in the overall cycle energy transfer. The temperature within the dead space is assumed to be constant. Hence, there can be no change in energy within the dead space over a cycle. The First Law of Thermodynamics requires that the enthalpy transferred to the dead space from expansion and compression spaces must be equal the enthalpy that the dead space returns to these spaces. Or,

$$\Delta m_e T_c + \Delta m_c T_e = (\Delta m_e + \Delta m_c) T_d \tag{13}$$

Rewritting equation (13) one has

$$T_d/T_e = (1 + \mu\theta)/(1 + \mu) \tag{14}$$

where

$$\mu = \frac{\Delta m_c}{\Delta m_e} = \frac{\kappa}{\theta}\left[\frac{1 + \cos(\phi_c - \alpha)}{1 + \cos\phi_e}\right]\left[\frac{1 + \delta\cos(\phi_e - \beta)}{1 + \delta\cos(\phi_c - \beta)}\right] \tag{15}$$

The relationship for T_d/T_e as expressed by equation (14) differs from the Schmidt Cycle relationship for T_d/T_e which is

$$T_d/T_e = (1 + \theta)/2 \tag{16}$$

The Schmidt Cycle relationship, equation (16), was obtained by assuming an average temperature, while equation 14 was obtained from an application of the First Law for an adiabatic dead space. Equations (14) and (16) are equivalent if μ is equal to 1. One can see from equations (9, 11) and (15) that $\mu = 1$ is not a general condition.

For equation (16) to be valid for all conditions, there must be heat transfer to the dead space (see equation (13)). This heat transfer is not accounted for in the overall energy balance for the Schmidt Cycle. Therefore, the Schmidt Cycle assumption, equation (16), is not based on thermodynamic principles as is the assumption of an adiabatic dead space, equation (14). The assumption of an adiabatic dead space represents the first of two assumptions used in this paper which differ from the assumptions used in the Schmidt Cycle Analysis. Equation (14) represents the major difference between the mathematical model presented here and the Schmidt Cycle model.

The mathematical model based on the assumption of an adiabatic dead space consists of equations (5–7, 9, 11, 14) and (15). For a set of design conditions (α, κ, λ and θ) and an initial estimate for the mass ratio μ, equations (14, 6) and (7) can be solved for T_d/T_e, β and δ, respectively. From equations (9) and (11) the angles ϕ_e and ϕ_c can be determined. Equation (15) can be used to check the estimate of the mass ratio μ. The value of μ can be up-dated and the process is repeated until convergences on μ is obtained. Once convergence is obtained, equation (5) gives the relationship between the cycle pressure p and crankangle ϕ.

Work of The Cycle

The work done in the expansion space is the cyclic integral of pdV. Using equation (1) and (5), the expansion space work is

$$W_e = -\frac{p_m V_E}{2}\sqrt{1-\delta^2}\int_0^{2\pi}\frac{\sin\phi\, d\phi}{1 + \delta\cos(\phi - \beta)}.$$

Following the procedure presented in reference [1], the angle $(\phi - \beta)$ is set equal to ψ. Substituting the angle ψ into the above integral and expanding, one has

$$W_e = \frac{-p_m V_E}{2}\sqrt{1-\delta^2}\left[\sin\beta\int_0^{2\pi}\frac{\cos\psi d\psi}{1 + \delta\cos\psi} + \cos\beta\int_0^{2\pi}\frac{\sin\psi d\psi}{1 + \delta\cos\psi}\right]$$

The value of the second integral is zero.
The first integral can be expressed as

$$\int_0^{2\pi}\frac{\cos\psi d\psi}{1 + \delta\cos\psi} = \frac{1}{\delta}\int_0^{2\pi} d\psi - \frac{1}{\delta}\int_0^{2\pi}\frac{d\psi}{1 + \delta\cos\psi}$$

The value of the first part of this integral is 2π. The value of the second part according to reference [4] is $2\pi/\sqrt{1-\delta^2}$. Hence, the cyclic work integral for the expansion space is

$$W_e = \frac{p_m V_E}{2}\pi\Delta\sin\beta, \tag{17}$$

where

$$\Delta \equiv 2\delta/[1 + \sqrt{1-\delta^2}] \tag{18}$$

Equation (18) is presented in reference [2] as an approximation for the work integral, which it is not.

The cyclic work integral for the compression space can be determined in the same manner as above. The expression for this work is

$$W_e = \frac{p_m V_E}{2}\kappa\pi\Delta\sin(\beta - \alpha). \tag{19}$$

The net work for the cycle is, of course

$$W_n = W_e + W_c = \frac{p_m V_E}{2}\pi\Delta[\sin\beta + \kappa\sin(\beta - \alpha)] \tag{20}$$

Using equation (6) to obtain expressions for $\sin\beta$ and $\cos\beta$, equation (20) can be reduced to

$$W_n = \frac{p_m V_E}{2}\pi\Delta\frac{\sin\alpha(1 - \theta)}{\sqrt{(\theta/\kappa)^2 + 1 + 2(\theta/\kappa)\cos\alpha}} \tag{21}$$

Thermal Efficiency of The Cycle

From a First Law balance for the expansion space, one can write

$$Q_e = W_e + \Delta m_e c_p (T_e - T_d) \tag{22}$$

Nomenclature

c_p = specific heat at constant pressure
k = ratio of specific heats
m = mass
p = pressure
p_m = mean pressure
R = gas constant
T = temperature
V = volume
V_E = reference volume, maximum expansion volume

v = specific volume
W = work
α = phase angle
β = pressure angle, defined by equation (6)
Δ = work term, defined by equation (18)
δ = pressure term, defined by equation (7)
η = thermal efficiency
η_c = carnot efficiency
η_R = regenerator efficiency
θ = temperature ratio, Tc/TE
κ = compression volume ratio

λ = dead volume ratio
μ = mass ratio
ϕ = crankangle
ψ = angle

Subscripts

c = compression space
d = dead space
e = expansion space
L = lower limit

Therefore, the thermal efficiency for the cycle is

$$\eta_L = \frac{W_n}{Q_e} = \frac{\sin\beta + \kappa\sin(\beta-\alpha)}{\sin\beta + \frac{k}{k-1}\frac{\sqrt{1-\delta^2}}{\pi\Delta}\left[\frac{1+\cos\phi e}{1+\delta\cos(\phi_e-\beta)}\right]\left(1-\frac{T_d}{T_e}\right)} \tag{23}$$

The second term in equation (22) represents the exchange in enthalpy between the expansion space the the dead space.

In reference [2] the regenerative process is assumed to be perfect. This assumption implies that $T_e = T_d$ and that the enthalpy exchange is zero. For the assumption of a perfect regenerator and use of equation (6), the thermal efficiency, equation (23), reduces to

$$\eta = 1 + \kappa\frac{\sin(\beta-\alpha)}{\sin\beta} = 1 - \theta = \eta_c, \tag{24}$$

which is the Carnot efficiency.

The validity of the perfect regenerator assumption is questionable when one considers the operation of the cycle. Mass from the expansion space transfers energy to an intermediate sink which in turn transfers energy to the mass from the compression space. The nature of the exchange is intermittant rather than steady. Hence, the temperature of the intermediate sink must be between the expansion space and the compression space temperatures. Since the average temperature of the dead space must be less than the expansion space temperature, the net enthalpy change between these two spaces cannot be zero. Therefore equation (23), not equation (24), is a more accurate representation of the thermal efficiency of the cycle. Equation (23) represents the second assumption which differs from the Schmidt Cycle analysis—nonperfect regeneration.

The dead space temperature determined by equation (14) is for an adiabatic dead space. The temperature T_d given by equation (14) represents the average energy in the dead space and is used to determine the mass within the dead space at anytime. This does not mean that there cannot be a temperature gradient in the dead space. Any gradient in the dead space will reduce the enthalpy exchange and improve the thermal efficiency.

The proper interpretation of equation (14) is that it predicts the lower limit of regenerator efficiency

$$\eta_{R_L} = (T_d/T_e - \theta)/(1-\theta) \tag{25}$$

and equation (22), therefore, represents the lower limit for cycle thermal efficiency. For the Schmidt Cycle assumption, $T_d/T_e = (1 + \theta)/2$, the lower limit for regenerator efficiency is $\eta_{R_L} = 0.5$.

Incorporating the regenerator efficiency into equation (23), the expression for thermal efficiency becomes

$$\eta = \frac{\sin\beta - \kappa\sin(\beta-\alpha)}{\sin\beta + \frac{k\sqrt{1-\delta^2}}{k-1\pi\Delta}\left[\frac{1+\cos\phi e}{1+\cos(\phi_c-\beta)}\right](1-\eta_R)(1-\theta)} \tag{26}$$

Equation (26) is valid for any value of regenerative efficiency. One can see that equation (25) reduces to the Carnot efficiency when $\eta_R = 1$.

It is the author's opinion that the limiting thermal efficiency for the Stirling engine is better represented by equation (23) rather than by the Carnot efficiency. The author bases his opinion on the fact that equation (23) was developed from the condition of an adiabatic dead space. Also, the Schmidt Cycle, at best (as does the mathematical model presented in this paper), predicts performance which is greater than the performance of an actual engine. According to Martinelli reference [5], the actual performance of a Stirling engine is one-third of the Schmidt Cycle performance. The author feels that the conservative value given by equation (23) is more realistic. Finally, all practical regenerative engine cycle, which the Stirling engine is, do not have the Carnot efficiency as their limiting thermal efficiency. The limiting thermal efficiency only becomes the Carnot efficiency for the case of zero heat addition.

The ratio of the maximum mass in the dead space to the mass exchanged with the expansion space is

$$\frac{m_{d\max}}{\Delta m_e} = \frac{2[1+\delta\cos(\phi_e-\beta)]}{1+\cos\phi_e}\sqrt{\frac{1+\delta}{1-\delta}}\,\lambda\,\frac{T_e}{T_d} \simeq \frac{\sqrt{1-\delta^2}\lambda}{(T_d/T_e)} \tag{27}$$

A desireable design condition for the cycle, see equation (7), is for the ratio λ to be small. One can further see from equation (27) that if λ is small, the mass exchanged with the dead space is greater than the maximum mass in the dead space. Equation (27) can be used to determine the mass of the regenerator required to prevent "hot gases" from being transfered into the compression space.

Parametric Relations

The mathematical model was used to determine the parametric relationships between cycle performance and the cycle independent variables — α, κ, λ and θ. The net work ratio, W_n/pV_E, is presented in Figs. 1–3. The relationship between the network ratio and the independent variables for the mathematical model are similar to that for the Schmidt Cycle as presented in reference [2]. The net work ratio increases with decreasing temperature ratio θ and dead space volume

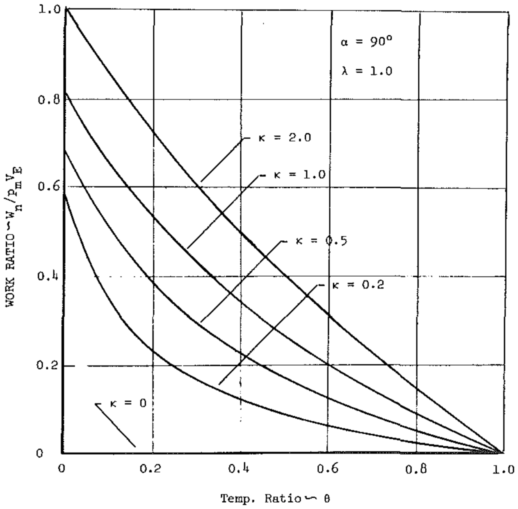

Fig. 1 Net work ratio, variable temperature ratio, variable compression volume ratio

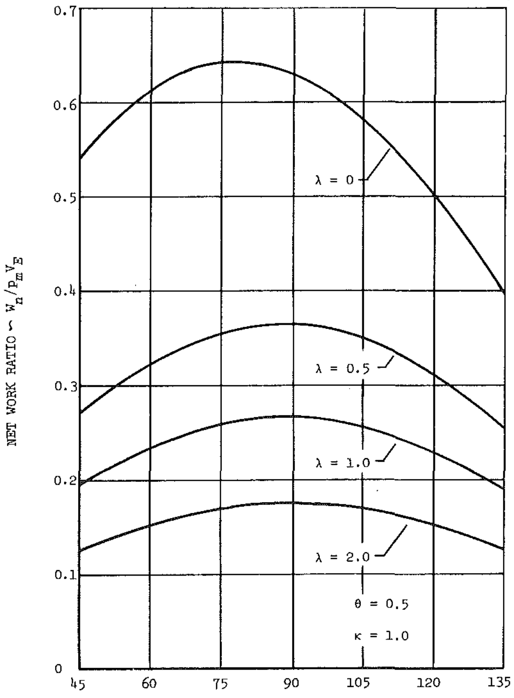

Fig. 2 Net work ratio, variable phase angle, variable dead volume ratio

ratio λ and with increasing compression volume ratio κ. The net work ratio obtains a maximum with phase angle α.

In general, the mathematical model gives lower values for the net work ratio than Schmidt cycle. This can best be seen from Fig. 3. The difference in the two analytical models is in the selection of the temperature ratio, T_d/T_e. This term effects the value of δ, (see equation (7)) and enters equation (7) as a product with the dead space volume ratio λ. Therefore, the larger λ is, the greater the differences between the two models. This effect is illustrated in Fig. 3. When the dead space volume ratio is zero, there is no differences between the two models. This is also illustrated in Fig. 3.

The relationship of the thermal efficiency-lower limit and the independent variables for the mathematical model is presented in Figs. 4–6. The difference between the two models for this performance factor is substantial. This is primarily due to the inclusion of the enthalpy flux in the mathematical model. The thermal efficiency-lower limit agrees with the Carnot efficiency only at $\theta = 1$. As the temperature ratio decreases to zero, the thermal efficiency obtains a limit much less than one (see Fig. 4).

Figures 5 and 6 show that the thermal efficiency is a function of the phase angle and the compression and dead space volumes. The thermal efficiency is not a constant with these variables as predicted by the Schmidt cycle. The thermal efficiency of an actual engine varies with these three variables because the regenerative effectiveness in an actual engine is less than one (see equation (26)).

It can be seen from Fig. 5 that the thermal efficiency maximumizes with the phase angle α. The maximum thermal efficiency occurs at

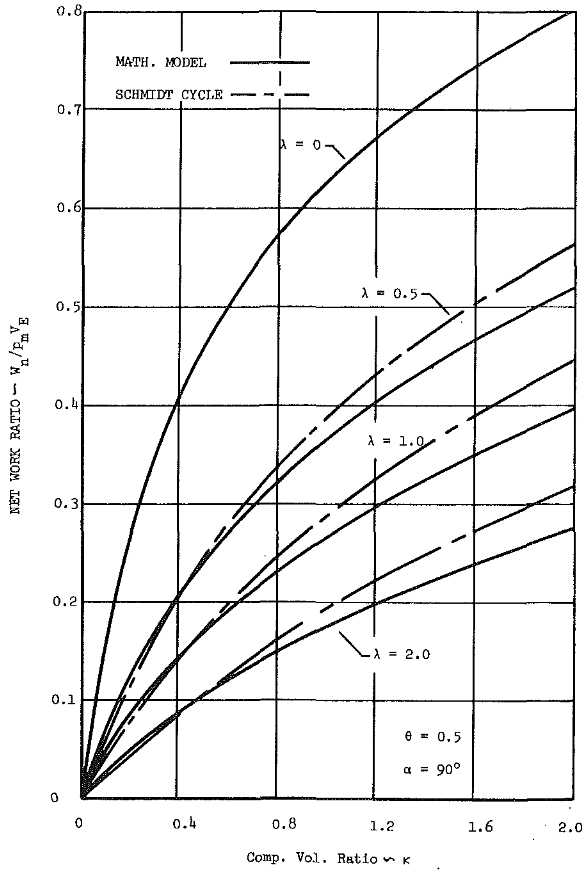

Fig. 3 Net work ratio, variable compression volume ratio, variable dead volume ratio

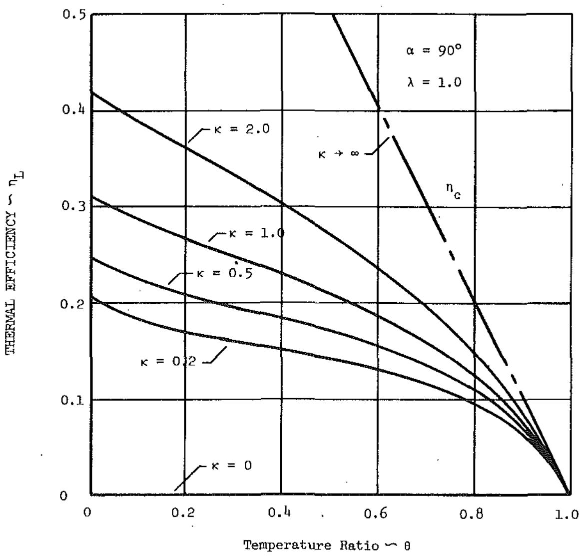

Fig. 4 Thermal efficiency, variable temperature ratio, variable compression volume ratio

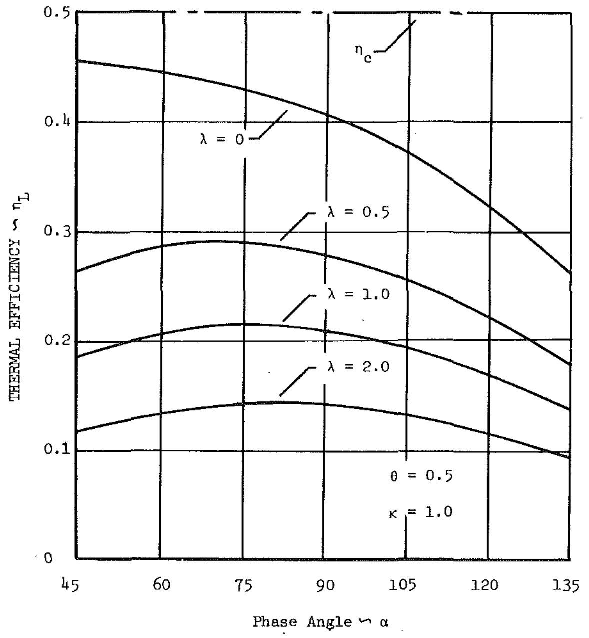

Fig. 5 Thermal efficiency, variable phase angle, variable dead volume ratio

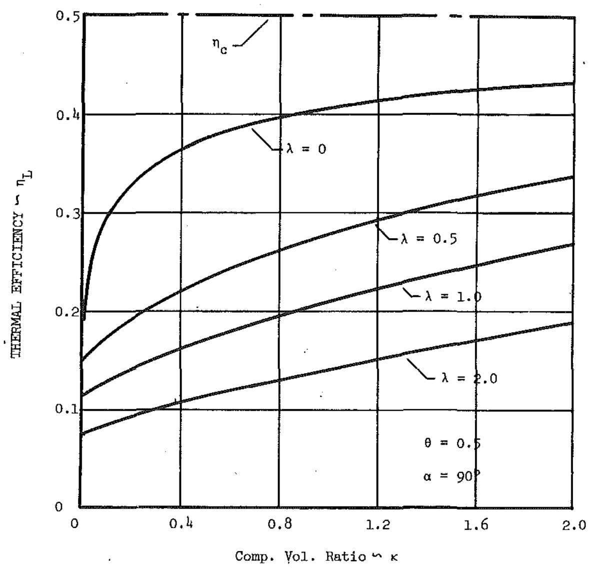

Fig. 6 Thermal efficiency, variable compression volume ratio, variable dead volume ratio

a phase angle less that the angle for maximum work. Again this is in agreement with the general results for engine cycle analysis—maximum efficiency occurs at a condition different than that for maximum work.

Limit Analysis

To fully understand the mathematical model, the net work ratio and the thermal efficiency have been determined for the limiting values of the independent variables.

It can be seen from equation (21) that the net work and, in turn, the thermal efficiency will vanish when the phase angle equals 0 or 180 deg. Rolle's theorem states that both of these performance factors must reach a maximum with the phase angle (see Figs. 2 and 5). By inspection of equation (21) it would appear that this maximum occurs at $\alpha = 90$ deg. This is not true because the term Δ and the enthalpy flux (see equation (23)) are functions of the phase angle α. An explicit relationship for these maximum conditions was not obtained.

For the condition $\theta = 1$, one can see from equation (21) that the net work and the thermal efficiency are zero.

Finite values for the two performance factors are obtained as the temperature ratio θ approaches zero. Again because of the complex nature of the model, explicit mathematical relations for this condition were not obtained. However, the expression for the term δ for $\alpha = 90$ deg is:

For $\theta = 0$

$$\delta = \frac{1 + \kappa[(1 + 3\delta^2)/(1 + \delta)]}{1 + (\kappa + 2\lambda)[(1 + 3\delta^2)/(1 + \delta)]} \tag{28}$$

Equation (28) can be solved by iteration. The solution to equation (28) can be used in equations (21) and (23) to determine the limiting values for net work ratio and thermal efficiency. The limiting values are indicated in Figs. 1 and 4.

For the condition $\kappa = 0$, equation (6) shows that $\beta = 0$. Therefore, the net work is zero for $\kappa = 0$ (see equation (20)). The thermal efficiency, however, attains a limit at $\kappa = 0$. As $\kappa \to 0$, the term T_d/T_e approaches one and the denominator as well as the numerator in equation (23) approaches zero. Applying the small perturbation theory near $\kappa = 0$, one can obtain the limiting expression for thermal efficiency. For the special case $\alpha = 90$ deg,

For $\kappa = 0$, $\alpha = 90$

$$\eta_L = \frac{1 - \theta}{1 + \left(\frac{k}{k - 1}\right)\frac{(1 - \theta)}{\pi\delta}\left[\frac{1}{\sqrt{1 - \delta^2}} + 1\right]} \tag{29}$$

where $\delta = 1/(1 + 2\lambda)$. It can be seen from equation (29) that the thermal efficiency is zero when $\delta = 1$ and 0 ($\lambda = 0$ and ∞).

As $\kappa \to \infty$ the angle β approaches the phase angle α and the term δ approaches one (see equation (7)). For $\delta = 1$ the enthalpy exchange is zero. From equation (21) and (23), the limiting values of net work and thermal efficiency are:

For $\kappa \to \infty$

$$W_n/p_m V_E = \pi \sin \alpha(1 - \theta) \tag{30}$$

and

$$\eta_L = (1 - \theta) \tag{31}$$

Note that, for this condition, the thermal efficiency is equal to the Carnot efficiency. Therefore, it is desirable to design engines with large values of compression to expansion ratio. Large values for κ will also increase the net work ratio. The net work per total volume ($V_E + V_c$) will decease as shown in reference [2].

The condition of $\lambda = 0$ will maximize the term δ and likewise the net work and efficiency for any given design condition (see Figs. 3 and 6). This indicates the desireability of small dead space values. A condition pointed out in reference [2].

Equation (7) shows for $\lambda \to \infty$ that the term $\delta \to 0$. Hence, for this condition, net work and efficiency are zero (see Figs. 3 and 6).

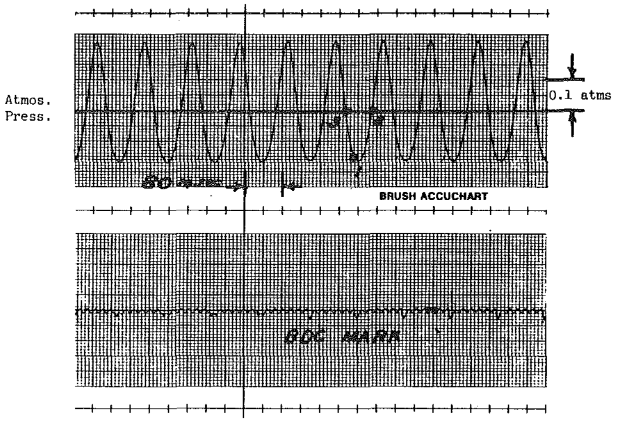

Fig. 7 Pressure-time trace

Table 1

	Math Model	Geometric	Work
Pressure Angle, β	59.65 deg	59.39 deg	56.98 deg
Net Work Ratio, $W_n/p_m v_E$	0.07487	0.07274	0.05282

Comparison with Experimental Results

Figure 7 is a pressure-time trace of a Stirling engine measured with a piezoelectric transducer. The test engine is a Cussons engine operating at 600 rpm under no load. The mean pressure in the engine is atmospheric and the fluid is air. The design parameters for the engine are—$\alpha = 90$ deg, $\kappa = 1.22$, $\lambda = 3.13$. The blip in Fig. 7 is from a timing light and indicates bottom dead center, BDC, for the total cylinder volume. Since BDC occurs before minimum pressure, Point 1, the engine is developing net work which is indicated work for this case.

The trace in Fig. 7 for constant engine speed appears to be of the form represented by equation (5). From the maximum and minimum values for pressure in Fig. 7, the term δ and the angle $(\psi_2 - \psi_1)$ can be determined. This was done for a number of traces. The average values and their standard deviation are:

$$\delta = 0.1909, \quad \sigma = 0.002, \quad (\psi_1 - \psi_3) = 104.3°, \quad \sigma = 3.6 \text{ deg}$$

From equation (5) for $p/p_m = 1$ and $\delta = 0.1909$, one can solve for the angle $(\psi_2 - \psi_3) - (\psi_2 - \psi_3) = 191.1$ deg. The total swept volume can be obtained by adding equation (1) and equation (2). The crank angle for the condition of BDC can be obtained by differentiating this sum with respect to the crank angle.

$$\phi_{\mathrm{BDC}} = \tan^{-1}(\kappa)$$

At minimum pressure $\phi = \beta$ (see equation (5)). Therefore, from geometry

$$\beta = \phi_{\mathrm{BDC}} + (\psi_2 - \psi_1) - (\psi_2 - \psi_3)/2 = 59.39 \text{ deg}$$

The work indicated was also measured with a dynamometer. Using equations (18) and (20) for $\delta = 0.1909$, the value for β can be computed. The "work" value and the "geometric" value are compared in Table 1.

Using the mathematical model and $\delta = 0.1909$, the effective value for the temperature ratio θ can be determined from a parametric analysis $- \theta = 0.713$. From equation (6) the "mathematical model" value β can be calculated. This value is compared with the other values in Table 1.

The p-v diagram for the engine using the mathematical model was determined and is presented in Fig. 8. The points in Fig. 8 are the experimental points transfered from Fig. 7.

The agreement between the mathematical model solution and experimental results is quite good, well within the accuracy of experimental data. It should be noted that the sensitivity of the net work ratio with the term δ is quite large. For the mathematical model it is 25 percent for 1 percent change in δ.

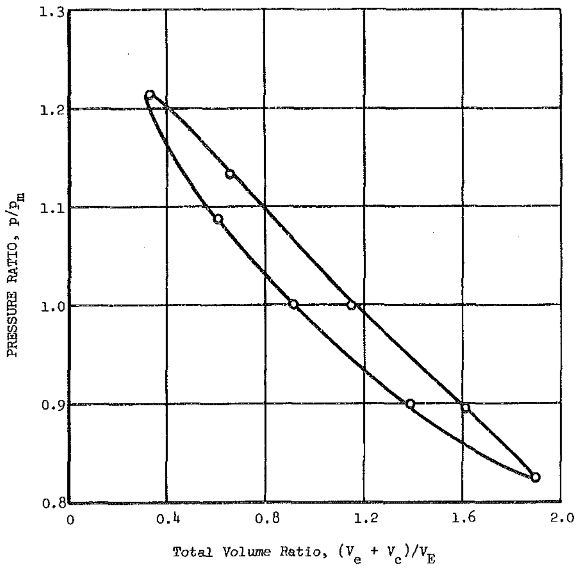

Fig. 8 ***P-V* diagram, theoretical and experimental**

Conclusion

Based on the assumption of an adiabatic dead space, a mathematical model for the analysis of the Stirling engine has been developed. The model is similar in form to the Schmidt Cycle. The model is more complex than the Schmidt Cycle and can not be expressed in a closed form. The model, in general, predicts performance values which are lower than the Schmidt Cycle.

The major difference between the two analytical models is that the mathematic model predicts a thermal efficiency which is a function of all design variables rather than the temperature ratio. This thermal efficiency has been interpreted as a lower limit. The functional relationship of thermal efficiency with all design variable has been shown to be true for any regenerative efficiency less than one.

A limit analysis of the design variables has been conducted. This analysis is useful in determining the design direction for the Stirling engine.

The *p-v* diagram generated from the mathematical model was compared with the measured diagram for an operating engine. The agreement is quite good.

References

1 Schmidt, G., "Theorie der Lehman Schen Calorischen Machine," *Zeitschrift des Vereines Deutscher Ingenieure,* Vol. 15, No. 1, 1871.

2 Walker, G, *Stirling-Cycle Machines,* Claredon Press, Oxford, 1973.

3 DeBrey, H., Rinía, H., and Van Weenen, F. L., "Fundamentals for the Development of the Phillips Air Engine," *Phillips Tech. Rev.,* vol. 9, No. 4, 1947, pp. 97.

4 Weost, R. C., Selby, S. M., and Hodgman, C. D., *Handbook of Chemistry and Physics,"* The Chemical Rubber Co., 46th Ed., pp. A171, 1966.

5 Martini, W. R., "Energy Storage via Heat Battery Plus Heat Engine," paper given at CSUI-ANL Conference on Energy Storage, Argonne National Lab., IU., Nov. 12, 1977.

M.S. Elkelish

A. Elsawaf

Senior S&D Analysts.

M. Barsoum

Staff S&D Engineer.

Pratt & Whitney Aircraft of Canada Ltd.,
Quebec, Canada

Application of the Semi-Loof Thin Shell Element to the Analysis of Aircraft Engine Structures

Most gas turbine engine structures consist of thin shells with multiple junctions. The curved isoparametric shell element gives unsatisfactory results when used for very thin shells. The Semi-Loof shell element was developed especially to deal with thin shell structures with sharp corners and multiple junctions. The Semi-Loof shell program was used at P&WC for the analysis of large engine structures. Application to the analysis of an engine static structural model, for which experimental data are also available, has confirmed the efficiency of the Semi-Loof shell element in comparison with the conventional isoparametric element.

Introduction

Most gas turbine engines consist of a number of different thin shell components. The isoparametric layered shell element [1] has been used frequently for the stress analysis of such components. Such an analysis exhibits a number of difficulties especially when the elements have a thickness/length ratio of 1/200 and less. This can be attributed to the spurious shear stiffness implied in the element formulation. The reduced integration technique [1-2] can help in getting better approximation, but the shear stiffness problem still exists for very thin shells.

The Semi-Loof shell element, developed by Irons [3] is designed especially to deal with thin shells, and to cope with sharp corners, multiple junctions and localized bending effects. It is one of the most efficient thin shell elements available today.

This paper illustrates the efficiency of the Semi-Loof shell element in comparison with the conventional isoparametric element when applied to the analysis of an engine static structure model, for which experimental data are also available.

Semi-Loof Shell Element

Figure 1 shows the nodal configurations of the Semi-Loof shell elements. The quadrilateral version has 32 degrees of freedom, while the triangular version has 24 degrees of freedom. These degrees of freedom are as follows:

(*a.*) Three displacements (u, v,w), in the global directions x, y, and z, at the corner and mid-side nodes.

(*b.*) Two normal rotations along each side, positioned at the locations of the Gauss integration points (Loof nodes)

This configuration avoids the problem of defining the slopes at the corners, which militates the introduction of a fictitious rotational degree of freedom, normal to the midsurface of the isoparametric shell element, in order to make the element capable of modelling multiple junctions.

In deriving the stiffness matrix, the Semi-Loof element is assumed to obey the Kirchoff-Love assumption for thin shells. This assumption implies that the normal to the midsurface of the shell before deformation, remains normal after deformation. Hence, a number of shear constraints are introduced to eliminate the strain energy due to shear strains. The element formulation is available elsewhere, and the interested reader is referred to references [3 and 4].

It has been shown numerically [3] that the element passes the patch test. Hence, it's convergence to the true solution, as the mesh is refined, is assured. It, also, exactly reproduces the rigid body motion modes.

A curved Semi-Loof beam element, having a configuration matching the shell element, Fig. 2, was developed [6]. A combination of the two elements can be used to solve thin shells with stiffening ribs.

Semi-Loof Computer Program. Irons [3] developed a computer program for the Semi-Loof thin shell element. A Semi-Loof beam element program was also developed by Albuquerque [6]. The two elements were combined together by Elsawaf [5], with an upgraded frontal solution [7] and the computer package was used to analyse some shell roofs.

The Semi-Loof computer package was further developed at Pratt & Whitney Aircraft of Canada Ltd., to be more suitable for industrial applications. Some of the features of this modified program can be summarized as follows:

(*a.*) The convenience of using triangular and/or quadrilateral curved shell elements in the structural modeling.

(*b.*) The ability to model shells, curved space frames and shell-beam structures, with variable thickness and geometrical properties.

(*c.*) The ability to use convenient coordinate systems for data input and/or solution output.

Contributed by the Gas Turbine Division of THE AMERICAN SOCIETY OF MECHANICAL ENGINEERS and presented at the International Gas Turbine Conference and Products Show, Houston, Texas, March 8-12, 1981. Manuscript received at ASME Headquarters, December 11, 1980. Paper No. 81-GT-104.

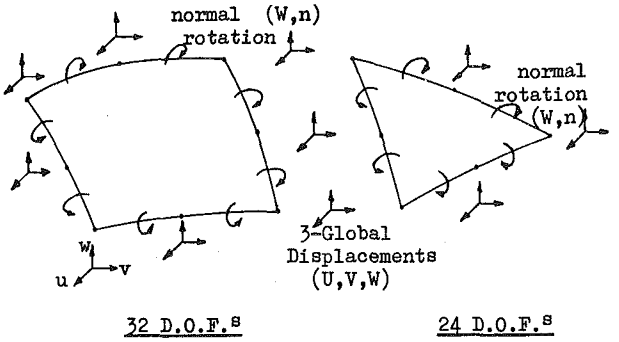

Fig. 1 Semi-Loof thin shell element configuration

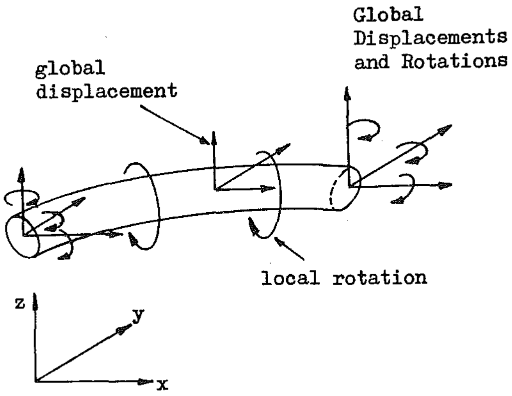

Fig. 2 The configuration of semi-loof beam element

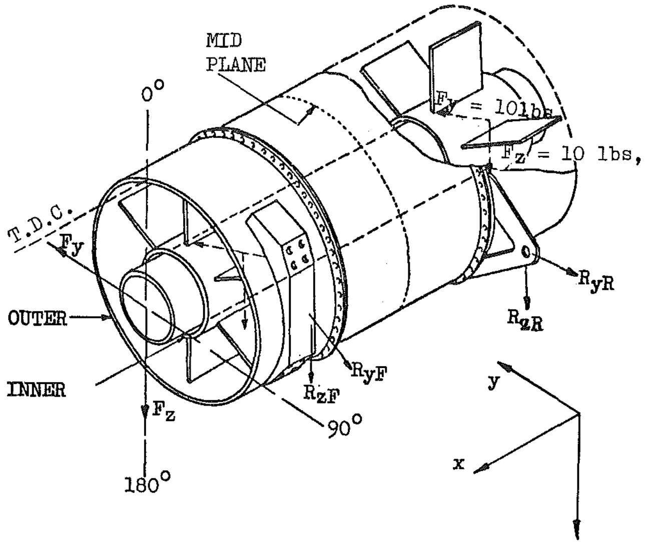

Fig. 3 Tested structure

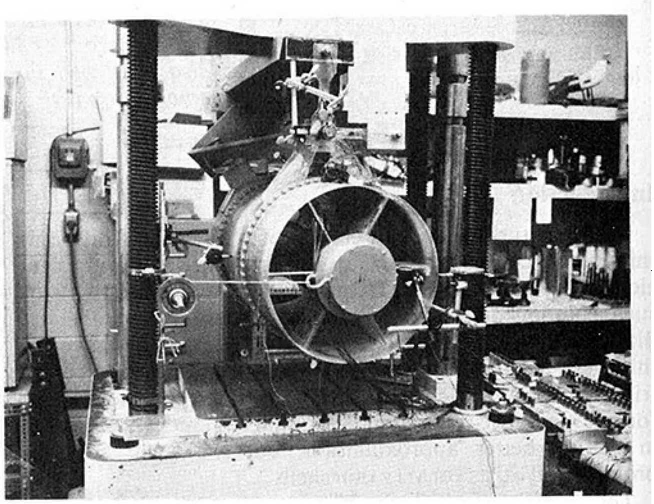

Fig. 4 Test setup

(*d*.) Pressure loads, point loads, self-weight and thermal loads can be handled by the program.

(*e*.) Prescribed and/or spring type boundary conditions can be applied. Spring elements can be also used to link any two nodes geometrically constrained with respect to each other.

Analysis of an Engine Static Structure Using the Semi-Loof Shell Element

The Semi-Loof program was used to analyse a photoelastic model that was fabricated similar to an engine static structure, Fig..3. The main purpose of the analysis was to determine the efficiency and the accuracy of the Semi-Loof program in the stress and displacement evaluation and the prediction of the load transfer from the engine mountings into the adjacent structures.

To determine the degree of efficiency and accuracy of the Semi-Loof program, a similar analysis was carried out on the same engine structural model using the layered isoparametric shell element.

Description of the Test Model. The geometry of the structure under consideration is shown in Figs. 3 and 4. This model simplifies the engine static casings by splitting it into three main components. The front and rear cylinders are representing the intake and exhaust ducts, and the middle cylinder represents a gas generator case. The intake and exhaust ducts are represented as outer and inner cylinders connected through six vanes equally spaced along the circumference. The engine is mounted at two planes as shown in Fig. 4, and the structure is totally symmetric about the X-Y plane.

The structural model was fabricated from Epoxy material and was instrumented with strain and dial gauges in order to determine stresses and deflections at selected points. In order to determine the load path through the engine, a calibrated tension bar system was mounted at the rear mount to determine the mount load sharing. The structure was loaded laterally and vertically by a total load of 20 lb (89 N). The load was acting equally on the inner front and rear cylinders over a bearing length of 3 in (76.2 mm).

The structure is fixed in space at the front mount pads and the rear mounting bracket. The rear bracket is only constrained laterally and vertically. The front mount pads are assumed to be fixed in all degrees of freedom for the F_y loading case. However, for the F_z loading case prescribed displacements, equal to the measured values, are imposed.

Finite Element Analysis. In the Semi-Loof analysis, two different finite element models were used. A preliminary coarse mesh, composed of 144 elements and 462 nodes was used in the F_y loading test case to evaluate the efficiency of the program in determining the load transfer through the structure. However, this mesh was found inaccurate for the F_z loading case and was refined to 314 elements and 919 nodes. Figure 5 shows the finite element meshes used for some components of the structures.

The conventional shell isoparametric element was also used to analyse the structure under the two sets of loading. The structure was discretesized into 614 elements and 2112 nodes, Figs. 6 and 7.

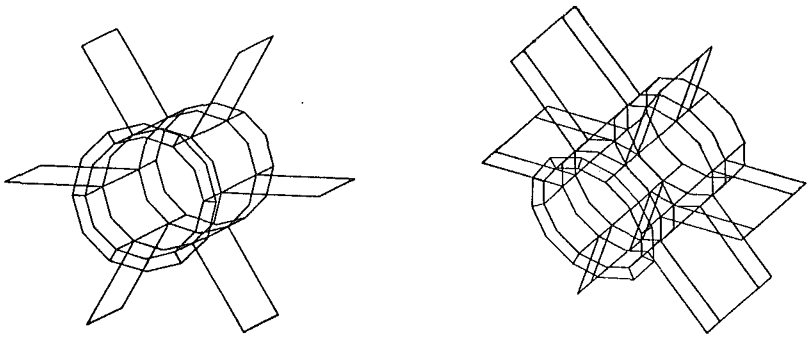
a) F_y LOADING - 144 ELEMENTS

b) F_z LOADING - 314 ELEMENTS

Fig. 5 Rear inner cylinder and vanes (Semi-Loof element)

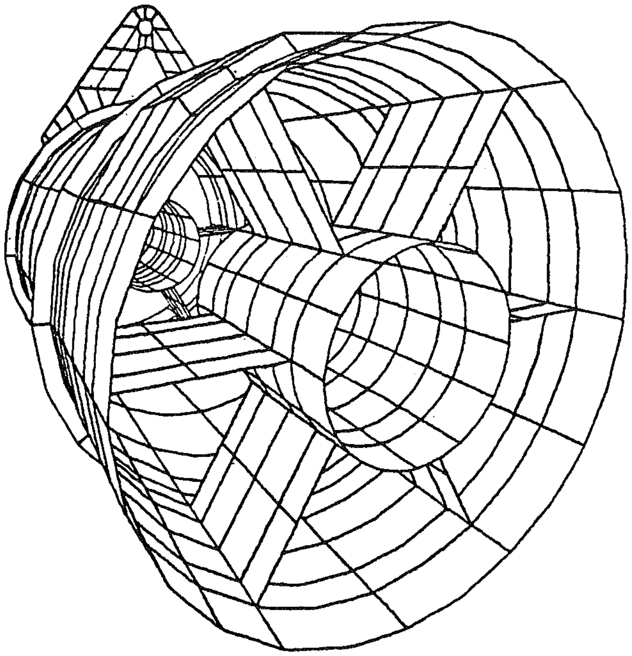
Fig. 6 Engine static structure finite element modelling

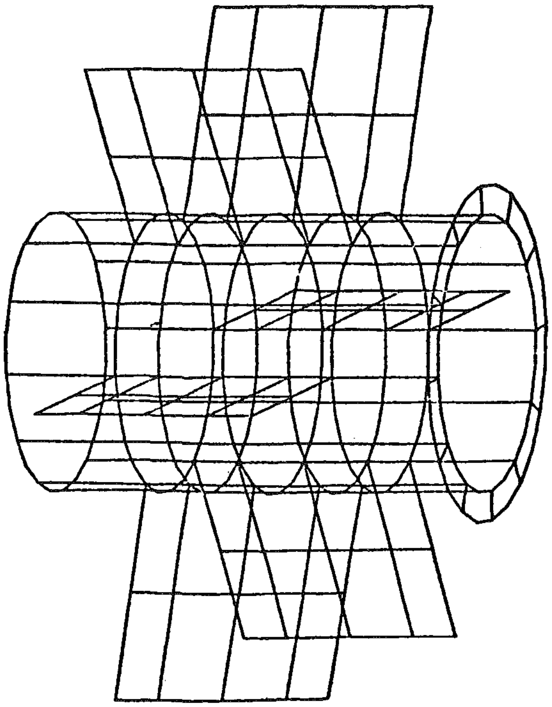
Fig. 7 Rear inner cylinder and vanes (isoparametric shell element)

Table 1 Results comparison for F_y loading

	Maximum Displacements of the Cylinders in the Y Direction ins(mms)				Reactions, lb (N)	
	Front cylinder		Rear cylinder		Front pads	Rear bracket
	Inner	Outer	Inner	Outer		
Isoparametric element	.044 (1.13)	.0120 (.305)	.0743 (1.888)	−.0044 (−.111)	6.99 (31.1)	13.01 (57.9)
Semi-Loof element	.0404 (1.03)	.0299 (.76)	.0405 (1.028)	.0226 (.565)	6.83 (30.4)	13.17 (58.6)
Experiment	.048 (1.22)	.0150 (.38)	.0470 (1.194)	.0070 (.178)	5.3 (23.6)	14.7 (65.4)

Results and Discussion. Table 1 contains a summary of the deflection and reaction measurements from the test, the Semi-Loof program and the conventional isoparametric shell element analysis for the F_y loading case. The main objective of the test was to determine the load transfer through the structure, therefore, the discrepancies in the displacement

continued on page 531

Continued from page 513

Table 2 Results comparison for F_z loading

	Maximum displacements of the Outer cylinders in the Z direction, in(mms)		Reactions, lb (N)	
	Front cylinder	Rear cylinder	Front pads	Rear bracket
Isoparametric element	0.122 (3.1)	0.133 (3.38)	17.28 (76.9)	2.72 (12.1)
Semi-Loof element	0.133 (3.378)	0.135 (3.43)	17.16 (76.4)	2.84 (12.6)
Experiment	0.128 (3.25)	0.138 (3.51)	16.9 (75.2)	3.1 (13.8)

Table 3 Comparison between Semi-Loof and isoparametric shell elements

	Items	Isoparametric element	Semi-Loof element
F_y Loading	No. of Element	614	144
	Execution Time	1000 secs	196 secs
F_z	No. of Elements	614	314
	Execution Time	1000 secs	230 secs

values did not dictate repeating the analysis with a finer mesh since a reasonable agreement was obtained for the reaction values.

However, for the F_z loading case, the mesh was refined and the measured front mount movements were inputed as prescribed displacements in the analysis. Table 2 shows reasonable agreement between the analyses and the test results. It is also clear that both analyses gave the same order of accuracy. However, the Semi-Loof analysis employed only half the number of elements used in the isoparametric shell analysis.

Table 3 shows a computer execution time comparison between the Semi-Loof element and the conventional isoparametric shell element analyses for the two cases of loading. This comparison is another proof of the reliability of the Semi-Loof shell element especially that the execution time was reduced by almost 90 percent in the first case of loading and about 75 percent in the second case.

Conclusions

1. The analysis shows the efficiency of the Semi-Loof program in obtaining the same accuracy as the isoparametric shell element with relatively coarser mesh, and reduced computer time.
2. No problem or ill-conditioning is expected from the Semi-Loof shell element in the analysis of very thin shells. The ratio between the element length to thickness does not affect the accuracy of the results as in the case of the conventional isoparametric shell element.

References

1 Zienkiewicz, O.C., *The Finite Element Method*, Third Edition, McGraw-Hill, New York, 1977.

2 Zienkiewicz, O.C., Taylor, R.L., and Too, J.M., "Reduced Integration Technique in General Analysis of Plates & Shells," *International Journal for Numerical Methods in Engineering*, Vol. 3, 1971, pp. 275-290.

3 Irons, B.M., "The Semi-Loof Shell Element," *Chapter in Symposium* on Thin Shells and Curved Members, Univ. College, Cardiff, 1974, Published by John Wiley, 1976, ed. Gallagher, R.H. and Ashwell, D.K.

4 Elaswaf, A., "Semi-Loof and Isobend Finite Elements," M. Sc. thesis, Univ. of Calgary, Alberta, 1976.

5 Elsawaf, A., "An Application of a Semi-Loof Shell and Beam Elements," *IASS World Congress* on Shells and Space Enclosures, Montreal, 1976.

6 Albuquerque, F., "A Beam Element for Use with the Semi-Loof Shell Element," M. Sc. thesis, University of Wales, Swansea, 1973.

7 Irons, B., "A Frontal Solution Program for Finite Element Analysis," *Int. Journal of Numerical Methods in Engineering*, Vol. 2, 1970.

A. K. Jasuja

Thermal Power Group,
School of Mechanical Engineering,
Cranfield Institute of Technology,
Cranfield, Bedford,
England

Airblast Atomization of Alternative Liquid Petroleum Fuels under High Pressure Conditions

A study has been conducted of the effects that fuel and air properties have upon the mean droplet size characteristics of a pre-filming airblast atomizer of the type commonly employed in the gas turbine engine. The fuels tested included kerosine, gas oil and two blends of gas oil in residual fuel oil. The tests were carried out over a wide range of air pressures (about 1 to 13 atmospheres), fuel viscosities (about 0.001 to 0.037 Ns/m²) and the spray mean drop sizes were measured using a laser light-scattering technique. The experimental data accumulated in the study is presented in the paper and it is concluded that the spray Sauter Mean Diameter performance of the atomizer studied can be predicted to a reasonable degree of accuracy, over the range of conditions studied, by a relatively simple correlating equation.

Introduction

It is generally accepted that the quality of the future petroleum fuels will deteriorate, requiring the gas turbine to burn increasingly viscous and less volatile, low-grade fuels. In order to minimize the deleterious influence of such a change, there is a real need to focus attention on the details of such combustion processes as spray atomization, evaporation, ignition etc. Although it is possible from a theoretical standpoint to compensate for the degradation in fuel viscosity and volatility by improvements in atomization performance, the extent of such an improvement in a practical situation may be either limited in scope or difficult to realize. Consequently, there is a growing requirement for experimental data aimed at quantifying these effects in gas turbine combustors.

The results of the atomization study under atmospheric pressure conditions, covering a variety of gas turbine type fuel atomizers operating with a wide range of alternative liquid petroleum fuels, were reported in reference [1]. This paper presents the experimental data collected in the course of the airblast atomization study under conditions of high pressure. Although reference [2] outlines some high pressure atomization data, the range of applicability as regards ambient air pressure and test fuel viscosity levels is very limited—i.e., data pertaining to low-viscosity liquids such as kerosine/water for pressures up to about 8.5 atmospheres. Further, there is no high pressure data whatsoever in the study outlined in reference [3]. Clearly, therefore, more information is required in order to cover the range of operating air pressures/fuel viscosities that are of relevance to the gas turbine, particularly in its industrial and marine applications.

Selection of Test Conditions

The fuels selected for this study comprised kerosine, gas oil and two blends of gas oil in residual fuel oil, type BS 2869 Class G, 3500 Second Redwood One (860 cSt.). The blends were designated R_{25} and R_{55} containing 25 percent and 55 percent residual fuel oil (by volume) respectively, the remainder in each case being gas oil. This enabled test fuel viscosity variation over a wide range, (see Table 1).

The choice of the atomizer type was limited, for this particular phase, to the prefilming type of airblast atomizer—a common feature of most modern high-pressure-ratio gas turbines in view of its superior combustion/pollution performance. Figure 1 shows the atomizer arrangement. The prefilmer spreads the fuel into a thin sheet that is enveloped by high velocity airstreams on both sides—pintle airstream on the inside and shroud airstream on the outside. The object of sandwiching a low velocity sheet of fuel by two high velocity airstreams is to promote maximum physical contact between the fuel and air and thereby set up high rates of shear.

The atomizer operating conditions covered a wide range of air properties as detailed below:

Atomizing air pressure. From about 1 to 13 atmospheres

Atomizing air pressure drop. From about 2 to 11 percent, being wider than that normally encountered in gas turbine combustors

Atomizer air to fuel mass ratio. From about 2 to 8.

Table 1 Physical Properties of Test Fuels

Fuel Property	Kerosine	Gas Oil	25 Percent RFO 75 Percent GO	55 Percent RFO 45 Percent GO
Density ρ_ℓ in kg/m^3 at 15°C	784	846	874	913
Surface tension σ_ℓ in N/m^3 at 20°C	0.0277	0.0299	0.0307	0.0331
Absolute viscosity η_ℓ in Ns/m^2 at 15°C	0.0013	0.0053	0.0149	0.0749
at 25°C	—	0.0040	0.0102	0.0435
at 35°C	—	0.0031	0.0073	0.0275

Contributed by the Gas Turbine Division for publication in the JOURNAL OF ENGINEERING FOR POWER. Manuscript received by the Gas Turbine Division January 28, 1980.

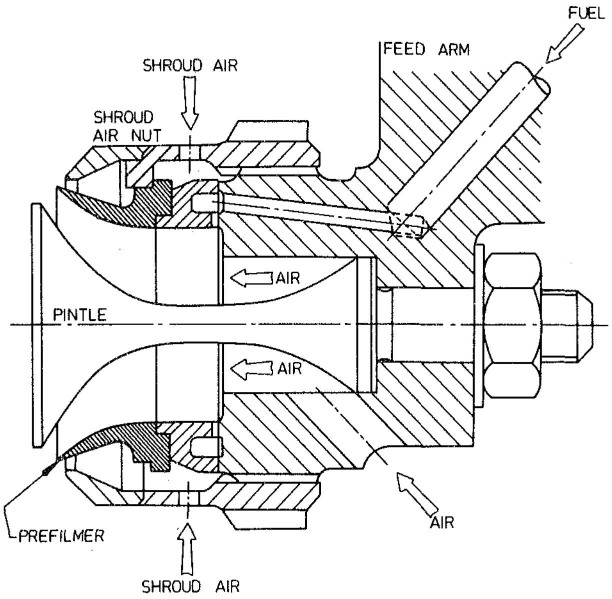

Fig. 1 The prefilming airblast atomizer

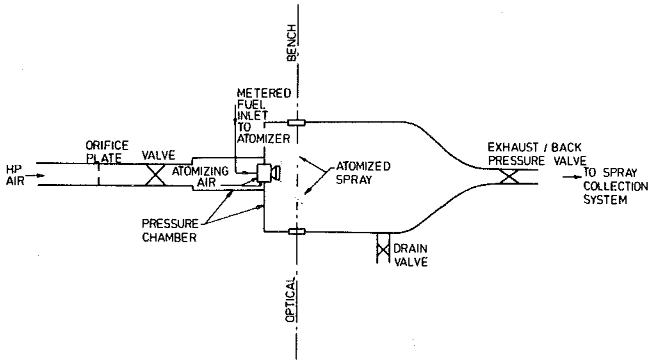

Fig. 2 Outline arrangement of the test installation

Experimental Details

Figure 2 shows the outline arrangement of the test facility. The atomizer was mounted in a pressure chamber connected to the School's high pressure air supply system comprising multistage Howden compressors. The air mass flow rate was measured using an orifice plate fitted with D and D/2 pressure tappings in accordance with BS1042. Fuel mass flow rate was measured using precision flowmeters, previously calibrated for each fuel at the appropriate working temperature.

As in the case of earlier study [1], the spray Sauter Mean Diameters were measured using the well-established laser light-scattering technique, an extension of that developed by Dobbins, et al. [4]. This is based on the principles of forward diffractive scattering of a parallel monochromatic beam of light as it passes through the fuel spray. For more details of the optical bench see references [1, 4, 5]. It is generally believed that spray SMD's down to about 20 μm can be measured reasonably accurately.

The pressure chamber was fitted with optical windows to enable laser beam access for measuring the atomized spray Sauter Mean Diameter under conditions of high pressure.

Results

Fuel Characterization. Many tests were carried out to determine the physical properties of the various fuels and the detailed results are given in Table 1. The mean absolute viscosities, in Ns/m^2, of the different test fuels at the working temperature for the ensuing atomization results were: kerosine—0.0013, gas oil—0.0058, R_{25}—0.0122 and R_{55}—0.0371.

Atomizer Performance. The effect upon SMD performance of varying the atomizer air to fuel mass ratio (AFR) for a range of ambient air pressures at a constant atomizer air pressure drop is illustrated in Figs. 3 and 4 for low-viscosity kerosine and high-viscosity R_{55} fuels, respectively. Figure 3 indicates that, in the case of kerosine, the atomizer AFR has a bearing on the atomizer SMD performance close to the atmospheric pressure condition only—at higher ambient air pressures there being no significant change in SMD values for an AFR change. As the fuel viscosity increases, the AFR influence upon SMD values begins to become apparent even at higher ambient air pressures. In the case of R_{55} fuel, the AFR effect seems to extend from atmospheric up to around 7 atmospheres, though to a noticeably diminishing degree. In airblast atomizer design, the scale tends to be related to AFR, and therefore due consideration must be given to the interaction of AFR, ambient air pressure and fuel viscosity.

The influence of atomizer air pressure drop, or alternatively airstream velocity, upon mean dropsize performance for various levels of ambient air pressure is depicted in Fig. 5 for kerosine, and in Fig. 6 for high-viscosity fuel R_{55}. Both these figures illustrate clearly the beneficial influence of increased levels of atomizing air velocity upon SMD performance. For atmospheric pressure conditions the atomizer air pressure drop and the atomizing air velocity were correlated by using the Bernoulli's equation for incompressible flow, while for high pressure conditions the calculations were based upon compressible flow.

Also brought out clearly in Figs. 3–6 is the noticeable improvement in atomizer performance as the ambient pressure of the atomizing air increases i.e. the atomizing air density. It should be pointed out here that in the case of 1 atmosphere data, the ambient pressure of 1 atmosphere is that prevailing downstream of the atomizer, making the atomizer upstream pressure a little above 1 atmosphere when taking into account the atomizer air pressure drop. In all other cases, the ambient air pressures quoted are the actual nominal atomizer upstream air pressures.

Figures 7–9 illustrate the effect of fuel quality degradation (essentially fuel viscosity) upon the mean drop size characteristics, for 1, 6.8 and 12.9 atmospheres, respectively. These results are for an atomizer air to fuel ratio of 4, although in fact a much wider range (2 to 8) was investigated.

The improvement in atomization quality as a result of an increase in atomizing air ambient pressure, for the entire range of fuels employed in this study, is illustrated by Figs. 10 and 11 for two typical atomizer air pressure drop levels. It is apparent from these figures that the improvement in dropsize performance with an increase in air pressure is more marked for the low-viscosity fuels such as kerosine and gas oil than for the higher-viscosity R_{55} fuel.

Analysis of Results

The data collected from the low-viscosity kerosine fuel tests were systematically evaluated and found to correlate with an equation of the form:

$$\mathrm{SMD}\ \alpha \left(\frac{\sigma_\ell}{\rho_a V_a^2}\right)^{0.45} \cdot (1 + 1/\mathrm{AFR})^{0.5} \tag{1}$$

Nomenclature

SMD = Sauter Mean Diameter, m
V = velocity, m/s
D = diameter of prefilmer, m
$\frac{\Delta P}{P}$ = atomizer air pressure drop, percent

AFR = air to fuel (liquid) mass ratio
ρ = density, kg/m^3
σ = surface tension, N/m
η = absolute viscosity, Ns/m^2

Subscripts

a = air
ℓ = liquid
f = fuel

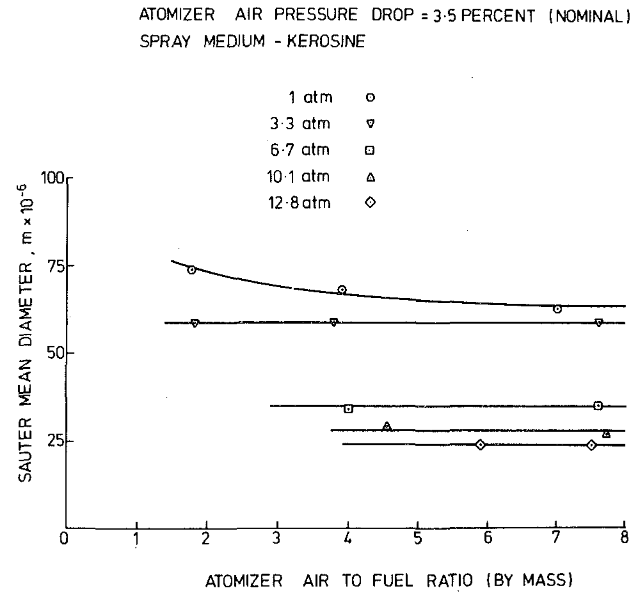

Fig. 3 Atomizer mean dropsize performance under varying ambient air upstream pressure and air to fuel ratio (kerosine)

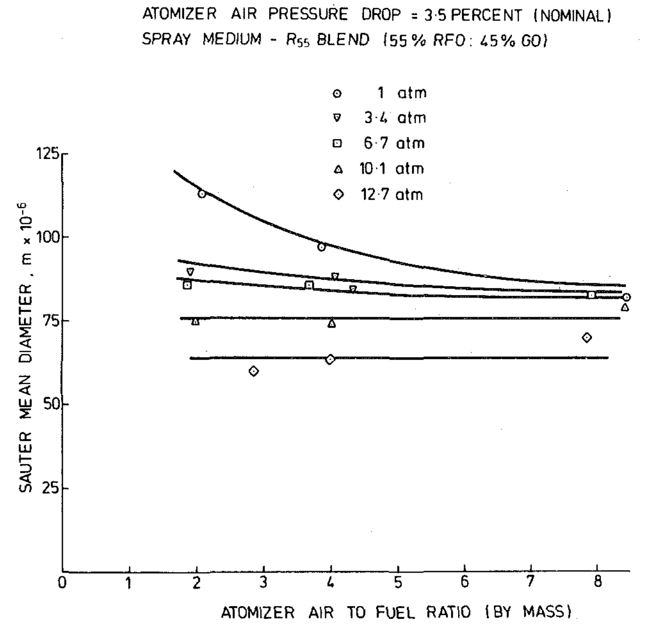

Fig. 4 Atomizer mean dropsize performance under varying ambient air upstream pressure and air to fuel ratio (R_{55} blend)

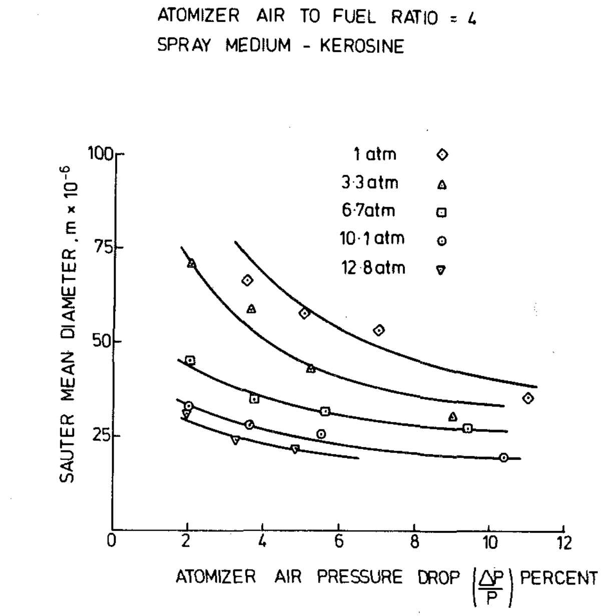

Fig. 5 Influence of varying atomizer air pressure drop and ambient air upstream pressure on spray mean dropsize

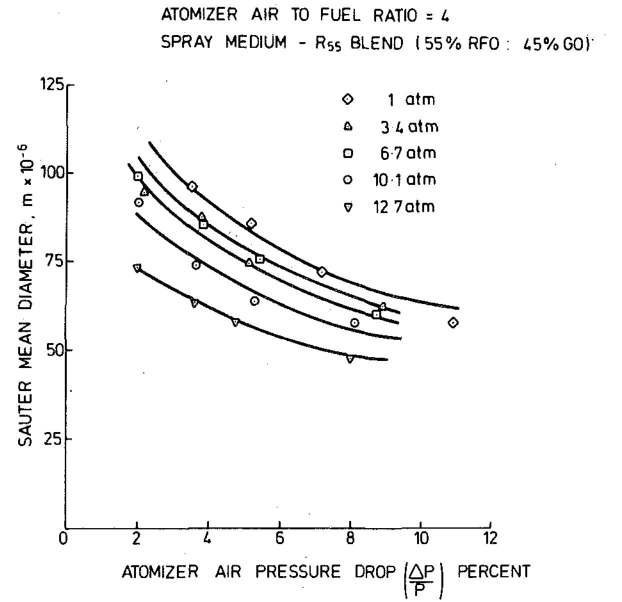

Fig. 6 Influence of varying atomizer air pressure drop and ambient air upstream pressure on spray mean dropsize

Examination of the high-viscosity dropsize data reveals that the fuel viscosity apparently exercises an influence somewhat independent of the air properties—namely air velocity and density, thus implying that to the right hand side of the equation (1) above should be added another term taking into account the effect of fuel viscosity upon SMD. As before, a log-log analysis of the high-viscosity data was conducted to yield:

$$\mathrm{SMD}\,\alpha\left(\frac{\sigma_\ell}{\rho_a V_a{}^2}\right)^{0.45}\cdot(1+1/\mathrm{AFR})^{0.5} + \left(\frac{\eta_\ell{}^2}{\rho_\ell\sigma_\ell}\right)^{0.375}\cdot(1+1/\mathrm{AFR})^{0.8} \quad (2)$$

It is interesting to note that the equation (2) above is not dimensionally consistent but can be made so by introducing the prefilmer diameter D as given below:

$$\mathrm{SMD} = A\left[\left(\frac{\sigma_\ell}{\rho_a V_a{}^2}\right)^{0.45}\cdot(D)^{0.55}\cdot(1+1/\mathrm{AFR})^{0.5} + B\left(\frac{\eta_\ell{}^2}{\rho_\ell\sigma_\ell}\right)^{0.375}\cdot(D)^{0.625}\cdot(1+1/\mathrm{AFR})^{0.8}\right] \quad \ldots\ldots (3)$$

or in the dimensionless form as:

$$\frac{\mathrm{SMD}}{D} = A\left[\left(\frac{\sigma_\ell}{\rho_a V_a{}^2 D}\right)^{0.45}\cdot(1+1/\mathrm{AFR})^{0.5} + \mathrm{B}\left(\frac{\eta_\ell{}^2}{\rho_\ell\sigma_\ell D}\right)^{0.375}\cdot(1+1/\mathrm{AFR})^{0.8}\right] \ldots\ldots (4)$$

where A and B are dimensionless constants, the values of which can be obtained from the experimental data.

The dimensionless group $\sigma_\ell/\rho_a V_a{}^2 D$, which is the inverse of Weber number as applied to air properties, represents the ratio of liquid surface tension to air inertia forces while the group $\eta_\ell{}^2/\rho_\ell\sigma_\ell D$ simply defines the fuel properties.

The level of correlation between the experimental data collected in this study with the predictions of equation (3) above with $A = 17 \times 10^{-2}$ and $B = 0.1$ is illustrated in Fig. 12 wherein most of the experimental values can be observed to fall within about ±25 percent of the predicted ones. The largest scatter arising due to the inability of the correlation to predict properly SMD values under atmospheric pressure conditions. It should, however, be noted that this correlation has only been tested for the one specific prefilmer diameter, i.e., $D = 17.5 \times 10^{-3}$m.

Discussion

The main differences between this work and that reported previously (see references [1] and [2]) are

1 the extended range of atomizing air pressures—from about 1 to 13 atmospheres,
2 the extended range of liquid fuel viscosity—up to about 0.037 Ns/m^2, and
3 the nature of SMD correlation.

Early work indicated that the air density exponents in the correlating equation were -1.0 and -0.425 for the first and second terms respectively. This work indicates that the air density exponent is -0.45 for the first term and the viscosity-dominated second term is

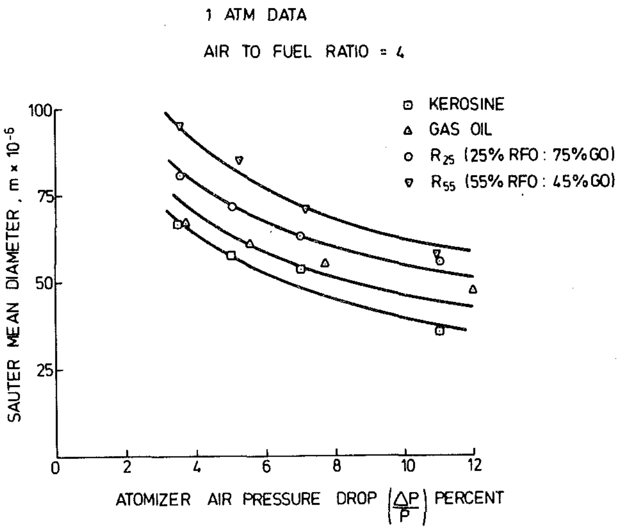

Fig. 7 Effect of varying atomizer air pressure drop and fuel type on mean dropsize

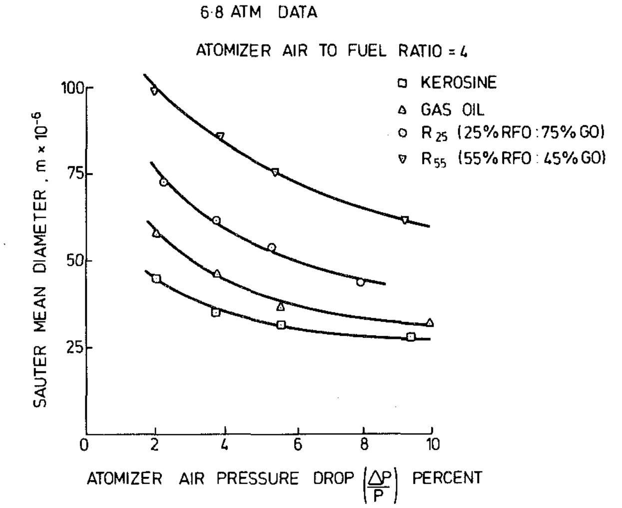

Fig. 8 Effect of varying atomizer air pressure drop and fuel type on mean dropsize

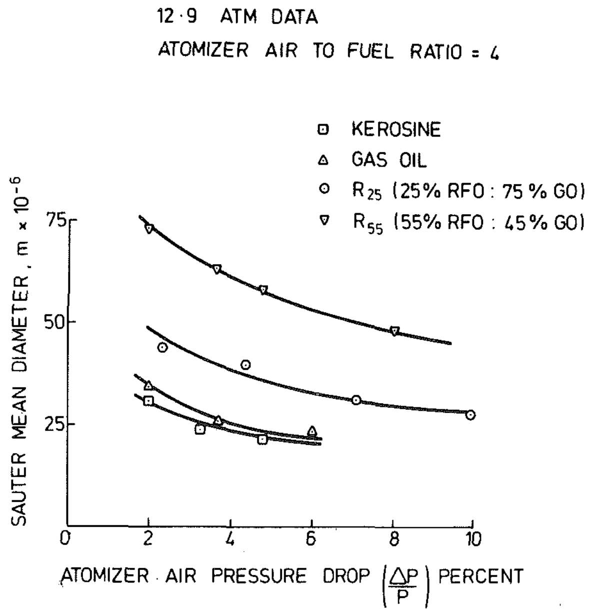

Fig. 9 Effect of varying atomizer air pressure drop and fuel type on mean dropsize

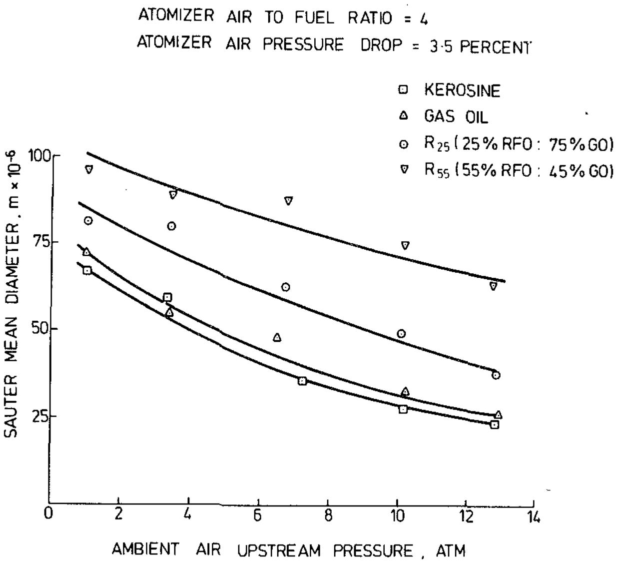

Fig. 10 Atomizer mean dropsize performance under varying ambient air pressures

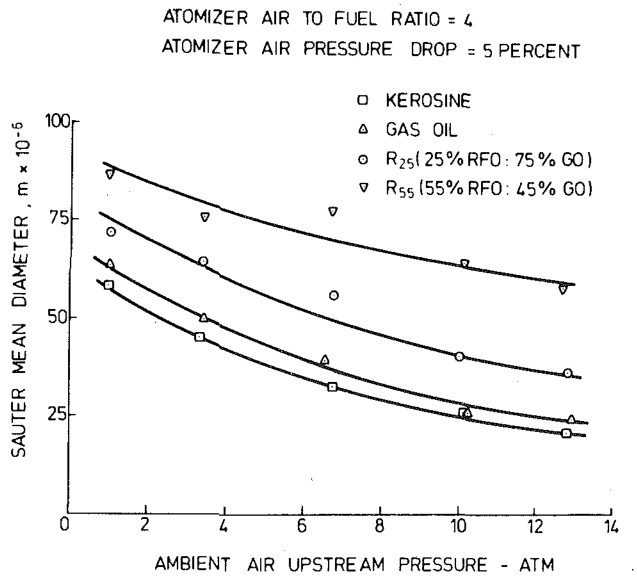

Fig. 11 Atomizer mean dropsize performance under varying ambient air pressures

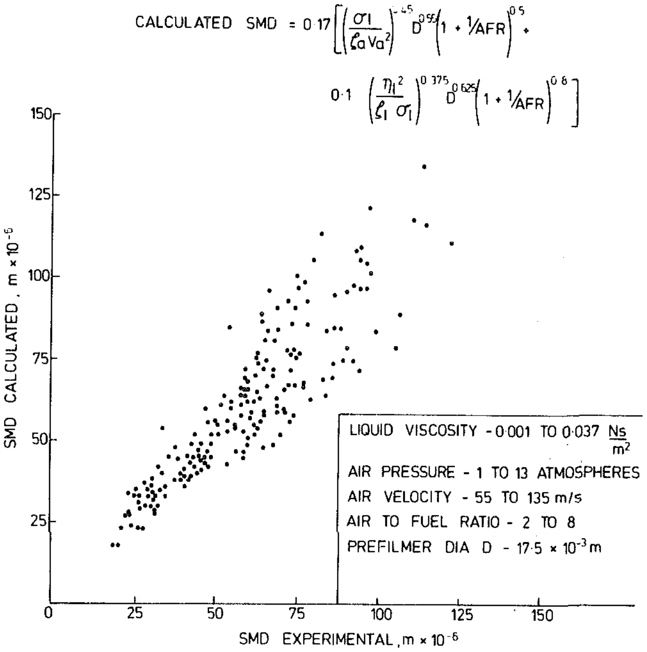

Fig. 12 Comparison of calculated and experimental SMD values

independent of the air density influence. These differences can be explained by the facts that

1 the data presented in this paper were obtained under closely controlled conditions, i.e., all variables with the exception of air density were held constant—this was not so in the early work. This accounts for the observed difference with respect to the influence of air density upon the first term of the SMD correlating equation.
2 the effect of air density upon the viscosity-dominated second term in the correlating equation had not been examined experimentally in the earlier studies.

It should be pointed out that, as in the previous study, the contribution of the viscosity-related second term in equation (3) changes from one of insignificance for the low-viscosity kerosine fuel to that of increasing significance for the higher-viscosity fuels. This is particularly so when operating at higher pressures.

Conclusions

1 The spray Sauter Mean Diameter performance of the atomizer studied in the present investigation, featuring a prefilmer diameter of 17.5×10^{-3}m, is predicted with a reasonable degree of accuracy by the following dimensionally consistent equation:

$$\mathrm{SMD} = 17 \times 10^{-2} \left[\left(\frac{\sigma_\ell}{\rho_a V_a{}^2} \right)^{0.45} \cdot (D)^{0.55} \cdot (1 + 1/\mathrm{AFR})^{0.5} + 0.1 \left(\frac{\eta_\ell{}^2}{\rho_\ell \sigma_\ell} \right)^{0.375} \cdot (D)^{0.625} \cdot (1 + 1/\mathrm{AFR})^{0.8} \right]$$

over the following ranges of operating conditions:

liquid viscosity = 0.001 to 0.037 Ns/m^2
liquid surface tension = 0.027 to 0.074 N/m
atomizer air to fuel ratio = 2 to 8
air velocity = 55 to 135 m/s
air pressure = 1 to 13 atmospheres

It must be noted, however, that the experimental verification of the influence of prefilmer diameter D upon the SMD equation must await results from atomizers of different dimensions.

2 The contribution of the viscosity-dominated second term in the above equation changes from one of insignificance for the low-viscosity kerosine fuel to that of increasing significance for the higher-viscosity fuels. This is particularly so when operating at higher pressures with high-viscosity fuels.

3 In the case of low-viscosity kerosine fuel, the influence upon SMD performance of atomizer air to fuel ratio variation (within the 2 to 8 range) is confined to the near atmospheric pressure condition only—there being no significant effect under higher pressure conditions. For the higher-viscosity fuels this influence extends higher up the pressure range.

Acknowledgments

The work reported in this paper is a part of the alternative fuels research contract financed by the Ship Department of the Procurement Executive, Ministry of Defence, Bath, England. The author gratefully acknowledges this support, and the permission to publish these results, together with the valuable discussions with the contract monitors Miss E. J. Macnair and Mr. C. A. M. Tayler (of MOD) and Mr. B. Jamieson (of the National Gas Turbine Establishment, Pyestock, Farnborough, Hants). Thanks are also due to the staff of the School of Mechanical Engineering, in particular Mr. R. Kenewell and Mr. P. Fleming for their valuable assistance.

References

1 Jasuja, A. K., "Atomization of Crude and Residual Fuel Oils," ASME JOURNAL OF ENGINEERING FOR POWER, Vol. 101, No. 2, Apr. 1979, pp. 250–258

2 Rizkalla, A. A., and Lefebvre, A. H., "The Influence of Air and Liquid Properties on Airblast Atomization," ASME *Journal of Fluids Engineering,* Vol. 97, No. 3, Sept. 1975, pp. 316–320

3 Lorenzetto, G. E., and Lefebvre, A. H., "Measurements of Drop Size on a Plain-Jet Airblast Atomizer," *AIAA Journal,* Vol. 15, No. 7, July 1977, pp. 1005–1010

4 Dobbins, R. A., Crocco, L., and Glassman, J., Measurements of Mean Particle Sizes of Sprays from Diffractively Scattered Light," *AIAA Journal* Vol. 1, No. 8, Aug. 1963, pp. 1882–1886

5 Godfrey, C., "An Assessment of a Light Scattering Technique for Dropsize Measurement," Cranfield Thesis, Dept. of Aircraft Propulsion, College of Aeronautics, Cranfield, Sept. 1969

A. R. Petruzzo
Francis Associates/SCI,
1033 Massachusetts Ave.,
Cambridge, Mass. 02238

Conserving Energy in Saudi Arabia

Planning the design of King Khalid Military City in Saudi Arabia has been under way for a number of years. In 1973, the joint venture team of Brown, Daltas, and Associates and Sippican Consultants International of Cambridge, Mass., and Rome, Italy, undertook the master planning and designing of a city to provide housing and service facilities for 70,000 people.

Located in a remote area, deep in the heart of Saudi Arabia, the city assumes an octagonal shape (Fig. 1), approximately 2.5 km across the widest part. In the design of the movement flow patterns within the boundaries, the compactness of the city provided the advantage of separation of vehicular and pedestrian traffic. As a result, a good deal of the area is a walkabout city. This same compactness provided the impetus for centralizing services which will make self-sufficiency possible in the vast, austere, beautiful surroundings of the desert.

One of the services required by this modern day city is air conditioning. To provide air conditioning, a chilled water plant is centralized with a 200 MW power plant nearby. Temperatures here climb as high as 122°F (50°C) in the summer. The main chilled water plant is located at the southeast corner and serves the chilled water distribution system shown in Fig. 1. This large chilled water plant which houses eight nominal 6500 ton chillers, presents an opportunity to utilize energy conservation measures in the cooling generation and distribution of the chilled water.

The chilled water system is divided into two main loops: the plant loop and the primary distribution loop. The plant loop system is a runaround loop commonly known as a rat-race type which insures constant flow through each chiller when each chiller is activated. By referring to Fig. 2 it can be further noted that water in the chilled water circuit is circulated through two closed runaround plant loops, one on each side of the plant. The plant loop is connected through a bridge type bypass to the primary distribution loop. The supply temperature leaving the chillers is set at 39°F (3.8°C). This cold leaving temperature is available for the primary distribution system which leads into the city ring loop. The city ring loop, shown in Fig. 1, provides a constant chilled water supply and return from either direction. If there is a point of repair in the city ring loop, isolation valves can be closed around the point of repair and branches on both sides can be kept in service. Outside the East and West side of the plant there are two forced draft cooling towers with four cells in each. Each cell will cool 13,000 gpm of condenser water from 100°F (37.7°C) to 85°F (29.4°C) when fully loaded. The cooling towers will be ceramic or cement asbestos filled. Each cell can be used interchangeably with each chiller. The chillers in turn are designed for a temperature drop of 17°F (9.4°C) at peak load.

There are ten condenser water centrifugal type water pumps, one for each chiller-condenser combination circulating water to each cooling tower and two serving as standby.

During high load conditions, the distribution system loop will operate with 39°F (3.8°C) supply chilled water and 56°F (13.3°C) return chilled water. The ring loop supplies the various branch circuits that finger out in radial fashion to buildings around the octagonal city.

In each of the buildings cooling is provided by package type air handling units. In the housing apartments, the air conditioning is provided by smaller fan coil units.

The central chillers will be package refrigeration units comprised of constant speed centrifugal compressors with inlet vane control to regulate refrigerant flow for varying load conditions. In this floor mounted package there will be a shell and tube evaporator chiller and a shell and tube condenser. Each compressor will be driven by a 7000 hp synchronous motor operating on 4160 V three phase.

The plant loop pumps are single stage 9200 gpm driven by 500 hp 4160 V three phase induction motors. The system distribution loop pumps are 9200 gpm driven by 1750 hp 4160 V three phase induction motors. The cooling towers are four cell concrete structures with a common basin. Concrete is utilized at this desert site for outdoor structures to withstand the corrosive action of the wind driven sand. In the tower, the cooled water will trickle down through the fill and be collected in the basin. The concrete basin has two deep sumps. The inner sump is an elongated chamber extending the entire length of one side of the basin and forms a settling chamber for the sand entrained in the water. The outer sump receives the water from the inner sump via a supernating action over a spillway. The outer sump provides a reservoir for the cooled clean water for the condenser water pump supply.

The city is comprised of a wide variety of building types as would be expected in a city of 70,000 people. The buildings are divided into the following categories: 7200 two and three story apartment houses with 20 dwelling units in each, eight schools, a 300 bed hospital, three motels, eight office buildings, 23 dining halls, and 72 barracks. There is a department store and 13 mosques. In the maintenance area, there are three workshops, three administration buildings, a cold storage warehouse, a bakery, a laundry, stockade, power plant, switchyard station, four fuel transfer buildings, and 32 service stations. The total building area is 2,500,000 square m^2(25,000,000 ft^2). Of the 25,000,000 ft^2 80 percent is air conditioned space.

In the major buildings of the city there will be approximately 800 air handling units of 30 to 40 tons capacity. In the housing apartment buildings there will be approximately 7200 fan coil units. A city in the United States of 70,000 people would have approximately the same building floor area, but it would not be as extensively air conditioned as this city in Saudi Arabia. Another dissimilarity is that this city in Saudi Arabia is very compact in area, only 2.5 km across the extremities of the octagon, which makes it more pedestrian in nature than most established older cities. Because of this compactness, central services become integrated and close knit. As a result a central chilled water system became very feasible.

During the master plan stage for this project, various schemes were analyzed. Two that were compared were Scheme I, utilizing a central chilled water plant and a companion gas turbine power plant close by, and Scheme II, utilizing unitary roof top air conditioning units air cooled with a central gas turbine power plant which would be remote to drive the air conditioning compressors. The summary of cost

---

Contributed by the Power Division for publication in the JOURNAL OF ENGINEERING FOR POWER. Manuscript received at ASME Headquarters January 28, 1980.

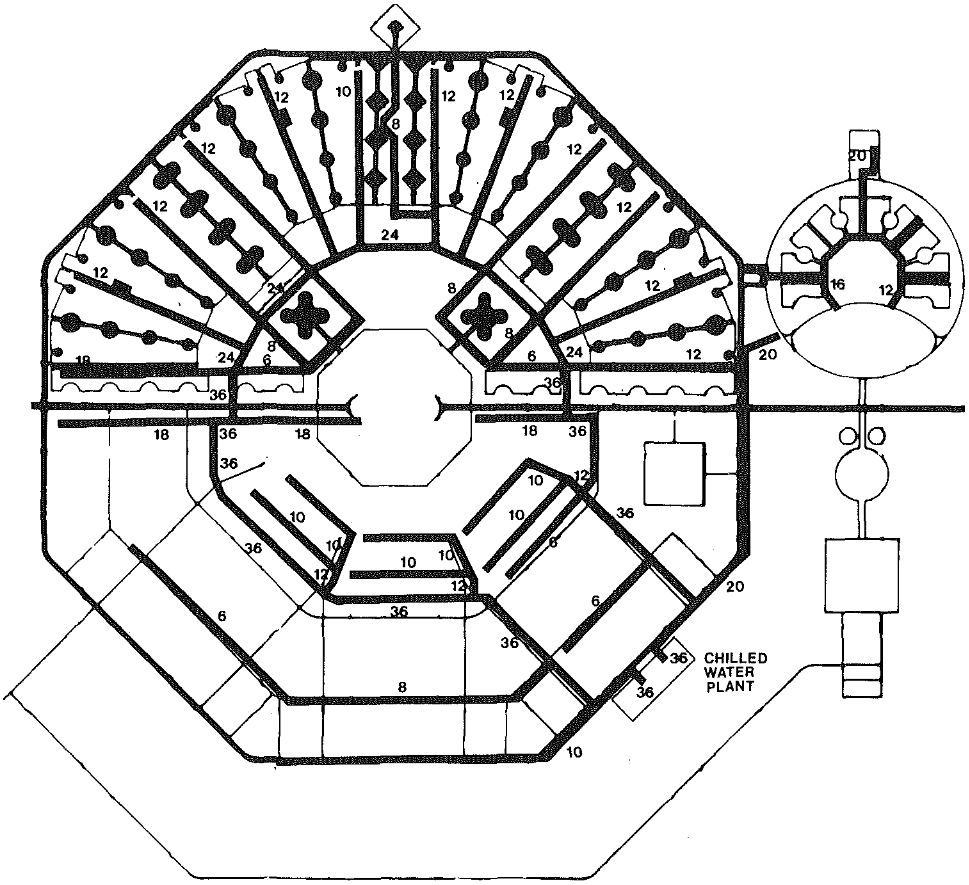

Fig. 1 Chilled water distribution system

comparison favored the central chilled water plant for two reasons: First, the chiller compressors work at less kW per ton (approximately 0.8 kW per ton) than the air cooled roof top unit compressors. Second, the central chillers will be put on line only when there is sufficient load to warrant an additional compressor resulting in the chiller compressors always working at a high capacity range in excess of 60 percent. In the scheme using roof top units, the small compressors would be often loaded below 50 percent capacity in the less efficient range causing the high 1.5 kW per ton factor. Also in the high load period the condensers would reject the compressor heat to a high temperature ambient that further compounds the inefficiency.

Scheme I

Refrigeration 52,000 Tons at 0.8 kW/Ton = 41600 kW

Refrigeration plant auxiliaries

System distribution pumps = 72,000 gpm at 490 ft head

$$\frac{72{,}000\ (490)}{3960 \times .83} = 10{,}734 \text{ hp} = 8007 \text{ kW}$$

Plant loop pumps = 73,600 gpm at 95 ft head

$$\frac{73{,}600\ (95)}{3960 \times .83} = 2127 \text{ hp} = 1586 \text{ kW}$$

Condenser water pumps = 104,000 gpm at 100 ft head

$$\frac{104{,}000\ (100)}{3960 \times .83} = 3164 \text{ hp} = 2360 \text{ kW}$$

Cooling tower fans

$$300 \text{ hp} \times 8 = 2400 \text{ hp} = 1790 \text{ kW}$$

$$\text{Total kW} = 55{,}343 \text{ kW}$$

For a season of 3000 full load hours kW = $166{,}029 \times 10^3$

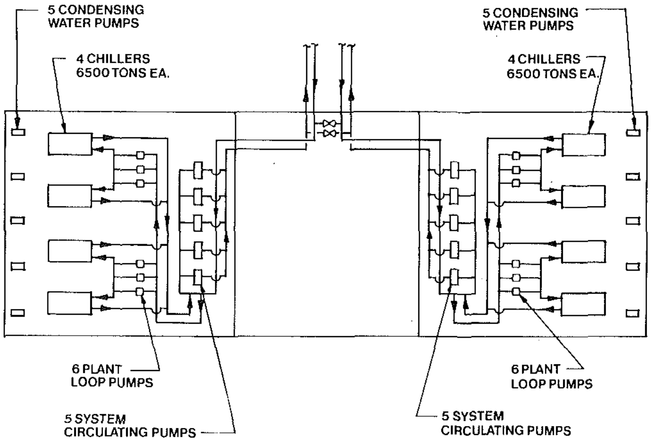

Fig. 2 Chilled water plant layout

Scheme II

Refrigeration 52,000 Tons at 1.5 kW = 78,000 kW

Note: 1.5 kW/ton to encompass lower efficiency of part load which will be an average of 50 percent during most of the operation. This includes an allowance for 122°F (50°C) ambient air operation. For a season of 3000 full load hours kWh = $234{,}000 \times 10^3$

Savings of Scheme I over Scheme II

$$\text{kWh per year} = 234{,}000 \times 10^3 - 166{,}029 \times 10^3$$

$$\text{kWh per year} = 67{,}971 \times 10^3$$

The power generated at the city will be produced by eight gas turbines site rated at 25 mW at 122°F (50°C) ambient. The heat rate at am-

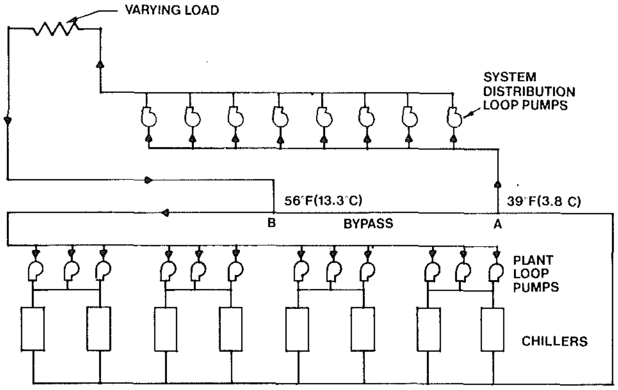

Fig. 3 Chilled water system loops

bient site condition will be approximately 13,215 Btu/kWh. The heat rate at ISO conditions is estimated to be 12,065 Btu/kWh. The average heat rate is between these quoted rates and is assumed to be 12,500 Btu/hr. Also, the current price of No. 2 diesel fuel for powering gas turbines was set at approximately 8 cents per gallon in November 1979. At this "in country" price the cost of electric power is:

$$\text{Cost} = \frac{12{,}500 \times 0.08}{140{,}000 \text{ Btu/gal}}$$

$$\text{Cost} = 0.007 \text{ dollars or } 0.7¢/\text{kWh}$$

Savings for power saved per year at 8¢ per gallon

$$\text{Savings} = 0.007 \times 67{,}971 \times 10^3$$

$$\text{Savings} = 475{,}797 \text{ dollars per year}$$

In reality, since the world price of crude is approximately six times the price of the No. 2 oil fraction, the savings in kWh represents a sum closer to 3,000,000 dollars per year for the true fuel value.

The central chilled water system will be a more flexible system, high in energy conservation. The maintenance will be less frequent and less difficult with chilled water air handling units in the city in comparison with the more mechanized roof top air conditioners with air conditioning compressors and condensers which historically require a higher degree of repair. The central chilled water system, once selected, presented a special set of opportunities. The vast interconnected distribution system with 70 mi (116 km) of transport piping varying in pipe size from 42 to 4 in. will store a huge volume of chilled water—3,000,000 gal. This constitutes a 40 min supply of cooling with all the chillers off the line during a peak high load time. This same huge cooling storage effect of the distribution chilled water smooths out the fluctuations in load. Consequently, the two loop system was designed for the central chilled water plant and the city. A system distribution loop was designed to accommodate the varying load and flow in the city by riding the distribution pump curve and adding pumps as necessary. The chiller plant loop was designed to provide constant flow through each chiller in incremental steps as the load requires.

In Fig. 3, chilled water system loops, the two main loops of the chilled water system, are shown. The system distribution loop varies in flow continuously as each 9200 gpm increment is passed from 9200 gpm up to 72,000 gpm as demand in the city builds. At these increments another chiller and plant loop pump is activated so that the flow in the plant loop will stay above the flow in the system distribution loop. With the plant loop flow staying ahead of distribution loop, the excess flow will pass through the bypass from A to B and continue in runaround fashion into the chiller return. This is the more usual operation procedure in order to insure 39°F in the supply water to the city at all times.

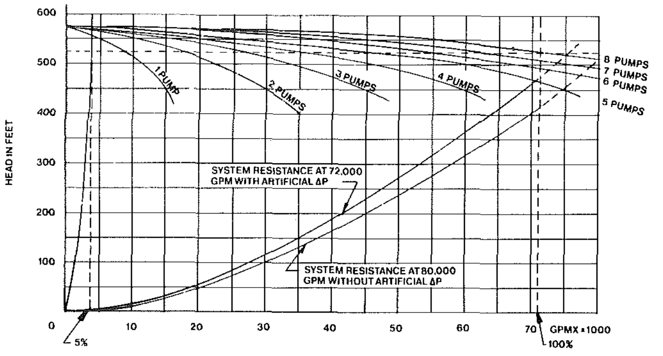

Fig. 4 Distribution system pumps operation

In Fig. 4, which represents the system resistance curves, it can be noted that the load varies from 5 percent load of 3600 gpm to 100 percent load at 72,000 gpm. The chilled water coils are controlled by two-way valves. These two-way control valves modulate open as load increases on each chilled water coil in the city causing the system resistance curves to change from a steep slope on the left to a shallow slope to the furthest right. The characteristic curves show eight single pumps running in parallel to produce the necessary flow in the distribution loop so that each will pump 9200 gpm against 525 ft head. It can be observed that six pumps can provide enough pump head to power 72,000 gpm through the resistance of the distribution loop. In an alternative operating procedure, utilizing fewer than eight pumps at full load, the distribution loop pumps could be turned on at approximately 12,000 gpm increments. With the system loop increasing in 12,000 gpm increments and the plant loop increasing in 9200 gpm increments at certain times, the distribution loop flow would exceed the plant loop flow. In the event the distribution loop flow exceeds the plant loop flow, the bypass flow will change direction from B to A mixing return water with the 39°F supply water from the plant loop. Energy conserving operation by the plant operators when the plant is in full service can utilize this alternative procedure provided that the 39°F supply is not absolutely essential and the distribution loop supply can be raised to a 40–42°F range. This would result in two energy savings. The first saving will be rendered by fewer distribution pumps being on line with less no load loss by the distribution pumps not activated. The second saving in energy is rendered by the fact that the higher distribution loop supply temperature will result in a higher distribution loop return temperature. This will cause the chillers to work at a lower kW per ton electrical demand—0.75 kW per ton instead of a 0.8 kW per ton. In addition to the energy savings, block load shedding can be done by taking one or more chillers off the line during peak periods and pumping from the cold source storage of the water in the underground chilled water distribution system.

The curves shown in Fig. 4 also indicate that the eight distribution pumps summation curve crosses the shallowest system resistance curve at the extreme point of 80,000 gpm. This provides excess distribution pump loop capacity equivalent to 56,000 tons utilizing the design average of 1.4 gpm per ton rate. The central chiller plant capacity also can be increased by increasing the chiller rotational speed to provide 7000 tons each. The chillers are designed with synchronous drive motors of 7000 hp each.

With this integrated design this uniquely compact, octagonal city will have all its cooling needs abundantly provided through the growth decade from 1980 to 1990. In the decades beyond, this single central plant, one of the largest in the world, will be pumping cold energy with constant load intensive, high efficiency response for this city's needs deep in the desert of central Arabia for a long time to come.

R. J. Ortolano
Engineering and Construction Department,
Southern California Edison Co.,
Rosemead, Calif.
Mem. ASME

J. A. La Rosa
Steam Turbine Division Engineering,
Westinghouse Electric Corp.,
Lester, Pa.
Mem. ASME

W. P. Welch
Marine Engineering Department,
Westinghouse Electric Corp.,
Sunnyvale, Calif.
Mem. ASME

Long Arc Shrouding—A Reliability Improvement for Untuned Steam Turbine Blading

An approach to the design and modification of untuned variable speed steam turbine exhaust blading has been found to be highly successful in eliminating fatigue failures due to the first tangential in-phase mode resonance. The approach consists of butt-welding the shrouds on the short arc blade groups to form a substantially longer arc length. The result is a significant reduction in vibratory stress at resonant speeds. Because of the ease with which the approach can be implemented in the field, backfitting is highly attractive to turbine operators. Availability benefits to the marine, utility, petrochemical, refining, industrial and commercial fields are anticipated.

Introduction

The availability of a steam turbine is dependent to a large degree on the turbine blading reliability. The loss of one of the longer blades may cause a forced outage of the unit and replacement and repair can involve an outage time of several weeks. Thus, great emphasis is placed by both the manufacturer and the user on a means of improving turbine blade reliability.

The major cause of turbine blade failure is high amplitude vibration in one or more of the natural modes of a turbine group leading to high cycle fatigue crack initiation and propagation and, in some cases, loss of a blade. Most often, these high cycle fatigue failures are caused by a forced vibration in which the frequency of a blade natural mode is directly coincident, or resonant, with the frequency of an excitation force which is present due to the nonuniform characteristics of the steam flow.

Conceptually, these forced vibration-induced blade failures can be forstalled by either designing blades strong enough to withstand resonant operation or by "tuning" the blades so that no resonance occur. Depending on the blade application, either or both of these techniques are used. For instance, in constant speed land steam turbines the last two or three stages are generally designed so that the first few modes are tuned and sufficient strength is provided to withstand possible higher mode resonances. In the case of the shorter, upstream blades whose frequencies are considerably higher, tuning of even the first tangential mode is usually impractical because of insufficient accuracy of frequency prediction techniques. For these blades, reliance is placed upon providing sufficient strength to withstand resonant operation in this mode. In variable speed machines where excitation frequencies exist throughout the operation range, tuning of the first tangential mode even the long last row blades is possible only at maximum speed, and sufficient strength must be provided to withstand probable resonances at other speeds.

Design-related blade failures, which have occurred in constant speed turbine untuned blading and in variable speed turbine blading, have, in many cases, been diagnosed to be due to a resonance in the first tangential in-phase mode. Corrective actions in these cases have generally taken the form of a redesigned blade in which the strength at the failure location has been increased, and, in some cases, the redesign also aimed at tuning or increasing the first mode frequency. However, there is another technique available for improving blade reliability. This involves neither strength nor frequency control, but rather a control of the energy input to a blade first mode vibration through the improved selection of blade group length. This technique, commonly called long-arc or harmonic shrouding is not a panacea for all turbine blade problems but has been very effective in certain applications and is the primary subject of this paper.

Background of Commonly Used Blade Groupings

The basic purpose of shrouding for turbine blades is to control radial flow and provide a smooth, continuous sealing surface, thereby minimizing thermal performance losses. A secondary and vital function of shrouding is to tie a blade to its neighbors and form a blade group that is less sensitive than a single blade to steam flow excitation. This excitation is caused by irregularities in steam flow that exist around the annulus of the blade path. As a consequence of the stiffening effect of shrouding, the grouped blade arrangement is superior dynamically in that the fundamental resonant frequencies of the group are higher than the corresponding single blade frequencies.

However, since grouping blades together introduces additional degrees of freedom, more vibration modes exist for a blade group within a given frequency interval as compared to a single blade. These group modes are quite complex with the blades in the group vibrating either in-phase or out-of-phase with each other and may be of three types—tangential, axial, or torsional. The number of these group modes increases as the number of blades in a group increases, and these modes must be analyzed and considered in order to assure a reliable design.

One consideration in the design of blade groups is the possibility that adverse internal strains may be developed due to assembly tolerances or, more importantly, rapid changes in turbine load which lead to temperature differences between the turbine rotor and the blade

---

Contributed by the Power Division of The American Society of Mechanical Engineers and presentated at the ASME-IEEE Joint Power Generation Conference, Long Beach, California, September 18–21, 1977. Manuscript received at ASME Headquarters June 14, 1977. Paper No. 78-JPGC/Pwr-12.

shroud. It is evident that this latter effect is a low cycle fatigue effect and, if the stresses are excessive, will lead to fatigue failures after many applications of fast temperature cycles.

This consideration, along with practical manufacturing and assembly reasons, has led steam turbine builders to adopt blade groupings limited to approximately 12 blades, so that one may say that over many years of practice, the custom has been to tie blades into packets ranging from 3 to 12 blades per group.

Design of Untuned Blading

Most commonly, the excitation forces, which supply the energy necessary to produce and sustain high amplitude forced blade vibrations, arise as a result of circumferential nonuniformities of the steam flow. These flow nonuniformities are caused by circumferential variations of gaging, pitch and incidence angle in the stationary and rotating blading, obstructions in the flow field such as inlet staybars, irregularities in construction such as open gaps at the horizontal joints of stator rings, and other flow disturbances such as those produced by steam extractions. Usually, the position and magnitude of the flow irregularity does not change with time, and thus a given blade sees the same pattern during each revolution. This excitation is called synchronous. Synchronous excitation can be shown to be mathematically equivalent to the sum of the discrete excitations at multiples of running speed, called harmonics. The magnitude of these excitation forces generally decreases with increasing harmonic. If a blade group has a natural frequency equal to a multiple, or harmonic, or running speed, a condition of resonance exists and large vibratory amplitudes may occur.

In constant speed turbines, it is possible to tune some natural modes of the longer blades out of resonance by keeping the natural frequencies in the middle half of the bandwidth between harmonics, as shown in Fig. 1. However, as the blade lengths are reduced and higher frequencies result, the bandwidth, in percent of the blade frequency, becomes narrow, making tuning difficult, and also the accuracy of frequency calculations becomes uncertain. Tuning becomes impractical when the shorter blade has a scatter band which cannot be confidently confined with the nonresonant portion of the Campbell diagram, and thus the primary design requirement must be that sufficient strength is provided to withstand resonant operation.

Variable speed turbines are used for driving ships, large pumps, blowers, compressors, and fans since the turbine operates well at a wide range of speeds with a minimum of control complexity. All the blading for these turbines is denied the privilege of tuning at all speeds and must operate, and usually without restriction, at speeds where blade natural frequencies may be exact multiples of running speed. Although the steam flow and torque may be reduced at these resonant speeds due to the system characteristics (e.g., a ship or a centrifugal pump), the blade loads may still be a large percentage of full load so that dangerous blade excitation may exist. These turbine blades, therefore, must be designed to strength requirements even more stringent than those for the constant speed machine.

Looking now at the overall blade path of a turbine, extending from the inlet steam chest to the exhaust annulus and contained in from one to three casings or cylinders in series, the blading may be generally described as HP (high pressure), IP (intermediate pressure), and LP (low pressure) blading. Our discussion here is concerned with all the LP blading, including the long, tapered, and twisted blading with relatively low first mode natural frequencies, so that the first mode is resonant at low multiples, i.e., harmonics, of running speed (2 to 8 for example) in the case of variable speed turbines and the untuned shorter length upstream LP blading in constant speed turbines.

Design practices for untuned blading vary within the industry, but it can be generally stated that acceptance criteria are based primarily on statistical evaluation of prior operating experience. At Westinghouse, this evaluation has led to the determination of the maximum probable vibratory stress that may be expected in a given stage of blading as a function of the fundamental frequency of the blading and the steady steam loading on the stage. For a reliable design, this probable vibratory stress must be less, by a specified margin of safety, than the expected fatigue strength of the blading. The fatigue strength is determined considering the effects of steady stresses, temperature, surface finish, and environment.

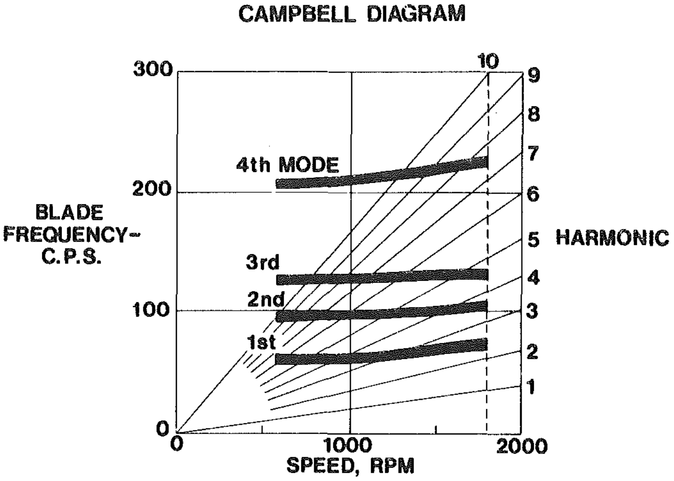

Fig. 1 Campbell diagram, last row

This design approach has proved over the years to yield satisfactory untuned blade designs. However, there have been exceptions in which due to larger excitation forces or greater degrees of material degradation due to environmental effects than previously experienced, blade failures have occurred. An increase in margins of safety to include these isolated cases would result in over-conservative designs in the vast majority of cases. To avoid this, and yet provide reliable operation for all untuned blading, the advantages of the harmonic, or long-arc shroud, concept have been utilized.

Marine Turbine Blade Failures Leading to the Long Arc Shroud Design

During the years prior to the mid-fifties marine turbine low pressure blading generally performed well. However, in the late fifties and early sixties, a number of marine turbine exhaust blade failures occurred. The failures involved tenons, air foils, and roots. Attempts made to correct the problems by under-shroud welding, blade redesigns to reduce vibratory stress, and various techniques to improve design strength were largely unsuccessful.

In order to obtain a resolution of the problem, considerable investigative work was performed. In one particular design which had failed, two identical single cylinder turbines had mirror image exhaust configurations to allow installation in a very compact hull envelope. A full-scale frequency and response test was run in the laboratory on the last three stages of a scrapped rotor of this design and is depicted in Fig. 2. The primary result of this test was that no stresses of sufficient magnitude to cause failure were measured, although several failures had occurred in both the last and next-to-last stages in operational turbines. At about that time, data were obtained which indicated that changes in water treatment created a corrosive environment which resulted in a degradation of the blade material fatigue strength. The measured blade stresses, when viewed with respect to the reduced fatigue strength, were then large enough to cause the failures observed. Further, when the design calculations were repeated using reduced fatigue strength values, the failures became predictable.

The problem which remained was: How could the design strength be increased or stresses reduced to permit reliable operation when operating in a corrosive wet steam environment?

Many of the designs had only a small difference in vibratory strength between the tenon, vane, and root. Therefore, corrective design, such as enlarging the tenon, had little effect on improving the strength of the blade base or root.

It is important to note here that several aspects of the failures were common. These were:

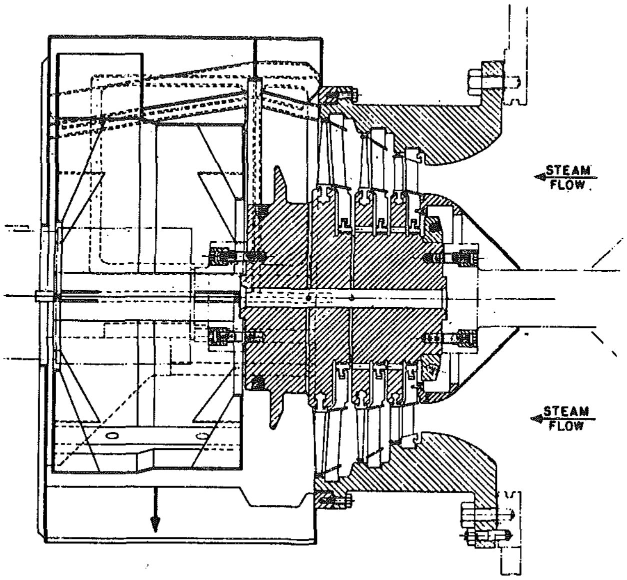

Fig. 2 Three-stage full-size laboratory test turbine

1 All blades were banded together in groups of 5 to 12 blades

2 All blades were operated in wet steam.

3 All blades were operated at variable speed, passing through and operating at as low as the third harmonic of running speed.

4 All failures were determined to be high cycle fatigue failures.

5 Many of the failures could be easily diagnosed as tangential mode failures as evidenced by the direction of fatigue crack propagation and the location of the cracks within the group.

Experimentally Measured Long Arc Shroud Benefits

As a solution to the problem, suppression of vibratory motion using shroud gap snubbers was considered. This was abandoned in favor of a 360 deg shroud based on successful British operation in certain applications. However, analysis indicated high hoop stresses and possible excessive tenon stresses due to anticipated thermal differences between the blading and rotor when cycling between ahead and astern operation.

To verify conclusively whether 360 deg butt-welded shrouds could sustain these thermal stresses and also to explore the benefits of a 360 deg continuous tie, two separate tests were run concurrently. First, in the last two stages of the laboratory test rotor, the shrouds on the original five and six-bladed groups were butt-welded together to form a continuous 360 deg shroud. Also, the last two stages in two production rotors were similarly modified.

The production rotors were run in their respective cylinders, and given rigorous ahead-astern cycling, deliberately producing significant thermal distortion. Upon examination, it was found that two of the four production shrouds which had been butt-welded suffered weld failures. It was, therefore, concluded that a rigid tie 360 deg shroud would not be acceptable as an immediate repair technique.

Concurrently, the laboratory test rotor was run with the 360 deg shroud to collect data which might be useful in the event that an acceptable continuous shroud could be developed. (This was later accomplished and verified in another series of tests.) The turbine was run up to full load and speed adjusted to the resonant speeds previously identified. However, no resonant stresses could be found. Then the entire speed range was traversed under normal load torques and still no resonant response could be detected. So complete was the lack of resonant response that it was at first believed there was a problem with the instrumentation. A thorough investigation of the wiring, slip rings, and other instrumentation revealed no operational problems.

The last stage was modified by parting the continuous shroud into two 180 deg arcs and the turbine run again. No tangential mode response was found over the entire speed range. Response in other modes was detected, but at very low stress levels. Again, the shrouds were parted, this time into 90 deg arcs. When the turbine was again run, a faint response was detected at a turbine speed corresponding to a first tangential mode resonance with the fourth harmonic of running speed. The stress level measured was negligible compared with the values originally measured for the five bladed groups. No other resonances or modes were detected.

Table 1 Application of long arc shrouds

	Semi-Continuous (180 deg) Shrouds			Harmonic Shrouds			
Turbine Supplier	Navy	Merchant	Land	Navy	Merchant	Land	Totals
Westinghouse	400	—	—	10	116	80	606
Licensees (Foreign)	1	54	—	—	175	12	242
Other (Domestic Turbine Manufacturers)	200						200
							1048

The shroud arc lengths were then reduced into even smaller lengths until the original five and six blade groups were restored. As each arc length was shortened, the response measured at resonance increased, although an accurate plotting of the degree of change as a function of arc length change was not possible because insufficient data was collected.

To the best of our knowledge, this was the first time resonant vibration suppression caused by forming a long arc length of less than 360 deg had been observed. Tests of the 180 deg shroud were repeated a short while later on a production unit and the benefits verified.

Early Implementation of Long Arc Concept on In-Service Marine Units

Since the 180 deg shroud resulted in a substantial vibratory stress reduction and presented no problem from the thermal stress view point, it was decided to apply this configuration as a backfit on existing units. Initial implementation of the 180 deg shroud was on the last two exhaust stages of more than 40 naval ship propulsion turbines. All backfitting was done using a shim-assisted butt-weld, except where new blading was installed. New blading was installed with one-piece 180 deg shroud pieces, exercising care that excessive distortion did not occur during riveting. Later, the same configuration was backfitted on many other naval ships, cargo ships and tankers employing either a shim-assisted or melt-through butt-weld. After being altered, no blade fatigue failures have occurred to date on any of the rows, including those which had experienced repeated failures with the short group configuration. This experience, over a 14 year period, demonstrates the beneficial effects that may be derived through the use of long-arc blading. Table 1 lists much of the experience with long arc shrouding to date.

Rigid Tie Required

An important aspect of the long arc shroud is that it is a rigid attachment to the blades through the tenon and it is nearly rigid between blades. This rigid attachment and rigid tie is necessary since one harmonic arch length (or two harmonic arc lengths) has forces being applied which alternately tend to pull the shroud apart and push it together tangentially. Where the blading must pass through tangential mode resonances, features which do not create a rigid tie may be incapable of attenuating a resonant vibration and buildup will occur.

The Long-Arc Concept

The role of group length in governing vibratory response of blading has been understood for many years and has been utilized to control or eliminate blade vibrations which may occur at nozzle passing frequency. For instance, at Westinghouse, certain control stage blading in constant speed turbines have been grouped in lengths of three or six blades per group with the total number of rotating blades in the row 50 percent greater than the number of nozzle vanes in the preceding stator ring. This design configuration[1] has been demonstrated both analytically and experimentally to completely suppress the fundamental tangential in-phase mode response to nozzle wake excitation.

Although group length selection has been extensively used for control of nozzle wake excited vibrations, there has been no general industry application of group length concepts to control or suppress vibrations resulting from a blade first mode resonance with low order multiples of the running speed. However, as demonstrated by the marine turbine experience, this can be a very powerful technique.

The Appendix provides an example of a simple analysis of the vibratory response in the tangential in-phase mode for any harmonic of excitation as a function of group length. In the more complete analysis used, the energy supplied by the excitation force per cycle of the group vibration is determined by computing the work done by the radially distributed force on each blade and summing this work over the entire blade group. The results of this analysis would show that for each group natural mode, there exists certain relationships between group length and harmonic of excitation in which the net energy supplied to the vibrations per cycle is zero. Conversely, there are other group length-harmonic relationships in which the net energy supplied is a maximum for a given mode.

To demonstrate, in a simple manner, the means by which group length influences energy input to a group vibration, the following nonrigorous treatment is offered. Imagine that you are observing an unshrouded row of blades in a turbine under load and operating at the speed resonant with the tangential mode vibrating at the fourth harmonic. In other words, for each revolution of the turbine, the blade vibrates four times or, as shown in Fig. 3(*a*), appears as four cycles of a sine wave over a 360 deg period. This, in turn can be illustrated as shown in Fig. 3(*b*) as the free standing blades vibrate back and forth tangentially. (Merely for the purpose of illustration, the vibration is shown as purely tangential, although usually the blade's tip motion is inclined to the axial direction by 10 to 30 deg.) Note that one cycle of the sine wave can be superimposed around the row to illustrate the motion of the blades from zero amplitude at the 0, 90, 180, and 270 deg positions. This is approximately as the blades would appear if you were to observe the row with a strobe light.

Now, if all the blades vibrating to the left are coupled with those vibrating to the right, vibratory motion cannot be sustained since the net energy to the group will be zero. It can be easily seen that arcs of 90 or 180 deg or 360 deg all produce systems with a net energy input of zero.

Such a configuration, where the group length is equal to one or more cycles of the sine wave of the excitation pattern, is referred to as a long-arc group. In the specific case of where the group length is one cycle of the sine wave, this configuration is called the harmonic shroud.[2] In general, it can be stated that for any group mode in which the blade deflections are in-phase, complete energy and thus vibration suppression can be accomplished by grouping the blades in lengths of the excitation force pattern of concern.

These results for the first tangential in-phase mode are shown in graphical form in Fig. 4 where the ordinate gives the ratio of the energy supplied to the shrouded group to the energy that would be supplied to a corresponding number of unshrouded blades. Since vibratory amplitude, or response, is directly related to the energy supplied by the excitation force, the ordinate is sometimes referred to as response factor. The abscissa, H/Ns, relates the harmonic of excitation, H, to the number of blade groups, or segments, Ns, in the complete row.

The results of the turbine tests referred to earlier can be explained by reference to Fig. 4. The row tested had 138 blades, shrouded as 18 groups of six blades and six groups of five blades, or 24 segments of nearly equal length. The groups had a first mode frequency of 357 Hz resonant with the fourth harmonic at 5350 rpm. Thus, H/Ns is approximately 4/24 or 0.167, and from Fig. 4, the energy ratio or response factor is 0.97. This means that the group vibratory amplitudes are 97 percent of those which would exist in a single blade given the same damping, frequency, blade deflection shape, and excitation force. However, when the short groups are joined to form 180 deg arcs, the parameter H/Ns becomes 4/2 or 2.0, and from Fig. 4, the response factor is zero. Thus, the total lack of vibratory response is predictable. Note also that for a continuous shroud (and fourth harmonic excitation), H/Ns becomes 4/1 or 4.0, and also results in a vibratory response of zero.

It should be noted that if the maximum speed resonance occurred at the fifth harmonic instead of the fourth, the vibratory stresses,

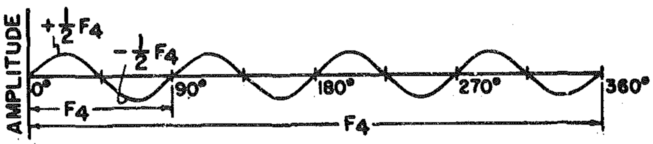

Fig. 3(*a*) Bladed row blade vibration with four cycles per 360 deg

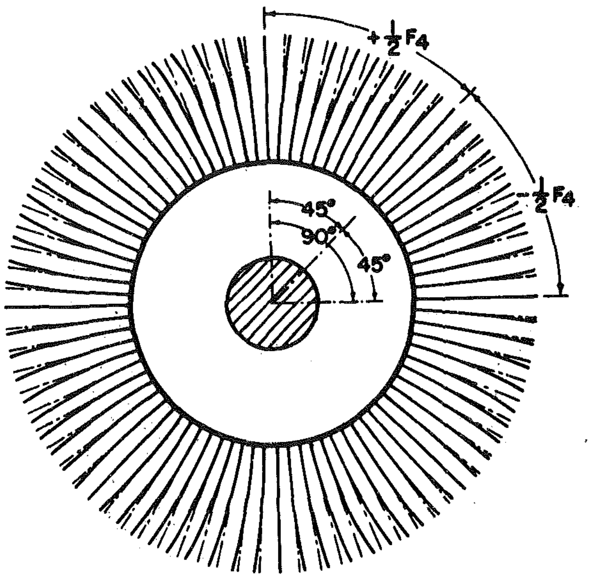

Fig. 3(*b*) Vibration of free-standing blades in a row, as excited by a fourth harmonic of rotation

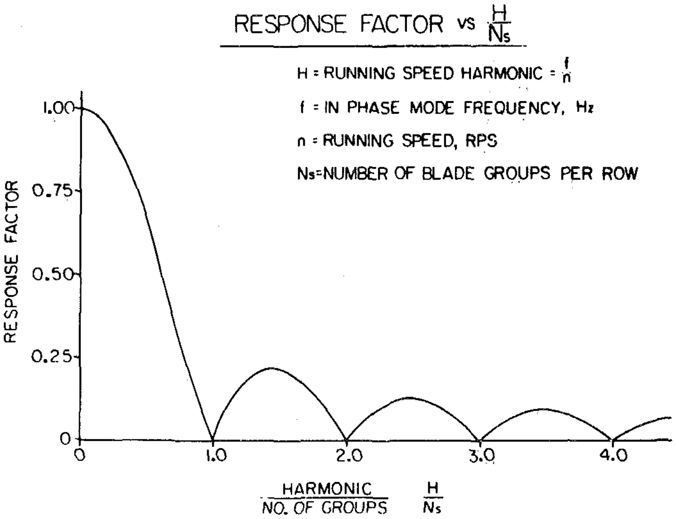

Fig. 4 Resonant (or forced) vibration suppression as influenced by length of shroud

---

[1] As covered by U. S. Patent 2258773, Oct. 4, 1941.

[2] As covered by U. S. Patent No. 3,588,278, June 28, 1971.

although considerably reduced, would have not been to totally suppressed in the 180 deg arch configuration. Reference to Fig. 4 shows that for $H/Ns = 5/2 = 2.5$, the group stress amplitude would be 0.14 or a reduction of about 85 percent. This degree of stress reduction should be more than sufficient to forestall fatigue failures in a short group design which had previously experienced distress. In addition, as the turbine operating speed is reduced, the blade will become resonant with successively higher harmonics. The odd numbered harmonics will have some resonant response, but at significantly lower levels when compared to short groups.

Although it is clear that long arch groups can either eliminate or drastically reduce first mode resonant response, caution should be exercised in utilizing this principle to insure that excessive stresses do not occur in other modes. The primary modes of concern are axial in which the deflection patterns appear as circumferential waves. It is possible that in some blade/shroud configurations, stress response in one of these modes can be critical. Although axial modes of short groups have rarely been the cause of failure in variable speed turbines, when the tangential modes are effectively suppressed the axial modes may become the troublesome modes. In anticipation of this, shroud designs, which provide for increased axial stiffness in the shroud, and continuous tying of the groups have been invented.[3]

Current Long Arc Shroud Application in Variable Speed Turbines

Variable speed turbines used for marine propulsion, compressor drives and feed pump drives currently use semi-continuous (180 deg) shrouding on smaller diameter exhaust stages. "Harmonic shrouding" is getting increased use by Westinghouse and their licensees due to reduced thermal and centrifugal distortion stresses when used on the large diameter stages. Table 1 summarizes this activity.

Current Long Arc Shroud Application in Constant Speed Turbines

Long arc applications in constant speed land steam turbines has thus far been limited to harmonic length groupings. A field implementation has involved an untuned low pressure blade which had experienced distress. Shop tests and analysis showed that the difficulties were due primarily to a first mode resonance at the seventh harmonic of running speed and also that the use of a harmonic grouping would significantly reduce first mode response. Accordingly, recommendations have been made to all owners of turbines utilizing this blade to weld together the existing small groups to form seven harmonic groups. At present, about 80 rows of this blading have been, or are, in the process of being so modified. The first rows of blading of this configuration have now operated successfully for approximately two years.

In new equipment recently designed for nuclear application, the low pressure untuned blading has been designed to standard procedures to provide sufficient strength to withstand first mode resonance. However, to insure complete reliability, the blading has also been grouped in harmonic lengths.

Marine Turbine Field Results to Date

Beginning in late 1963, when the first unit using a semi-continuous shroud was put in service, the results have been as follows:

1 No recurrence of failure has occurred once a semi-continuous shroud was used.

2 On some rows where the shroud width was approximately 1 in., the shim spacer butt-weld was found cracked during a routine inspection. No other defects were found. The butt-welds were converted to the melt-through design which eliminated the cracks at the base of the shim.

3 On one design where cracks were occurring at the base of a stellite having a sharp-cornered notch, failure correction was attempted using five segments (not a harmonic arc length) in lieu of the six blades/group. Evidence of poor drainage of the extraction line upstream of the stage and adverse water treatment was found when the design failed again. Ultimately, a new blade design was installed without the stellite notch, the drainage problem was corrected, and a three-segment harmonic shroud was installed. The modified design has been 100 percent successful with over 10 years of service.

4 To correct tenon, stellite cracks and base of blade failures in a boiler feed pump drive turbine, the design was modified on the last three rows from five blade groups to 180 deg segments. On two turbines having an upward exhaust, long sections of shroud were torn off when water accumulated in the exhaust when the drain pump malfunctioned and the alarm failed to activate. These deficiencies are being corrected and have *not* been identified as a failure of the long arc shroud to reduce steam induced vibratory stress.

In summary, over 100 rows of blades have been altered to semi-continous or harmonic shrouds, an appreciable percentage of them representing failure-prone designs. Excepting those instances given in the foregoing with extenuating circumstances, no further trouble has occurred.

Conclusions

The semi-continuous and harmonic shrouds—collectively referred to herein as long arc shrouds—have been highly successful in elimination fatigue failure problems in variable speed turbines and have become a standard design feature. Also, the use of harmonic shrouds has been recently introduced into the design of untuned blading in central station constant speed turbines.

It is likely that there are many variable and constant speed turbines such as those used in petrochemical, industrial, refining, commercial, marine, and utility service that have or will have failure problems that can be corrected by the long arc shroud.

The butt-weld approach to producing a long arc shroud has been very successful. Recent improvements in welding techniques have made the process a routine task and have eliminated the possibility of weld cracking in service.

Turbine testing, either in the laboratory or in the field, is often essential in analyzing a particular problem and should be encouraged by the industry. Laboratory testing permits the manufacturer greater latitude in analyzing design features and improving reliability and should, therefore, be a routine tool used by the designer of power steam turbines.

Acknowledgments

The authors wish to acknowledge the contributions made in the development of this concept by Mr. Harold L. Hildestad (Westinghouse Electric Corp.), whose guidance in the development of the first butt-welds, and the calculation approach used for the first long arc shrouds were of significant value. The assistance provided by Mr. Harold W. Semar (Westinghouse Electric Corp., retired), in the development of subsequent harmonic shroud calculations is also appreciated. And finally, the assistance provided by Mr. Lon Mayr (Westinghouse Electric Corp., retired), in the initial development of the full penetration butt-weld, and the subsequent implementation of this approach by Mr. John Kutz (Southern California Edison Co.), is also recognized and appreciated.

APPENDIX

Harmonic Excitation of Grouped Blades

A single unlashed unshrouded blade in resonance with the Nth harmonic of turbine rotation vibrates with its velocity in phase with the Nth harmonic exciting force. The work done on the vibrating blade per revolution of the rotor is

$$W = \pi N F_0 y_0$$

where F_0 is the amplitude of the exciting force (of frequency $N \times$ rps)

---

[3] As covered by U. S. Patents 3606578, Sept. 20, 1971, and 3702221, Nov. 7, 1972.

and y_0 is the average amplitude of blade vibration, averaged over the blade height. F_0 is the component of force in the direction of the vibration.

Now a group of M unconnected blades would be subject to a work input per revolution of

$$MW = \pi MNF_0y_0.$$

It should be noted that an essential aspect of this mode is that each blade in the group is vibrating with a small difference in phase with its neighbors, even though all the blades have the same amplitude, y_0.

Now consider a group of M blades connected with a long shroud so that each blade must vibrate in phase with all the other blades in the group, and at the same amplitude, y_0. The arrangement is as shown in Fig. 5, where the subterfuge has been adopted of allowing *the rotor to be fixed and letting the force pattern move to the right* with a velocity equal to the blade speed so that each blade sees an alternating force of

$$F = F_0 \cos \omega_N t, \text{ where } \omega_N = N\Omega_s$$

$$\Omega_s = 2\pi n_s, \text{ where } n_s = \text{rotor revs/s}$$

The resultant force on the group of M blades, at any time t is

$$F_R = \sum_{q=-M/2}^{M/2} F_0 \cos\left(\omega_N t + \frac{2\pi q\beta}{2\pi/N}\right),$$

where β = spacing between blades, radians, q = blade number, N = harmonic of rotation resonating the blade group.
or

$$F_R = F_0 \sum_{-M/2}^{M/2} \cos(\beta N_q + \omega_N t)$$

For a large number of blades the summation is equivalent to an integration, which is

$$F_R = \int_{-M/2}^{M/2} F_0 \cos(N\beta q + \omega_N t)dq$$

$$= \frac{F_0}{N\beta}\left[\sin\left(N\beta\frac{M}{2} + \omega_N t\right) - \sin\left(-N\beta\frac{M}{2} + \omega_N t\right)\right]$$

The maximum value of F_R occurs at $t = 0$ and may be considered the resultant force amplitude acting on the group. This resultant force is proportional to energy supplied to the group.

$$F_R - \text{Grouped} = \frac{F_0}{N\beta} 2 \sin N\beta\frac{M}{2}$$

$$= F_0 \frac{\sin\left(N\beta\frac{M}{2}\right)}{N\beta/2}$$

The equivalent force, F_R, acting on M single ungrouped blades is MF_0, so that the ratio of resultant forces acting on grouped and ungrouped blades is:

$$\frac{F_R - \text{Grouped}}{F_R - \text{Single Blades}} = \frac{F_0\dfrac{\sin(N\beta M/2)}{N\beta/2}}{F_0 \cdot M}$$

$$= \frac{\sin\dfrac{N\beta M}{2}}{\dfrac{N\beta M}{2}} = \frac{\sin\dfrac{N\alpha}{2}}{\dfrac{N\alpha}{2}},$$

where α is the length of shroud, radians. If λ is the wavelength of Nth harmonic force, radians, then:

$$\frac{F_R - \text{Grouped}}{F_R - \text{Single Blades}} = \frac{\sin \pi\dfrac{\alpha}{\lambda}}{\pi\dfrac{\alpha}{\lambda}}$$

where α and λ may be in radians, degrees or fractions of a complete revolution. Expressed in terms of harmonic number H and N_s, the number of shroud sections per row, the equation is:

$$\frac{F_R - G}{F_R - s} = \frac{\sin \pi H/N_s}{\pi H/N_s}$$

Since the amplitude of blade vibration is proportional to the magnitude of the exciting force, this ratio is a direct measure of the attenuation effect of long arc shrouds, for the tangential mode of blade vibration as well as any other mode where the blades of the group vibrate in phase at the same amplitude. The ratio is plotted in Fig. 4, from which curve it may be seen that when the shroud length equals the wavelength of the harmonic excitation ($\alpha/\lambda = H/N_s = 1$), the attenuation of input force (and energy) is complete. The same is also true when the ratio is 2, 3, 4, or any other integer, these latter cases representing long shrouds that span more than one wavelength of the exciting force.

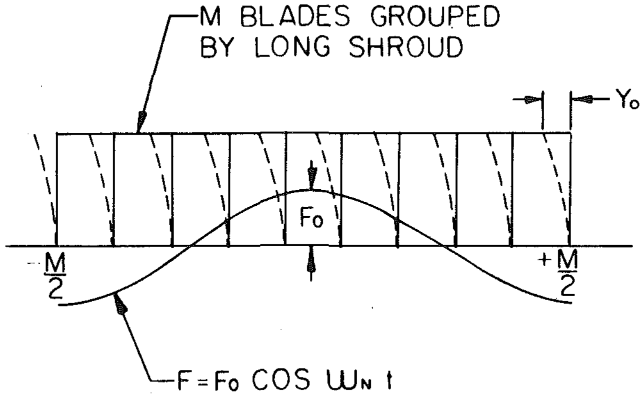

Fig. 5 Tangential mode vibration superimposed on one cycle of a cosine wave

and y_0 is the average amplitude of blade vibration, averaged over the blade height. F_0 is the component of force in the direction of the vibration.

Now a group of M unconnected blades would be subject to a work input per revolution of

$$MW = \pi MNF_0 y_0.$$

It should be noted that an essential aspect of this mode is that each blade in the group is vibrating with a small difference in phase with its neighbors, even though all the blades have the same amplitude, y_0.

Now consider a group of M blades connected with a long shroud so that each blade must vibrate in phase with all the other blades in the group, and at the same amplitude, y_0. The arrangement is as shown in Fig. 5, where the subterfuge has been adopted of allowing *the rotor to be fixed and letting the force pattern move to the right* with a velocity equal to the blade speed so that each blade sees an alternating force of

$$F = F_0 \cos \omega_N t, \text{ where } \omega_N = N\Omega_s$$

$$\Omega_s = 2\pi n_s, \text{ where } n_s = \text{rotor revs/s}$$

The resultant force on the group of M blades, at any time t is

$$F_R = \sum_{q=-M/2}^{M/2} F_0 \cos\left(\omega_N t + \frac{2\pi q\beta}{2\pi/N}\right),$$

where β = spacing between blades, radians, q = blade number, N = harmonic of rotation resonating the blade group.
or

$$F_R = F_0 \sum_{-M/2}^{M/2} \cos\left(\beta N_q + \omega_N t\right)$$

For a large number of blades the summation is equivalent to an integration, which is

$$F_R = \int_{-M/2}^{M/2} F_0 \cos\left(N\beta q + \omega_N t\right)dq$$

$$= \frac{F_0}{N\beta}\left[\sin\left(N\beta\frac{M}{2} + \omega_N t\right) - \sin\left(-N\beta\frac{M}{2} + \omega_N t\right)\right]$$

The maximum value of F_R occurs at $t = 0$ and may be considered the resultant force amplitude acting on the group. This resultant force is proportional to energy supplied to the group.

$$F_R - \text{Grouped} = \frac{F_0}{N\beta} 2 \sin N\beta\frac{M}{2}$$

$$= F_0 \frac{\sin\left(N\beta\frac{M}{2}\right)}{N\beta/2}$$

The equivalent force, F_R, acting on M single ungrouped blades is MF_0,

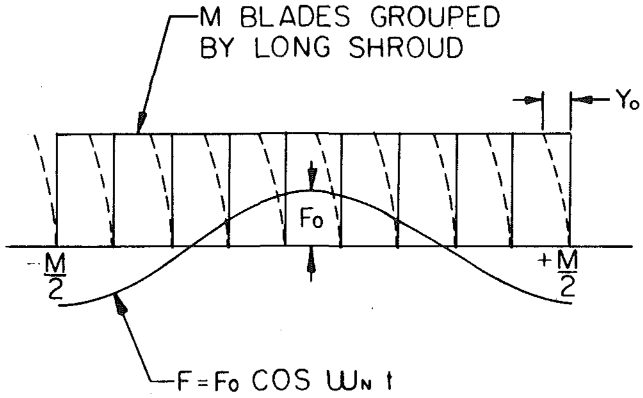

Fig. 5 Tangential mode vibration superimposed on one cycle of a cosine wave

so that the ratio of resultant forces acting on grouped and ungrouped blades is:

$$\frac{F_R - \text{Grouped}}{F_R - \text{Single Blades}} = \frac{F_0 \dfrac{\sin(N\beta M/2)}{N\beta/2}}{F_0 \cdot M}$$

$$= \frac{\sin\dfrac{N\beta M}{2}}{\dfrac{N\beta M}{2}} = \frac{\sin\dfrac{N\alpha}{2}}{\dfrac{N\alpha}{2}},$$

where α is the length of shroud, radians. If λ is the wavelength of Nth harmonic force, radians, then:

$$\frac{F_R - \text{Grouped}}{F_R - \text{Single Blades}} = \frac{\sin \pi\dfrac{\alpha}{\lambda}}{\pi\dfrac{\alpha}{\lambda}}$$

where α and λ may be in radians, degrees or fractions of a complete revolution. Expressed in terms of harmonic number H and N_s, the number of shroud sections per row, the equation is:

$$\frac{F_R - G}{F_R - s} = \frac{\sin \pi H/N_s}{\pi H/N_s}$$

Since the amplitude of blade vibration is proportional to the magnitude of the exciting force, this ratio is a direct measure of the attenuation effect of long arc shrouds, for the tangential mode of blade vibration as well as any other mode where the blades of the group vibrate in phase at the same amplitude. The ratio is plotted in Fig. 4, from which curve it may be seen that when the shroud length equals the wavelength of the harmonic excitation ($\alpha/\lambda = H/N_s = 1$), the attenuation of input force (and energy) is complete. The same is also true when the ratio is 2, 3, 4, or any other integer, these latter cases representing long shrouds that span more than one wavelength of the exciting force.

DISCUSSION

R. P. Kolb.[4] Prior to the publication of the subject paper, the Turbine Division of what is now Transamerica Delaval Inc. conducted a series of rotating turbine blade vibration tests. One objective of the program was to demonstrate the effectiveness of long arc shrouds on medium height blades. The blades were first tested with shroud bands forming five blade groups. These shrouds were later welded in sequence to produce two 180 deg arc groups. Our results corroborate the findings published in the subject paper.

The first mode tangential motion (420 Hz) was suppressed with the introduction of the longer arc shroud. The blades were constrained to vibrate at relatively high frequencies (1700 Hz) in a complex mode. The effect on stress levels was even more dramatic. Peak measured stresses at the base of the profile were reduced to approximately one-fifth their previous value. All peak stresses occurring at various resonant points in the operating range are shown in Fig. 6.

This design technique has proved immensely valuable for controlling resonant low harmonic induced stress levels for steam turbine blades used in low pressure sections of the machines. To date, no blade-shroud failures have occurred in these long arc shroud configurations attributable to design considerations. However, experience has shown that careful attention to detail with respect to the weld technique of joining the shroud arcs together is necessary in order to avoid some random failures in the weld locations.

---

[4] Transamerica Delaval, Inc., Turbine and Compressor Division, Trenton, N.J.

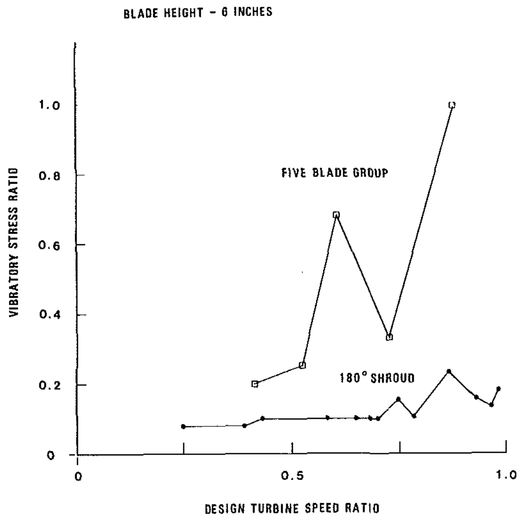

Fig. 6 Comparison of measured peak stresses for a typical strain gage: five blade shroud and 180 deg shroud

Authors' Closure

Mr. Kolb's comments are welcomed, particularly since the De Laval designs have benefited from the application of the long arc shroud concept. His comment that there should be particular attention to detail with respect to the welding technique is appreciated. As a matter of fact, that was the reason why the shim-assisted butt-weld was replaced with a full penetration weld. The stronger weld design eliminates the two small unfused areas that would normally occur in the shim-assisted butt-weld. In addition, the shim-assisted butt-weld is more prone to crack when an axial seal knife edge (commonly used in impulse, variable speed turbines) is made in the shroud or cover. We have not seen any incidents where weld cracks occurred after we used the melt-through (full penetration) butt-weld in our equipment on either an axial or radial seal design.

DISCUSSION

N. F. Rieger.[5] The authors are to be commended for their contribution of the long-arc shroud concept. This idea appears to offer a convenient solution for certain blading problems, by decoupling (or de-excitation) of the mode in question. The writer would like to ask the following questions:

1 Do the authors have any experience in the use of long-arc shrouding with reference to the axial and torsional modes of a blade group? Whereas the natural frequency of the lowest (in-phase) tangential and axial modes might be affected only slightly by the substitution of a long grouping of blades versus a short blade grouping, the frequency of the torsional modes would appear to be strongly influenced by the associated increase in shroud moment of inertia. This suggests that additional care may be needed in the selection of the arc length to ensure that the decoupling of a troublesome tangential mode does not introduce some new group resonance with a lowered torsional (or other) mode.

2 It also appears that long-arc shrouding might cause an increase in the steady bending stress, especially in the end blades of a long group, as follows: If the shrouds are installed or formed at zero rpm so that no initial prestress exists, at operating speed the blade group could experience additional tangential bending load as a result of the difference between the tangential expansion of the disk rim from centrifugal loading and the lack of tangential expansion of the shroud. This effect is shown in Fig. 7. The resulting tip deflection might thereby impose an additional tangential bending moment which has its maximum effect at the root attachment regions of the end blades of the group. Is there any experience to indicate whether this moment could cause a stress problem for long-arc shrouding?

Major ingredients in the successful application of the long-arc shroud technique would appear to be, first, precise identification of all potentially troublesome modes, and second, determination of all modes likely to be strongly excited by the non-steady forces of the steam path once this "fix" is installed. The first step can be undertaken by wheelbox testing, by calculation, or both. The second step seems to require some form of specific stage test, because insufficient information is otherwise available at present or the excitation spectra of turbine stages to permit accurate dynamic stress calculations, particularly in the per-rev region. Recognizing the cost and scheduling problems which wheelbox tests represent suggests that some further research toward the development of general procedures for inexpensive measurement or characterization of stage excitation spectra may be very desirable. It also suggests that the long-arc shroud technique requires design analysis care equal to that given in the original blade group design.

Some information on vibrations of blade groups with long-arc shrouds has been obtained by the writer. Sample results are summarized in Table 2 for short shroud, long shroud, and long shrouded, tiewired groups. It is seen that frequencies for the tangential and axial modes T1 and A1 are not greatly affected by the long-arc shroud, but the torsional mode R1 is substantially lowered. Certain higher modes are affected even more strongly. The long shroud introduces many more group modes, and it broadens the frequency range of the group modes. The influence of a tiewire on the group modes with and without the long-arc shroud is also indicated in Table 2. It is seen that

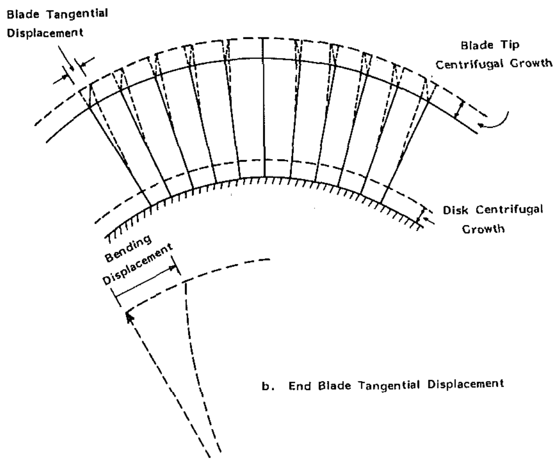

Fig. 7 Tangential bending of blades due to shroud circumferential stiffness

Table 2 Comparison of calculated natural frequencies for blade groups with and without long shroud and tiewire.

Mode	Six Blade Group	Twelve Blade Group With Long Shroud	Twelve Blade Group Long Shroud, Tiewire
A1	863	850	845
R1	990	902	890
T1	1052	1044	1183
A2	1644	1002	1000
R2	3120	1320	1311
A3	3848	1971	1962
R3	—	2919	2912
T21	4360	4126	5036
A4	—	3984	4045
T22	4481	4676	5694
R4	—	—	5153
T23	4580	4828	6095
A5	—	—	5992
T24	4948	4890	6188
T25	5187	4970	6355
		etc.	etc.

A = Axial mode, R = Torsional mode, T = Tangential mode.

---

[5] Stress Technology Incorporated, Rochester, New York.

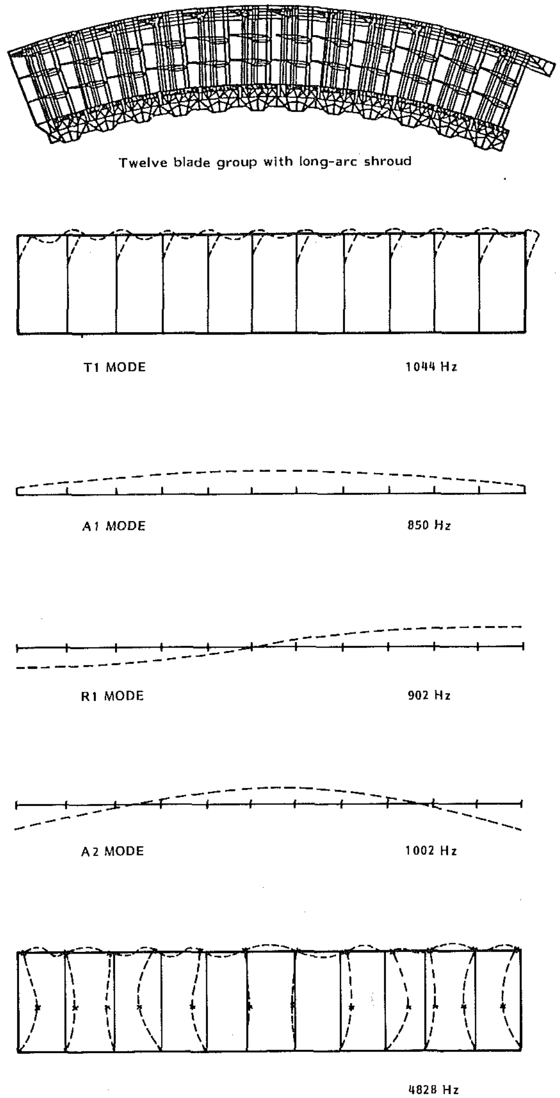
Twelve blade group with long-arc shroud

T1 MODE 1044 Hz

A1 MODE 850 Hz

R1 MODE 902 Hz

A2 MODE 1002 Hz

4828 Hz

Fig. 8 Modes for 12 blade group with long shroud

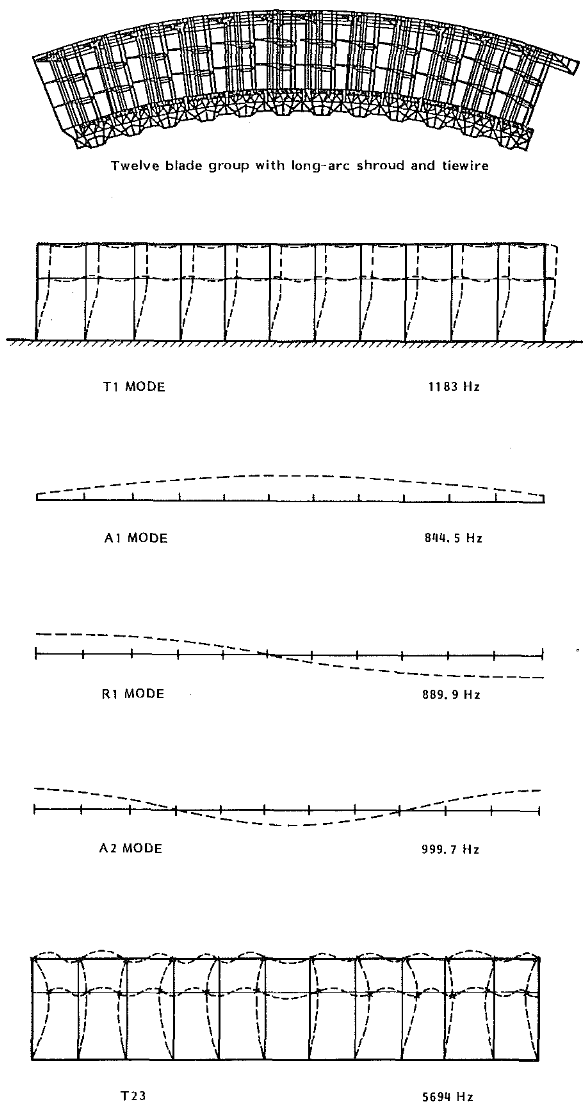
Twelve blade group with long-arc shroud and tiewire

T1 MODE 1183 Hz

A1 MODE 844.5 Hz

R1 MODE 889.9 Hz

A2 MODE 999.7 Hz

T23 5694 Hz

Fig. 9 Mode for 02 blade group with long shroud and tie wire

the long-arc shroud effectively suppresses the tangential mode as the authors have stated. The tiewire also effectively raised the frequency range of the group modes. Examples of selected modes taken from this study are shown in Figs. 8 and 9.

It is heartening to note the attention which this paper directs toward the reduction of problems in the lower (per-rev) modes. In the past, per-rev excitation problems of blading have received less attention in the published literature than, for example, nozzle-passing frequency problems. In the writer's experience, blade problems attributable to per-rev excitations represent an equally important subject. This paper is therefore welcome for its elegant contribution, and for the attention which it draws to the per-rev excitation problem.

Authors' Closure

Dr. Rieger's comments are welcomed since he obviously appreciates the fine points of implementing such a modification and the possible hazards of such a change. In Dr. Rieger's first question, he asks if the authors have any experience in the use of long-arc shrouding with reference to the axial and torsional modes of a blade group. In all of those applications involving variable speed turbines, one must assume that axial and torsional modes will be resonant at some running speed. However, in all of these applications no distress was experienced after the long arc modification, even though resonance in these modes obviously occurred.

However, in tuned stages, where the long arc will beneficially attenuate a marginally resonant tangential mode, the possibility of tuned axial and torsional modes becoming resonant is a definite concern. It can be shown schematically that the in-phase axial mode sees the same benefits from long arc shrouding as does the tangential mode, depending on the stiffness of the shroud. The effect of increasing the arc length on the axio-torsional modes is a lowering of the frequencies of the "X," "U," "S" and "W" modes as well as the more complex modes above them.

It would be difficult to tune all of these modes out of resonance even on a constant speed turbine, and therefore most turbine designers seeking the benefits of long arc ties in higher loaded designs resort to some form of continuous tie to control the amplitude of responsive modes. In the continuous tie form, tangential in-phase and axial in-phase modes are not normally responsive to steam induced vibration sources. In addition, axio-torsional modes will match the resonant harmonic, producing lower amplitudes than with harmonic arc lengths.

As was mentioned in the paper, numerous schemes have been developed to accomplish this effect. Recently, one of the authors developed a continuous/harmonic shroud design which seeks to achieve the benefits of the long arc in the tangential and axial modes by using a rigid tie between large groups of blades. In addition, a field retrofittable, flexible connector is installed between each long arc to constrain the end motion of the arcs when vibrating in any of the many axio-torsional modes. This design has been filed for U.S. Patent, and will probably be implemented into service within the next year.

In response to the second question, the concern regarding centrifugal distortion has also been given considerable attention, both at the inception of the design in the 180 deg form in 1963 and at numerous times since then. Ignoring temperature, the radial positioning of the end blades of a long arc shrouded group do tend to bend inward due to growth in the disk caused by centrifugal strain. In addition, the slight outward bending of the spans of shroud between rivets also contributes to an inward bending of the outer blades in the arc. Temperature differences between the rotor and blading will also contribute to inward bending under normal and stabilized operating conditions. However, these bending stresses are steady stresses and although they could contribute to stress corrosion cracking in a corrosive environment, this apparently has not yet occurred.

In the larger diameter, constant speed turbines there is a significant benefit in modifying to the harmonic arc length rather than a 180 deg arc since the steady bending stresses mentioned above are reduced. In addition, these stages will require attention regarding axio-torsional mode vibratory stresses mentioned earlier and the risk of corrosion assisted failure in "Wilson line" stages could further emphasize the need for continuous ties.

DISCUSSION

A. B. Dodd, Jr.[6] I appreciate the opportunity to comment on this paper. First, I would like to complement Mr. Ortolano for a good presentation of an important, well written and timely paper.

As mentioned in the paper, the long shroud concept was the result of an extensive test program in the early 1960's by Westinghouse, with Navy support, to solve blade failures in a very important class of Navy ships. Subsequent to this, long shrouds have been used in a large number of in service Navy steam turbine designs to successfully correct problem stages, and is being used as an important design tool for new turbine designs. The use of long shrouds has virtually eliminated blade failures in the last and next to last stages in Navy designs.

It is, however, important to recognize that long shrouds are effective only in eliminating fundamental tangential mode blade vibration problems; therefore, each design must be analyzed to determine that other vibration modes, such as axial or axial-torsional modes are not involved. Blade failures in Navy designs have all been established to be tangential mode problems and the long shroud approach in every case has been the correct design modification. Based on this experience, which has also confirmed that the long shroud bands do not introduce other unexpected problems, consideration is being given to changing Navy specifications for steam turbines to require long shrouds for all blade stages where the fundamental tangential natural frequency is calculated to be less than seven times turbine full speed running frequency.

The application of long shrouds as a design modification is unique in that it can be backfitted in an existing design at a relatively low cost since no new designed parts are required, and minimum disruption and loss in down time is involved. The modification is accomplished by welding the existing short shrouds together at each gap to obtain the necessary longer shrouds. In designs where only the last stage blades are involved, it may be possible to make the welds in place inside of turbine exhaust without lifting the turbine casing. A large number of Navy turbines have been opened and inspected after 10–12 years of operation, and no repeat blade problems or cracking of shroud welds have been found.

Referring to Table 1, the application of semi-continuous shrouds by other domestic turbine manufacturers has been predominately Navy and not all merchant as indicated.

As a final comment on the subject of blade failures, the Navy sees a real need for the following to reduce the number of unexpected in service blade problems:

1 Greater emphasis on testing to verify frequencies, identify troublesome vibratory modes, and better control excitation sources.

2 Development of a uniform calculation method which can accurately predict the vibratory characteristics and stress levels in a variety of blade/wheel configurations. Also the calculation method must be able to correctly evaluate the effects that changes in these basic configurations have on vibratory characteristics and stress levels. Present calculation methods used by the manufacturers are each different and are heavily dependent on their own past designs and failure experiences. The Navy keeps finding the hard way that present calculation procedures do not reliably predict the success of a new or slightly modified design/configuration.

Authors' Closure

Mr. Dodd's comments are welcomed, including his verification of the fine performance of this modification in Navy vessels. His concern about the possible disturbance of axial and axio-torsional modes is appreciated and has been discussed earlier. The modifications used to produce a *continuous/harmonic* shroud also incorporates the existing blading design and the modification can be made in the field. His comments regarding the differences in the manufacturers' calculation methods are understood and probably will not change unless the Navy produces a uniform system for evaluating their suppliers' equipment. Since the Navy buys the design as well as the hardware, such an approach would be reasonable in their case; however, in the utility/industrial power industry, this approach would immediately have problems in that the necessary ingredients to evaluate a design may not be available to the purchaser of the equipment, and such information is usually considered proprietary by the manufacturer.

Additional Closure by W. P. Welch

The discussions of Messrs. Dodd and Kolb and Dr. Rieger add significantly to the value of the paper and are appreciated by the authors. It is certainly true that long arc shrouds alter the axial and torsional natural frequencies and add markedly to their number, making the complete analysis of the stage more complex when these higher modes are considered to be significant or likely to be severely excited.

The experience of this author's former company with marine turbines has been that the low pressure stages do not suffer from serious excitation in the torsional and higher (beyond the first) axial modes, except in the stages where there are abnormal flow aberrations due, for example, to poorly designed extraction belts. This experience tends to support the belief that the low harmonic axial excitations are small in magnitude in well designed stages.

At the time of writing the paper the harmonic shroud had seen less than ten years of service. Delay in publication for the transactions has caused four additional years to elapse, and in this interval additional turbines have been put into service by the author's former company. In our activity, marine turbines, as well as those of our licensees, there have been no troubles reported or observed on stages having long arc or harmonic shrouds attributable to these improvements or indicating failure to suppress harmonic resonant response.

Summary

The comments made by the three reviewers of this paper are very much appreciated. Each of them attended the presentation of the paper and made their comments in person. Since the time when the paper was presented, continued implementation of the long arc con-

---

[6] Naval Sea System Command, Washington, DC.

cept has proceeded in steam turbines. The continued implementation within the Southern California Edison Company (SCE) system has grown steadily, and has recently included the last three rows of another auxiliary turbine design for a total of 24 more rows, plus several additional rows of marginally tuned 14 in. blade on a constant speed main unit. The benefits of these modifications have been evaluated and have been found to avoid costs in excess of an estimated 50 million dollars for the Southern California Edison Company alone during the years 1973 through 1981. These savings include repair costs avoided, fuel differential costs avoided, and construction costs avoided.

A. K. Chambers
Research Associate.

J. R. Wynnyckyj
Associate Professor.

E. Rhodes
Professor and Chairman.

Department of Chemical Engineering,
University of Waterloo,
Waterloo, Ontario, Canada

A Furnace Wall Ash Monitoring System for Coal Fired Boilers

This paper describes the successful development of an ash-deposit monitoring system for use in large pulverized-coal fired boilers. Using commercially proven heat flux meters the system measures the severity of ash deposition by measuring the net decrease in heat flux through the boiler walls. Testing of a prototype in two Canadian Utility boilers burning Western coals has shown that the system gives a reliable measure of the cleanliness of furnace walls and of the effectiveness (or failure) of soot blowers to remove deposits. Indications are that the system will be valuable in improving efficiency of boiler operations and in minimizing slagging and fouling problems when firing difficult coals.

Introduction

In the operation of a pulverized-coal fired boiler a significant fraction of the ash contained in the coal is deposited on the water walls of the combustion chamber and on the tubes of the boiler's convection section. The ash deposits modify the radiative (adsorptive) properties [1, 2] of the surfaces and, having a low termal conductivity, they insulate the tubes from the flame. Both of these effects interfere with efficient flame and gas to tube heat transfer.

Much work has been done on the problem, and most of it has been reviewed [3–5]. The relationship between rank, chemical composition and mineral distribution in coals has been linked to well established coal evaluation tests [5, 6] such as the ash fusion and softening temperatures, the viscosity-temperature curve [7, 8] and ash sintering strength [8]. Furthermore, good progress has been made in linking these tests with the fouling[1] behavior of the coals involved under actual boiler conditions [23].

In addition to coal-related causes, factors which are a function mainly of furnace conditions exert a strong influence on ash deposition. An important one is a high local fuel/air ratio [22] (and existence of reducing conditions during combustion, even though an overall excess of air may be provided) and impingement of such flames onto furnace walls [5]. Also some coal deposits exhibit variable ash mineralization. Fouling properties can, therefore, vary widely within a nominally constant coal supply, as for example at the power station studied in this work. This fact is a serious obstacle to maintaining smooth control of boiler operation.

Ash deposits on water walls of the boiler furnace begin [9] as a result of impact of individual nodules 1 to 3 cm or more in size. The nodules are very porous agglomerates of the fly ash cenospheres, described elsewhere [10]. Further buildup of finer agglomerates, as well as deposition of additional nodules onto (or next to) the already adhering ones densifies and thickens the deposit. The authors' recent investigations [9] have shown that, when still relatively loose, this deposit is in a very dynamic state. While new material deposits some of the less strongly adhering portions fall off under their own weight or are torn off by the turbulent gas (a phenomenon probably related to the recently discovered turbulent bursts [11]). As fouling proceeds, there is general densification by deposition of new ash, as well as by sintering. Upon thickening under conditions of continued high heat flux there is then fusion of the top surface of the deposit. Buildup of nodules on this surface may continue. Such plastic deposits are no longer self-cleaning and must be removed by sootblowers.

While soot blowing can usually deal with deposits which form when operation is under control, a not infrequent occurrence is the buildup of catastrophic deposits, i.e., many inches or even feet in thickness and resistant to soot blowing. Experience shows that such deposits may be made to fall off by sudden changes in boiler load, often having to be repeated several times. In extreme cases shutdowns for cleaning are unavoidable. Such upsets are proven to be associated with major departures of coal-ash properties from average values, and oversight or malfunctions in boiler control.

The practical implications of ash deposits, those which are reflected directly in the capital and operating costs of generating stations, are as follows: Because of the generally-decreased heat fluxes, a larger heat transfer surface is required than otherwise would be the case. There has been a dramatic increase in furnace size for a particular load (as measured by the specific furnace release rate, W/m^2 of furnace area) of new installations between 1968 and 1978 in the U.S. and Canada [12]. This fact is linked to the increased use of the fouling type coals, a trend which is likely to continue. Increased initial cost of new plants is thus a direct result of fouling phenomena. The economies of operation of an existing generating station are directly linked to the efficiency of use of heat transfer surfaces. Boiler operation is controlled by maintaining superheat steam temperature and flow rate by use of the available operating variables such as gas re-circulation, burner tilt, gas tempering, and steam attemperation. A need for frequent use of these adjustments, not to mention load changes or boiler shutdowns, is evidence of less than optimal cleanliness of furnace walls and indicative of uneconomical operation. In typical power stations of today, even a small fraction of rated efficiency loss due to malfunction or poor control translates into thousands of dollars.

At the present time, however, the boiler operator is not provided with any direct measurement of the degree of fouling of the combustion chamber (nor of the convection section). Soot blower actuation is based on his judgement of the indirect evidence from economizer temperature, burner position or amount of gas recirculation, etc. Surprisingly, moreover, no reference could be found in the literature

---

[1] The terms fouling and slagging are used to denote the products of ash deposition. There is confusion as to the meaning of the terms in the literature. In this paper, only the term fouling is used and it encompasses the case of deposits where there may be fusion of the deposit surface.

Contributed by the Fuels Divison of The American Society of Mechanical Engineers for presentation at the Winter Annual Meeting, November 16–21, 1980, Chicago, Illinois. Manuscript received at ASME Headquarters July 9, 1980. Paper No. 80-WA/Fu-1.

concerning development of ash-deposit monitoring instrumentation to provide him with such means. (The effect of ash deposits on heat flux has been examined in a test boiler [16].) Furthermore, attempts to automate sootblowing based on monitoring the above mentioned signals and subjecting them to on-line computer processing [13] have been made. These appeared promising but were not successful, underscoring the need for direct monitoring of ash buildup. Similarly, it is widely recognized [12, 15] that to prevent serious convection section fouling, the furnace exit temperature must be maintained below a definite value, set in accordance with the fouling tendency of the particular coal ash. No reliable means has, however, been as yet made available to the operator to continuously monitor the exit gas temperature.

In this paper we report on the successful development of an instrument system to monitor furnace wall ash deposits in commercial boilers. The system is based on the use of two heat flux meters, both viewing the furnace flame. One meter (henceforth to be called the "clean meter") is always maintained free from any deposits and thus receives the full heat flux from the flame, equivalent to that to be received by a perfectly clean water wall. The other meter (to be referred to as the "fouled meter") is allowed to be fouled by ash deposits in an identical manner to the water walls themselves. The output of the two meters is coupled via suitable electronic circuits to give a signal proportional to only the ash-deposit effects. The components of this system are based on reliable designs which have undergone extensive testing in furnace service. The investigations which lead to this development have been conducted in industrial boilers burning high-fouling, low-rank western coals. The observations made in the course of this work have yielded new data concerning ash deposition dynamics and heat-flux diminishing effects of ash deposits. Accordingly, this paper is also concerned with reporting these. Also evidence is presented which fully supports and extends the experience gained at the Detroit Edison Generating Station [14], that recording infrared optical pyrometers may be used as efficient and reliable indicators of furnace exit temperature.

Description of the Ash Monitoring System

In the course of this project, three different utility boilers were studied rather extensively. The test instrumentation installed on these boilers typically consisted of several heat flux meters, installed on the combustion-chamber water walls in areas of anticipated heavy ash buildup, air cleaned heat flux meter probes installed in inspection ports adjacent to the wall mounted heat flux meters, and recording radiation pyrometers installed near the entrance to the convection section of the boilers. In one of the test installations, a radiation pyrometer was also installed adjacent to a wall-mounted heat flux meter. The output of all meters was monitored for several months using multi-channel strip chart recorders

Heat Flux Meter. The heat flux meter chosen for use in this project was a commercially available disk-type meter of the Northover and Hitchcock design, described in detail in their paper [17]. Figure 1 gives a cross-sectional view of this meter attached to a boiler tube. Heat flowing to the disk surface is conducted away radially to the cylindrical meter body and through the attachment weld to the boiler tube. The thermal resistance of the disk causes a temperature difference between the disk center and periphery. The meter disk and body are made of dissimilar metal. Wire leads of the same metal as the meter body are connected to the body and the centre of the disk. In this way, a thermocouple junction is formed. The e.m.f. generated is proportional to the magnitude of the disk radial temperature difference and thus to the heat flux to the meter.

In the development of this instrument, the disk and body materials were chosen to give both durability in the combustion chamber environment and a calibration which is nearly independent of the heat flux meter temperature. Northover and Hitchcock's studies of the meter have shown an experimental calibration of 6.78×10^{-6} mV/(W/m^2) with a 95 percent confidence limit for ten meters of $\pm 0.67 \times 10^6$ mV/(W/m^2). The meter has been designed also for ease of installation. The latter requires merely the drilling of a hole through the boiler casing for the meter leads, and welding of the meter body to the boiler tube.

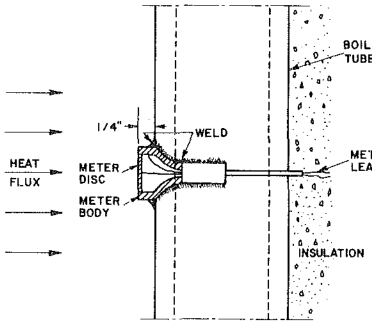

Fig. 1 Heat flux meter arrangement

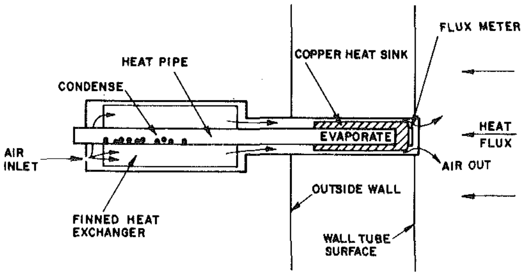

Fig. 2 Clean flux meter probe

The Clean Heat Flux Meter Probe. Figure 2 shows the design of the clean heat flux meter probe, developed presently and found particularly advantageous. A Northover and Hitchcock type heat flux meter is attached to a copper heat sink which is connected to a ⅝ in. dia heat pipe [18]. (An evacuated tube filled to about 5 percent of its volume with water.) A heat exchanger mounted on the condenser end of the heat pipe makes use of the cleansing air supply to cool the heat pipe. Previous testing [9] indicated that an envelope of air could be used to prevent ash depositing on the heat flux meter surface. This air jet caused a decrease in the magnitude of the heat flux striking the heat flux meter by less than 5 percent. In this way, a low-maintenance probe requiring only a supply of filtered service air is obtained. The relatively low operating temperature (200°C) of the probe, it is felt, aids in keeping its heat flux meter free of ash deposits.

This clean flux meter probe was mounted in a modified inspection port door for ease of installation on the boiler. It is, however, suitable for installation in any special or occasional openings in a combustion chamber wall. Because, in the present tests, the probe was usually positioned about 3 m to the side of the wall mounted heat flux meter, the probe was mounted at an angle of 10 deg so that both meters would view the similar areas of the combustion gases.

Figure 3 is a photo of the front of the clean heat flux meter probe after two months of service in a boiler without cleaning during or after service. As can be seen, the meter has remained virtually free of ash deposits.

Radiation Pyrometers. Two infra-red pyrometers, Ircon Models 300T5C and 1100, were installed on the boilers. The pyrometers were sensitive in the wave-length band from 0.7 to 0.97 and 2.0 to 2.6 μm.

Nomenclature

A = heat transfer area (m^2)
F = convection factor, clean flux meter
$\overline{GS}_1$ = overall view factor, which includes emissivities of source and sink (m^2)
h = convective heat transfer coefficient (W/m^2 − K)
T = temperature (K)
Q = heat transfer (W)
σ = Stefan-Boltzman constant (W/m^2 − K^4)

Subscripts

c = clean meter
f = fouled meter
g = gas
s = surface

Table 1 Battle River ash characteristic

PROXIMATE ANALYSIS		DRY BASIS
Moisture (%)		--
Ash (%)		15.1
Volatile Matter (%)		41.4
Fixed Carbon (%)		43.5
HEATING VALUE:		
B.T.U./1b		10674.
FUSIBILITY OF ASH: Atm °F	OXIDIZING	REDUCING
Initial Deformation Temp.	2246.	2138.
Softening Temp. (Spherical)	2318.	2228.
Softening Temp. (Hemispherical)	2390.	2336.
Fluid Temperature	2471.	2453.
ASH ANALYSES (%):		
a) Silicon Dioxide	47.28	
b) Aluminum Oxide	20.16	
c) Iron Oxide	5.30	
d) Calcium Oxide	10.29	
e) Magnesium Oxide	1.92	
f) Titanium Dioxide	0.71	
g) Manganese Oxide	0.06	
h) Molybdenum Trioxide	--	
i) Chromium Oxide	0.02	
j) Nickel Oxide	--	
k) Vanadium Pentoxide	--	
l) Sodium Oxide	2.35	
m) Potassium Oxide	0.83	
n) Phosphorous Pentoxide	0.68	
o) Sulphur Trioxide	7.46	

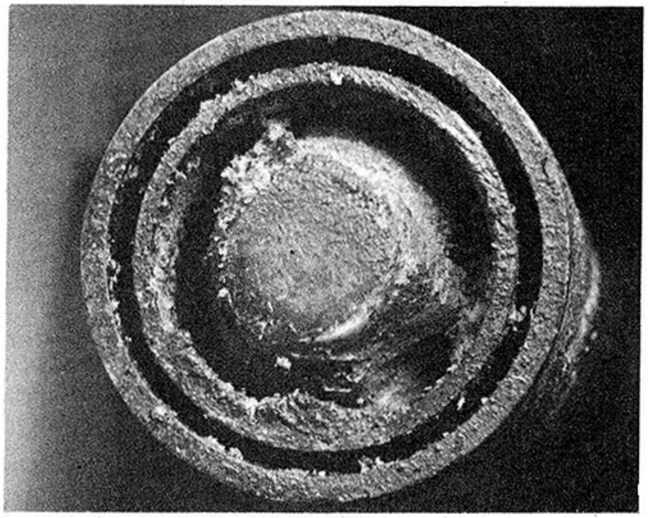

Fig. 3 Photograph of clean flux meter probe after two months of service

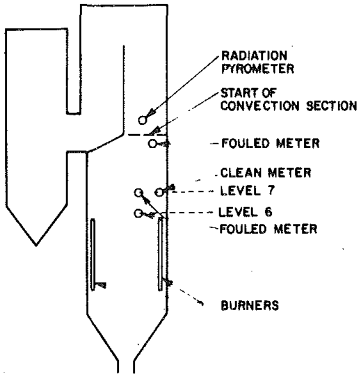

Fig. 4 Location of instruments on boiler

They were mounted on inspection port doors, focusing on a point 4.5 m into the boiler gases, and kept free of ash with an air purge. Standard pyrometers were modified to give a response time of about ten seconds.

Test Locations. The instruments described above were installed at the Battle River Generating Station of the Alberta Power Company in Forestburg, Alberta. The boiler was a 150 MW Combustion Engineering Superheater corner-fired pulverized coal boiler. It operated at a pressure of 1800 psi (1.24×10^7 Pa) and a superheat steam temperature of 1000°F (538°C). The reheat temperature was controlled by burner tilt which controlled the fireball position. Wall soot blowers were located at two levels above the burner, the first about 3.0 and the second 6.3 m above the burners. The wall blowers were spaced 2.7 m apart. The coal burned at the plant was a sub-bituminous 'C' coal with coal and ash analysis as shown in Table 1.

The location of the test instruments is shown in Fig. 4. One fouling heat flux meter at level 6 was 1.1 m to one side of a sootblower and 3 m above the burners; another, 1.1 m to the side of a sootblower at level 7; the third on the wall just below the furnace exit. The clean heat flux meter probe was intalled level with the second fouled meter 3.0 m away from it. The radiation pyrometer was installed about 1.5 m above the furnace exit aimed between the primary superheat and reheat convection tube sections.

Two additional test programs, involving five fouling flux meters, were conducted also at the Boundary Dam Station of the Saskatchewan Power Company and the Lakeview Generating Station of Ontario Hydro. The results of these test programs have been similar, only corroborating the Battle River results. They will not be described in detail here but have been, in part, described elsewhere [19].

Characteristics of Fouled Heat-Flux Meter Signals

The firing of the Battle River boiler (as is the case with most C.E. boilers of this type) is controlled so as to maintain constant superheat and reheat steam temperatures while maintaining the steam flow required by the turbines. The tendency of the superheat temperature to rise (usually related to a high furnace exit gases temperature) is counteracted by changing the burner tilt in the downward direction. Extreme downward burner tilt combined with a high furnace exit gas temperature is taken as indicative of excessive fouling of the combustion chamber walls. Individual sootblowers are actuated mechanically according to a preset sequence with one furance level being cleaned at a time. The start and frequency of a blowing cycle for a given level is decided upon by the operator, given the above steam temperature and burner position information. Level 6 requires significantly more frequent blowing than level 7.

Figures 5 and 7 are photographs of portions of recorder charts produced by fouled combustion-chamber meters. The charts refer to boiler operation using the "same" Battle River Coal, at full load (150 MW) and controlled in allegedly the same manner. Time proceeds from right to left and the unit outputs are shown as heat flux in watts/m^2 (converted from millivolts using the Northover and Hitchcock calibration factor given above). Henceforth, the traces labelled 'I' will refer to the meter on level 6 and those labelled 'II' to the meter on level 7. One should note the different flux scales and the significantly higher fluxes recorded at level 6. Note also the zero time offset for the traces. Curve I leads curve II by 15 min.

Near zero time (chosen arbitrarily) all curves show a large upward step shift. This is typical of the effect produced when the sootblower near the meter is activated, cleaning off the ash deposits on the meter. Other such shifts occur at time $\frac{3}{4}$, $2\frac{1}{2}$ and 5 hr in Fig 5(*c*), and $1\frac{3}{4}$ hr in Fig. 5(*d*). Subsequently, the meters build up with ash and heat flux through the water walls decays. The following features of the traces are noteworthy adn representative of ash buildup patterns in this and probably most other boilers, burning fouling coals.

1 The maximum flux to the wall, about 500,000 W/m^2 (Fig. 5(*a*), curve I) in the Battle River case persisted for only a very short time after a sootblow. There was consistently a decrease to less than 85 percent of maximum within 10 min. In the fouled condition, flux rates as low as 8 percent of the clean-wall flux were observable (e.g., Fig. 5(*b*) at 7 hr). In the usual Battle River operation, as reflected by the

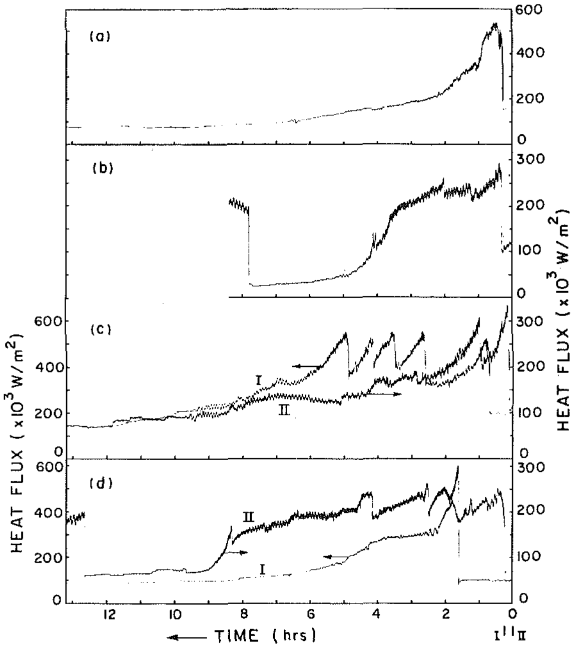

Fig. 5 Fouled meter outputs. I. level 6, and II. level 7. Note zero time offset.

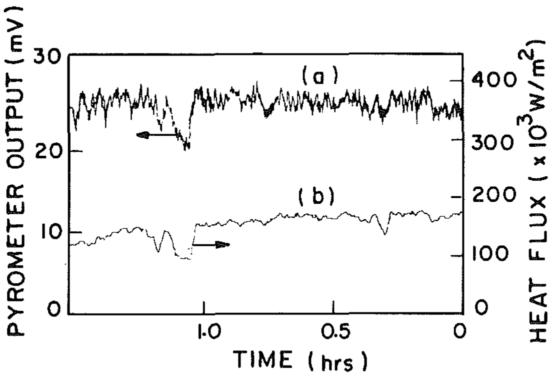

Fig. 6 Correlation between radiation pyrometer (*a*) and fouled flux meter (*b*) signals

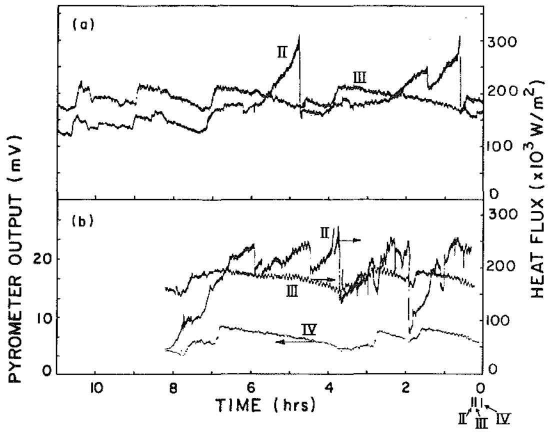

Fig. 7 Correlation between clean (III) and fouled (II) flux meter signals. Curve (IV) is an infra-red pyrometer signal originating from the convection section.

observations of these two meters over a four month period, water walls were cleaned when the flux reached 15–25 percent of the clean-wall values.

2 There was considerable day-to-day and hour-to-hour variation in the decay rate of a particular flux meter signal. For example, considering curve II in Fig. 5(*b*), little ash deposited initially, as indicated by a relatively steady reading over the first 3 hr, but the flux then dropped to only 8 percent of the clean condition in a further 2 hr. In Fig. 5(*c*), on the other hand, is shown a case where the signal decreased to 50 percent roughly exponentially over 2 hr. Similar variations in decay rate are shown by curves I. The large sudden jumps in the flux in curve II at 2½, 4 and 9 hr in Fig. 5(*d*) and curve I in Fig. 5(*c*), are due to ash and furnace changes to be explained below. The important message of these results is a confirmation of the operator belief that the rate of ash buildup is not predictable.

3 A characteristic feature of all the traces was the decrease in the "noise" (the short term variation in the meter signal) as the ash buildup continued. This noise originated from the short-term variation in the flame radiating power.[2] The decay in the noise is interpreted here to have resulted from the ash layer exhibiting thermal inertia; the real variations in flame radiating power were dampened out in the wall flux when the latter was less than about 100,000 to 150,000 W/m^2. In fact, preliminary indications were that a comparison of the initial and later-time noise was a good measure of the thickness and degree of consolidation of an ash deposit.

Fluctuations in Heat Flux not Caused by Ash Deposits

Curve I of Fig. 5(*c*) and curve II of Fig. 5(*d*) contained numerous sharp increases in the measured heat flux. These sudden increases could be caused by either sudden increases in flame radiating power or by changes in the insulating effect of the ash covering the meter (including shedding of the ash deposit). If the fouled meter signal is to be used as a measure of ash deposition only, there is a need for a direct measurement of flame radiating power. Were such a signal available, the above two effects on heat flux through the water walls could be separated.

Initially a radiation pyrometer was used to monitor changes in the flame radiating power. Figure 6 is a photograph of the recorder trace from a fouled heat flux meter on the same chart with a trace from a radiation pyrometer installed adjacent to it at a distance of 1.4 m. The pyrometer monitored the heat flux from the flame in the radiation band between 2.0 and 2.6 μm. The time response of the two meters to fluctuations in the flame radiating power was very similar. This was especially evident, for example, at 0.3 and 1.1 hr. Though the above results were obtained at the Lakeview Generating Station, the system behavior at Battle River was identical. The radiation pyrometer, therefore, is potentially a means to null out variations in flame radiating power from a flux meter signal.

However, because of the ease of signal conditioning, an air-cleaned heat flux meter probe was found prefereable for this purpose. Figure 7(*a*) is a photograph of two portions of recorder charts where the outputs from the level 7 fouled meter (curve II) and the level 7 clean meter (curve III) are shown. Figure 7(*b*) contains the above two outputs and also the output from a radiation pyrometer (curve IV).

The clean meter outputs of Fig. 7 show a characteristic saw-tooth pattern. A sharp decrease occurred during sootblows (such as at time 0.7 hr in Fig. 7(*a*) and 1.7 hr in Fig. 7(*b*) followed by a gradual increase until the next sootblow. A very similar pattern was seen in the radiation pyrometer output, which was located between the primary superheater and reheater tube passes and therefore gave a direct indication of furnace exit gas temperature. This pattern was evidently caused by the increase in combustion gas temperature (flame radiating power) as progressively thicker and denser ash deposits insulated the water walls. When the water walls were sootblown, the combustion gases quickly cooled, causing a drop in heat flux to the

---

[2] The term "flame radiating power" has been chosen to denote the combined effects of flame temperature and gas emissivity on the radiative heat flux to the water walls. This could be affected by many variables such as coal composition, excess air, burner setting, ash cleaning in other areas of the boiler, etc.

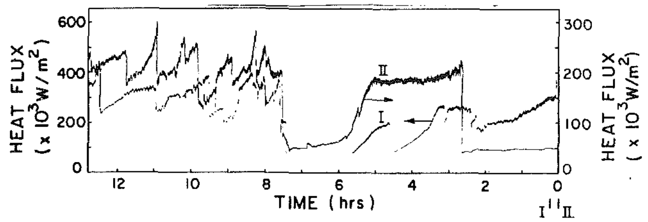

Fig. 8 Fouled meter outputs during major boiler load changes

clean meter and a decrease in furnace exit gas temperature. Additional decreases in the output of the radiation pyrometer, as at 2.7 and 6.8 hr, were caused by sootblowing of the primary superheat tubes. This cleaning caused a further drop in the temperature of the gases reaching the pyrometer.

Examining the fouled and clean meter signals together now allows more conclusive statements about the ash deposits. For example, considering the sharp changes in curve II between 4 and 7 hr in Fig. 7(*b*) and at 1.6 hr in Fig. 7(*a*), one notes that at these times the clean flux meter signal was quite steady. The sharp increase must, therefore, have been caused by changes in the ash deposit covering the fouled meters. Shedding of some or all of the ash covering the meter would cause such sharp increases, and our conclusion was that this was the case here and also in Fig. 5(*c*), noted earlier.

In Fig. 7(*a*) at times between 6 and 11 hr there are increases and decreases in curve II, which are not consistent with typical behavior of the fouled meter signal discussed so far. However, the simultaneous clean heat flux meter output, curve III, contains the same flux variations. This indicates unambiguously that the variations in curve III were not due to ash deposits. Rather they were caused by real variations in flame radiating power and were overlain on the ash deposit effects. The radiating power variations were caused by any number of boiler operating control changes referred to earlier.

Effect of Boiler Load Changes on Ash Deposits. Figure 8 is a record of the level 6 and level 7 heat flux meter outputs during a change of boiler load. Up to a time of 7.2 hr, the load was 100 MW (60 percent of rated load) and was then increased to 160 MW. As before in Fig. 5, the rate of deposition of ash was more pronounced at level 6 than level 7, also at the lower load. The increase in boiler load at 7.2 hr was accompanied by a general increase in heat flux to both meters, as the firing rate increased. The load change, moreover, caused not only the shedding of the very heavy ash deposit that existed at 7.2 hr but, for several hours thereafter, there continued to be a great deal of ash shedding, as shown by the highly variable signal of both curves I and II. This behavior is in full agreement with operator experience that thermal stresses resulting from the evolving temperature patterns in the whole boiler structure during and after a load change may be used as a method of shedding stubborn ash deposits.

Development and Performance of The Prototype Instrument

Probe Components. An ash deposit monitoring instrument suitable for use by boiler operators in routine boiler control should provide a single output related only to the severity of the deposit. From the recorder-chart data so far discussed it is evident that a combination of both the fouled and clean flux meter outputs should yield such a signal. Were the outputs (in millivolts) of the two flux meters equal (when both were in the clean state!), then the two signals could be electrically subtracted as shown in Fig. 9(*a*) to yield the required net signal. The two signals were, however, not equal, mainly because the clean and fouled meters were in different locations.

The following analysis shows that the correction needed to make Q_c, the clean meter signal, equal to Q_f°, the fouled meter signal when the latter is in the clean state, is a simple multiplication by a constant, to be henceforth called the F factor. Heat transfer to heat flux meter may be written as [20]

$$Q = \overline{GS}\,\sigma(T_g^4 - T_s^4) + ha(T_g - T_s)$$

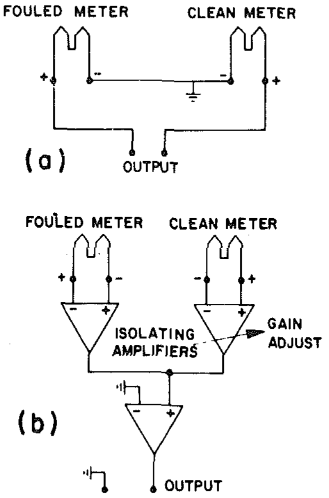

Fig. 9 Ash deposit probe circuit, schematic

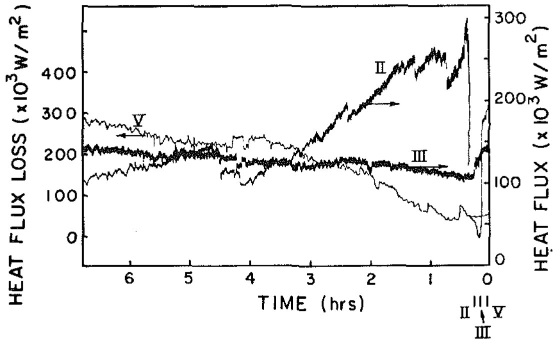

Fig. 10 Combined system signal

It has been shown that in a boiler furnace, the contribution of convection is negligible [21] and the second term on the right hand side may be disregarded. When the flux meter is in a clean state, the fourth power of the meter temperature T_s is small relative to the fourth power of the effective flame temperature T_g. Thus we have

$$Q = \overline{GS}\,\sigma T_g^4$$

A difference in heat flux through the two meters, therefore, is a result of only the difference between the overall new factors $\overline{GS}$ for the two meter locations. Thus,

$$F = \frac{(\overline{GS})_f}{(\overline{GS})_c}$$

and

$$Q_f^\circ = FQ_c$$

Note that the '*F*' factors could ideally be made unity be placing the two meters side by side in an otherwise identical geometric configurations. The considerably lower heat flux to the clean meter (compare ordinates in Figs. 7 and 10) and was due to the fact that it was located near the furnace corner where adjacent walls reduced the field of vision.

Another problem in the electrical subtraction of the two flux meter signals was the fact that on combining the fouled and clean flux meter signals, in accordance with Fig. 9(*a*), relatively large common mode voltage was found between the two meters, evidently due to a thermal e.m.f. generated by the junction of the heat flux meter and boiler tube. Thus, an electrical circuit for combining the two signals must also isolate the two meters electrically to eliminate this e.m.f. Figure 9(*b*) shows the still relatively simple electronics package used to connect the two meters. The '*F*' factor applied to the clean meter could be adjusted, by means of adjustable amplifier gain, to give a zero system output when both flux meters were in a perfectly clean state.

Results. The combined signal using the above circuit is shown in Fig. 10, curve V, as a photograph of an actual recorder chart. The clean (curve II) and fouled (curve III) meter signals are also shown. The combined signal was expressed as 'loss of heat flux (W/m^2)' and was zero in the clean condition, i.e., immediately after a sootblow, such as at 0.2 hr. It increased slowly as the ash deposit built up. The effect of ash shedding from the fouled meter at about 0.5 and 1.0 hr (note that curve III leads curve II which leads curve IV) showed up on the combined meter signal as a drop in the signal strength as it should (note that the clean meter signal was constant during that time). There are short decreases in the flux monitored by the clean heat flux meter at time 2.0 and 4.2 hr which may have been due to ash deposition on the clean meter. This soon disappeared, along with the corresponding blips on the combined output trace. The apparent maximum in the combined curves was due to two abrupt but small changes in the ash properties, clearly seen on the fouled meter output trace, curve II, at 4.2 and 4.5 hr.

The curves in Fig. 10 are quite typical of those obtained over a period of two months when the two flux meters operated as a prototype ash monitor, connected as shown in Fig. 9(*b*). Apart from establishing the feasibility and reliability of the system, this test made evident three other facts:

1 When sootblowers were effective and deposits were indeed removed, the meter returned to zero after the sootblow. Often, however, this did not happen, indicating poor ash removal efficiency, another type of valuable process information.

2 The combined ash deposit monitoring system does not give a direct measure of ash thickness. It is felt, however, that the measurement of heat flux loss is a more useful signal since it gives a direct measure of the effect of ash on the critical operating parameter; heat transfer. Nevertheless, mathematical modelling presently ongoing, will yield calculated ash deposit thickness from the measured heat flux data and ash deposit physical properties.

3 Improved boiler control, and potentially sootblower automation, requires the specification of a unique value of the system signal. The magnitude of loss of heat flux could be a source of this unique value or the amount of damping of heat flux variation is another promising possibility. Further operating experience is needed and will be gained by recording both the fouled meter and combined signal during normal boiler operation.

Comments on Routine Industrial Use of Ash Monitoring Probes

The combined ash deposit probe was tested in continuous operation at the Battle River Generating Station for over a two month period. This field trial of the instrument package followed several months of active testing, separately, of the fouled meters and the clean meter probes. The package can thus be considered to be a proven industrial prototype. The Northover and Hitchcock heat flux meters have a proven durability in industrial scale combustion chambers [17]. In our tests, several meters were still operating as fouled meters after nearly two years of satisfactory service. These meters may be readily installed during annual boiler shutdowns and should easily last a one year campaign. The clean meter probe configuration shown in Fig. 2 should prove equally rugged. The design requires an air supply only and is easily installed and/or removed for periodic cleaning and servicing.

Further testing is required to determine the number of ash-deposit monitors needed to instrument a boiler for routine use. Evidently, several will be necessary to obtain information representative of the condition of the furnace as a whole, including fouling-prone areas. A single heat flux meter system samples an insignificant area of the whole water wall. Nevertheless, a single system, not even located at the level of maximum fouling, proved surprisingly effective. During the prototype test, the operators found that it significantly improved their routine control decisions.

Conclusions

1 An ash-deposit monitoring system, suitable for use in the combustion chambers of large boilers, has been developed and tested. The output signal is the decrease in heat flux through water walls due to fouling, a direct measure of the significant variable.

2 Further work is required to develop this monitoring system for use in soot blower automation. Good potential for this end has, however, been shown.

3 It has been shown that heat fluxes through water walls of boilers operating on low rank Western coal routinely fell to less than 20 percent of their maximum values as a result of fouling. A substantial improvement in boiler capacity and operating cost is, therefore, indicated with improved heat transfer surface cleanliness.

4 New data have been contributed on the growth mechanism of deposits of low-rank coal ash and on resulting furnace behavior.

(*a*) The fouled meter signal shows that ash buildup is a dynamic process involving accretion, sintering, as well as continued shedding and re-deposition.

(*b*) The clean heat flux meter signals show that flame radiating power varies cyclically as ash deposits on water walls form and are removed.

5 The use of recording infra-red radiation pyrometers has been shown to be a reliable means of monitoring the furnace exit temperature of industrial boilers.

Acknowledgements

This work stems from a research and development contract placed by the Canadian Electrical Association with the University of Waterloo. The Canadian Electrical Association is gratefully acknowledged for this funding and their guidance during the course of the research.

Ontario Hydro, Alberta Power Limited and Saskatchewan Power Corporation are thanked for making the boiler experiments possible.

Mr. Bruce Paley of Babcock and Wilcox, Canada Ltd. drew the authors' attention to the Northover fluxmeter during proposal development.

References

1 Mulcahy, M. F. K., Boow, J., Goard, P. R. C., "Fireside Deposits and Their Effect on Heat Transfer in a Pulverized-fuel-fired Boiler Part I: The Radiant Emittance and Effective Thermal Conductance of the Deposits," *Journal of the Institue of Fuel,* Vol. 39, 1966, pp. 385–394.

2 Mulcahy, M. F. R., Boow, J., Goard, P. R. C.; "Fireside Deposits and Their Effect on Heat Transfer in a Pulverized-fuel-fired Boiler Part II: The Effect of the Deposit on Heat Transfer from the Combustion Chamber Considered as a Continuous Well-stirred Reactor," *Journal of the Institute of Fuel,* Vol. 39, 1966, pp. 394–398.

3 Reid, W. T., *External Corrosion and Deposits—Boilers and Gas Turbines,* American Elsevier, New York, 1971, pp. 16–18.

4 Wall, T. F., et al., "Mineral Matter in Coal and the Thermal Performance of Large Boilers," *Progress in Energy and Combustion Science,* Vol. 6, Pergamon Press, 1979, pp. 1–29.

5 Babcock and Wilcox, "Steam/Its Generation and Use," Babcock and Wilcox Co., New York, 1972, pp. 15-11 to 15-14.

6 Attig, R. C., Duzy, A. F., "Coal Ash Deposition Studies and Application to Boiler Design," Presented to American Power Conference, Chicago, Ill, Apr, 1969, p. 4.

7 Sage, W. L. McIlroy, J. B., "Relationship of Coal Ash Viscosity to Chemical Composition," *Trans. ASME* Vol. 62, 1960, pp. 145–155; Nicholls, P., Reid, W. T., "Viscosity of Coal Ash Slags," *Trans ASME* Vol. 62, 1940, pp. 141–153.

8 Barnhart, D. H., Williams, P. C., "The Sintering Test—An Index to Ash Fouling Tendency," *Trans AMSE* Vol. 78, 1956, pp. 1229–1236.

9 Chambers, A. K., Wynnyckyj, J. R., Rhodes, E., Unpublished Research, University of Waterloo, Waterloo, Ont., Can.

10 Raask, E., "Cenospheres in Pulverized-Fuel Ash," *Journal of the Institute of Fuel,* Sept. 1968, pp. 339–344; Ramsden, A. R., "A Microscopic Investigation into the Formation of Fly-Ash during the Combustion of a Pulverized Bituminous Coal," *Fuel,* Vol. 48, 1969, pp. 121–137.

11 Cleaver, J. W., Yates, B., "A Sub Layer Model for the Deposition of Particles from a Turbulent Flow," *Chemical Engineering Science,* Vol. 30, 1976, pp. 983–992; Cleaver, J. W., Yates, B., "The Effect of Re-entrainment on Particle Deposition," *Chemical Engineering Science,* Vol. 31, 1976, pp. 147–151.

12 Gray, R. J., Moore, G. F., "Burning the Sub-Bituminous Coals of Montana and Wyoming in Large Utility Boilers,"ASME Paper No. 74-WA/FU-1, New York, 1974.

13 Chappell, R. E., Locke, J. W., A Mathematical Approach to Automation of Sootblower Controls," Presented at the American Power Conference, Chicago, Ill., Apr 28, 1965.

14 Evans, J., Monroe Power Plant, Detroit Edison Co., Monroe, Michigan, personal communication.

15 Burnett, D. J., "Steam Generator Design for Canadian Coals," presented at Canadian Electrical Association Thermal & Nuclear Power Section, Winnipeg, Manitoba, Oct., 1976.

16 Borio, R. W., Goetz, G. J., Levasseur, A. A., "Slagging and Fouling Properties of Coal Ash Deposits as Determined in a Laboratory Test Facility," ASME Winter Annual Meeting, 1977, p. 10.

17 Northover, E. W., Hitchcock, J. A., "A Heat Flux Meter for use in Boiler Furnaces," *Journal of Scientific Instruments,* Vol. 44, 1967, pp. 371–374.

18 Chi, S. W., *Heat Pipe Theory and Practice,* McGraw-Hill, New York, 1976.

19 Chambers, A. K., Wynnyckyj, J. R., Rhodes, E., "Development of a Monitoring System for Ash Deposits on Boiler Tube Surfaces," Presented to the National Heat Transfer Symposium, Edmonton, Alberta, Canada, Oct, 1980.

20 Hottel, H. C., and Sarofin, A. F., *Radiative Transfer,* McGraw-Hill, New York, 1967.

21 Morgan, E. S., "Errors Associated with Radiant Heat Flux Meters when used in Boiler Furnaces," *Journal of the Institute of Fuel,* Vol. 47, June, 1974, pp. 113–116.

22 Hein, K. R. G., "Research into the Combustion and Fouling Behavior of Brown Coals," R. W. Bryers, Editor, ASME Symposium Ash Deposits and Corrosion due to Impurities in Combustion Gases, Hemisphere Publishing, McGraw-Hill, 1978, pp. 77–83.

23 Friedrich, F. D., Lee, G. K., Mitchell, E. R., "Combustion and Fouling Characteristics of Two Canadian Lignites," ASME JOURNAL OF ENGINEERING FOR POWER, v. 94, Series A No. 2, April 1972, pp. 127–132.

A Detailed Transient Model of an OTEC Evaporator

M. C. Chapman
Hermetic Motor Department
General Electric Co.
Holland, Mich.

G. T. Heydt
Purdue Electric Power Center
Purdue University
West Lafayette, Ind.

Ocean thermal energy conversion (OTEC) is a process in which a working fluid is alternately evaporated and condensed in heat exchangers fed by shallow and deep ocean water, respectively. The expansion of the working fluid permits extraction of useful work in a low pressure turbine. Models of the OTEC cycle often consider the evaporator and condenser units simply as having sufficient capacity (steady-state model) or with simple linear low-order models. In this paper, the evaporator is modeled in detail including the nonlinearities of two phase boiling, enthalpy-temperature relationship, and mixed phase fluid flow and heat exchange. The evaporator considered is of the cross-flow type using propane as the working fluid, however, the technique is valid for any channel configuration and working fluid provided that vertical flow exists in the working fluid. The model is used for transient studies in a wide range of working states.

I Ocean Thermal Energy Conversion

The continuous collection of solar radiation by the earth's oceans provides a potentially useful source of energy that is stored in the form of a temperature gradient between the warm surface water and the cooler water layers beneath. One possible method of extracting this energy is to use this gradient to operate a Rankine cycle heat engine. In an ocean thermal energy conversion (OTEC) power plant which operates on this principle, a working fluid with suitable thermodynamic properties is pumped through an evaporator heat exchanger where indirect heat transfer from warm sea water induces boiling. The gaseous fluid which exits the evaporator is then used to drive a turbogenerator for electric power production. After the useful work has been extracted from the working fluid, a high quality saturated liquid-vapor mixture drains from the turbine into another heat exchanger where the cold water pumped up from the ocean depths condenses it back into the liquid phase. Although the efficiency of such a power plant is generally limited to about three percent or less, a large enough facility could convert sufficient solar energy to make the concept economically feasible under some conditions. References [1–5] provide a small sampling of the literature on this subject.

The majority of modeling techniques used for the OTEC cycle are steady-state or quasi-steady-state. In such models, the heat exchangers are usually modeled with little detail. Transient studies, including start-up and shut-down simulations, are not possible; in this paper, however, the OTEC cross-flow evaporator for propane-sea water is modeled in considerable detail. Further, one can build a strong case for the need for a transient simulation considering the design of evaporator controllers, turbine controllers, and excitation systems for the synchronous generators. Additionally, the transient values of key pressures and temperatures may be important design considerations particularly in automatic control design. The evaporator is of the plate-fin type which might be used under conditions of 28°C sea surface temperature, 6.6°C deep water temperature, in a 1.0 MWe module. Figure 1 shows the evaporator's position in the OTEC cycle; note that pressure-enthalpy-mass flow rate $(P, H, \dot{M})$ are the common input-output variables. The notations T_{sw} and $\dot{M}_{sw}$ are the sea water temperature and mass flow rate in the evaporator, and z denotes the liquid level in the evaporator. The modeling techniques are largely consistent with modern, conventional, steam boiler technology [6]. Figure 2 and Table 1 show typical dimensions for a 1.0 MWe evaporator [7].

II Heat Transfer Model

The elementary expression

$$\dot{Q} = UA\Delta T$$

describes the heat flow, $\dot{Q}$, per unit time for a heat exchange over ΔT temperature difference. The terms U and A are the heat transfer coefficient and area associated with the transfer. For a propane plate-fin exchanger,

$$U = \left[\left[\frac{A_p}{A}\left[1 - \frac{A_f}{A_p}\left[1 - \frac{\tanh \ell \sqrt{\frac{2h_p}{k\delta}}}{\ell \sqrt{\frac{2h_p}{k\delta}}}\right]\right] h_p\right]^{-1} + \frac{aA}{kA_w} + \frac{1}{h_{sw}}\right]^{-1}$$

Evaluation of U is complicated by the fact that h_p and h_{sw} are both functions of the fluid properties and flow rates. In fact, before an expression can even be found for these two film conductances, an analysis of the fluid flow in the channel must be done to determine the type of flow expected (i.e., Laminar or turbulent) and the ranges of the various parameters (e.g., Prandtl, Reynolds, and Froude numbers) used to define the regions of applicability of the film conductance correlations. Although better correlations are available, the following heat transfer film conductance coefficient correlations have been selected to illustrate the type of heat transfer phenomena and to provide an initial basis in developing the model.

1 Sea water [9]

$$h_{sw} = 68.75 \text{ J/s-m}^2\text{-K}.$$

2 Subcooled liquid propane [9]

$$h_p = \begin{cases} 4035k, & \mathrm{Re}_L < 2000 \\ 17.09k\mathrm{Pr}^{0.5}\mathrm{Re}^{0.83}, & \mathrm{Re}_L > 2000 \end{cases},$$

Contributed by the Power Division for publication in the JOURNAL OF ENGINEERING FOR POWER. Manuscript received at ASME Headquarters July 23, 1980.

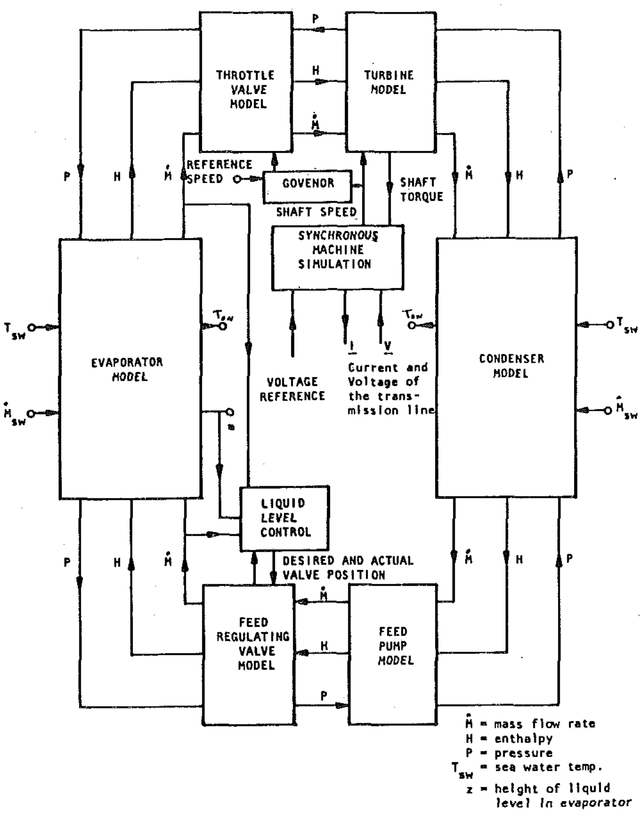

Fig. 1 **Block diagram of the major components**

where, Pr, and Re are defined in the Appendix. Note that for Re_L much greater than 2000, an alternate expression for h_p must be used since h_p now depends on Nu as well. This high range of Re_L was not considered. The dichotomy at $\mathrm{Re}_L = 2000$ is based loosely on the transition from laminar to turbulent flow.

3 Saturated liquid-vapor propane [10]

$$h_p = 0.015\frac{k_L}{D_{eq}}\left[1 + \left[1 - \frac{(1-\mathrm{X})\rho_G}{X\epsilon\rho_L}\right]^{-0.5}\right]^{-1}$$

$$(\mathrm{Re}_L\mathrm{Fr}_L)^{0.3}\frac{X}{1-X}\left[\frac{\rho_L}{\rho_G}\right]^{0.3}\left[\frac{\mu_L}{\mu_G}\right]^{0.8}\mathrm{Re}_L^{0.35}\mathrm{Pr}_L^{0.42}$$

where ϵ is the two-phase flow parameter discussed in the Appendix.

4 Superheated propane [9]

$$h_p = 0.439\mathrm{Pr}^{0.6}\mathrm{Re}^{0.8}.$$

The presence of the Prandtl, Reynolds, and Froude numbers in the expressions for h_p indicates that the propane heat transfer film conductance coefficient is a function of the propane thermal conductivity, specific heat, specific volume, dynamic viscosity, and mass flow rate, and therefore is a function of both time and position in the channel. This suggests that the fluid must be considered in properly defined regions to allow the "lumping" of properties within a given channel volume so that the i^{th} region (or i^{th} "control mass"),

$$\dot{Q}_i = U_iA_i\Delta T_i.$$

Note that a wide range of forms exist in the literature for the film conductance expressions required. The four expressions given above should be carefully reviewed before implementing a simulation—particularly for configurations other than that described.

III Fluid Flow

The fluid flow behavior of the propane in the channel is characterized by a balance of forces on the fluid from both the external pressure difference across the evaporator and the internal pressure drops associated with friction, gravity, and acceleration. Mathematically, this is expressed as

$$F_a = F_u - F_d - F_f - F_g,$$

where F is the net force on the fluid and the subscripts a, u, d, f, and g denote acceleration, up, down, friction, and gravity, respectively. The accelerating force associated with some quantity of mass M_i and the cross-sectional area, A_c, is

$$\frac{M_i}{A_c}\ddot{z}_i = P_{u,i} - P_{d,i} - P_{f,i} - P_{g,i}.$$

Note that $P_{u,i}$ and $P_{d,i}$ are the pressures existing at the boundaries of M_i. $P_{u,i}$ is equal to the evaporator inlet pressure minus the pressure drop across the propane beneath the lower boundary of M_i. Likewise, $P_{d,i}$ is calculated as the evaporator outlet pressure plus the pressure drop across the propane above the upper boundary of M_i. The gravitational pressure drop term, $P_{g,i}$, is simply

$$P_{g,i} = \frac{M_ig}{A_c},$$

where g is the acceleration of gravity. The frictional pressure drop is more difficult to calculate; different correlations are needed for the two-phase flow region and the single-phase flow regions. As outlined by Dukler, et al. [11], the term $P_{f,i}$ can be approximated as

$$P_{f,i} \doteq \frac{2G_T^2f_0\Delta z_i}{gD_{\mathrm{eq}}\rho}$$

for single-phase flow, and

$$P_{f,i} \doteq \frac{2G_T^2f_0\Delta z_i}{gD_{\mathrm{eq}}\rho_{\mathrm{NS}}}\alpha(\lambda)\beta$$

for two-phase flow. In these expressions, G_T = mass velocity; g = *acceleration of gravity*; D_{eq} = *equivalent diameter of the channel*; λ = ratio of volumetric flow rates of liquid to gas; f_0 = friction factor for single-phase flow evaluated at the mixture Reynolds number (Re), $= 0.0014 + 0.125/\mathrm{Re}^{0.32}$; ρ_{NS} = density of mixture; $\overline{R}_L$, $\overline{R}_G$ = average in place fraction liquid and gas; and α and β are given by [11]

$$\alpha = 1 + \frac{-\ell\mathrm{n}\lambda}{1.281 - 0.478(-\ell\mathrm{n}\lambda) + 0.444(\ell\mathrm{n}\lambda)^2 - 0.094(-\ell\mathrm{n}\lambda)^3 + 0.0084(-\ell\mathrm{n}\lambda)^4}$$

$$\beta = \frac{\rho_L\lambda^2}{\rho_{NS}\overline{R}_L} + \frac{\rho_G(1-\lambda)^2}{\rho_{NS}\overline{R}_G}.$$

It is worthwhile to note that the approach taken here is not restricted to crossflow heat exchangers or propane. Virtually any heat exchanger configuration may be analyzed by the method outlined, and nearly any suitable working fluid may be substituted for propane (e.g., ammonia) with appropriate change in thermophysical properties.

IV Steady-State Calculations

The steady-state is of interest in transient modeling since initial conditions are calculated using steady-state expressions and it pro-

Nomenclature

a = wall thickness = 2.54×10^{-4}m
A = total outside area of the plate-fin panel = 34.41 m^2
A_f = total fin area of the plate-fin panel = 13.13 m^2
A_p = total area of the contact with propane = 45.91 m^2
A_w = average area of wall = $0.5(A + A_p)$ = 40.66 m^2
δ = fin thickness = 1.27×10^4 m
h_p = film conductance of propane
h_{sw} = film conductance of sea water
k = thermal conductivity of evaporator material = 58.15 J/m-s-K
ℓ = one-half the fin length = 3.175×10^{-4}m

vides a check for transient algorithms. In the steady state, all the heat transferred to the propane goes to increasing its enthalpy (assuming the feed pump supplies the bulk of the kinetic energy and that potential energy change is negligible). Accordingly, it becomes convenient to define three variable length sections of the channel to correspond to the subcooled liquid, saturated liquid-vapor, and superheated vapor regions. The length of these blocks corresponds to how much area is needed to change the enthalpy over the range defined for each block under the prevailing heat transfer and mass flow rates. Since the heat transfer process has been shown to be highly dependent upon the fluid properties, and because these properties vary widely throughout the saturated liquid-vapor range, it is advisable to further subdivide this section into smaller blocks corresponding to different qualities of vapor. The heat transfer in the steady state is $\dot{Q}$,

$$\dot{Q} = \begin{cases} C_{sw}\dot{M}_{sw}\Delta T_{sw} \text{ from sea water} \\ UA\dfrac{z_i}{z}(T_{sw,\text{ave}} - T_{p,\text{ave}}) \text{ across fluid films and channel walls} \\ C_p\dot{M}_p\Delta T_p \text{ into propane, single phase regions} \\ \Delta H_p\dot{M}_p \text{ into propane, saturated region} \end{cases}$$

The notation z_i denotes the length of the i^{th} variable length block, z equals the total channel length, and C_{sw} and C_p are the constant pressure specific heat capacities of sea water and propane, respectively. Simultaneous solution of these equations yields the following expressions for use in the algorithm:

1 Height of the variable length blocks.

$$z_1 = z\,\frac{C_p\dot{M}_p(T^1_{p,\text{out}} - T^1_{p,\text{in}})}{C_{sw}\dot{M}_{sw}(T_{sw,\text{in}} - T^1_{sw,\text{out}})}$$

$$z_i = z\,\frac{\Delta H_p\dot{M}_p}{C_{sw}\dot{M}_{sw}(T_{sw,\text{in}} - T^i_{sw,\text{out}})}$$

$$z_n = z - \sum_{i=1}^{n-1} z_i$$

2 Temperature of the sea water exiting each block and at the evaporator outlet.

$$T^i_{sw,\text{out}} = \frac{2C_{sw}\dot{M}_{sw}T_{sw,\text{in}} + UA(T^i_{p,\text{in}} + T^i_{p,\text{out}} - T_{sw,\text{in}})}{2C_{sw}\dot{M}_{sw} + UA}$$

$$T^n_{sw,\text{out}} = \frac{(z_nUAC_{sw}\dot{M}_{sw} + 2zC_{sw}\dot{M}_{sw}C_p\dot{M}_p - zUAC_p\dot{M}_p)T_{sw,\text{in}} + zUAC_p\dot{M}_pT_p^{n-1}}{z_nUAC_{sw}\dot{M}_{sw} + 2zC_{sw}\dot{M}_{sw}C_p\dot{M}_p + zUAC_p\dot{M}_p}$$

$$T_{sw,\text{out}} = \frac{1}{z}\sum_{i=1}^{n} z_iT^i_{sw,\text{out}}$$

3 Evaporator propane outlet temperature and enthalpy.

$$T_{p,\text{out}} = T^n_{p,\text{in}} + \frac{Z_nC_{sw}\dot{M}_{sw}}{C_p\dot{M}_p}(T_{sw,\text{in}} - T^n_{sw,\text{out}})$$

$$H_p = f(P_{p,\text{out}}, T_{p,\text{out}})$$

where $f(P_p, T_p)$ is the functional approximation for the pressure versus enthalpy curve in the superheated vapor region.

V Discussion of the Transient Model

In the steady-state model, the concept of a control volume was introduced to define regions of applicability for various formulae. Since steady-state analysis is independent of time, the equations for each control volume are quite simple; however, if a control volume is used in a transient or time-variant problem, the simplicity dissolves since the possible difference in control volume inlet and outlet mass flow rates must be considered. Alternately, consider the use of control masses which are defined to encompass a definite amount of mass within a flexible boundary. For analytical convenience, the flow through these boundaries is prohibited. This departure from reality is compensated by shrinking the volume of the control mass. The problem of fluid flow is now stated in terms of the center-of-mass motion of these control masses through the channel. The lumping of properties within the control mass is established to simplify the problem while maintaining enough reality to fit the physical configuration. Although lumping all the properties (e.g., enthalpy and temperature) into a single value for each control mass is a temptation, anticipation of propane state equation constraints [7] prohibits such action for the liquid-vapor and vapor control masses.

Cross-sectional planes perpendicular to the axis of the propane channel form the top and bottom boundaries of each control mass. The four remaining boundaries are provided by the channel walls. It is assumed that no fluid can cross the boundaries so that all fluid flow in the channel corresponds to control mass motion. This assumption is an approximation; however, as the number of control masses increases, the error introduced by this approximation decreases; also, the volumetric decrease of control masses to compensate for the cross-boundary flow compensates for the error. There are three basic control mass types. A liquid control mass is used to represent a definite quantity of subcooled liquid propane. All liquid control masses used in the model have the same mass, which is chosen to be constant during any particular simulation. Uniform temperature and enthalpy distributions are assigned to each control mass. A liquid-vapor control mass is used which differs from the liquid control mass in two respects: first, the liquid-vapor control mass consists of two equal mass re-

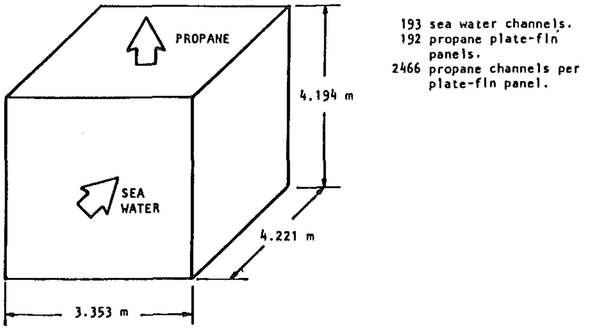

Fig. 2(*a*) Overall dimensions of a 1MWe module of the evaporator

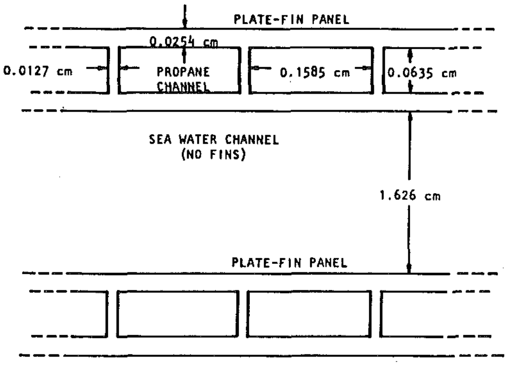

Fig. 2(*b*) Plate-fin panel dimensions

Fig. 2 Propane evaporator geometry

Table 1 OTEC power plant specifications

Total Capacity	24 MWe
Generation Voltage	13.8 KV
Number of Synchronous Machines	3
Speed of Synchronous Machines	1200 RPM
Plant Height	550 m
Cold Water Pipe Length	450 m
Cold Water Pipe Diameter	5.8 m
Plant Displacement	45,360,000 kg
Distance to Shore	4560 m
Heat Exchanger Type	Plate-Fin
Working Fluid	Propane
Surface Temperature	28°C
Deep Water Temperature	6.6°C
Efficiency	3–5 percent

gions—each half contains the same amount of mass as does a single liquid control mass; secondly, separate sets of uniformly distributed fluid properties are associated with each half. Pressure, temperature, enthalpy, vapor quality, and height variables are superscripted with "+" and "−" signs to designate the upper and lower halves, respectively. Vapor control masses are defined identically to liquid-vapor control masses except for the vapor quality, which is always equal to unity by definition. Thus the channel consists of a stack of liquid control masses at the bottom, a stack of liquid-vapor control masses in the middle, and possibly a stack of vapor control masses on top.

Certain possible boundary conditions which are discussed at this point require the use of three hybrid control masses. A hybrid liquid-vapor control mass is defined to occur when the bottom liquid-vapor control mass has lower half properties corresponding to a subcooled liquid. This bottom region is, in fact, the top liquid control mass. Thus, once the top liquid control mass changes phase, this liquid-vapor control mass will revert to the basic form discussed above. It is important to note the difference in the liquid/liquid-vapor phase boundary positions for these two liquid-vapor control masses. The basic case has a phase boundary occurring coincident with its bottom boundary while the phase boundary passes thru the center-of-mass in the hybrid case. This difference will necessitate the use of different calculations in various sections of the model. To indicate the presence of the top liquid control mass in the bottom liquid-vapor control mass (i.e., the hybrid case) in a digital implementation, the logical variable LLV is defined to be true when this situation occurs. LLV is considered false, otherwise. The letters of this control variable denote *L*iquid in the *L*iquid-*V*apor. Depending upon the initial value of LLV, a liquid to liquid-vapor phase change may or may not alter the total number of liquid-vapor control masses, which is designated by the integer variable NLV. Clearly, if LLV is true when the phase change occurs, the number of liquid-vapor control masses remains unchanged. However, if LLV is false initially, the phase change results in increasing the value of NLV by one. In either case, the variable LLV is complimented after each individual liquid control mass phase change occurs.

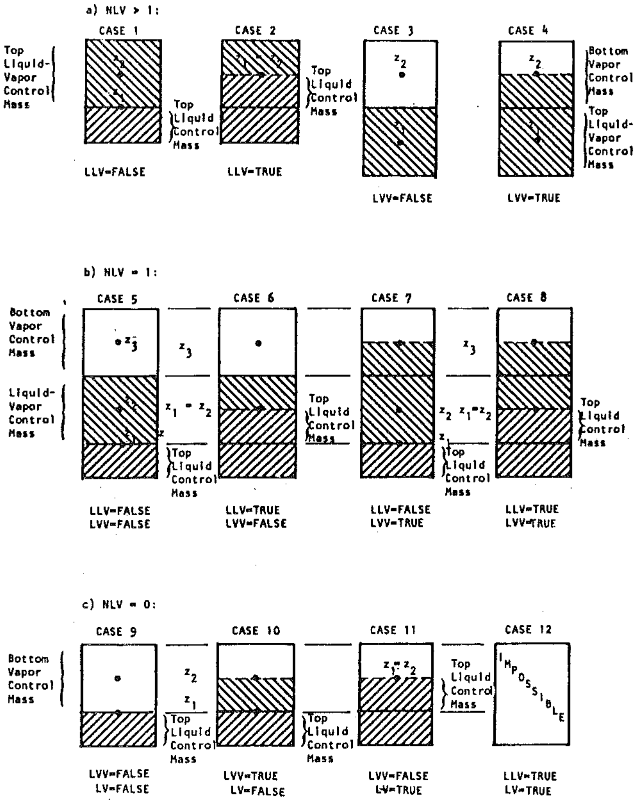

Fig. 3 Possible boundary configurations

The same reasoning is used to explain the possibility of the hybrid vapor control mass in which two cases occur. First, it is possible for the lower half of the bottom vapor control mass to be liquid. This situation is analogous to the bottom liquid-vapor control mass when LLV is true. Thus, another control variable is used to indicate the presence of this condition. If the letters LV are used to mean *L*iquid in the *V*apor, a logical variable LV which is true indicates the existence of this case. Secondly, a hybrid vapor control mass may occur with saturated liquid vapor in the lower half of the bottom control mass. *L*iquid-*V*apor in the *V*apor control mass is indicated by the control variable LVV being true. Notice that the condition of both LV and LVV being true cannot exist because the lower half of the bottom vapor control mass can only exhibit a single set of properties at a given moment in time. When LV is true the value of NLV must equal zero, so a liquid-vapor to vapor phase change is not possible. However, this type of phase change can occur when LVV equals true even if NLV equals zero. Since the liquid-vapor undergoing the phase change occupied the lower half of the bottom vapor control mass, such a change will not affect either NLV or NV. Here NV has been chosen to represent the number of vapor control masses within the channel and is the third integer control variable. Updates of NLV and NV occur for any liquid-vapor to vapor phase changes when the initial value of LVV is false. NLV is decreased by one while NV is increased by one. After each such phase change detection LVV is complemented. A liquid to liquid-vapor phase change when LV is true does not alter the values of either NLV or NV. NL does decrease by one and LV and LVV are both complemented. Figure 3 shows all possible boundary conditions.

Using these control mass definitions, a transient model is developed based on Newton's second law and the definition of velocity. Chapman [7] obtains

$$\dot{v} = \frac{A_c}{m}(P_u - P_d - P_f) - g$$

where A_c is the channel cross-sectional area and for liquid $P_f = \Delta z f_L(v, T)$, for liquid-vapor $P_f^{\pm} = \Delta z^{\pm} f_{LV}^{\pm}(v, T^{\pm}, X^{\pm}, \Delta z^{\pm})$, for vapor $P_f^{\pm} = \Delta z^{\pm} f_v(v, T^{\pm}, \Delta z^{\pm})$. Also, for the liquid-vapor and vapor control masses,

$$P_{f,i} = P_{f,i}^{+} + P_{f,i}^{-}.$$

For a vapor control mass, the ideal gas law is rewritten in terms of control mass,

$$P^{\pm} = \frac{\left(\dfrac{nR}{2A_c}\right) T^{\pm}}{\Delta z^{\pm}}.$$

This leads to modeling the control mass as a center-of-mass sandwiched between two ideal gas "springs". The spring constant, k, is equal to the numerator of the equation and therefore is a function of temperature. The forces associated with P_u and P_d act on the center-of-mass through these springs. Since adjacent vapor control masses have the same pressure at the coincident boundary and hence within adjacent halves, the two springs separating the centers-of-mass are compressed under the same force. Thus, the pressure is expressed as

$$P_1^{\pm} = \frac{k_1^{\pm} + k_2^{\pm}}{\Delta z_1^{\pm} + \Delta z_2^{\pm}},$$

where $P_1^{\pm}$ are the upper and lower boundary pressures associated with control mass 1. Control mass 2 is the adjacent control mass sharing the boundary of interest. Thus for the i^{th} vapor control mass, (using $R' = nR/2A_c$)

$$P_u = \frac{R'(T_i^{-} + T_{i-1}^{+})}{z_i - z_{i-1}}, \quad P_d = \frac{R'(T_{i+1}^{-} + T_i^{+})}{z_{i+1} - z_i},$$

The liquid-vapor control mass model differs from the vapor control mass model in two respects: Since only a portion of the fluid is vapor, the spring constants must be modified to account for this and the spring constant becomes

$$k^{\pm} = R' X^{\pm} T^{\pm},$$

where X is the vapor quality. Secondly, the liquid portion of the control mass occupies a volume which contributes to the height of the control mass. The length associated with spring compession is

$$\Delta z_s^{\pm} = \Delta z^{\pm} - L(1 - X^{\pm}),$$

where the subscript s refers to spring length and

$$L = \frac{m}{2\rho_L A_c}$$

is the length of the liquid mass, $m/2$, with mass density, ρ_L. Therefore

$$P_u = \frac{R'(X_i^- T_i^- + X_{i-1}^+ T_{i-1}^+)}{z_i - z_{i-1} - L(2 - X_i^- - X_{i-1}^+)}$$

$$P_d = \frac{R'(X_{i+1}^- T_{i+1}^- + X_1^+ T_i^+)}{z_{i+1} - z_i - L(2 - X_{i+1}^- - X_i^+)} .$$

The final step in developing the model is the selection of the various propane enthalpy, position, and velocity variables for use as state variables. The enthalpy state equations are derived from the energy balance,

$$\dot{H} = \frac{1}{m}(\dot{Q} + V\dot{P} - \dot{E}_k - \dot{E}_p)$$

$$= \frac{1}{m}[UA(T_{sw} - T) + V\dot{P}) - v(a + g).$$

Utilization of intrinsic properties of propane as represented by its pressure-enthalpy diagram allows elimination of the nonstate variables such as temperature. Thus, combination of the fluid flow equations and energy balance equations relating heat transfer to changes in enthalpy provides a complete transient model [7].

VI Transient Model Summary

The evaporator transient model is summarized by combining the velocity equations, pressure functions, and enthalpy state equations. To condense the notation in writing the model state equations, subscripts A–F are used on P and $\dot{P}$; Table 1 contains the key for interpreting these subscripts. The state equations are [7]

$$\dot{z}_i = \begin{cases} v_i,\ i = 1, 2, \ldots, (\mathrm{NLV} + \mathrm{NV} + 1), \text{ LVV and } LV \text{ false,} \\ v_i,\ i = 1, 2, \ldots, (NLV + NV), LVV \text{ or } LV \text{ true,} \end{cases} \qquad (1)$$

$$\dot{v}_{NL} = \begin{cases} \dfrac{2A_c}{(NL)m}\left[P_{\mathrm{in}} - P_A(z_{NL}, z_{NL+1}, H_{NL}^+, H_{NL+1}^-) - \displaystyle\sum_{i=1}^{NL} P_{f,i}\right] - g, \\ LVV \text{ and } LV \text{ false} \\ \dfrac{2A_c}{(NL+1)m}\left[P_{\mathrm{in}} - P_B(z_{NL}, z_{NL+1}, H_{NL+1}^-) - P_{f,NL}^+ - \displaystyle\sum_{i=1}^{NL} P_{f,i}\right] - g, \\ LVV \text{ or } LV \text{ true,} \end{cases} \qquad (2)$$

$$\dot{v}_{NL+1} = \begin{cases} \dfrac{A_c}{m}[P_A(z_{i-1}, z_i, H_{i-1}^+, H_i^-) - P_c(z_i, z_{i+1}, H_i^+, H_{i+1}^-) - P_{f,i}] - g, \\ LVV \text{ and } LV \text{ false} \\ \dfrac{A_c}{m}[P_B(z_{i-1}, z_i, H_i^-) - P_c(z_i, z_{i+1}, H_i^+, H_{i+1}^-) - P_{f,i}] - g, \\ LVV \text{ or } LV \text{ true} \end{cases} \qquad (3)$$

where $i = NL + 1$,

$$\dot{v}_i = \frac{A_c}{m}[P_{LV}(z_{i-1}, z_i, H_{i-1}^+, H_i^-) - P_{LV}(z_i, z_{i+1}, H_i^+, H_{i+1}^-) - P_{f,i}] - g, \qquad (4)$$

where $NL < i < NL + NLV$,

$$\dot{v}_{NL+NLV} = \frac{A_c}{m}[P_{LV}(z_{i-1}, z_i, H_{i-1}^+, H_i^-) - P_D(z_i, z_{i+1}, H_i^+, H_{i+1}^-) - P_{f,i}] - g, \qquad (5)$$

where $i = NL + NLV$,

$$\dot{v}_{NL+NLV+1} = \frac{A_c}{m}[P_D(z_{i-1}, z_i, H_{i-1}^+, H_i^-) - P_v(z_i, z_{i+1}, H_i^+, H_{i+1}^-) - P_{f,i}] - g, \qquad (6)$$

where $i = NL + NLV + 1$,

$$\dot{v}_i = \frac{A_c}{m}[P_v(z_{i-1}, z_i, H_{i-1}^+, H_i^-) - P_v(z_i, z_{i-1}, H_i^+, H_{i+1}^-) - P_{f,i}] - g, \qquad (7)$$

where $NL + NLV + 1 < i < NL + NLV + NV$,

$$\dot{v}_{NL+NLV+NV} = \frac{A_c}{m}[P_E(z_{i-1}, z_i, H_{i-1}^+, H_i^-) - P_{\mathrm{out}} - P_{f,i}] - g, \qquad (8)$$

where $i = NL + NLV + NV$,

$$\dot{H}_i = f_1(\dot{P}_F, U_i, T_{sw}, T_i, v_{NL}, a_{NL}, z_{NL}, NL, i),\ 1 \le i \le NL, \qquad (9)$$

$$\dot{H}_{NL+1}^- = f_2(\dot{P}_F, U_{NL+1}^-, A_{NL+1}^-, T_{sw}, T_{NL+1}^-, \times \rho_{NL+1}^-, v_{NL}, v_{NL+1}, a_{NL+1}) \qquad (10)$$

when LVV or LV are true,

$$\dot{H}_i^+ = f_3(\dot{P}_{LV}, U_i^+ U_{i+1}^-, A_i^+, A_{i+1}^-, T_{sw}, T_i^+, T_{i+1}^-, \times \rho_i^+, \rho_{i+1}^-, v_i, v_{i+1}, a_i) \qquad (11)$$

$$\dot{H}_{i+1}^- = f_4(\dot{P}_{LV}, U_i^+, U_{i+1}^-, A_i^+, A_{i+1}^-, T_{sw}, T_i^+, T_{i+1}^-, \times \rho_i^+, \rho_{i+1}^-, v_i, v_{i+1}, a_{i+1}). \qquad (12)$$

where $NL < i < NL + NLV$,

$$\dot{H}_{NL+NLV} = f_3(\dot{P}_D, U_i^+, U_{i+1}^-, A_i^+, A_{i+1}^-, T_{sw}, T_i^+, T_{i+1}^-, \times \rho_i^+, \rho_{i+1}^-, v_i, v_{i+1}, a_i) \qquad (13)$$

$$\dot{H}_{NL*NLV+1} = f_4(\dot{P}_D, U_i^+, U_{i+1}^-, A_i^+, A_{i+1}^-, T_{sw}, T_i^+, T_{i+1}^-, \times \rho_i^+, \rho_{i+1}^-, v_i, v_{i+1}, a_{i+1}), \qquad (14)$$

where $i = NL + NLV$,

$$\dot{H}_i^+ = f_3(\dot{P}_v, U_i^+, U_{i+1}^-, A_i^+, A_{i+1}^-, T_{sw}, T_i^+, T_{i+1}^-, \rho_i^+, \rho_{i+1}^-, v_i, v_{i+1}, a_i) \qquad (15)$$

$$\dot{H}_{i+1}^- = f_4(\dot{P}_v, U_i^+, U_{i+1}^-, A_i^+, A_{i+1}^-, T_{sw}, T_i^+, T_{i+1}^-, \times \rho_i^+, \rho_{i+1}^-, v_i, v_{i+1}, a_{i+1}), \qquad (16)$$

where $NL + NLV < i < NL + NLV + NV$, and

$$\dot{H}_{NL+NLV+NV}^+ = f_5(\dot{P}_{\mathrm{out}}, U_i^+, A_i^+, T_{sw}, T_i^+, \rho_i^+, v_i, a_i), \qquad (17)$$

where $i = NL + NLV + NV$.

The number of simultaneous ordinary differential equations to be solved is

$$N = \begin{cases} NL + 4NLV + 4NV + 2, LLV \text{ and } LV \text{ false} \\ NL + 4NLV + 4NV - 1, LLV \text{ or } LV \text{ true.} \end{cases} \qquad (18)$$

In applying these model state equations in a simulation, it must be remembered that many of the variables and terms are also functions of the state variables. The simplified notation used above is only partially successful in conveying this information. In particular, the

Table 2 P or $\dot{P}$ function required

Case	*A*	*B*	*C*	*D*	*E* $(NV = 0)$	*E* $(NV = 1)$	*E* $(NV > 1)$	F
1	*LB*	—	*LV*	—	*LV*	—	—	*LB*
2	—	*LV*	*LV*	—	*LV*	—	—	*LV*
3	—	—	—	*UB*	*LV*	*UB*	*V*	—
4	—	—	—	*LV*	*LV*	*LV*	*V*	—
5	*LB*	—	*UB*	*UB*	*LB*	*UB*	*V*	*LB*
6	—	*UB*	*UB*	*UB*	—	*UB*	*V*	*UB*
7	*LB*	—	*LV*	*LV*	*LB*	*LV*	*V*	*LB*
8	—	*LV*	*LV*	*LV*	—	*LB*	*V*	*LV*
9	*JB*	—	*V*	—	—	*JB*	*V*	*JB*
10	*LB*	—	*V*	—	—	*LB*	*V*	*LB*
11	—	*V*	*V*	—	—	—	*V*	*V*

frictional pressure drop term, P_f, and the overall heat transfer coefficient U must be evaluated. These two terms are responsible for introducing almost all of the non-linearity in the evaporator and hence provide the motivation for pursuing a numerical solution.

VII Summary

Steady-state and transient models have been developed for a plate-fin heat exchanger for use in an OTEC. The model includes nonlinear effects of the heat exchange mechanism, friction, and thermodynamics. Control masses for liquid, liquid-vapor, and vapor are used in the model which is suitable for numerical solution. Numerical quantities for a propane, 1 MWe module have been calculated.

Acknowledgments

The authors acknowledge the support of the Purdue Electric Center in this work and the work of Mr. J. S. Sigg of the W. A. Lewis Company, Portsmouth, Ohio. Mr. Sigg developed the original design parameters of a 24 MWe OTEC for potential use on Tutuila Island in American Samoa.

References

1 Sigg, J. S., and Heydt, G. T., "State Variable Analysis, Control, and Feasibility of Design of an Ocean Thermal Power Plant," Report No. TR-EE 76-45, PCTR 33-76, School of Electrical Engineering, Purdue University, West Lafayette, Ind, 1976.

2 McGowan, J. G., Connell, J. W., "Heat Exchanger Design for Ocean Thermal Difference Power Plants," ASM Paper 74-WA-OCT-4, Oct 1974.

3 Lavi, A., Zener, C., "Plumbing the Ocean Depths, A New Source of Power," *IEEE Spectrum*, Oct 1973, pp. 22–27.

4 U. S. Department of Energy, "Ocean Thermal Energy Conversion," DOE/ET-0031/1, Washington, D. C., Febr 1978.

5 Rumbaugh, J. H., Garrity, T. F., Cohen, R., Sullivan, R. L., "Thermal Energy Conversion—Tapping the Sea Depths," *IEEE Spectrum*, Aug 1979, pp. 42–48.

6 Paynter, H. M., "Thermodynamic Process Dynamics in Boiler Modeling," *Proceedings of the Seminar on Boiler Modeling*, The Mitre Corp., Nov. 6–7, 1974.

7 Chapman, M. C., "OTEC Power Plant Transient Analysis: An Approach to Digital Computer Simulation of the Evaporator," Technical Report TR-EE 79-34, Purdue University, West Lafayette, Ind, Sept 1979.

8 Kays, W. M., and London, A. L., *Compact Heat Exchangers*, 2nd Ed. McGraw-Hill, New York, 1964.

9 Reynolds, W. C., and Perkins, H. C., *Engineering Thermodynamics*, McGraw-Hill, New York, 1975.

10 Chawla, J. M., "A Correlation of Convective Heat Transfer Coefficient for Two-Phase Liquid Vapor Flow," *Proceedings of 4th International Heat Transfer Conference*, Paris-Versailles, 1970.

11 Dukler, A. E., Wicks, M., III, and Cleveland, R. G., "Frictional Pressure Drop in Two-Phase Flow: B. An Approach Through Similarity Analysis," *AIChE Journal*, Vol. 10, No. 1, Jan. 1964, pp. 44–51.

APPENDIX

Calculation of Prandtl, Reynolds, and Froude Numbers for 100 Percent Flow and Calculation of Film Conductances

Chapman [7] recommends the use of the following parameters for 100 percent flow rates in both the propane and sea-water channels: in the sea-water channel, at 28°C,

viscosity $\mu = 8.327 \times 10^{-4}$ kg/m-s
thermal conductivity $k = 0.6084$ J/s-m-K
specific heat $C_p = 4179$ J/kg-K
mass flow rate $\dot{M} = 3.466$ kg/s
cross-sectional area $A_c = 6.818 \times 10^{-2}\text{m}^2$
equivalent diameter $D_{\text{eq}} = 3.239 \times 10^{-2}$m.

In the propane at 20°C, 100 psia, the liquid parameters are

viscosity $\mu = 1.100 \times 10^{-4}$ kg/m-s
thermal conductivity $k = 0.09640$ J/s-m-K
specific heat $C_p = 2672$ J/kg-K
mass flow rate $\dot{M} = 3.74 \times 10^{-4}$kg/s
cross-sectional area $A_c = 1.01 \times 10^{-6}\text{m}^2$
equivalent diameter $D_{\text{eq}} = 9.07 \times 10^{-4}$m
specific volume $V = 1.935 \times 10^{-3}\text{m}^3$/kg

and the gaseous parameters are

viscosity $\mu = 8.27 \times 10^{-6}$ kg/m-s
thermal conductivity $k = 1.81 \times 10^{-2}$ J/s-m-K
specific heat = 1680 J/kg-K.

Therefore, for the 1 MWe module example considered

(i) for liquid propane

$$\text{Pr}_L \equiv \frac{C_p \mu}{k} = 3.049 \quad \text{Re}_L \equiv \frac{\dot{M} D_{\text{eq}}}{\mu A_c} = 3053$$

$$\text{Fr}_L \equiv \frac{v^2}{g D_{\text{eq}}} = \frac{(\dot{M} V / A_c)^2}{g D_{\text{eq}}} = 57.76$$

(ii) for gaseous propane

$$\text{Pr}_G = \frac{C_p \mu}{k} = 0.766 \quad \text{Re}_G \frac{\dot{M} D_{\text{eq}}}{\mu A_c} = 40{,}610.$$

Proceeding to calculate the film conductances, if sea water flow occurs in laminar flow (Re < 2000), then [9]

$$h_{sw} = 3.66 \frac{k}{D_{\text{eq}}} = 68.75 \text{ J/s-m}^2\text{-K}.$$

For the propane, several film conductances must be used since for low flow rates of propane, one correlation applies, while at higher flows a switch to another correlation must be made to account for the change from laminar to turbulent flow. Also, the larger range in temperature that must be covered by this film conduction correlation makes it necessary to account for the temperature dependence of k, the thermal conductivity. For $\text{Re}_L < 2000$:

$$h_p = 3.66 \frac{k}{D_{\text{eq}}} = 4035\text{k}.$$

For $\text{Re}_L > 2000$:

$$h_p = 0.0155 \frac{k}{D_{\text{eq}}} \text{Pr}^{0.5} \text{Re}^{0.83} = 17.09\text{k}\text{Pr}^{0.5}\text{Re}^{0.83}.$$

Chawla [10] obtains h_p for saturated liquid-vapor propane as

$$h_p = 0.015 \frac{k_L}{D_{\text{eq}}} \left[1 + \left[1 - \frac{(1 - X)\rho_G}{X \epsilon \rho_L}\right]^{-1/2}\right]^{-1} \times (\text{Re}_L \cdot \text{Fr}_L)^{0.3} \frac{X}{1 - X} \left[\frac{\rho_L}{\rho_G}\right]^{0.3} \left[\frac{\mu_L}{\mu_G}\right]^{0.8} \text{Re}_L^{0.35} \text{Pr}_L^{0.42}$$

where the subscripts L and G refer to properties evaluated at the saturated liquid saturated vapor points of propane and X represents the quality of the liquid-vapor mixture and is defined as

$$X = \frac{\dot{M}_G}{\dot{M}_L + \dot{M}_G}.$$

The term ϵ is the two phase flow parameter which is given in [10] graphically but may be approximated by

$$\ell n \epsilon = 0.924 \ell n \frac{1 - X}{X} (\text{Re}_L \text{Fr}_L)^{-1/6} \left[\frac{\rho_L}{\rho_G}\right]^{0.9} \left[\frac{\mu_L}{\mu_G}\right]^{-0.05} + 1.25.$$

the ρ and μ terms are the densities and viscosities of the liquid and gaseous propane. A correlation which may be used for superheated propane is,

$$h_p = 0.022 \frac{K}{D_{\text{eq}}} \text{Pr}^{0.7} \text{Re}^{0.8} = 0.439 \text{ Pr}^{0.6} \text{ Re}^{0.8} \; J/s\text{-}m^2\text{-K}.$$

M. G. Gulič
Faculty of Mechanical Engineering,
University of Belgrade,
Belgrade,
Yugoslavia

D. D. Gvozdenac
Institute of Fluid, Thermal, and Chemical
Engineering,
Faculty of Technical Sciences,
University of Novi Sad,
Novi Sad,
Yugoslavia

A Mathematical Model for Heat Transfer in Combustion Chambers of Steam Generators

This paper describes a mathematical model for determining the total heat transfer in combustion chambers of steam generators. The model is based on the energy balance of radiation in a spherical combustion chamber which is divided into a combustion zone and gaseous zone. The model was tested on a Hewlett-Packard Type 9815 A computer with 2008 program memories. Calculations were made for a number of steam generator combustion chambers of different furnace loads for which all important factors were established. The model allows a didactic analysis of factors influencing the process of combustion and heat transfer.

Introduction

The need for increased power, more exact working conditions, and other demands that are being made of modern combustion chambers, have in recent years led to the development of numerous mathematical and even physical models for predicting the processes taking place within them. This is primarily related to mathematical models which give the information necessary for the design of combustion chambers in the easiest and least expensive manner.

The newer, and more sophisticated mathematical models which can be used to determine the distribution of heat throughout the chamber wall, can be basically summarized by the two best known methods:

1 the zonal method, proposed by Hottel [1, 2], in which the uptake and distribution of heat throughout the chamber wall can be determined on the basis of the energy balance of the final elements.

2 Spalding's method, which, in addition, allows determination of the flow, temperature and concentration fields in the combustion chamber by numerical solution of transfer equations.

Despite their originality and indubitable advantages over other methods, the main shortcoming of these methods are the insufficiently determined entry data. This refers, specifically, to the course of the process of combustion and the possibility of correctly determining the dependence of absorption coefficients on local temperatures and the temperature of the heat source.

Spalding's method is physically more complex, but its application is still mainly confined to two-dimensional models because of difficulties in determining turbulence in three-dimensional models.

The task of the dimensionless mathematical model, which is shown here, is significantly simpler in comparison to the models above, because it is confined exclusively to the determination of heat transfer within the combustion chamber and the determination of the most significant process parameters. The distribution of heat within the combustion chamber will be determined using the light model [3], which will be the subject of another paper.

Mathematical Model

We imagine a spherical model chamber with a concentrically placed flame (Fig. 1), which furnishes constant values of local shape factors between the flame and the chamber wall. In this way the problem is significantly simplified. Isocolar areas, that is areas with the same degree of combustion in the combustion zone are represented by concentric spheres, while in the gaseous zone, which is positioned between the flame and the chamber wall, the concentric spheres represent isothermal areas. The combustion products leave the spherical chamber radially through the bounding walls.

It is assumed that the radiation of the flame and the gaseous zone is grey, and that the emissivity and absorptivity in both zones are constant and fixed at the characteristic predetermined temperatures.

Due to its simplicity, a similar model has already been used a few times for solving these problems [4, 5].

From the above assumptions the effective radiation from the flame to the gaseous zone can be presented by the following expressions

$$\dot{Q}_{12} = 4\pi r^2 \epsilon_{cc1} \Gamma_s T_1{}^4 + \dot{Q}_{21}\,(1 - \epsilon_{cc1}) \tag{1}$$

$$\dot{Q}_{21} = \phi_{21} \pi (R + r)^2\, \epsilon_{cc2}\, \Gamma_s T_2{}^4 + \dot{Q}_{12} \phi_{21}\,(1 - \epsilon_{cc2}) \tag{2}$$

Where

$$\phi_{21} = \left(\frac{2r}{R + r}\right)^2 \tag{3}$$

is the shape factor.

In the same manner it is possible to determine the effective radiation from the gas layer to the chamber wall and the reverse.

Thus we get

$$\dot{Q}_{23} = \pi\,(R + r)^2\, \epsilon_{cc2} \Gamma_s T_2{}^4 + \dot{Q}_{32}\,(1 - \epsilon_{cc2}) \tag{4}$$

$$\dot{Q}_{32} = \phi_{32}\, 4\pi R^2 \Gamma_s \overline{\epsilon_{cc3} T_3{}^4} + \dot{Q}_{23}\, \phi_{32}\,(1 - \bar{\epsilon}_{cc3}) \tag{5}$$

$$\phi_{32} = \left(\frac{R + r}{2R}\right)^2 \tag{6}$$

Heat which in the stationary state is transferred to the gas layer by the flame, is equal to

---

Contributed by the Power Division for publication in the JOURNAL OF ENGINEERING FOR POWER. Manuscript received at ASME Headquarters July 23, 1980.

$$\dot{Q}_1 = \dot{Q}_{12} - \dot{Q}_{21}$$

$$= \mathcal{H}^{2/3} A_3\Gamma_s\epsilon_{cc1} \frac{\left[1 - (1-\epsilon_{cc2})\left(\frac{2}{1+\mathcal{H}^{-1/3}}\right)^2\right] T_1{}^4 - \epsilon_{cc2}\, T_2{}^4}{1 - \left(\frac{2}{1+\mathcal{H}^{-1/3}}\right)^2 (1-\epsilon_{cc1})(1-\epsilon_{cc2})} \tag{7}$$

where

$$\mathcal{H} = \left(\frac{r}{R}\right)^3 \tag{8}$$

which is the degree to which the chamber is filled by the flame, namely, the ratio of the flame volume to the total volume of the chamber.

For determining the heat transferred from the gas layer to the furnace walls, equations (4–6) and 8 apply.

$$\dot{Q}_2 = \dot{Q}_{23} - \dot{Q}_{32} = \left(\frac{1+\mathcal{H}^{1/3}}{2}\right)^2 A_3\Gamma_s\epsilon_{cc2} \times \frac{\left[1 - (1-\bar{\epsilon}_{cc3})\left(\frac{1+\mathcal{H}^{1/3}}{2}\right)^2\right] T_2{}^4 - \overline{\epsilon_{cc3}T_3{}^4}}{1 - \left(\frac{1+\mathcal{H}^{1/3}}{2}\right)^2 (1-\epsilon_{cc2})(1-\bar{\epsilon}_{cc3})} \tag{9}$$

In the above equations $\bar{\epsilon}_{cc3}$ and $\overline{\epsilon_{cc3}\cdot T_3{}^4}$ signify the mean values of the mentioned quantities. These values are introduced because of incomplete screening of the chamber walls.

The mean degree of chamber screening, mean radiation of the band form concept of the chamber walls with isolated fire clay wall parts having adiabatic properties, and the mean emissivity of the so defined bounding surface of the combustion chamber are used for their definition.

$$\bar{x} = \frac{\sum_{i=1}^{n} x_i A_i}{A_3} \tag{10}$$

$$\overline{\epsilon_{cc3}T_3{}^4} = (1-\bar{x})\,\epsilon_{cc2}T_2{}^4 + \bar{x}\epsilon_{cc3}T_3{}^4 \tag{11}$$

$$\overline{\epsilon_{cc3}} = (1-\bar{x})\,\epsilon_{cc2} + \bar{x}\epsilon_{cc3} \tag{12}$$

Using these approximate relations, the heat transferred to the walls of the combustion chamber can be presented as

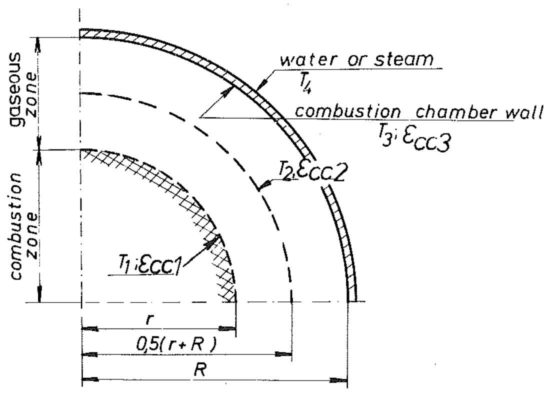

Fig. 1

The heat transferred in the combustion chamber can also be determined by the decrease in enthalpy of the products of combustion.

$$\dot{Q} = \dot{M}_f\,(h_F - h_F{}'') \tag{14}$$

In the stationary state it will be

$$\dot{Q}_1 = \dot{Q}_2 = \dot{Q}_3 = \dot{Q}$$

This equation represents the prime condition of this mathematical model.

With the above relations, the heat efficiency of the screen surfaces, can be determined. This is the ratio between the heat received by the fluid and the heat radiated on to the walls of the chamber. This is often used in practical calculations [6] and the isothermal light model [3].

$$Q_2 = \left(\frac{1+\mathcal{H}^{1/3}}{2}\right)^2 A_3\Gamma_s\epsilon_{cc2} \times \frac{\left\{1 - \left(\frac{1+\mathcal{H}^{1/3}}{2}\right)^2 [1 - \bar{x}\epsilon_{cc3} - (1-\bar{x})\,\epsilon_{cc2}] - \epsilon_{cc2}(1-\bar{x})\right\} T_2{}^4 - \bar{x}\epsilon_{cc3}\overline{T}_3{}^4}{1 - \left(\frac{1+\mathcal{H}^{1/3}}{2}\right)^2 (1-\epsilon_{cc2})[1 - \bar{x}\,\epsilon_{cc3} - (1-\bar{x})\epsilon_{cc2}]} \tag{13}$$

Nomenclature

a = coefficient of beam extinction, (m^{-1})
A^r = ash content in fuel, (percent)
A = area, (m^2)
C^r = fuel carbon content, (percent)
Γ_s = black body radiation (Stefan-Boltzmann) constant, (W/m^2K^4)
d = diameter of particles of the fuel or ash, (μm)
$\dot{D}$ = steam production in the boiler, (kg/s)
Δh_u = lower heating capacity of fuel, (kJ/kg)
H^r = fuel hydrogen content, (percent)
h = specific enthalpy, (kJ/kg)
h_F = effective heat production in the combustion chamber, (kJ/kg)
$\dot{M}_f$ = mass flow of combustion products, (kg/s)
P = pressure, (MPa)
$\dot{q}_{fl}$ = heat flow rate in the flame, (W/m^3)
$\dot{q}$ = heat flux density, (W/m^2)
$\dot{Q}$ = total heat flow rate, (W)
r, R = radius, (m)
r_{H_2O} = volume ratio of steam in combustion gases, (percent)
r_{RO_2} = volume ratio of CO_2 and SO_2 in combustion gases, (percent)
s = mean thickness of gas layer, (m)
t = temperature, (°C)
T = absolute temperature, (K)
V = volume, (m^3)
V_g = specific volume of combustion products under normal conditions, ($m_N{}^3/kg$)
x = degree of screening of combustion chamber,
δ = thickness, (m)
ϵ = heat resistance, (m^2K/W)
ϵ_{cc} = emissivity, ()
$\mathcal{H}$ = degree of filling of combustion chamber by flame, (−)
λ = heat conduction coefficient, (W/mK)
λ_a = air excess coefficient, (−)
Ψ = heat efficiency of the screened surfaces, (−)
ρ = density, (kg/m^3)
τ = optical density, (−)
ϕ = shape factor (−)

Subscripts

a = adiabatic
b = burner
f = fuel
F = combustion chamber
fl = flame
w = wall
1 = combustion zone
2 = gaseous zone
3 = combustion chamber wall
4 = heated fluid

Superscripts

$''$ = outgoing
− = mean

$$\Psi = \frac{\dot{Q}_{23} - \dot{Q}_{32}}{\dot{Q}_{23}} = \frac{\left\{1 - \left(\frac{1 + \mathcal{H}^{1/3}}{2}\right)^2 [1 - \bar{x}\epsilon_{cc3} - (1 - \bar{x})\epsilon_{cc2}] - \epsilon_{cc2}(1 - \bar{x})\right\} T_2^4 - \bar{x}\epsilon_{cc3}T_3^4}{[1 + (1 - \epsilon_{cc2})(1 - \bar{x})]T_2^4 + \bar{x}\epsilon_{cc3}\left(\frac{1}{\epsilon_{cc2}} - 1\right) T_3^4} \tag{15}$$

For a given fuel and excess air, the enthalpy of the combustion products can be described by a second degree polynomial in which the coefficients a_i, b_i and c_i are determined by the method of least squares.

$$h_F'' = a_i T_F''^2 + b_i T_F'' + c_i \tag{16}$$

The isotropic emissivity of the flame and gas layer depend on their integral optical densities

$$\epsilon_{cc1} = 1 - \exp(-\tau_1) = 1 - \exp(-s_1 a_1) \tag{17}$$

$$\epsilon_{cc2} = 1 - \exp(-\tau_2) = 1 - \exp(-s_2 a_2) \tag{18}$$

The thickness of the gas layers are determined as a function of the optical densities [7] by the following relations

$$s_1 = 3.6 \frac{V_1}{A_1} C_1 = 0.339\, \mathcal{H}^{1/3} A_3^{1/2} C_1 \tag{19}$$

$$s_2 = 3.6 \frac{V_2}{A_2} C_2 = 0.339 \frac{1 - \mathcal{H}}{1 + \mathcal{H}^{2/3}} A_3^{1/2} C_2 \tag{20}$$

where

$$C_1 = \frac{\tau_1 \exp(-\tau_1)}{\tau_1 - 1 + \exp(-\tau_1) + \tau_1 \exp(-\tau_1)} \tag{21}$$

$$C_2 = \frac{\tau_2 \exp(-\tau_2)}{\tau_2 - 1 + \exp(-\tau_2) + \tau_2 \exp(-\tau_2)} \tag{22}$$

We determined the coefficient of beam extinction with data which is often used but still incompletely checked [6, 8].

Equation (23) was used for calculation of the combustion of liquid and gas fuels, while for the combustion of solid fuels in air suspension and in layers, equation (24) was employed.

$$a = k_1(1 - 0.37 \cdot 10^{-3}) + k_2(1.6 \cdot 10^{-3}\,\mathrm{T} - 0.5) \tag{23}$$

$$\mathrm{a} = k_1(1 - 0.37 \cdot 10^{-3}) + k_3 T^{-0.66} + k_4 \tag{24}$$

The coefficients (k_1 to k_4) are determined on the basis of the suggested equations in Table 1 [6, 8].

The coefficients of beam extinction in the combustion and gaseous zones are determined for appropriate temperatures (T_1, T_2) and layer thickness (s_1, s_2). Using these values, an expression for optical densities of both zones results

$$\tau_1 = a_1 s_1 = 0.339\, \mathcal{H}^{1/3} A^{1/2} a_1 C_1 \tag{25}$$

$$\tau_2 = a_2 s_2 = 0.339 \frac{1 - \mathcal{H}}{1 + \mathcal{H}^{2/3}} A_3^{1/2} a_2 C_2 \tag{26}$$

Assuming that the flame and the combustion products in the gaseous zone are isotropic, that the emissivity of the products of combustion does not change in the whole temperature range, that the wall temperature is constant, and that the heat is transferred exclusively by radiation, the mean temperature of the gaseous zone can be defined as Stefan's temperature, determined for a one dimensional process of heat transfer [9].

$$T_2 = \left[T_3^4 + \frac{4\, T_3^3 (T_1 - T_F'')}{\ln \frac{(T_3 + T_F'')(T_3 - T_1)}{(T_3 - T_F'')(T_3 + T_1)} - 2 \operatorname{arctg} \frac{T_3(T_1 - T_F'')}{T_3^2 + T_F'' \cdot T_1}} \right]^{0.25} \tag{27}$$

The dependence between the wall temperature and its degree of blackness can be represented by a linear relation.

$$\epsilon_{cc3} = C_1 - C_2 T_3 \tag{28}$$

The coefficients in this equation were determined experimentally, and are given in Table 2 [10, 11].

The Fourier expression for heat conduction is used to determine the heat exchange with the heating fluid. In our case

Table 1

No.	Suggested equations	
1	$k_1 = \left[\frac{0.78 + 1.6\, r_{H_2O}}{\sqrt{\frac{p}{0.098}}\, s(r_{H_2O} + r_{RO_2})} - 0.1\right] (r_{H_2O} + r_{RO_2})$; p (MPa)	
2	$k_2 = 0.068\,(1.45 - 0.45\,\lambda_a'') \frac{C^r}{H^r}$; for gas fuels: $\frac{C^r}{H^r} = \sum \frac{m}{n} C_m H_n$ for $\lambda_a'' = 3.2$ the coefficient is $k_2 = 0$	
	$k_3 = \frac{b}{d^{2/3}} \cdot \mu = \frac{b}{d^{2/3}} \cdot \frac{10\, A^r a'}{V_g}$; $b = 5$ – for brown coals, and lignites $b = 3.7$ – for anthracite, coke and other solid fuels	
3	$a' = 0.9 - 0.96$	for combustion in flight (air suspension)
	$a' = 0.2 - 0.30$	for combustion in layers
	$d = 13\ \mu m$	grinding in slow paced mills
	$d = 16\ \mu m$	grinding in medium paced and fast paced mills
	$d = 20\ \mu m$	combustion in layers
4	$k_4 = 0.03 - 0.05$	0.03 – for combustion in layers 0.04 – for combustion in flight (air susp.) 0.05 – for combustion in primary combustion chambers

Table 2

No.	State of the heated surface	Temperature range (K)	C_1 (−)	$10^3 \cdot C_2$ (K^{-1})	Source in literature [10, 11]
1	Loosely piled ash	300–600	0.960	0.10	R. S. Prasolov
2	Loosely piled ash	400–1200	1.199	0.400	M. F. R. Mulsahy
3	Solidly piled ash	400–1300	0.906	0.060	M. F. R. Mulsahy
4	Cindery surfaces	700–1600	0.880	0.107	M. F. R. Mulsahy
5	Ceramic Covered pipes	600–1600	0.876	0.095	Lebedev. Temkin

Table 3

		Entry values*					
Fig.	Independent variable	$\dot{M}_f$ (kg/s)	$\epsilon_2 \cdot 10^3$ (m^2K/W)	T_4 (K)	λ_a (−)	$\mathcal{H}$ (−)	$\bar{x}$ (−)
3	λ_a	1.090	3.556	504	−	0.42	0.954
3	ϵ	1.090	−	504	1.05	0.42	0.954
4	$\mathcal{H}$	1.090	3.556	504	1.05	−	0.954
4	$\mathcal{H}$	1.090	3.556	504	1.05	−	0.954
5	$\mathcal{H}$	1.635	3.556	504	1.05	−	0.954
5	$\mathcal{H}$	1.635	3.556	504	1.05	−	0.954
6	$\dot{M}_f$	−	3.556	504	1.05	−	0.954
6	$\dot{M}_f$	−	3.556	504	1.05	0.42	0.954
7	$\bar{x}$	1.090	3.556	504	1.05	0.42	−
7	$\bar{x}$	1.090	3.556	504	1.05	0.42	−

* In all calculations constant entry data are: $A_3 = 188.65$ m^2; $\phi = 0.99$, $h_f = 38393$ KJ/kg

$$T_3 = \frac{\dot{Q}\epsilon}{A_3} + T_4 \tag{29}$$

In this expression ϵ represents the heat resistance between the wall surface and the heated fluid, that is

$$\epsilon = \frac{1}{\alpha_4} + \sum_{i=1}^{n} \left(\frac{\delta}{\lambda}\right)_i \tag{30}$$

In this way, all the heat resistances of the combustion chamber wall are taken into consideration.

The degree of filling of the combustion chamber by the flame is an entry of considerable importance, which, being dependent on the kinetics of the combustion process, significantly influences the work of the combustion chamber. Previous research [12–14] has shown that, in the diffuse region of combustion, this value can be presented as a function of the power of one burner ($\dot{Q}_b$ − MW), their number (n − pcs) and the volume of the combustion chamber (V_3 − m^3).

Thus for the combustion of fluid and gaseous fuels the degree of filling of the chamber can be very roughly determined by an empirical formula.

$$\mathcal{H} = k_5 \frac{k_6 n \dot{Q}_b{}^{3/2}}{V_3} \tag{31}$$

$$k_5 = 1 \div 2$$

$k_6 = 0.30$ for natural gas and 0.55 for fuel oil, by conventional air excess coefficients.

For combustion of coal dust in air suspension this value can be, for example, determined by a similar formula (n = number of burner outflows).

$$\mathcal{H} = k_7 \frac{1.6\, n\{\exp\,[1.45(1 - \lambda_a'')]\}(\dot{Q}_b{}^{1.35} + \dot{Q}_b{}^{0.8}\, d^2)}{V_3} \tag{32}$$

$$K_7 = 1.0 \div 1.4$$

d = particle diameter which corresponds to the residue in the sieve which is 1 percent in the granulometric diagram according to Rosin, et al. (mm).

The heat which is effectively generated in the combustion chamber (h_F) was determined according to the well-known procedure CKTI [6].

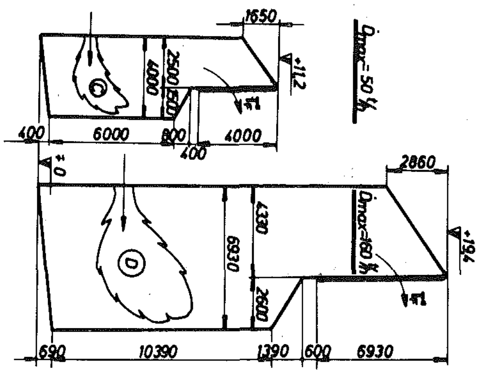

Fig. 2

Equations (7, 8) and (13–29) represent a system which needs to be solved. We used an iterative procedure determining values $\dot{Q}_1$ (equation (7)), $\dot{Q}_2$ (equation (13)) and $\dot{Q}_3$ (equation (14)) assuming flame temperatures to be T_1 and the temperature in the combustion products in exciting the combustion chamber T_F''. Errors in determining the values $\dot{Q}_1$, $\dot{Q}_2$ and $\dot{Q}_3$ were less than 0.5 percent. A Hewlett-Packard computer 9815 A with 2008 program memories was used to solve the system of equations.

Test of the Mathematical Model

In order to establish the behaviour, sensitivity and the applicability of this complex mathematical model, a number of calculations were carried out for the combustion chamber of an industrial steam generator heated by fuel oil. The nominal capacity was 13.89 kg/s, and the cross section is shown in Fig. 2.

The calculations were done using the different entry data which are given in Table 3. Some results of the calculations for this example are presented in Figs. 3–7.

Figure 3 presents the influence of the air excess coefficient and heat resistance of screen surfaces on the fundamental parameters of the combustion chamber. The temperatures of outgoing combustion products established by the old and the new CKTI standard methods are also indicated in the lefthand diagram, as well as the data for heat efficiency of the screen surfaces. These data are different from the data used in the aforementioned method [6]. In addition, the heat efficiency depends on the working conditions of the combustion chamber. This is understandable because, by changing the working conditions, the conditions for heat transfer in the walls of the combustion chamber are also changed.

The right-hand diagram in Fig. 3 shows the influence of heat resistance of the screen surfaces on the same parameters. It especially influences the temperature change of the combustion chamber wall,

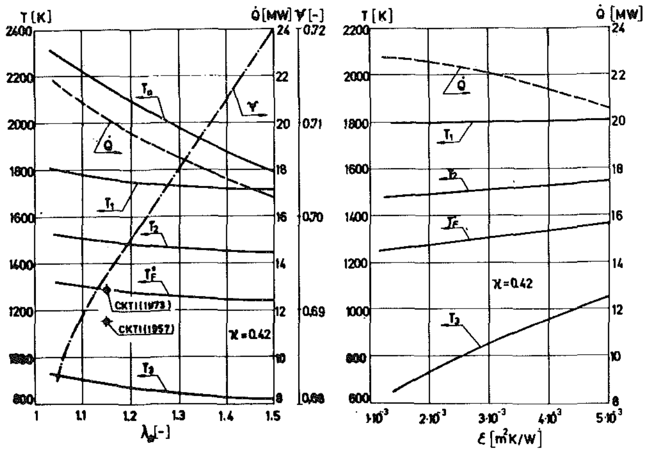

Fig. 3

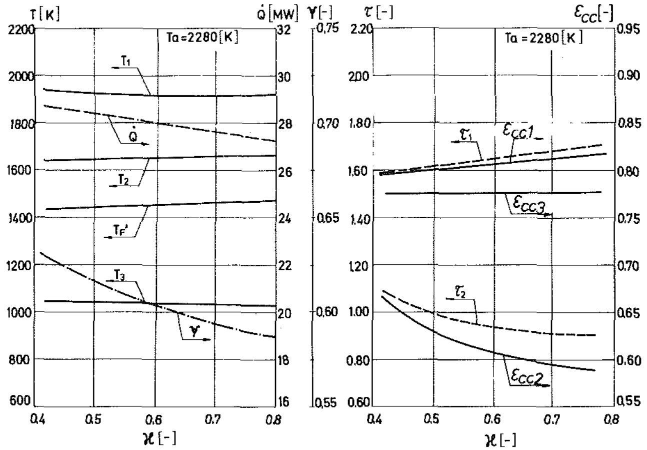

Fig. 5

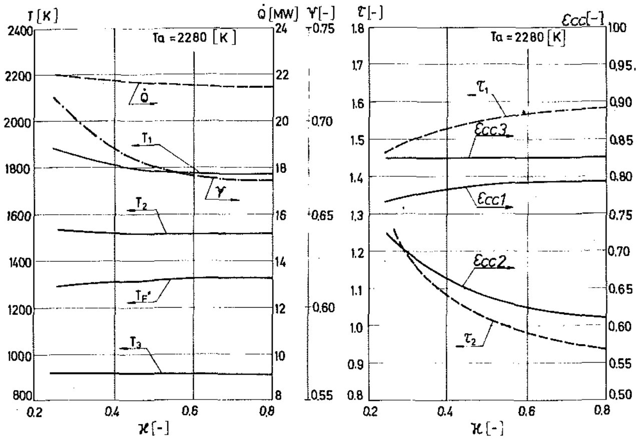

Fig. 4

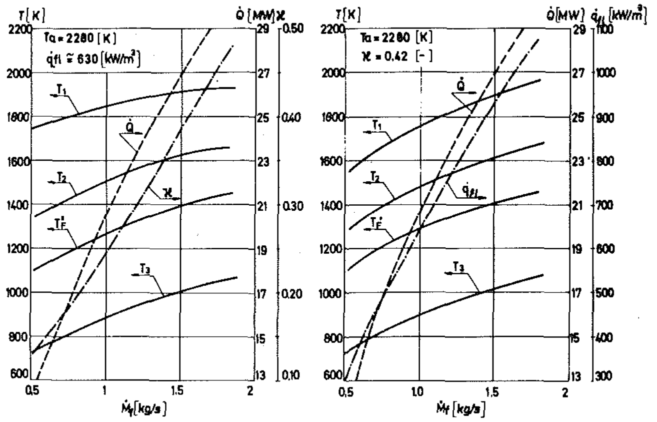

Fig. 6

which makes it easier to analyse the sticking of ash to the screen pipes. This is not characteristic of the common methods of evaluation.

The next point which we wished to examine was the degree of filling of the combustion chamber by the flame and the heating capacity of this combustion chamber. Figure 4 presents the nominal power of the combustion chamber, while in Fig. 5. the same data are determined for 50 percent overload of the combustion chamber.

It is evident that the degree of filling of the combustion chamber by the flame influences has little effect on the heat transferred in the combustion chamber. Nevertheless, it significantly changes the physical characteristics of the flame, especially the combustion products in the gaseous zone, i.e., exactly those values which will be used in experimental determination of heat distribution in the light model [3].

Furthermore, with the increased power of the combustion chamber the heating efficiency of the screen surfaces decreased significantly. This means that an incorrectly estimated degree of filling of the chamber by the flame in the light model would cause a marked deformation of the simulated heat flux.

Figure 6 shows the desired values as a function of the power of the combustion chamber. For the diagram on the left a characteristic is the constant value of the heat flow rate in the flame ($\dot q_{f1} \cong 630$ kW/m^3), but for that on the right a constant flame volume.

It can be seen that, in both examples, the total heat transfer in the combustion chamber is approximately equal and that with the reduced power of the combustion chamber, and especially with the decreased flame heat flow rate, the temperature of the flame zone sharply falls, which was expected.

In Fig. 7 all the values are shown as functions of the mean degree of screening. In this case, also, we obtain the expected results.

As the size of the combustion chamber significantly influences the process of heat transfer, we wished to examine also the behaviour of

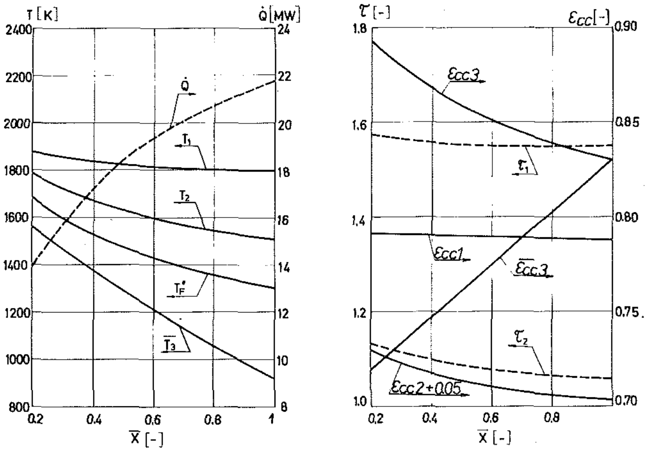

Fig. 7

the developed mathematical model in geometrically similar combustion chambers. To that end we considered a geometrically similar combustion chamber with a heat capacity which was over three times larger. This is shown in Fig. 2, right. At the same relative heat transfer the heat capacity of this combustion chamber would be [15].

$$\dot M_{fD} = \dot M_{fC}\left(\frac{V_{FD}}{V_{FC}}\right)^{0.708} = 3.5\ \text{(kg/s)} \qquad (33)$$

All the significant values and characteristics of both combustion chambers are given in Table 4.

On the basis of these results it is concluded that the mathematical model fits the laws of heat transfer in geometrically similar combustion chambers exceptionally well. Namely, with the increase in size

Table 4

No.	Value	Symbol	Dimension	Chamber geometry C	D
1	Nominal boiler production	$\dot{D}$	kg/s	13.89	44.60
2	Lower heat power of the fuel	Δh_u	kJ/kg	38979	38979
3	Free heat in the chamber-per kg	h_F	kJ/kg	38393	38393
4	Fuel flow	$\dot{M}_f$	kg/s	1.09	3.5
5	Degree of chamber isolation	ϕ	–	0.99	0.99
6	Coefficient of air excess	λ_a''	–	*1.10*	*1.10*
7	*Adiabatic temperature*	T_a	K	2213	2213
8	Heat resistance of ash layer	ϵ	m^2K/W	0.0356	0.0356
9	Coefficient	C_1	–	1.199	1.199
10	Coefficient	C_2	–	0.0004	0.0004
11	Steam temperature	T_4	K	504	504
12	Mean degree of screening	$\bar{x}$	–	0.954	0.954
13	Chamber volume	V_3	m^3	147	764
14	Area of the chamber	F_3	m^2	188.67	564.78
15	Degree of filling of chamber by flame	$\mathcal{H}$	–	0.4208	0.4659
16	Flame temperature	T_1	K	1779	1756
17	Temperature od the cooling zone	T_2	K	1498	1489
18	Temperature of screen pipes	T_3	K	894	922
19	Temperature at the chamber end	T_F''	K	1296	1296
20	Heat transferred in the chamber	$\dot{Q}$	MW	20.635	66.161
21	Flame emissivity	ϵ_{cc1}	–	0.783	0.848
22	Gas zone emissivity	ϵ_{cc2}	–	0.645	0.718
23	Mean degree of wall emissivity	$\bar{\epsilon}_{cc3}$	–	0.832	0.825
24	Heat efficiency of the screen surface	Ψ	–	0.690	0.673
25	Relative heat uptake in the chamber	$\mu = \dot{Q}/\Delta h_u \dot{M}_f$	–	0.486	0.498

of the chamber the degree of filling by the flame also increases, giving an unchanged relative heat uptake by the chamber. Deviation from these laws is insignificantly small and amounts to 2.4 percent, so that this test can be considered as an indirect verification of the model.

Finally, the applicability of the model to boilers of different sizes and conceptions which burn various fuels in layers and in air suspension was examined. Six boilers with characteristics given in Table 5 were considered. The sizes of these boilers varied in a wide range

Table 5*

No.	Symbol	Dimension	Boiler combustion chamber A	B	C	D	E	F
			CHAMBER CHARACTERISTICS					
1	D_{max}	t/h	0.666	14	50	160	230	***** 650
2	p	MPa	0.30	1.1	2.8	2.8	9.9	13.7
3	t_s	°C	–	350	400	400	510	540
4	t_{fv}	°C	70	105	130	130	215	240
5	n**	pcs	1	grate	2	2	4 × 3	4 × 3
6	***	–	fueloil	coal	fuel oil	fuel oil	coal	lignite
7	Δh_u	kJ/kg	42998	13984	28225	38225	15282	6280
8	h_F	kJ/kg	43027	14365	38383	38393	17216	7172
9	$\dot{M}_F$	kg/s	0.00127	0.933	1.090	3.500	1.39	91.11
10	λ_a	–	1.20	1.30	1.15	1.15	1.20	1.25
11	t_a	°C	1716	1331	1940	1940	1858	1273
12	V_3	m^3	0.0315	56	147	746	1210	5669
13	F_3	m^2	0.716	100	188.78	564.78	700	1933.7
14	ϕ	–	0.97	0.985	0.990	0.990	0.995	0.998
			CALCULATED CKTI					
15	Ψ	–	0.457	0.599	0.710	0.700	0.680	0.439
16	ϵ_{cc1}	–	0.210	0.510	0.537	0.990	0.650	0.800
17	ϵ_{cc3}	–	0.366	0.724	0.620	0,999	0.600	0.891
18	$\dot{Q}$	MW	0.0254	4.86	21.15	74.08	84.88	162.36
19	t_F''	°C	952	880	967	887	1117	1002
20	diag	****	A	B	C	D	E	F
			SUGGESTED CALCULATION					
21	Ψ	–	0.654	0.586	0.694	0.678	0.658	0.606
22	ϵ_{cc1}	–	0.186	0.268	0.778	0.843	0.709	0.790
23	ϵ_{cc2}	–	0.122	0.294	0.640	0.713	0.566	0.627
24	ϵ_{cc3}	–	0.803	0.791	0.836	0.829	0.808	0.843
25	ϵ	m^2K/W	0.0035	0.0083	0.0036	0.0036	0.0030	0.004
26	$\mathcal{H}$	–	0.398	0.250	0.421	0.466	0.500	0.600
27	$\dot{Q}$	MW	0.0183	4.134	20.10	64.76	86.59	171.69
28	t_F''	°C	1161	948	1014	1015	1098	986

* All calculation were done according to CKTI-1957, except the calculations for the chamber of boiler C, which was done according to method CKTI-1973, with Ψ = 0,7.

** Represents the number of chamber burners

*** Fuel type

**** Symbols in the diagram, Fig. 8

***** This value does not take into consideration the additional heating of the steam at the exit from the high pressure part of the turbine.

from 50 kW to 500 MW and over, of gross heat power. For all the given boilers we made alternative calculations for the combustion chambers according to the CKTI method and the suggested method.

Figure 8 graphically shows the deviations of heat transferred in the combustion chambers calculated by the given methods. For large chambers these values agree well, while in the smaller chambers greater differences are observed. This is logical in view of the fact that the CKTI method is designed for larger combustion chambers [16]. Greater deviations in the smaller chambers should be ascribed to the greater influence of the flame zone size in those chambers, which was determined in the previous analyses of this model.

Deviations of the emissivity, however, are unexpectedly great and, aside from this, do not obey any laws. They should be, according to our opinion, attributed to the nonconformity of the Gurvich model [6] to the physical essence of the process and to incompatible values for the integral coefficient of beam extinction.

Conclusion

The proposed model is considerably different from the other mathematical models that are used for the estimation of heat transfer in combustion chambers of steam generators. In contrast to the mathematical methods, which in recent times have been oriented towards multidimensional zonal models, this method is based on a dimensionless model. While this model does not allow the determination of heat distribution throughout the chamber walls, we hope to eliminate this shortcoming in the future by combining this model with the isothermal light model, which should solve this complex problem.

By such distribution, the role of the mathematical model is greatly simplified. It allows more attention to be devoted to determining more correctly the integral physical characteristics of the factors in the process of combustion, which is necessary because it is hoped that the distribution of heat throughout the chamber wall will be left to the physical model.

The conductive heat transfer was also indirectly included in the model. This is very significant for studies of the process of sticking of mineral matter to the screened surfaces and the covering by slag. This model offers possibilities for adaption to combustion chambers with significant convective transfer, for example, the cyclonic and similar combustion chambers.

Even though the model is somewhat complicated due to intertwining of the desided values, it can be successfully solved even on simpler digital computers.

It is noteworthy to point out that this model is founded on sound physical laws, which is its basic advantage. However, this cannot be held for the empirical formulas which are used to determine the degree of filling of the chamber by the flame and for the integral coefficient of beam extinction in both zones. They can cause, especially for the burning of poorer fuels, an illogical increase of flame temperature above the adiabatic, but even in such cases the heat transferred in the combustion chamber is within expected boundaries.

In spite of this, the demonstrated mathematical model can be successfully used in engineering practice for determining the heat transfer in the combustion chambers of steam boilers.

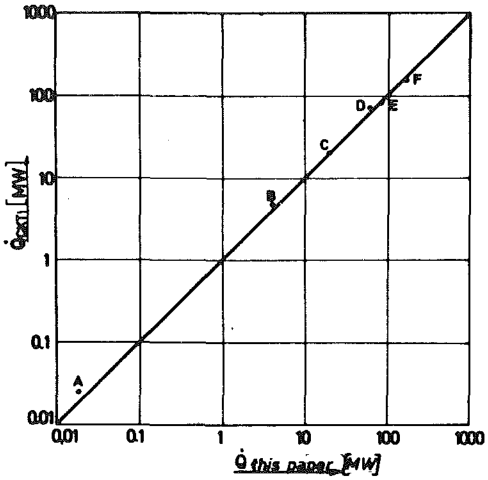

Fig. 8

References

1 Hottel, H. C., Hoyt, C., and Cohen, E. F., "Radiant Heat Exchange in a Gas Filled Enclosure: Allowance for Non-Uniformity of Gas Temperature," *AIChE Journal*, Vol. 4, 1958, pp. 3–14.

2 Hottel, H. C. Hoyt, C., and Sarofim, A. F., *Radiative Transfer*, McGraw-Hill, New York, 1967.

3 Gulič, M., "Light Model Method for Simulation of the Radiant Heat Distribution in the Combustion Chamber," Sixth Int: Heat Transfer Conf., Toronto, Vol. 2, Aug. 1978, pp. 43–48.

4 Ledinegg, M., *Dampferzeugung, Dampfkessel, Feuerungen*, Springer Verlag, Berlin, 1966.

5 Franke, U., "Berechnung der Wärmeübertragung in Brennkammern mit Strahlender Flamme," *Brennstoff-Waerme-Kraft* Vol. 27, No. 11, 1975, pp. 434–438.

6 *Teplovoy Raschot Katelyh Agregatov—Normativni Metod*, Energiya, Moskow, 1973.

7 Gulič, M., "A New Formula for Determining the Effective Beam Length of Gas Layer of Flame", *Heat Transfer in Flames*, Scripta Books, Washington, 1974, pp. 201–208.

8 Bloh, A. G., *Teplovoy Izluchenye v Katelnyh Ustanovkah*, Energiya, Leningrad, 1967.

9 Gulič, M., "Concerning the Transfer of Heat in Cooled Channel," Zbornik radova Mašinskog fakulteta, Novi Sad, 1967. (in Serbo-Croatian).

10 Filimonov, S. S., et al., "Opredelenye Privedennoj Pogloshchatel'noj Sposobnosti Luchevosprinimayushchih Poverhnostej Topochnyh Kamer," *Teploenergetika*, No. 8, 1968, pp. 39–42.

11 Mulsahy, M. F. R., Boow, J., and Goard, P. R. C., *Journal of the Institute of Fuel*, Vol. XXXIX, No. 308. Sep. 1966.

12 Altmann, W., et al., "Strömungsvorgänge in Feuerungssystemen von Braunkohle-Dampferzeugern," *Energietechnik*, Vol. 26, No. 6, 1976.

13 Leihert, H., "Erdgasfeurung Fuer Dampferzeuger," *Energie und Technik*, Vol. 24, No. 7–8, 1972, pp. 251–254.

14 Lentze, B., and Günther, R., "Ausbrand und Wärmeentwicklung in Erdgasdiffusionflammen," *Brennstoff-Waerme-Kraft*, Vol. 27. No. 10, 1975. pp. 387–394.

15 Gulič, M., "The Interdependence of the Combustion and Cooling Zones in Geometrically Similar Fuel Oil Combustion Chambers," *Mašinstvo*, XXII, No. 7, 1973, pp. 1321–1324 (in Serbo-Croatian).

16 Gulič, M., "A Critical Look at the Determination of the Degree of Blackness of the Flame by the Normative Heat Estimation CKTI Method," *Minel*, No. 1, 1972, pp. 39–43 (in Serbo-Croatian).

R. A. Wenglarz
Westinghouse R&D Center,
Pittsburgh, Pa. 15235

An Assessment of Deposition in PFBC Power Plant Turbines

Using turbine deposition models and data from PFBC (pressurized fluidized bed combustion) pilot plant/cascade experiments, deposit buildup rates and turbine maintenance intervals to remove deposits are projected for a PFBC power plant system. The power plant consists of a 10 atmosphere PFB boiler with a matching 10:1 pressure ratio turbine and a gas cleanup system to remove particulates from combustor product gases before entering the turbine. The effects on turbine deposition of three alternative particle cleanup systems are evaluated. Turbine deposit removal intervals to prevent excessive power drops due to deposition are found for the alternative gas cleanup systems.

Introduction

A major consideration for the eventual development of future coal-fired pressurized-fludidized bed combustor (PFBC) power plants is the tolerance of gas turbines to the particle laden expansion gases from the combustor. Particles in these expansion gases can deposit on turbine aerodynamic surfaces to degrade turbine performance and can erode vanes and blades to reduce their structural integrity and also decrease turbine performance. The power plant gas cleanup system must reduce particle carryover to levels which enable acceptable combustion turbine performance, reliability and availability.

The following provides a mechanistic evaluation of deposition in large utility turbines operating with PFBC power plants using a turbine deposition model and data obtained from small cascade tests. These evaluations are conducted for an existing utility turbine matched to a 10 atmosphere PFB boiler plant. Deposition rates, power drops, and turbine maintenance intervals for various particulate cleanup systems are assessed.

Mechanisms of Deposition

The primary mechanisms of particle delivery in turbines [1] are (1) inertial impaction, (2) turbulent eddy diffusion, and (3) Brownian diffusion.

For inertial impaction, particle inertia causes its trajectory to deviate from flow streamlines in vane and blade passages where the flow is turned. Particles can thereby impact the vane and blade surfaces. Arrival rates due to this mechanism of delivery decrease with decreasing particle diameters and inertias, becoming very small for particle diameters less than one micron.

For turbulent eddy diffusion, particles become entrained in eddies of turbulent boundary layers and are swept toward the blade and vane surfaces. Although these turbulent eddies dissipate as they approach the surfaces, the particles continue traveling by free flight toward the surfaces due to their inertia. Increasing the freestream velocity at the boundary layer edge increases the intensity of the turbulent eddies and the particle velocity during free flight and increases particle arrival rates at the surface. For increasing boundary layer thicknesses, particles are slowed more by viscous drag because they must traverse greater distances during free flight and particle arrival rates at the surface decrease. Decreasing particle diameters also results in greater slowing by viscous drag and decreasing arrival rates which fall off rapidly in the 0.1 to 1.0 μm particle diameter range.

For the third mechanism of particle delivery, Brownian diffusion, very small particles are transported to turbine surfaces by random impacts with thermally agitated gas molecules. Molecular impacts more greatly affect particle motion for decreasing particle diameters so that rates of delivery to turbine surfaces due to Brownian diffusion increase with decreasing particle diameter and start to dominate turbulent eddy diffusion at particle diameters in the vicinity of 0.1 μm.

Although the thermophoresis mechanism of particle delivery has received recent attention [2], this mode of transport is expected to be relatively unimportant compared to those described above for PFBC utility turbines. Thermophoresis delivery is due to boundary layer thermal gradients which are relatively small for PFBC turbines because their moderate inlet temperatures require little or no vane and blade cooling. Furthermore, no appreciable particle carryover has been measured from PFBC pilot plants in the size range from 0.01 to 0.1 μm for which thermophoresis particle delivery forces more closely approach delivery forces of the other mechanisms of transport.

Two models have been developed at Westinghouse that are capable of predicting particle arrival rates on turbine vane and blade surfaces. The first determines arrival rates due to the combined effects of turbulent eddy diffusion and Brownian diffusion. The theoretical basis for this model along with experimental verifications will soon be reported in the open literature. The second model determines arrival rates due to inertial impaction and utilizes the same analytical approach [3] that has been used to evaluate erosion in combustion turbines because the mechanism of particle delivery for inertial impaction deposition is precisely the same as for erosion.

The PFBC Power Plant/Turbine System

Deposition evaluations have been conducted for a large utility turbine operating with a 10 atmosphere PFBC boiler plant. For this plant (simplified schematic given by Fig. 1) the turbine compressor provides pressurized air to fluidize a bed where coal is combusted with a sulfur removing sorbent. The combustion gases are passed through a particulate removal system and into the turbine expander which drives an electric generator in addition to the compressor. The turbine exhausts through a heat recovery unit which heats feedwater that

---

Contributed by the Corrosion and Deposits Division of the AMERICAN SOCIETY OF MECHANICAL ENGINEERS and presented at the Winter Annual Meeting, Chicago, Ill., November 19, 1980. Manuscript received at ASME Headquarters July 23, 1980. Paper No. 80-WA/CD-1.

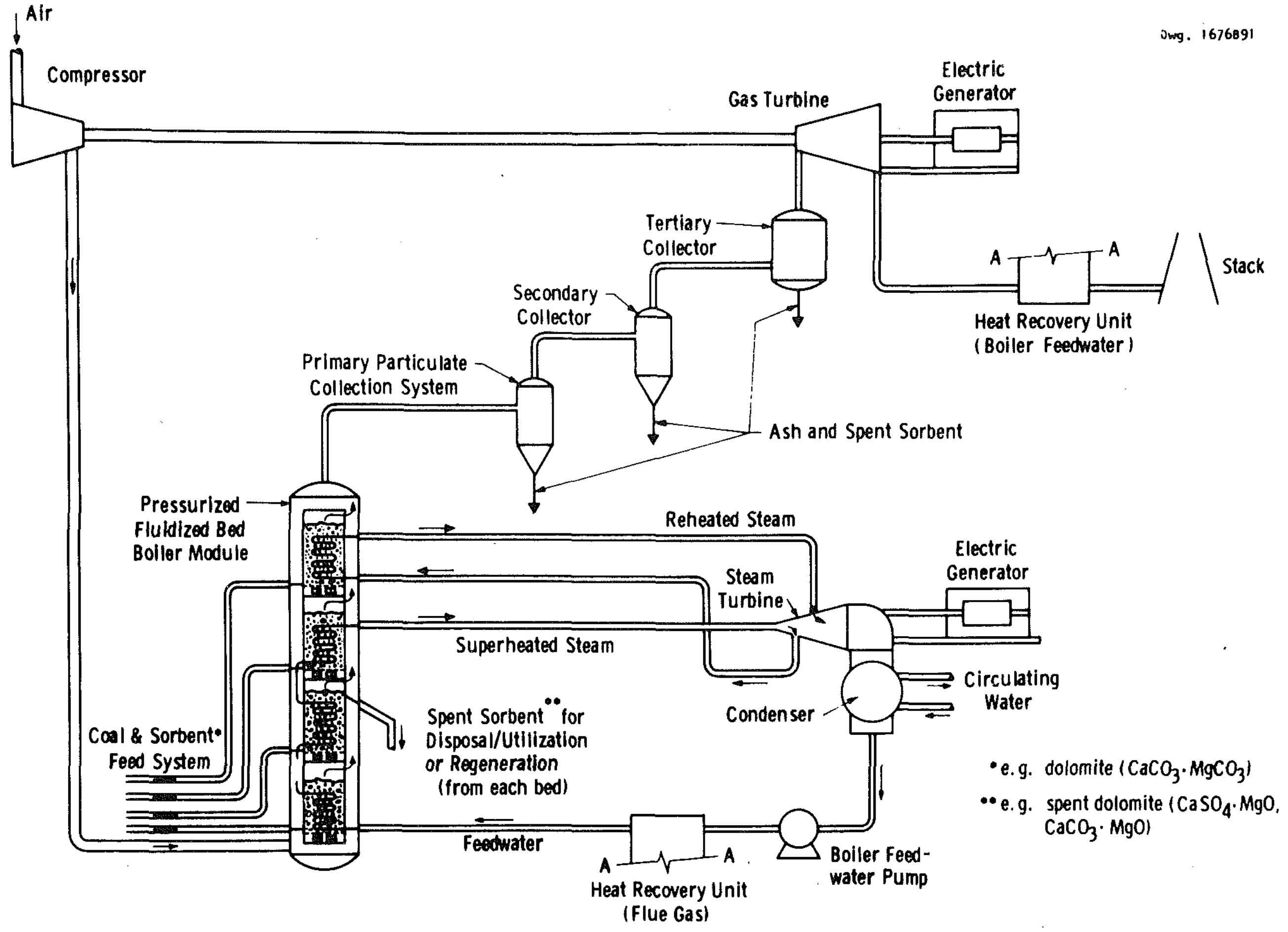

Fig. 1 Pressurized fluidized bed boiler-power plant schematic

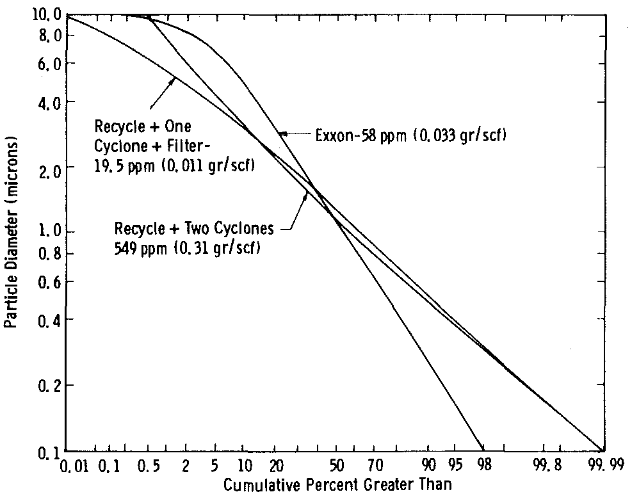

Fig. 2 Partical loadings and size distributions entering turbine

passes through boiler tubes in the fluidized bed providing high pressure steam. The steam is expanded through a steam turbine which also drives an electric generator. The combustion turbine is a single shaft machine with about 50 MW power output, a pressure ratio of about 10:1 and inlet temperature of 871°C (1600°F).

Three alternative cleanup systems are considered for the power plant. The first cleanup system is considered to pass the same particulate loading and distribution to the turbine as the average measured at the EXXON PFBC pilot plant after three cyclones. The average loading measured over 735 hr of cascade testing at EXXON was 58 ppm (0.033 gr/scf) with 90.9 percent of the particulate mass in the 0 to 5 μm range, 9 percent in the 5 to 10 μm range and 0.1 percent greater than 10 μm in diameter [4]. The EXXON distribution is shown in Fig. 2 along with distributions for the two other alternative particle cleanup systems for the 10 atmosphere plant. These consist of (1) one recycle cyclone stage with two cleanup cyclone stages and (2) one recycle cyclone stage, one cleanup cyclone stage and a final granular bed filter stage. The recycle cyclones of the 10 atmosphere plant do not remove material from the system but recirculate captured fines back to the bed to minimize loss of material blown out of the bed before being completely combusted.

Except for the EXXON distribution, all the distributions in Fig. 2 were obtained from a Westinghouse model [5] which projected carryover from the fluidized bed of the power plant and the material passed through the cleanup systems using data on removal efficiencies measured in small scale cleanup device tests. The three cyclone cleanup system particle loadings projected by the carryover model were much higher than those measured passing through three cyclones at the EXXON PFBC pilot plant. This was mainly due to the unexpectedly high overall efficiency of the EXXON third cyclone compared to past performance measurements and analytical calculations for similar cyclones. No satisfactory explanation appears evident for this unexpectedly beneficial cyclone performance. However, a partial explanation for the higher performance measured at the EXXON pilot plant compared to the predicted three stage cyclone performance may be smaller size (an resulting higher efficiency) for the EXXON third stage cyclone.

For each of the above alternative cleanup systems, deposit buildup rates in the first expander stage, turbine power output losses, and turbine maintenance intervals have been calculated utilizing the deposition models described above and available data from PFBC pilot plant cascade tests.

Particle Arrival Rates

Turbulent Eddy and Brownian Diffusion. The calculation of particle delivery rates due to diffusion required determination of near surface gas velocities just outside the vane and blade boundary layers which then enabled determination of characteristics (velocities, wall shear, etc.) within the boundary layers. Near surface gas velocities and boundary layer characteristics were calculated with standard computer programs which have been used by turbine designers to engineer vane and blade contours.

Near surface velocities and boundary layer thicknesses versus fraction of axial chord are shown in Fig. 3 for the stator suction surface and in Fig. 4 for the rotor suction surface of the 10:1 pressure ratio turbine. Velocities and boundary layer thicknesses for pressure surfaces were also calculated but are not given.

The results from the boundary layer calculations were used as inputs to the turbulent eddy/Brownian diffusion deposition model to determine particle arrival rates, expressed in terms of deposition velocity, versus location on the turbine vanes and blades. Deposition velocity (K) is the arrival rate (N) at a surface location normalized to the particle concentration (C_{in}) at the vane or blade passage inlet and is defined by

$$K = N/C_{\text{in}} \tag{1}$$

The local arrival rate can be obtained by multiplying the deposition velocity by the inlet concentration.

Figures 5 and 6 show the deposition velocity versus axial location on the stator suction and pressure surfaces, respectively, of the 10:1 pressure ratio turbine. The component of deposition velocity due to the combined effects of turbulent eddy and Brownian diffusion are given for particle diameters ranging from 0.01 to 10 μm. These curves show insignificant deposition velocities near the leading edge followed by an abrupt increase. The location of this abrupt change is at the transition from a laminar to a turbulent boundary layer. Upstream of this location, only Brownian diffusion is in effect and the abrupt increase in deposition velocity corresponds to the initiation of turbulence and the relatively great influence of turbulent eddy diffusion.

Downstream of the location of transition, the deposition velocities for the pressure surface and suction surface have opposite trends. Deposition velocities for the pressure surface tend to increase in progressing from transition toward the trailing edge, but tend to de-

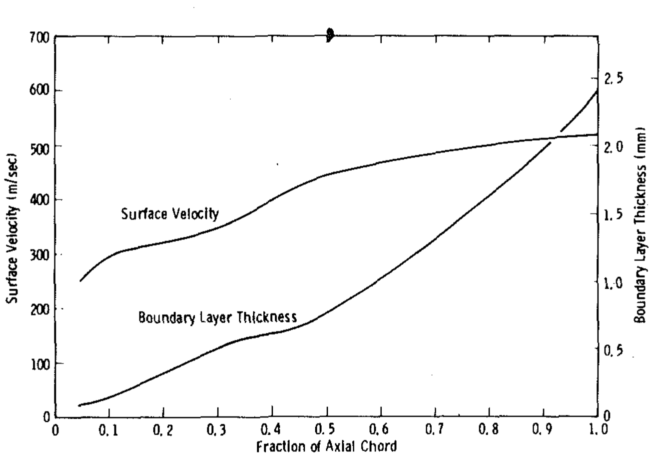

Fig. 3 Velocity and boundary layer thickness for stator suction surface

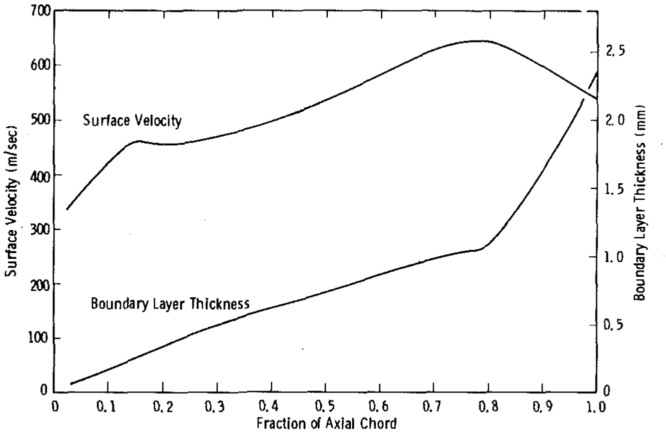

Fig. 4 Velocity and boundary layer surface for rotor suction surface

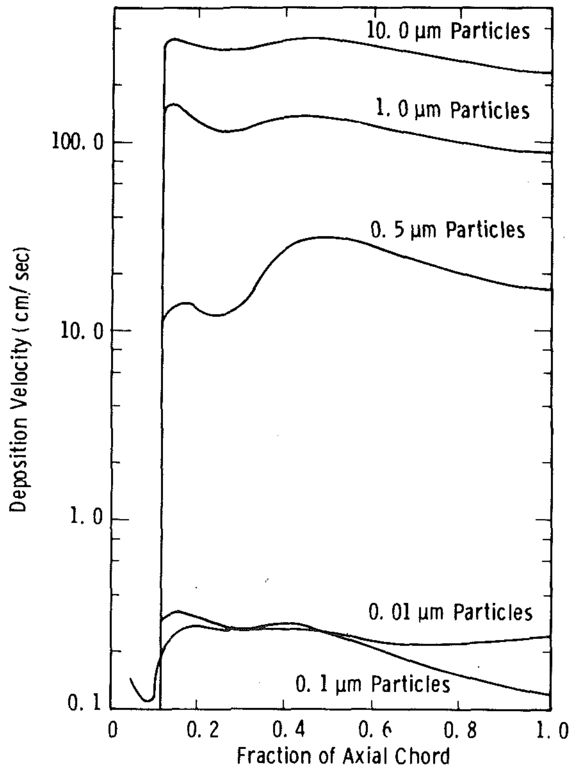

Fig. 5 Deposition velocities for stator suction surface

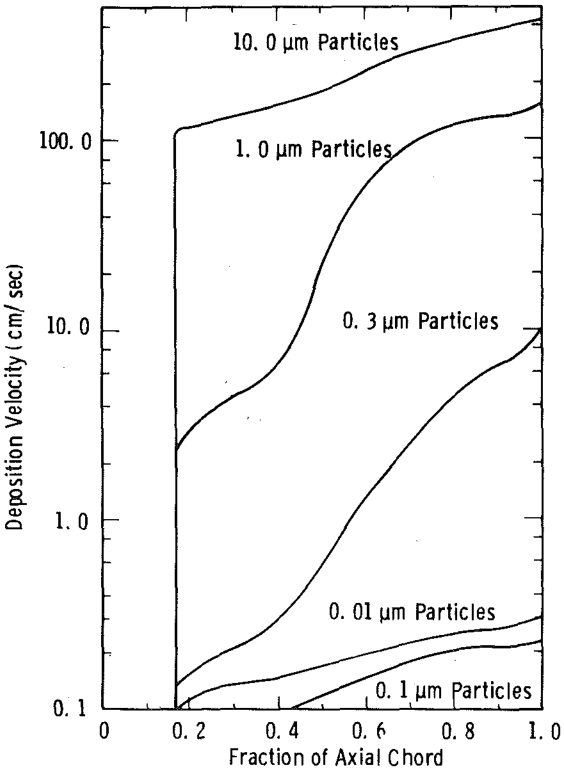

Fig. 6 Deposition velocities for stator pressure surface

crease for the suction surface. These trends are related to the differences in velocity profiles for the two surfaces.

As previously discussed, particle arrival rates due to turbulent eddy diffusion increase with velocity and decrease with boundary layer thickness. The near surface velocity at the pressure surface steadily increases to the maximum trailing edge value. The effect of increasing velocity dominates the effect of increasing boundary layer thickness and the deposition velocity for the pressure surface increases in progressing from the location of transition to the trailing edge. The near surface velocity at the suction surface increases rapidly in the nose region to achieve a relatively high value very near to the leading edge and then experiences a relatively gradual average rate of change over the remainder of the downstream surface. Consequently, for the suction surface, the effect of the thickening boundary layer dominates the effect of the gradual velocity change and the deposition velocities tend to decrease in progressing from the location of transition to the trailing edge. However, as will be shown later, the greatest deposit buildup on suction surfaces may not occur at transition for loosely bonded deposits because particle removal forces are expected to prevent an abrupt change in deposit buildup.

The tendency for the highest suction surface particle arrival rates to occur at transition and the highest pressure surface particle arrival rates to occur at the trailing edge is further illustrated by Figs. 7 and 8 for the rotor suction and pressure surfaces, respectively, of the 10:1 pressure ratio turbine. These figures also clearly demonstrate the effect of particle size on arrival rates. Deposition velocities drop rapidly in the 1 to 0.1 μm particle diameter range due to the rapid decrease in turbulent eddy diffusion effects for decreasing particle sizes. At particle diameters in the vicinity of 0.1 μm. Brownian diffusion starts to dominate and for further decreasing diameters, the deposition velocities tend to increase.

Figures 7–8 suggest the benefits of improving hot gas particle removal systems in order to pass particle distributions with lower average diameters than the approximately 1 μm value associated with three stages of cyclones. Even holding the overall particle concentration constant, the average particle arrival rates due to diffusion could be reduced by more than one order of magnitude for a 0.3 μm average particle diameter and by more than two orders of magnitude for a 0.1 μm average particle diameter.

Inertial Impaction. As previously indicated for both diffusion and inertial impaction, particle arrival rates are most significant for particle diameters above 1 μm. For 1 μm and larger particles, arrival rates due to inertial impaction have been calculated and compared to those due to diffusion.

Table 1 shows these comparisons, giving the ratio of inertial impaction deposition velocities to Brownian plus turbulent diffusion deposition velocities on the stator of the 10:1 pressure ratio turbine. For the particle size range of significance to PFBC turbines, rebounding particles from the pressure surface have insufficient inertia to transverse the passage and impact the opposite suction surface so that suction surface inertial impacts occur only in the nose region. However, multiple impacts downstream of rebounds do affect inertial impaction arrival rates on the pressure surface. Table 1 shows that the inertial impaction/diffusion ratio decreases in progressing from the nose to the trailing edge and tends to increase with particle diameter. Particle arrival rates due to inertial impaction are seen to dominate those due to diffusion on the near nose region of the suction surface and over the entire pressure surface. This dominance of inertial impaction can be shown to be even greater for the rotors than for the stators due to the higher inertial impaction particle capture efficiencies of the rotors.

Since the inertial impaction is also the mechanism of particle delivery for erosion, the turbine pressure surfaces can experience either erosion or deposition depending on whether the particles are hard and tend to remove the alloy surface and any particles that arrived by diffusion or are molten or semi-molten and tend to stick on the surface. Initial deformation temperatures (as measured by standard cone ash-fusion tests) of most coal ashes exceed 1093°C (2000°F) while the inlet temperature for the turbine is 871°C (1600°F). Accordingly, the bulk of the particles entering the turbine is hard so that erosion rather

Table 1 Inertial impaction/diffusion deposition velocity rates—10:1 pressure ratio turbine stator

Location / Particle Diameter (μm)	Nose Suct. Surf.	Nose Pres. Surf.	Mid-Chord Pres. Surf.	Trail. Edge Pres. Surf.
1	1.4×10^5	2.2×10^5	23.4	2.4
3	2.9×10^5	1.2×10^6	25.3	4.9
9	5.7×10^6	8.5×10^6	47.7	20.2

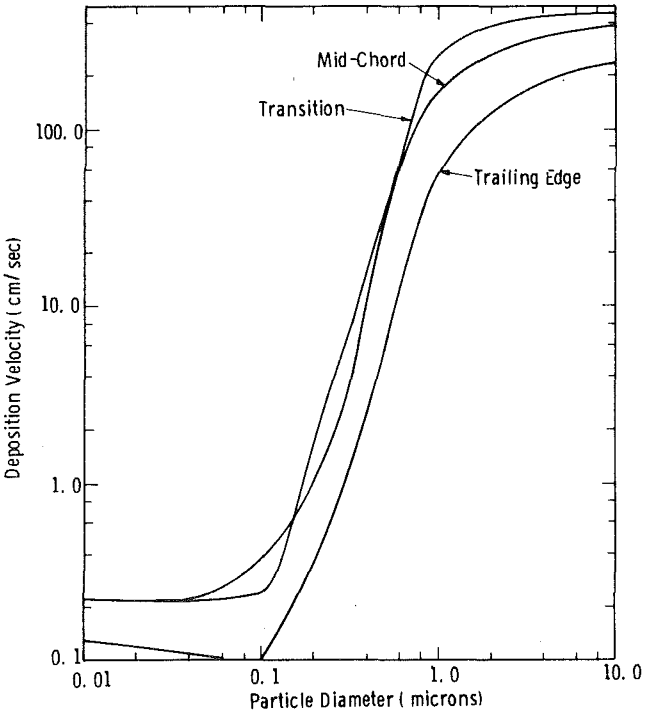

Fig. 7 Deposition velocities for rotor suction surface

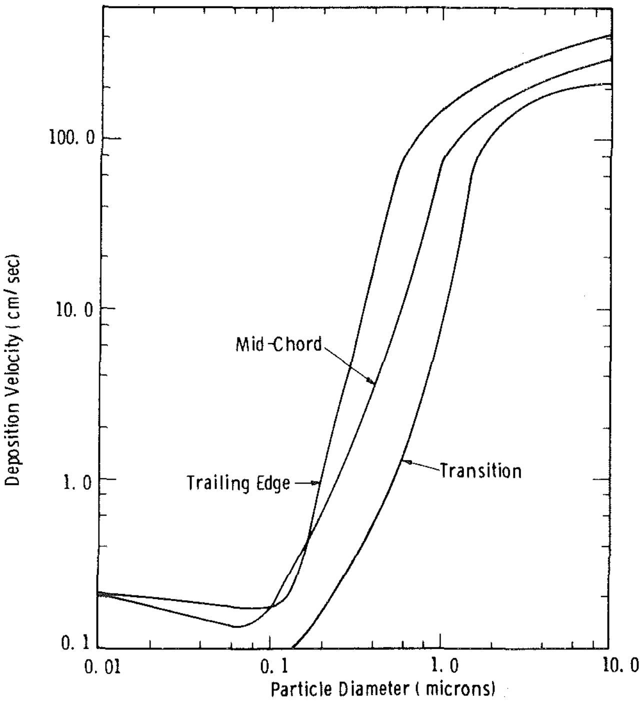

Fig. 8 Deposition velocities for rotor pressure surface

than deposition is expected to dominate on the pressure surfaces and suction surfaces at the vane and blade noses, except perhaps in the vicinity of the stagnation points where hard particles might embed in the surface for near normal impacts. Pressure surface erosion rather than deposition was, in fact, observed to dominate during cascade tests sponsored by DOE and conducted by General Electric at the EXXON PFBC pilot plant [6]. Consequently, the following will consider pressure surface deposition to be insignificant and will evaluate effects of suction surface deposition only.

Particle trajectories are generated for the above inertial impaction evaluations. Observations of those trajectories which just grazed the nose region (see Fig. 9 for 3 μm particle trajectories) reveals that particle inertia prevents larger particles from closely following the suction surface profile. Particles are deflected away from the suction surface boundary layer which becomes depleted of particles with diameters greater than about 1 to 2 μm. Particles above this size are not available to be delivered through the boundary layer to the suction surface by diffusion. This effect was seen during the GE/EXXON cascade tests for which virtually all particles in the suction surface deposits were observed to be smaller than about 1.5 μm in diameter. Consequently, the following suction surface deposition calculations will consider a particle size cutoff of 1.5 μm.

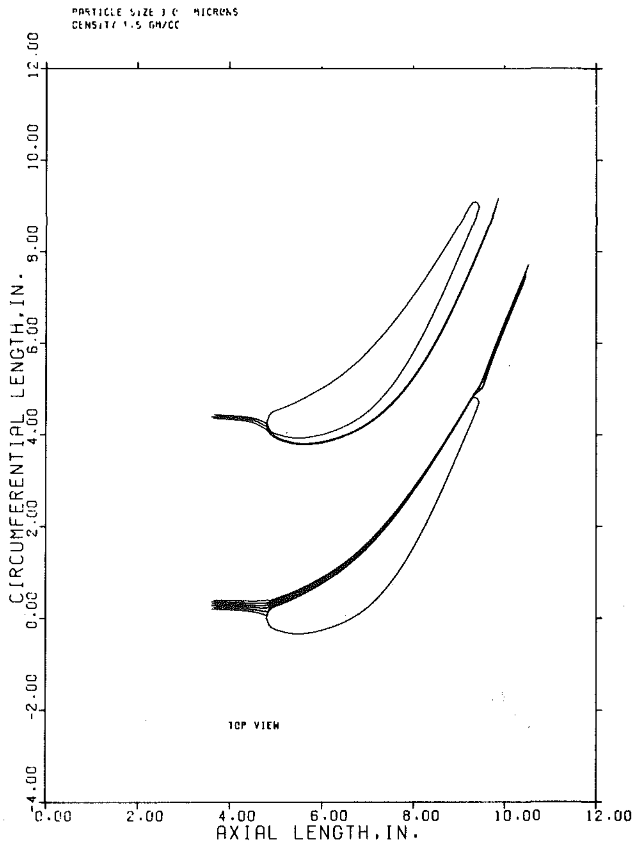

Fig. 9 Partical trajectories in stator, 3 μm particles

Arrival Rates Versus Cleanup System Performance. For a particle size cutoff of 1.5 μm, Figs. 10 and 11 give particle arrival rates (gm/cm^2 per 1000 hr) versus surface location on the stator and rotor suction surfaces of the 10:1 pressure ratio turbine. Arrival rates are shown for the three power plant/particle cleanup systems previously described.

Adherence Fraction

Using the particle arrival rates which have been obtained with a determination of the particle packing density in the deposit and particle adherence fraction (i.e., the net fraction of arriving particles that stay on the surface), deposit buildup rates for the turbine can be calculated. Values for the particle packing density and adherence fraction can be obtained from GE/EXXON cascade test data.

During the cascade tests a vane trailing edge suction surface deposit buildup of about $\frac{1}{8}$ in. was measured after a 250 hr test segment. The deposit consisted of loosely bonded particles and had the soft and fluffy appearance of fines collected by the third cyclone. Consequently, the third cyclone ash container density measured at 0.72 g/cc is considered to be the particle deposit packing density.

An approximate analysis using the gas velocities through the cascade passages and estimated cascade vane boundary layer thickness was used to estimate a value for particle arrival rates on the vane suction surface trailing edges. This value was determined to be about 5 percent higher than that for the 10:1 pressure ratio turbine stator. Using this particle arrival rate for the cascade vanes with the measured cascade deposit buildup rate and a particle packing density in the deposit of 0.72 g/cc, the particle adherence fraction for the cascade was determined to be 0.043, i.e., 4.3 percent of the arriving particles stayed at the suction surface trailing edges. This value of adherence fraction is considered to be appropriate to regions past mid-chord, but not the regions in the vicinity of transition. Aerodynamic forces

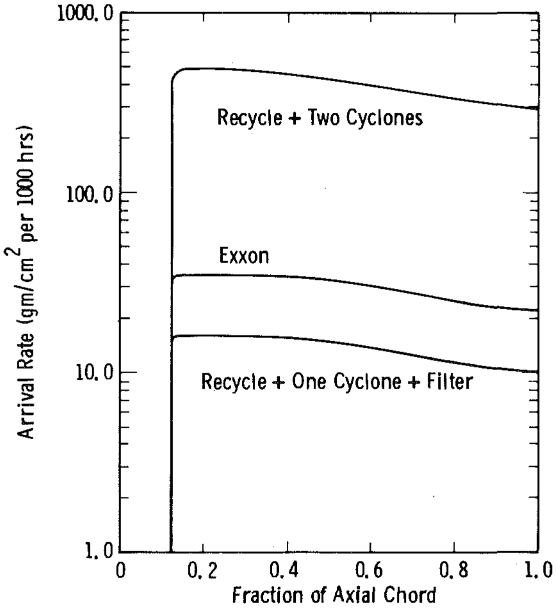

Fig. 10 Mass arrival rates for stator suction surface

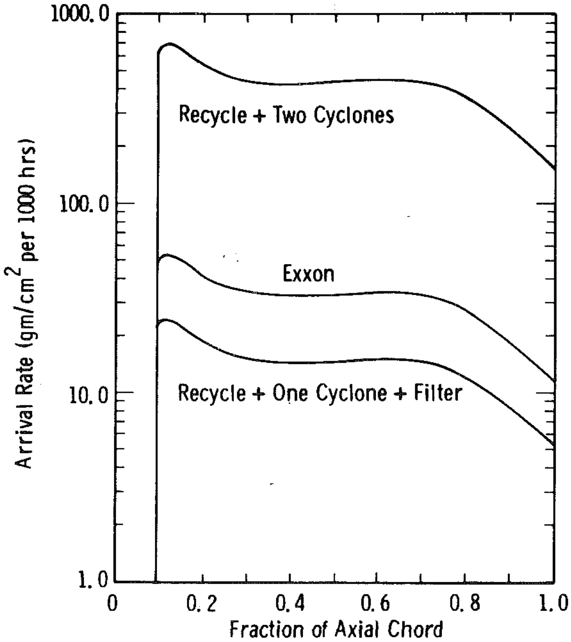

Fig. 11 Mass arrival rates for rotor suction surface

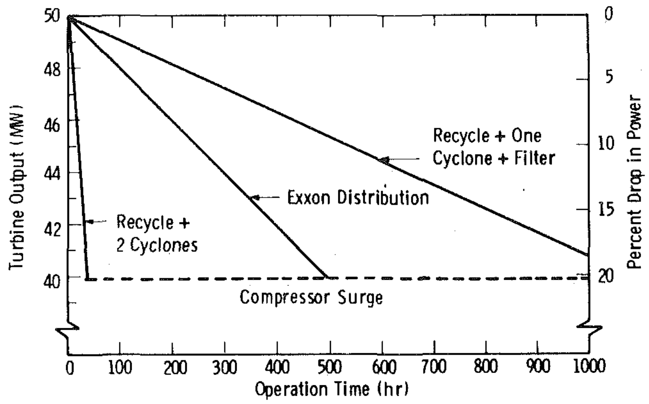

Fig. 12 Power drop due to deposition for 10:1 pressure ratio turbine

would prevent an abrupt increase in deposit thickness associated with the abrupt increase in arrival rates at transition. The GE/EXXON cascade suction surface deposit contours observed downstream of mid-chord suggest that the mechanism of particle removal may be turbulent bursts. These bursts can occur within the fluid sublayer regions near the surface and can detach and eject particles away from the surface [7]. The removal forces, area density of turbulent bursts and frequency of turbulent bursts all increase with mean surface shear stress.

The trailing edge particle arrival rates shown in Figs. 10 and 11 multiplied by the 0.043 adherence fraction give the mass/unit area buildup rate on the first vane and blade of the turbine. Division by the particle packing density of 0.72 g/cc gives the deposit thickness buildup rates.

Turbine Power Degradation

A primary degrading effect of deposition is flow blockage at the throats of the vane and blade passages. The percentage rate of passage closure is higher in the stator than the rotor for the turbine. Consequently, turbine power degradation was determined for flow blockage at the stator throat and is shown versus alternative gas cleanup systems in Fig. 12 for the 10:1 pressure ratio turbine.

The curve in Fig. 12 associated with the EXXON particle loading indicates that deposit removal every 250 operation hours is necessary for the 10:1 pressure ratio turbine to limit the drop in power to less than 10 percent.

Should cleanup efficiencies of the third cyclone stage for future utility power plants not reach the unexpectedly high values measured at the EXXON miniplant, deposit removal intervals could be much shorter than given above. For third cyclone efficiencies typically measured in small scale tests, Fig. 12 shows that a 20 hr deposit removal interval to limit power drops to less than 10 percent is predicted for the 10:1 pressure ratio turbine operating with a cleanup system consisting of a recycle cyclone stage plus two stages of cleanup cyclones.

Replacement of the final cyclone stage with a granular bed filter stage substantially decreases the deposit removal frequency. For the third stage filter, Fig. 12 shows that the power drop is limited to less than 10 percent by a 540 hr deposit removal interval.

Figure 12 indicates much higher maintenance frequencies than are usually required for utility turbines. However, loose suction surface deposits such as observed during the GE/EXXON cascade tests might possibly be dislodged during turbine startup or load variations of, if necessary, probably would be removed fairly easily with standard turbine maintenance techniques for deposit removal such as water washing on perhaps a modified form of nutshelling. Since these maintenance approaches might have to be conducted at turbine cranking speeds or operating conditions for which the compressor flow rate may be insufficient to sustain fluidization of the bed, deposit removal may be a significant power plant operational consideration.

The GE/EXXON tests were conducted at cascade inlet temperatures somewhat lower than 871°C (1600°F). Consequently, the above results appear to be appropriate to first stages of PFBC turbine with inlet temperatures less than 871°C (1600°F) for which observation of the loosely bonded suction deposits in the GE/EXXON cascade tests suggest particle attachment is due to such weak forces as Vander Waals (molecular) attraction with a minimal effect of molten subspecies from the ash bonding the deposits. However, at higher turbine inlet temperatures (perhaps above the 884°C (1623°F) melting point of Na_2SO_4) molten deposit bonding complexes might result in greater adhesion fractions, faster deposit buildup and turbine power degradation rates, and more tenacious deposits which are harder to remove. Should the primary bonding agent in the suction surface deposits from the GE/EXXON tests be molten subspecies rather than weak forces such as molecular attraction as suggested above, deposit buildup rates for turbine inlet temperatures below 871°C (1600°F) might also be sensitive to temperature in addition to trace element chemistry of the power plant feedstock.

Acknowledgments

Work performed on this project was funded by EPRI under the direction of William W. Slaughter, Fossil Fuel and Advanced Systems Division.

References

1 Moore, M. J., and Crane, R. I., "Aerodynamic Aspects of Gas Turbine Blade Corrosion," from *Deposition and Corrosion in Gas Turbines,* edited by A. B. Hart and A. J. B. Cutler, Halstead Press, New York, 1973.

2 Vermes, G., "Thermophoresis—Enhanced Deposition Rates in Combustion Turbine Blade Passages," ASME paper 78-WA/GT-1, 1978.

3 Menguturk, M., and Sverdrup, E. F., "Calculated Tolerance of a Large Utility Gas Turbine to Erosion Damage by Coal Ash Particles, " from *Erosion: Prevention and Useful Applications,* edited by W. F. Adler, American Society for Testing and Materials, special technical publication 664, 1979.

4 Nutkis, M. S., Bertrand, R. R., and Loughnane, M. D., "Hot Corrosion/Erosion Testing of Materials for Application to Advanced Power Conversion Systems Using Coal Derived Fuels," EXXON monthly technical report No. 32, Dec. 1978 for DOE contract No. EX-76-C-01-2452.

5 Keairns, D. L., Ciliberti, D. F., et al., "Engineering Evaluation of Hot Glass Clean-up Systems for Pressurized Fluidized Bed Combustion CTIU," Westinghouse Research Laboratories report to Argonne National Laboratories, contract No. 31-109-38-3566, Nov. 1976.

6 McCarron, R. M., Beltran, A., and Grey, D., "The Corrosion/Erosion Behavior of Some Gas Turbine Superalloys, Cladding, and Coatings in the Effluent from a PFBC Combustor," Conference on Advanced Materials for Alternate Fuel Capable Directly Fired Heat Engines, Castine, Maine, July 30 to Aug. 3, 1979.

7 Guven, H. R., "Deposit Removal in Turbulent Flows Due to Viscous Sublayer Activities," M. S. Thesis in Department of Mechanical Engineering, Bogazici University, Istanbul, Turkey, Mar. 1979.

DISCUSSION

1 Introduction

Daniel E. Rosner[1] **and Juan Fernandez de la Mora.**[2] R. A. Wenglarz's (RAW) assessment of ash deposition in a turbine downstream of a pressurized fluidized bed (coal) combustor (PFBC) [1] provides a timely summary of the neglected area of *mass* transfer in the gas turbine (GT) industry. While further details of RAW's procedures will be of interest, we focus attention here on: (*a*) recent advances in our understanding of particle mass transport; (*b*) parts of RAW's assessment which warrant re-examination in the light of (*a*); and (*c*) areas in need of further research. Our common goal is to increase the accuracy and generality of predictions. Attention is directed here at both *inertial* [2–4] and *thermophoretic* [5] particle deposition, and the relevant dimensionless groups. Details are available in the references cited below.

For reasons discussed below RAW's procedures may systematically *overestimate* deposition rates for particles above 0.5 μm dia (as in Region B, Fig. 1) and *underestimate* deposition rates for particles well below 0.1 μm dia (Region A, Fig. 1). These would not be compensating effects, however, since more than 50 percent of the *depositable* particle mass is above 0.5 μm dia, and less than 3 percent of the depositable particle mass is less than 0.1 μm dia. Thus, RAW's mass arrival rate estimates may be too high—indeed, we wonder whether this accounts for most (if not all) of the 4.3 percent (apparent) "adherence fraction"?

2 Inertial Effects on Particle Deposition at Low Overall Mass Loadings: Relevant Recent and Current Research

It is convenient to regard the local time-averaged mass arrival rate for a particular size class as the product:

$$-\dot{m}_p''(\text{arrival}) = \rho_e u_e \cdot \mathrm{St}_m\{x/L, \ldots\} \cdot \omega_{p,e}\{x/L, \ldots\} \quad (2.1)$$

where St_m is the *mass* transfer coefficient (Stanton number) and $\omega_{p,e}$ the local *mass* fraction for this particle size (class) at the edge of the boundary layer (BL). As recognized by RAW, particle inertia can influence *both* St_m and $\omega_{p,e}$, and in different ways.

2.1 Particle Phase Compressibility and $\rho_{p,e}/\rho_{p\infty}$. GT calculations are usually based on deterministic individual particle trajectory analyses, but for some purposes it is more fruitful to view the particles as comprising the "molecules" of a "fluid" phase which coexists in the same space as the host (carrier) fluid [6,7,8]. While the host fluid may exhibit nearly constant density behavior, the particle fluid may exhibit variable density,[3] i.e., for that size class ρ_p varies appreciably in space and that particle fluid may be said to be "compressible". Similarly, even when the host fluid may not "separate" from the blade, the particle fluids may. In general, one cannot assume that for any size class $\rho_{p,e}(x) = \rho_{p,\infty}$, i.e., the *local* mass loading $\omega_{p,e}(x)$ of particles of a given size class cannot be equated to that in the upstream gas. Downstream on the suction surface, RAW accounts for this by introducing the idealization of a sharp cut-off diameter (ca. 1.5 μm dia) above which no particles are (locally) present. But, even at subcritical Stokes' numbers, inertially induced particle phase "compressibility" influences deposition rates elsewhere, too—e.g., in the forward stagnation region and along the concave (pressure) surface of the blade there is an *inertial enrichment* of the local particle concentration [7,8], associated with local *increases* in deposition rate over that expected for equation (2.1) using $\omega_{p,e} = \omega_{p,\infty}$.

2.2 Eddy Impaction and the Anticipated Effects of Streamwise Curvature. Particle inertia depletes the availability of larger particles to the turbulent BL downstream on the suction side, but also *increases* the effective transfer coefficient $\mathrm{St}_m\{x/L, \ldots\}$ for those particles present, because of "eddy impaction"—i.e., particles entrained in eddies moving toward the wall are presumably "thrown" through the viscous sublayer, circumventing the slower alternative of, say, Brownian diffusion. Irrespective of *h*ow RAW includes this mechanism, it is known that on smooth, flat, uncooled surfaces such mass transfer data are reasonably well-correlated in terms of the dimensionless particle stopping time t_p^+ [3, 10], and St_m(eddy impaction) increases monotonically up to t_p^+-values near 20. However, above this value St_m plateaus, and evidently begins to decrease [3, 10], presumably due to the inability of the eddies to "get a handle on" sufficiently sluggish particles. This is an important feature which, under RAW's conditions, we would have expected to set in at particle diameters below 1.5 μm. A second feature of many GT applications, which may also contribute to an overestimate in the deposition rate of "large" particles (area B in Fig. 1) on the suction surface is the presence of appreciable *streamwise curvature* of GT blade surfaces. In view of particle inertia, this produces a "centrifugal drift velocity" of the "particle fluid" v_p(drift), given approximately by $[u(y;x)]^2 t_p/R$ (where $R \equiv$ prevailing streamwise *radius of curvature* and t_p the particle stopping time) directed *away* from the blade surface on the suction side ("centrifugal blowing"). Clearly, if this drift velocity evaluated at the particle stopping distance is not negligible compared to the host fluid rms fluctuating velocity, $v(\mathrm{rms}) \equiv \overline{(v'v')}^{1/2}$, responsible for ordinary eddy impaction, there should be a streamwise curvature effect on particle deposition rates by eddy impaction, in this case a reduction. For a more detailed treatment of such inertial effects, see [12]; however, we remark here that while $v_p(\text{drift})/v(\text{rms}) \ll 1$ for the "large" particle data of [4], streamwise blade curvature may appreciably reduce the suction surface deposition rates of ca. 1.5 μm particles under conditions such as those treated by RAW [1]. For particle

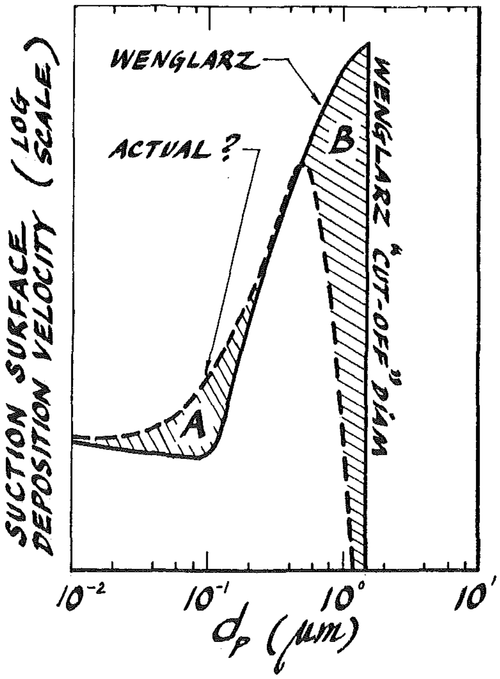

Fig. 1 Suction surface deposition velocity (or $u_e \mathrm{St}_m$) over the spectrum of particle sizes in a PFBC-GT application [1]

---

[1] Professor of Chemical Engineering, Department of Engineering and Applied Science; Yale University, New Haven, Conn. 06520.

[2] Post-doctoral Research Engineer, High Temperature Chemical Reaction Engineering Laboratory, Yale University, New Haven, Conn. 06520.

[3] Here ρ_p is *not* the average intrinsic density of an *individual* particle $(m_p/(\pi d_p^3/6))$.

sizes *below* the range dominated by eddy impaction a particle "centrifugal drift" effect on St_m remains in principle [12] but is negligible in this PFBC-GT application.

3 Thermophoretic Effects on Particle Deposition; Relevant Recent and Current Research

Since most of the aerosol mass in the PFBC application is centered near particles of ca. 1 μm dia, and current utility turbines operate with blades which are not actively cooled, RAW's neglect of *thermophoresis* in his fouling estimates appears reasonable. However:

(*a*) even blades not actively cooled operate somewhat lower than the recovery temperature of the combustion gas (a 20K temperature difference, ΔT, would not be uncommon, due to heat conduction through the blade root, etc.);

(*b*) even a small mass deposition rate of sub-0.1 μm particles could have a large effect on system performance, owing to differences in chemistry and melting point between small and larger particles (e.g., sub 0.1 μm droplets, down to individual vapor molecules, of molten salts are more corrosive and often provide a "glue" for binding the larger particles to the surface).

Thus, it may still be important to accurately predict the deposition rate of sub-0.1 μm dia particles, shown below to be appreciably influenced (ca. 3.7-fold augmentation near 0.1 μm) by the thermophoretic force which acts on them in the viscous sublayer. Since this effect assumes even greater importance for actively cooled blades [5, 13, 14], we briefly outline our recent approach and results [15–22].

Vermes [13, 14] correctly called attention to the importance of thermophoretic effects in GT applications involving *cooled* blades. However, his quantitative (particle trajectory) treatment cannot be defended in portions of the gas BL where eddy and/or ordinary Brownian diffusion also occur [19, 22]—in such regions it is more fruitful to adopt the abovementioned Eulerian particle phase continuum approach. Thermophoresis produces a transverse particle drift velocity $-\alpha_T D_p \partial \ln T/\partial y \equiv v_T$, where $\alpha_T D_p$ may be regarded the thermophoretic particle diffusivity [18, 20]. This "suction" acts *in concert with Brownian diffusion* enabling particles to cross the viscous sublayer. At small values of $\Delta T/T_w$[4] the dominant effect of thermophoresis is an augmentation of $\mathrm{St}_m\{x/L, \mathrm{Re}, \mathrm{Sc} \ldots\}$, by a factor dependent upon the group [15, 19, 20, 21]:

$$-B_T = (\alpha_T Le)_w \cdot \frac{\mathrm{St}_h}{\mathrm{St}_{m,o}} \cdot \frac{\Delta T}{T_w} \qquad (3.1)$$

Here $\alpha_T Le$ is the thermophoretic particle diffusivity/host gas *thermal* diffusivity ratio, and St_h is the *heat* transfer Stanton number. For particles of 0.1 μm dia and $\Delta T \approx$ 20K we estimate that in the present case $B_T \approx -3.6$. According to references [15, 18, 22] this will produce an St_m augmentation factor near[4] $B_T/[\exp(B_T)-1]$, or about 3.7-fold! By d_p as small as 0.01 μm the thermophoretic effect would be negligible (cf. Fig. 1, region A) at this assumed ΔT-value but appreciable for strongly cooled blades. For further examples of the importance of thermophoresis in appreciably augmenting particle capture in the size range ordinarily most difficult to capture, see [18, 21].

4 Concluding Remarks

A more comprehensive perspective is emerging on the relative roles of convection, Brownian diffusion, eddy diffusion, thermophoresis and particle inertia on small particle mass transport to surfaces, including quantitative methods describing their important *interactions* over the entire spectrum of particle sizes. This work needs to be extended in support of future GT developments and related technologies (e.g., heat exchangers, gas cleanup equipment). We mention the treatment of transpiration or film-cooled surfaces [25, 26], effects of streamwise curvature [12, 13], surface roughness, mainstream turbulence, particle re-entrainment, etc. This will require carefully articulated experimental and theoretical programs, with operating GT experience motivating relevant laboratory experiments [27–30]. We hope this discussion,[5] together with Wenglarz's analysis [1] and the references cited, clarify the important role of *mass* transfer in GT applications, and suggest accurate design procedures for future high performance-low maintenance combustion-driven gas turbines [31].

Additional References

1 Wenglarz, R. A., "An Assessment of Deposition in PFBC Power Plant Turbines," ASME JOURNAL OF ENGINEERING FOR POWER, This issue.

2 Friedlander, S. K., and Johnstone, H. F., "Deposition of Suspended Particles from Turbulent Gas Streams," I/EC *49*, pp. 1151–1156, 1957

3 Liu, B. Y. H., and Agarwal, J. K., "Experimental Observation of Aerosol Deposition in Turbulent Flow," Journal Aerosol Science Vol. 5, p. 155, 1974.

4 Parker, G. J., and Lee, P., "Studies of the Deposition of Submicron Particles on Turbine Blades," *Proceedings Institute Mechanical Engineers.* Vol. 186, pp. 519–526, 1972.

5 Nomura, M., Morishita, T., and Kan, S., "An Experiment of Deposit Formation on the Surface of an Air-cooled Gas Turbine Blade," *Proceedings 1977 Tokyo Joint Gas Turbine Congress*, 1977, pp. 566–573.

6 Marble, F. E., "Dynamics of Dusty Gases," *Annual Review of Fluid Mechanics*, Annual Reviews, Palo Alto, CA, 1970, pp. 397–446.

7 Fernandez de la Mora, J. and Rosner, D. E., "Inertial Deposition of Particles Revisited and Extended; Eulerian Approach to a Traditionally Lagrangian Problem," *Journal of Physicochemical Hydrodynamics*, Pergamon Press, New York, in press 1981.

8 Fernandez de la Mora, J., "Deterministic and Diffusive Mass Transfer Mechanisms in the Capture of Vapor and Particles," Ph.D. Dissertation, Yale University, Department of Engineering and Applied Science, Dec. 1980.

9 Fernandez de la Mora, J., and Rosner, D. E., "Effects of Inertia on the Diffusional Deposition of Small Particles to Spheres at Low Reynolds' Numbers," *Journal Fluid Mechanics* (submitted Mar. 1981).

10 Cleaver, J. W., and Yates, B., "A Sublayer Model for the Deposition of Particles from a Turbulent Flow," *Chemical Engineering Science*, Vol. 30, 1975, pp. 983–992.

11 Friend, W. L. and Metzner, A. B., "Turbulent Heat Transfer Inside Tubes and the Analogy Among Heat, Mass and Momentum Transfer," *AIChE Journal*, Vol. 4, 1958, pp. 393–402.

12 Rosner, D. E. and Fernandez de la Mora, J., "Effect of Small Particle Centrifugal Drift on Deposition Rates to Surfaces with Streamwise Curvature," (in preparation, 1981).

13 Vermes, G., "Thermophoresis-Enhanced Deposition Rates in Combustion Turbine Blade Passages," ASME JOURNAL OF ENGINEERING FOR POWER, Vol. *101*, 1979, pp. 542–548.

14 DeCorso, S. M. and Vermes, G., "Description of Program to Develop Combustion Turbine Design Guidelines Based on Deposition/Corrosion Considerations," *Proceedings of 1st Conf. on Advanced Materials for Alternative Fuel Capable Directly Fired Heat Engines* (J. W. Fairbanks, J. Stringer, eds.), Report #CONF-790749, 1979 pp. 287–300.

15 Rosner, D. E., Chen, B. K., Fryburg, G. and Kohl, F., "Chemically Frozen Multicomponent Boundary Layer Theory of Salt and/or Ash Deposition Rates from Combustion Gases," Comb. Sci. and Tech. Vol. *20* 1979 pp. 87–106.

16 Kohl, F. J., Santoro, G. J., Stearns, C. A. Fryburg, G. C., & Rosner, D. E., "Theoretical and Experimental Studies of the Deposition of Na_2SO_4 from Seeded Combustion Gases," *Journal Electrochemical Society* Vol. *126*, 1979 pp. 1054–1061.

17 Srivastava, R. and Rosner, D. E., "A New Approach to the Correlation of Boundary Layer Transfer Rates with Thermal Diffusion and/or Variable Properties," *International Journal Heat Mass Transfer*, Vol. 22, 1979, pp. 1281–1294.

18 Rosner, D. E., "Thermal (Soret) Diffusion Effects on Interfacial Mass Transport Rates," *Physicochemical Hydrodynamics*, Pergamon Press, New York, Vol. *1*, 1980 pp. 159–185.

19 Rosner, D. E., and Fernandez de la Mora, J., "Recent Advances in the Theory of Salt/Ash Deposition in Combustion Systems," *Proc. DOE/EPRI First Conference on Advanced Materials/Alternate Fuel Capable Directly Fired Engines* (Castline Me., 1979) CONF-790749, December 1979, pp. 301–330.

20 Rosner, D. E., "Mass Transfer from Combustion Gases," Paper No, 59a, Presented at the AIChE 73rd National Meeting, Nov 16–20, 1980 Chicago IL (Session on Combustion Fundamentals).

21 Rosner, D. E., Israel, R., and Zydney, A., "Effect of Thermophoresis on the Minimum Attainable Aerosol Diffusional Deposition Rate Before the Onset of Inertial Impaction," ACS/IEC-81 Winter Symposium on Aerosol Systems, January 26–28, 1981.

22 Rosner, D. E., Fernández de la Mora, J., and Vaziri, S., "Particle Transport Across Turbulent Nonisothermal Boundary Layers," ASME

---

[4] *More generally,* $\Delta T/T_w$ *is not small and actual augmentations will be less* than this because ω_p at the outer edge of the Brownian diffusion sublayer drops below $\omega_{p,e}$ [22, 23].

[5] This laboratory gratefully acknowledges the research support of NASA under Grants NSG 3107 and 3169, and AFOSR under contract F49620-76-C-0020. *The authors also acknowledge helpful discussions with R. Israel, S. Gokoglu, and A. Zydney (at Yale) and C. Lowell, F. Kohl, C. A. Stearns and S. Benford (at NASA).*

JOURNAL OF ENGINEERING FOR POWER, to be submitted 1981.

23 Goren, S. L., "Thermophoresis of Aerosol Particles in the Laminar Boundary Layer on a Flat Plate," *Journal of Colloid Interface Science*, Vol. *61*, 1977 pp. 77–85.

24 Friedlander, S. K., *Smoke, Dust and Haze—Fundamentals of Aerosol Behavior*, J. Wiley and Sons, New York, 1977.

25 Rosner, D. E., & Gokoglu, S., "Role of Thermophoresis in Offsetting the Fouling Rate Advantages of Effusion-Cooled Turbine Blades," in preparation, 1981.

26 Rosner, D. E., and Fernández de la Mora, J., "Aerosol Deposition Behavior on Gas-Film Cooled Solid Surfaces," in preparation, 1981.

27 Rosner, E. E., and Seshadri, K., "Experimental and Theoretical Studies of the Laws Governing Condensate Deposition from Combustion Gases," *Eighteenth International Symposium on Combustion*, in press, 1980.

28 Seshadri, K., and Rosner, D. E., "Optical Methods of Dew Point and Deposition Rate Measurements in Salt/Ash-Containing Combustion Gases 1. B_2O_3(l) Deposition Rates by the Interference Method and Comparison with Theory," *Amer Institute Chem Engineers Journal*, submitted, 1980.

29 Seshadri, K. and Rosner, D. E., "Polarization (Ellipsometric) Measurement of Condensate Deposition and Evaporation Rates in Salt/Ash-Containing Gases," Combustion and Flame, in press, 1981.

30 Rosner, D. E., Seshadri, K., Fernandez de la Mora, J., Fryburg, G. C., Kohl, F. J., Stearns, C. A., and Santoro, G. J., "Transport, Thermodynamic and Kinetic Aspects of Salt/Ash Deposition Rates from Combustion Gases," *Proceedings 10th Materials Research Symposium: Characterization of High Temperature Vapors and Gases*, (J. W. Hastie, ed. NBS Spec. Public. 561, U. S. Govt. Printing Office, October 1979, pp. 1451–1474.

31 Lowell, C. E., Grisaffe, S. J., and Levine, S. R., "Toward More Environmentally Resistant Gas Turbines: Progress in NASA-Lewis Programs," NASA TMX 73499 Presented at the *Third Conference on Gas Turbine Materials in a Marine Environment*, Bath, England, September 20–23, 1976.

Author Closure

The discussion by Professor Rosner and Dr. Fernandez de la Mora appears to be directed to both the general state-of-the-art of turbine deposition modeling and the specific application of the turbine deposition model to a PFBC turbine in the subject paper.

Their general comments recommended that additional work is necessary to quantify interactions between the various deposition mechanisms over the entire spectrum of particle sizes. This author certainly agrees with that viewpoint and that further developments will be necessary to adequately model all of the possible particle size ranges and deposition regimes that could occur in gas turbines.

The specific comments of Rosner and Fernandez de la Mora (and their Fig. 1) suggest that a substantial overestimation of PFBC turbine deposition rates may have resulted from neglecting two factors: (i) centrifuging of particles away from the blade suction surface due to particle flight on a curved path, and (ii) larger particles having sufficient inertia that they are not readily entrained in turbulent eddies. However, these factors were not neglected, but were incorporated empirically through the use of the GE/EXXON cascade test data to determine the particle cutoff diameter for the turbine deposition calculations. These factors were certainly in effect for those cascade tests and contributed to virtually all particles being smaller in diameter than about 1.5 μm in the cascade vane suction surface deposits.

As indicated by Rosner and Fernandez de la Mora, the particle centrifugal drift velocity component is inversely proportional to the prevailing particle flight path radius of curvature, R. Although the effect on suction surface deposits is significant at the vane nose and immediately downstream where R is relatively small, it is not expected to be important at the critical regions past mid-chord where deposit buildup constricts the passage throat and where the calculated buildup was used to determine the turbine power drops shown in Fig. 12. At these downstream locations, R is very large. Professor Rosner has informed this author that his comments were based on calculations using a value of R equal to the turbine vane chord. However, Fig. 9 shows that R is perhaps more than an order of magnitude greater than the chord at the critical downstream regions.

Professor Rosner has also kindly provided this author with the equations that he and Fernandez de la Mora used to evaluate $t_p{}^+$, which above a value of about 20 indicates a plateau eventually followed by a decrease in particle delivery by turbulent eddies. Since Rosner and Fernandez de la Mora did not have available all of the detailed boundary layer characteristics of the PFBC turbine for their calculation of $t_p{}^+$, this author applied their equation for $t_p{}^+$, which yielded a value of about 0.7 μm particle diameter at which turbulent eddy delivery starts to plateau. This compares to a peak delivery value of about 0.4 μm dia indicated in Fig. 1 of the discussion of Rosner and Fernandez de la Mora. If the peak in the dashed curve by Rosner and Fernandez de la Mora were shifted to the corrected value of 0.7 μm, the region A between that curve and the solid curve would be greatly decreased, especially if the plateau described in their discussion but not shown on their Fig. 1 were incorporated.

Only a minimal mass of particles smaller than 0.1 μm (Fig. 2 shows 2 percent down to 0.1 percent) are carried over from PFBC systems. Also, the particle delivery rates due to Brownian and turbulent diffusion for 0.1 μm particles are nearly two orders of magnitude lower than for 0.5 μm particles as shown in Fig. 5. Because of very low rates of delivery for the very small amount of particles in the 0.1 μm range, the 3.7 fold increase in delivery rate of 0.1 μm particles due to thermophoresis determined by Rosner and Fernandez de la Mora insignificantly affects the mass arrival rates on the turbine blade surfaces.

This author appreciates the discussion of Rosner and Fernandez de la Mora and has found their comments very informative. They have pointed out additional mechanisms affecting the observed depletion of larger particles in cascade and turbine blade suction surface deposits and have provided approximate means other than cascade test data for quantifying that depletion.

J. D. Shenker
A. R. White
B. D. Ziels
Diamond Power Specialty Co.
Lancaster, Ohio

Water Tempered Cleaning Medium for Sootblowers

Injection of relatively small amounts of water into the air or steam blowing medium of long retractable sootblowers can result in many benefits in initial cost, operational cost, and functional operation of sootblower systems. This paper explores the possibilities that this method of sootblowing presents, and includes experimental data on the operation of test systems. Thermal shock tests have been performed on superheater and waterwall tubes, and boiler tube samples have been analyzed after long term operation with combined air and water mist sootblowing.

Introduction

In the past decade, there has been a trend to larger utility boilers and more extensive use of low grade, high slagging and fouling coals. These trends have placed additional burdens on sootblower systems. Sootblowers are being used to span greater distances and are operated more frequently than in the past. Sootblower reliability and the ability to operate these blowers in a timely manner are more important concerns than ever before for maintaining boiler availability and efficiency.

One area of long retractable sootblower system design that affects the reliability of sootblowers and the frequency of sootblower operation is the availability of sufficient blowing medium for adequate lance tube cooling. The heat loads on lance tubes in the high temperature gas zones of boilers result in blowing medium requirements for lance tube cooling that are often significantly larger than would be required for cleaning. Many field tests have been conducted by Diamond Power to determine the heat flux to lance tubes for various boiler designs and under various operating conditions. The empirical data shows that the heat transfer to the lance tubes in the pendant sections of a boiler is a function of the fourth power of the local absolute gas temperature. This fourth power relationship results in much larger blowing medium flow rates for relatively few blowers in the upper furnace area and pendant section entrance than are required for the rest of the blowers.

This situation leads to several disadvantages, especially when air is used as the blowing medium. First, the capacity of the air compressor system must be sufficient to supply these relatively few high flow blowers. This results in higher capital costs. Secondly, the large demands on the air supply during the operation of these high flow blowers usually places severe restrictions on which other sootblowers can be blown concurrently with the high consumption blowers. This situation limits the flexibility of sootblower system operation. To compound the problem, the blowers in the high gas temperature zones are usually critical to the control of slagging and fouling throughout the boiler, and in many cases they need to be operated more often than other sootblowers. Sootblower reliability is also more difficult to achieve in these zones of the boiler. Large pieces of slag will often fall on lance tubes, and also a loss or reduction of blowing medium for any reason will cause rapid overheating of the lance tube in these areas of the boiler.

One method of reducing the aforementioned problems with sootblowers in the high gas temperature zones is to add water to the air or steam blowing medium. Relatively small amounts of water added to the air or steam blowing medium greatly reduce the flow requirement of the primary blowing medium. In fact, lower lance tube metal temperatures are achieved in this mode of operation than can be obtained with the high air or steam flow rates. We call this type of operation water tempering. The reason for the effective cooling of water tempering is that the water forms a film along the lance tube wall and greatly increases the inside heat transfer coefficient. The benefits of this system are: the possibliity of lower compressor system capital costs, more flexibility in blower operation, lower energy consumption, and longer lance tube life. The area of concern when using water tempering is the effect of the water on boiler tubes.

Considerable research has been done on the use of water tempering in the following areas:

1 Water and air flow requirements for effective lance tube cooling

2 The effects of this type of sootblowing on superheater and water wall tubes

3 Development of a reliable system to supply the water in a manner that would limit any detrimental effects to boiler tubes

The remainder of this paper addresses the results of the research and development in the three aforementioned areas.

Blowing Medium Requirements

Figure 1 shows an example of a utility boiler with gas temperature zones as specified for sootblower application. The air flow requirements for the various sootblowers are shown in Table 1. The conventional air flow rates either required for cooling or cleaning are listed along with the air flow rates and maximum water flow rates for water tempered operation. The required water flow rates in Table 1 are based on maintaining the enhanced cooling effectiveness of water tempered sootblowing at full blower extension. The flow rate can be varied during the blower travel, and in fact, there are benefits to this type of operation which are discussed later. The water flow requirements were determined in field tests with instrumented sootblowers.

It can be seen that a significant savings of air capacity can be realized for blowers in the higher temperature gas zones. The reduction in required air flow rates can be used to blow more blowers concurrently, thereby reducing cycle time, or it can be used to reduce the required air compressor capacity.

Contributed by the Power Division for publication in the JOURNAL OF ENGINEERING FOR POWER. Manuscript received at ASME Headquarters August 1, 1980.

Table 1 Comparison of conventional air flow rates and air flow rates with water tempering

Blower Number	Conventional Airflow (SCFM)	Tempered Airflow (SCFM)	Tempered Maximum Water Flow (GPM)
1, 2	10,500[1]	2,500	10
3-10	7,000[1]	2,500	7
11-16	3,900[1]	3,900[1]	—
17-22	2,300	2,300	—
23-26	2,200	2,200	—
27-30	1,450	1,450	—
31-34	1,150	1,150	—
35-38	1,150	1,150	—

[1] Air flow rate determined by lance cooling requirements.

Note: Conversion Factors: 1 SCFM = 0.472 L/s
1 GPM = 0.0631 L/s

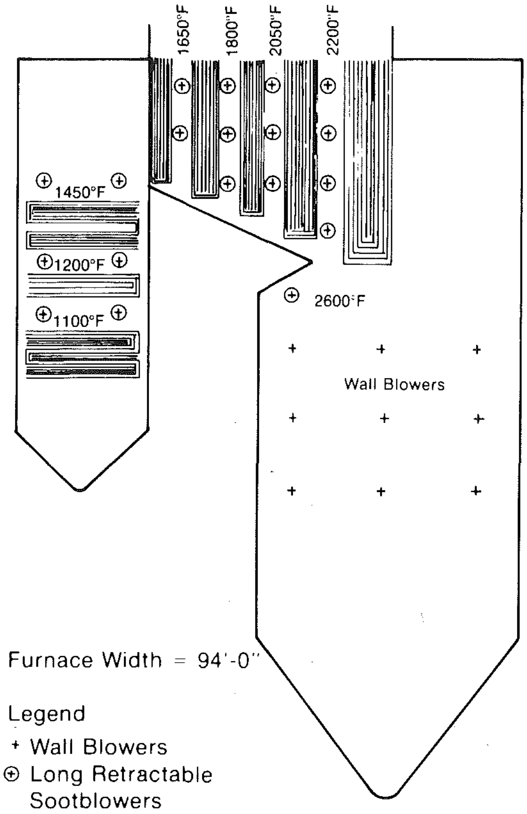

Fig. 1 Utility boiler with gas temperature as specified for sootblower application. Conversion Factor: 1 in. = 25.4 mm

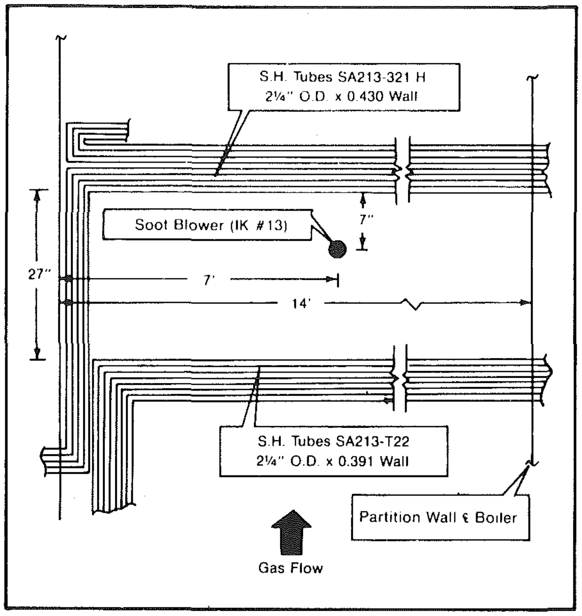

Fig. 2 Location of test sootblower in the boiler cavity at Allen Station. Conversion factors: 1 ft = 0.3048 m, 1 in. = 25.4 mm

Fig. 3 Surface of the 2.25 percent Cr—1 percent Mo superheater tube from Allen Station after 2400 quench cycles (16×)

Effects of Water Tempering on Boiler Tubes

Experimental water tempering systems were set up on two different boilers to assess the effects on boiler tubes. One system was used to clean superheater tubes, and the other system was used to clean water wall tubes. In each case, thermocouples were installed in the boiler tubes and tests were run to measure the boiler tube thermal transients with water tempered sootblowing. Sootblowing operating parameters, such as water flow, blower speed, nozzle diameter, and nozzle arrangement, were varied and the effects of these parameters on the boiler tube temperature were determined. The experimental water tempering systems were also operated for extended periods of time in the normal sootblowing sequence, and boiler tube samples were taken periodically.

One of the experimental water tempered systems was in operation at Allen Station of the Tennessee Valley Authority from July 1973 to June 1976. The boiler is cyclone fired with vertical gas flow throughout the boiler. A sketch of the boiler cavity in which the sootblower was installed is shown in Fig. 2. The blower location was chosen because the blower cleans both high temperature stainless steel and low alloy superheater tubes. The blower was operated in the regular blowing sequence with 4 gpm (15 L/min) of water added to 2500 SCFM air flow.

Tube samples taken from the vicinity of the test blower showed that the water tempered sootblowing was causing a surface cracking of the boiler tubes that is sometimes referred to as "alligator hiding." This condition is shown in Fig. 3. This effect has been seen before both with water sootblowing and with steam sootblowing where significant amounts of condensate were present. The State Electricity Commission of Victoria, Australia (SECV) has done considerable research on this phenomenon in conjunction with their studies on water blowing. Of particular interest were laboratory tests in which they repeatedly quenched metal specimens and periodically measured the depth of the surface cracks [1, 2]. These tests were done for different metals and metal temperatures. Two of the results from these tests have especially important implications for the use of water in sootblowers.

1 Crack growth rate decreases as the number of quench cycles increases.

2 The depth of the surface cracks increases with higher levels of tube metal temperature.

Our field data corroborate the trend shown in the SECV laboratory tests with regard to the decrease in crack growth rate with the number of quench cycles. Figures 4 and 5 show the field data from Allen Station plotted along with the most similar laboratory tests. It should

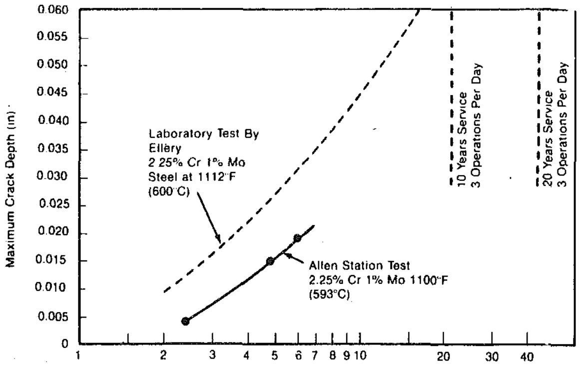

Fig. 4 Maximum crack depth versus the number of quench cycles for 2.25 percent CR—1 percent Mo steel tubes at 1100°F (xx°C). Conversion factor: 1 in. = 25.4 mm

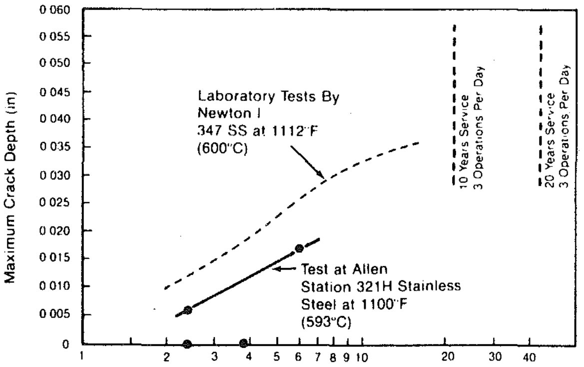

Fig. 5 Maximum crack depth versus the number of quench cycles for 321 H tubes at 1100°F (593°C). Conversion factor: 1 in. = 25.4 mm

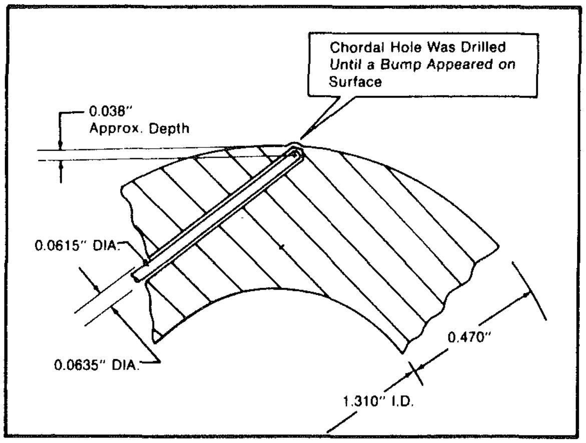

Fig. 6 Installation of thermocouples in superheater tubes. Conversion factor: 1 in. = 25.4 mm

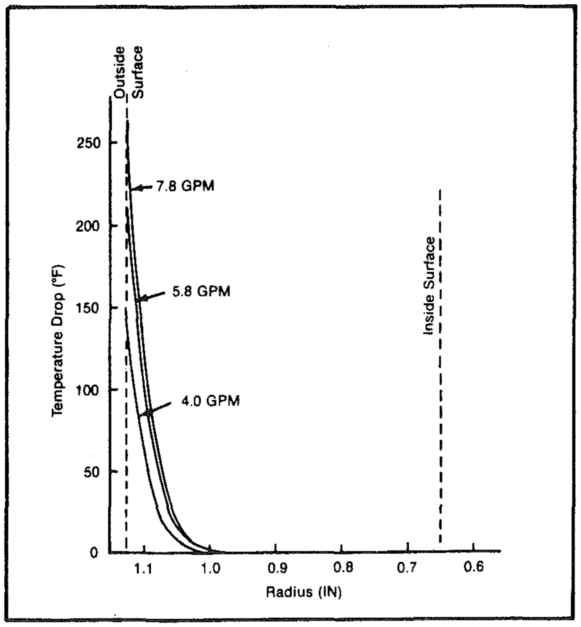

Fig. 7 Semi-empirical temperature drop profile in the SA213-T22 tubes at Allen Station. Conversion factors: 1 in. = 26.4 mm; °F = 9/5°C + 32

be noted that these graphs are semi-log plots. The graph in Fig. 4 is for 2.25 percent Cr-1 percent Mo steel at 1100°F (593°C). It can be seen that our field samples follow the trend of the laboratory samples although the crack depths are smaller in the field samples. The reason for the difference in magnitude is thought to be related to the severity of the quench. The SECV laboratory samples were quenched to the temperature of the water whereas the boiler tubes at Allen Station were not subject to as severe a temperature transient.

Figure 5 shows the same type of plot for the 321 H stainless steel tubes from Allen Station along with the 347 stainless steel tube SECV laboratory data. The sootblower was located only 7 in. (178 mm) from the stainless steel tubes. This situation resulted in some tubes being missed by the air-water jet and more severe temperature transients on the tubes that were impinged upon by the blowing medium. The tube samples that had no surface cracking were apparently missed by the air-water jet.

Thermal shock tests were conducted with thermocouples that were installed in the Allen Station boiler tubes. These tests helped explain the metallurgical observations and indicated what sootblower design parameters could be manipulated to minimize the level of thermal shock.

Small diameter sheathed thermocouples were installed in boiler tube sections as shown in Fig. 6. Prior to the installation of these tube sections in the boiler, the thermal response of the thermocouples was tested in the laboratory.

Fine gauge wire thermocouples were spot welded to the outside surface of the tubes adjacent to the chordal thermocouples and the response of the chordal thermocouples was determined by comparison with the surface thermocouples. A thermal model was developed to predict the response of the subsurface chordal thermocouple when the tube surface was thermally shocked. This computer model was used to obtain surface and subsurface temperatures.

The nature of the thermal transients in the boiler tubes, as determined from the thermal shock tests, did much to explain the metallurgical findings. The maximum temperature drop profile in the tube wall was found to be as shown in Fig. 7. It can be seen that the temperature gradient is very steep at the surface, but decreases rapidly at points inward from the tube surface. Thermal stresses can be relatively high at the tube surface depending on the magnitude of the temperature gradient; however, these stresses are restricted to a region very close to the tube surface. This temperature pattern explains why the growth rate of the surface cracks diminishes as the cracks start to extend into the tube.

The magnitude of the thermal transients on the boiler tube surface was found to be influenced by several factors. The factors identified were: (1) water flow rate, (2) speed of jet across the tube, (3) angle between the tube surface and the jet axis, (4) alignment of the boiler tube centerline and the jet axis, and (5) position around the circumference of the boiler tube.

The magnitude of the tube surface temperature drop was found to be an essentially linear function of the water flow rate. Some of the data are shown in Fig. 8 for a blower speed of 100 in./min (2540 mm/min) ⅞ in. (xx mm) dia nozzles. It can be seen that the alignment of the jet and the tube centerline has a very significant effect on the magnitude of the surface temperature drop. Off-center jets greatly reduced the thermal shock. It can also be seen in Fig. 8 that the stainless steel tubes showed greater temperature drops. Analysis of all the data indicates that this was mainly due to the slower velocity of the blowing medium jet across these tubes. The stainless steel tubes

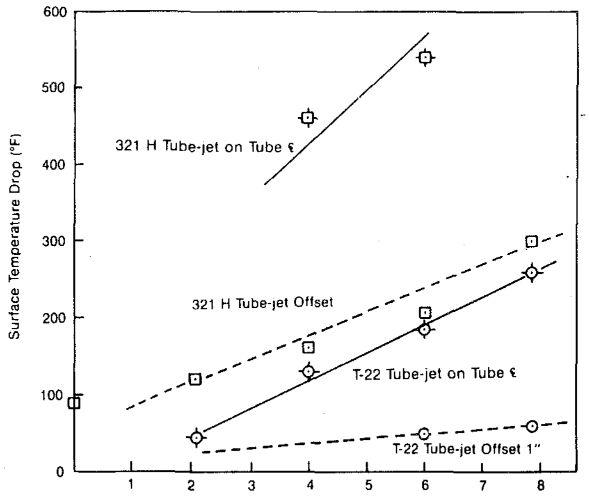

Fig. 8 Surface temperature drop versus water flow rate for SA213-T22 tubes at Allen Station. Conversion factors: °F = 9/5°C + 32; gpm = 3.79 L/min

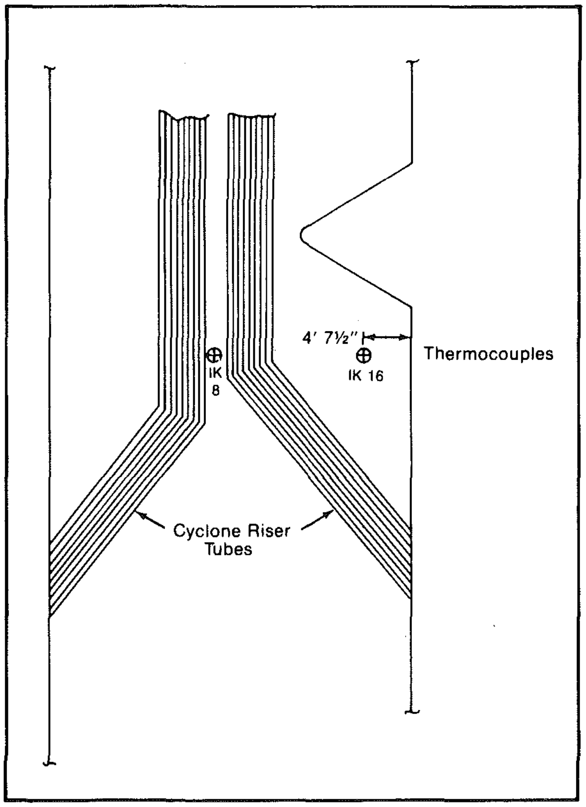

Fig. 9 Location of water tempered sootblowers at New Madrid Station. Conversion factors: 1 ft = 0.3.48 m; 1 in. = 25.4 mm

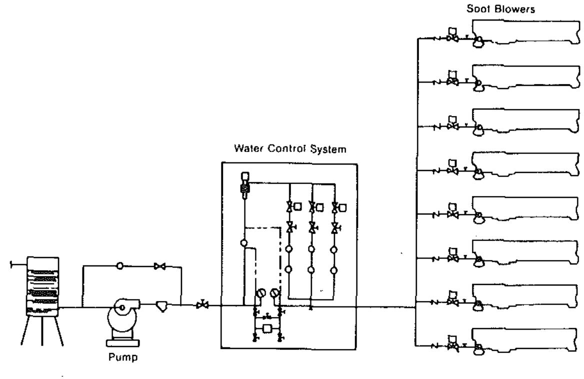

Fig. 10 Schematic of water piping for water tempering system

were closer to the sootblower, and therefore, the progression velocity of the jet along these tubes was less than along the low alloy tubes. This lower jet progression velocity results in a longer residence time of the jet on the tube.

Another experimental water tempering system was installed at New Madrid Station of Associated Electric Cooperative in 1975. Figure 9 shows the upper furnace area of this unit and the location of the test sootblowers. These sootblowers are cleaning furnace wall tubes and cyclone riser tubes. The tube metal temperature is only about 700°F (371°C) and the tubes are made of carbon steel.

Thermal shock tests were conducted with thermocouples installed in the furnace wall tubes near IK #16. The thermal transients measured in this location were quite low. The largest temperature drop measured in any test was 40°F (22°C). The reason for the temperature drops being so much lower than at Allen Station is thought to be due to the greater distance from the blower to the boiler tubes and the lower tube metal temperature.

A detailed analytical thermal fatigue analysis was not possible with the Allen Station superheater tubes because of the high but very localized stresses. However, the water wall tubes at New Madrid could be analyzed by more conventional procedures because the thermal transients were smaller and the tube walls were thinner. A two-dimensional computer model was used with the highest measured temperature transient as the boundary condition. The stresses that result from this analysis indicate infinite fatigue life using the guidelines of Section VIII of the ASME Boiler Code.

Water Tempering System Design

A schematic diagram for a water tempering system is shown in Fig. 10. The water control system has multiple branches with fixed orifices. The pump and orifices are sized such that the water flow rate in the branchlines is relatively insensitive to fluctuations of sootblower pressure. As a sootblower travels into the boiler, the water flow rate is increased in predetermined steps to maintain enough liquid water to cool the lance tube. During retraction of the blower, the water flow is lowered in steps. Limit switches on the sootblowers are actuated by the blower carriage which in turn actuates motor operated ball valves in the water control system to achieve the flow changes. One water control system can be used for blowers in different gas temperature zones by proper placement of the limit switches. It would generally be beneficial to have one water control system for each side of the boiler so that opposite blowers can be operated simultaneously.

This type of system has been proven to be very reliable. A system like this has been in operation at New Madrid Station since 1975, and very little maintenance has been required. The flow rate control is simple and stable.

Conclusions

Water tempered sootblowing shows promise of being a viable tool to achieve greater sootblower system flexibility, lower capital costs, reduced maintenance costs and reduced operating costs by decreasing the air or steam flow required for long retractable blowers. Field testing and analytical modeling have provided much information about the effects of this type of sootblowing on boiler tubes, and means to minimize detrimental effects have been developed.

Although some deterioration of the superheater tubes was observed in the form of surface cracking, the experimental data indicate that these surface cracks grow at decreasing rates with time. If the trend in surface crack depth observed at Allen Station is extrapolated 20 yr with three blower operations per day, the maximum crack depth is only about 0.050 in. (1.27mm). An extrapolation of this magnitude is subject to much uncertainty, but the main point is that the effects on boiler tubes are long term in nature, and can be monitored. In this manner, if any repairs should be necessary, they can be made during planned outages. Also, only the boiler tubes that are directly impinged upon seem to be affected. If tube shields were installed on the boiler tubes directly facing the sootblower, the effects of water tempering should be virtually eliminated.

The data indicate that even lower risks are involved when using water tempered sootblowing to clean water-cooled furnace wall tubes. Sootblowers under the nose arch are prime candidates for water tempered operation. These blowers require the highest cooling flows and are vulnerable to damage from falling slag. The lower air or steam flow requirements and the lower lance tube metal temperatures that result from water tempered sootblowing are of definite benefit in this application.

Acknowledgments

The authors would like to express appreciation to Associated Electric Cooperative and the Tennessee Valley Authority for their cooperation and to the personnel at Allen Station and New Madrid Station for their assistance in the field testing.

The work of H. W. Wahle and R. H. Best of the Babcock & Wilcox, Alliance Research Center, in the thermal and stress analysis of the boiler tubes was invaluable to the authors. Also the fine support provided by many DPSC Engineering personnel, particularly that of R. E. Huston and J. C. Cavinee, was a major factor in the success of this development and test effort.

References

1 Newton, J. D., "Thermal Fatigue and the On-Load Water Jet Cleaning of Superheaters," presented at IIW Public Session and Metals Technology Conference, Sydney, Australia, 1976.

2 Ellery, A. R., "Investigation into the Likelihood of Thermal Fatigue Damage to Furnace and Superheater Tubes Caused by On-Load Water Deslagging," ASME Paper No. 73-WA/CD-5, 1973.

R. Razgaitis
Assistant Professor.

D. A. Guenther
Associate Professor,
Department of Mechanical Engineering,
The Ohio State University,
Columbus, Ohio

Separation Efficiency of a Cyclone Separator with a Turbulence-Suppressing Rotating-Insert

This paper presents further experimental investigations with a cyclone separator. Specifically, an altered wall boundary condition, that of an internal rotating insert, as a technique which not only enhances the separating field, but, more importantly, diminishes the turbulence level within the cyclone is discussed. The data presented clearly illustrate that the proposed geometry is both turbulence suppressing and separation enhancing. Additional data presented for the efficiency with the insert show more than 10 percentage point improvement even for modest rotation rates. This improvement in the cyclone separator efficiency is significant and increases the potential of the cyclone as an air pollution control device.

Introduction

For the past several years there has been a continuing research effort at Ohio State University aimed at defining and attaining the limits of separation efficiency for cyclone separators [1–6]. The motivation for this effort is due to three factors: (1) where they can be applied, these separators are unexcelled in their virtues of simplicity and low cost; (2) the ultimate separation efficiency of cyclones with fine-particulate aerosols, we believe, has not yet been attained; and (3) new applications such as direct-cycle fluidized-bed combustors, will require new separation devices (perhaps of only modest efficiency) which are able to operate in environments naturally suited to advanced cyclone concepts.

Our current efforts are directed at examining the influence of altered wall-boundary conditions upon the velocity profiles and the separation characteristics of the cyclone. Specifically, we have modified a commercially available cyclone by the introduction of a rotatable cyclindrical insert several cm smaller than the inside diameter of the cyclone wall (nominally 91 cm or 3 ft) and as tall as the straight cylindrical section of the cyclone (150 cm or 5 ft). With our present facility, the insert may be rotated at constant speed in either direction at rates up to 375 rpm. The apparatus has been described in earlier reported work [6] and is shown in schematic form in Figs. 1 and 2.

Our investigation into the influence of the altered wall boundary condition upon cyclone performance has been in three phases. First, a theoretical perspective of the cyclone led to the conclusion that the ultimate efficiency of this separator concept had not yet been attained by any known device, that the mechanism for such an attainment would have to be via the suppression of wall turbulence eruption rates, and that providing a rotating insert would be an effective method of turbulence suppression and hence, of enhancing particulate separation [1–4]. The second phase of our work focused upon the measurement of various turbulence parameters within the cyclone-insert for a particulate-free flow; we found that, roughly speaking, the turbulence intensity (normalized upon various bases) was halved by rotation at 200 rpm in the favorable direction (defined as rotation in the same direction as gas motion) and doubled by the same rotation rate in the unfavorable direction when compared to the fixed-insert data [5–6]. Some typical results for velocity fluctuations in the helical plane (defined by the plane containing the radius and velocity vectors) normalized by the local helical velocity are shown in Fig. 3 for three different rotation rates (+ designating rotation in the same direction as air rotation) and for one air flow rate through the cyclone (82.1 SCMM) as a function of the radius normalized by the radius of the insert. Now, we are reporting the results of the third phase of our work for which actual particulate separation data as a function of insert rotation rate have been determined using coal fly ash entrained in ambient air.

A Perspective of Cyclone Separation Theories

Because cyclones have been used for more than a hundred years, paucity of separation theories is not a problem. However, it is not now, nor is it ever likely to be, possible to predict cyclone separation efficiency starting from first principles. The flow field within the cyclone is exceedingly complex and ranks as one of the most sophisticated fluid mechanical problems regularly encountered.

Theories have proceeded along two conventional lines: following the history for a single particle (or, occasionally a carefully characterized particulate distribution) and determining trajectories from injection to contact with the outer wall, or separation modelling by intuitive argument based upon dimensional analysis using simple fluid mechanics. We shall call these approaches trajectory analysis and parameter analysis, respectively.

Trajectory analysis which originally considered laminar-flow equations only [7–11], has reached a relatively sophisticated level in the past several years through the incorporation of turbulence models [12–14]. Computer simulation using this technique is presently being done [15]. One should not be misled, however, into concluding that the fluid mechanics of the cyclone is a closed science. The trajectory equations depend heavily upon several empirically based coefficients such as the number of fluid turns, the turbulence re-ingestion distribution, etc. If one has modelled the fluid mechanics properly, and it is often difficult to be sure, then these coefficients can be determined from a limited number of experiments and should then allow efficiency predictions for operating conditions, such as gas temperature

---

Contributed by the Power Division of THE AMERICAN SOCIETY OF MECHANICAL ENGINEERS and presented at the Industrial Power Conference, Houston, Texas, October 26–29, 1980. Revised manuscript received at ASME Headquarters August 6, 1980. Paper No. 80-IPC-Pwr-11.

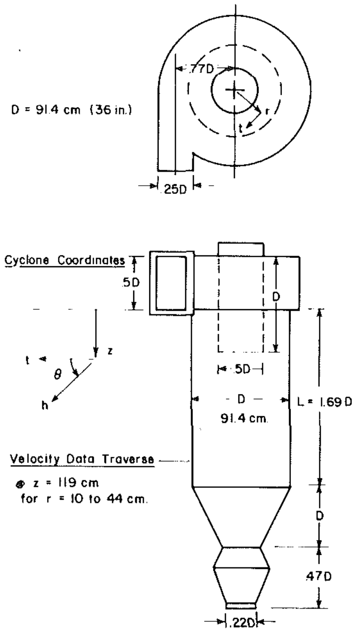

Fig. 1 Cyclone

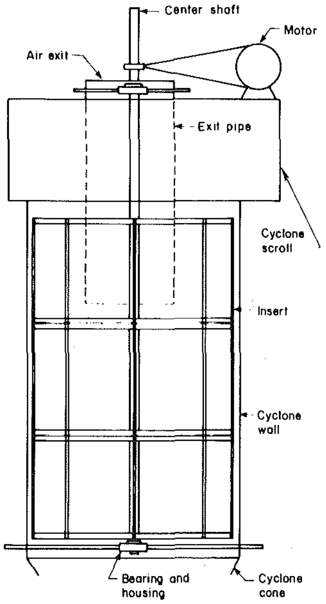

Fig. 2 Cyclone insert

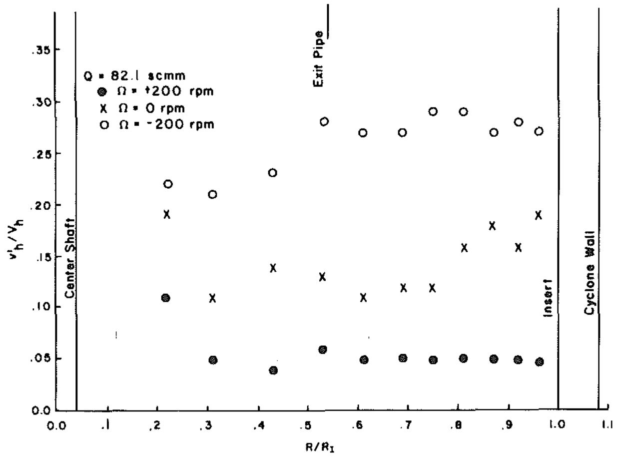

Fig. 3 Helical turbulence intensity

and injection velocity and for particulate conditions, such as density and diameter, which have not been experimentally examined. Further, one would hope that these predictions could be extended to geometries substantially different from those used to obtain the original family of coefficients. There are many equations based upon this analysis in the literature [16–17].

The perspective of parameter analysis, which also has a long history [18–21], is one which we shall adopt here. Our purpose in doing so is to illuminate what we feel to be the salient fluid-mechanical feature of the rotating insert. In simplest terms, we could view this as a two-parameter problem wherein the dependent variable, the separation efficiency, is a function of a single independent parameter, the separation number.

$$\eta = f(S) \tag{1}$$

where S represents a single fluid-mechanical/particulate grouping which characterizes the separation process. The simplest view of the ingredients that must comprise S is that the separation occurs as a result of the balance between the centrifugal force caused by the particulate being carried along approximately circular fluid streamlines and the retarding drag force caused by the particulate phase radially crossing the fluid streamlines. If one assumes spherical, small particulate (so that the particulate Reynolds number is less than 3 or so, allowing Stokes' drag model), and circular streamlines, these two competing forces may be expressed as

$$F_c = \left(\frac{\tilde{\rho}\pi\tilde{d}^3}{6}\right)\left(\frac{\tilde{V}_\theta^2}{r}\right) \tag{2}$$

$$F_d = 3\pi\mu\tilde{V}_r\tilde{d} \tag{3}$$

where the tilda superscript designates particulate phase properties (density, diameter, tangential and radial velocities), r the instantaneous radial position of a particle, and μ the medium viscosity.

Since fine particulate respond rapidly to their environment, these two forces are in approximate equilibrium throughout separation process. Thus, solving equations (2) and (3) for the separating velocity yields

$$\tilde{V}_r = \frac{\tau\tilde{V}_\theta^2}{r} \tag{4}$$

where the usual definition of relaxation time, τ, has been invoked ($\tau \equiv \tilde{\rho}\tilde{d}^2/18\mu$). This formulation is unsatisfactory as the root of a dimensionless parameter because its value varies throughout the cyclone. If we attempt to express the tangential velocity in terms of a more-basic quantity we find that

$$\tilde{V}_\theta|_{SB} = r\omega \tag{5}$$

$$\tilde{V}_\theta|_{PV} = \Gamma/2\pi r \tag{6}$$

where SB designates solid body rotation and ω the associated rotation rate and PV identifying potential vortex motion with Γ representing the circulation. Confined vortical flows can be approximated as SB motion in the core region and PV motion in the outer annular region (although the data for cyclones show a much flatter velocity profile than this model suggests). If one assumes that the separation process is dominated by the behavior within the PV region, then one can write

$$\tilde{V}_\theta|_{PV} \cong \frac{aR_iV_i}{r} \tag{7}$$

where the subscript i refers to the mean injection conditions of the inlet scroll and the circulation has been modelled as being constant fraction, a, of the injection circulation.

Now, it would be expected that the separation efficiency would increase with increasing $\tilde{V}_r$ for a fixed particulate residence time (which is determined by V_i and the cyclone geometry), and that it would decrease for decreasing residence time for a fixed $\tilde{V}_r$. Further, since the particulate phase is injected at value of r near the cyclone radius (R) we will assume that $r \cong R$. This leads one to postulate that the separation parameter for the cyclone is given by

$$\eta = f(S) = f\left(\frac{\tilde{V}_r}{\tilde{V}_\theta}\right) = f\left(\frac{\tau a V_i}{R}\right) \tag{8}$$

By analogy to the Deutsch-White equation for electrostatic precipitators, this equation may be reformulated to account for the effect of continuous redistribution of unseparated particulate due to wall turbulence as

$$\eta = 1 - \exp\left[-f\left(\frac{\tau a V_i}{R}\right)\right] \tag{9}$$

Although much more sophisticated versions of this approach exist in the literature [14–21], our purpose is served by the above equation. The three main ingredients determining efficiency are accurately portrayed: inlet velocity (usually expressed in terms of the volumetric flow rate, Q), cyclone radius, and particulate diameter (within τ).

The crucial and erroneous conclusion which can be drawn from equation (1) is as follows: For any specified efficiency desired, say 0.99, $f(S)$ may be determined (e.g., 4.61); then, after some testing to determine a proper functional dependency of f upon S (and a simple linear relationship is often adequate) and of a suitable value of a, then for any given particulate and medium the necessary V_i for a given R or the necessary R for a given V_i may be found. The critical defect in this method is the missing effect of observed decreases in efficiency for increases in V_i or decreases in R beyond certain optimum values. The mechanism for explaining this important phenomenon is missing from equation (9) and all known published correlations.

We believe that this behavior or regression of η for increasing S occurs because of the influence of turbulence bursting in the near wall region which is always present for high Reynolds number flows but is particularly enhanced for flows by concave surfaces such as the outer wall of a cyclone. This effect greatly alters the separation mechanics in the near-wall region [12]. We are then led to postulate that

$$S = f\left(\frac{\tau a V_i}{R}, \frac{\tilde{V}_r}{\hat{V}_r}\right)$$

where it has been recognized that $\tilde{V}_r$, which is the relative outward particulate motion, may be significantly affected by some mean, turbulence-induced, inward velocity due to rapid, energetic bursting (represented by $\hat{V}_r$).

There are two important points to be made. First, this added parameter, $\tilde{V}_r/\hat{V}_r$, can be expected to be relatively unimportant for large particulate diameters because $\tilde{V}_r$ is much larger than $\hat{V}_r$. For small diameters $\tilde{V}_r/\hat{V}_r$ becomes small and in the wall region this ratio can approach one and for sufficiently high V_i or small R can even become less than one, accounting for the observed regression in efficiency. Secondly, $\hat{V}_r$ can be expected to be dependent upon V_i and R as follows

$$\hat{V}_r = \phi(V_i/R) \tag{11}$$

based upon the recognition that the wall turbulence bursting rate (frequency, size, concentration, and intensity of bursts) will be dependent upon the Reynolds number of the flow near the wall (thus V_i) and the radius of curvature of the concave surface which is known to be an important parameter of bursting [22–24]. In an earlier paper [6] we suggested that the Reynolds number of a cyclone might be characterized by the grouping $Q/\nu D$ where Q is the volumetric flow rate ($= V_i A_i$), ν the dynamic viscosity of the medium, and D the cyclone diameter. Since this relationship has the form suggested by equation (11), we may postulate that

$$\frac{\tilde{V}_r}{\hat{V}_r} = g\left(\frac{\nu R}{V_i A_i}\right) \tag{12}$$

By substituting this concept into equation (9), we obtain

$$\eta = 1 - \exp\left[-f\left(\frac{\tau a V_i}{R}\right) g\left(\frac{\nu R}{V_i A_i}\right)\right] \tag{13}$$

where g designated the functional dependence of η upon the reciprocal cyclone Reynolds number.

Equation (13) provides a plausible and, we believe, phenomenologically correct characterization of cyclone efficiency (apart from geometrical scaling effects). The salient feature of this relationship is the counter-productive nature of attempts to increase efficiency by increasing V_i or decreasing R.

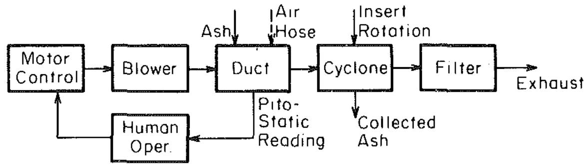

Fig. 4 Block diagram of facility

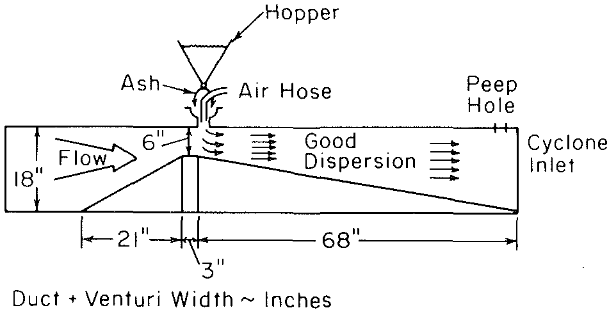

Fig. 5 Fly ash feeding system

The obvious purpose of this line of reasoning is the identification of the physical limitations to high efficiencies for fine particulate separation and, naturally, strategies to circumvent these limitations. The traditional line of work has been to augment the f function in equation (13)—the enhancement of the separation potential. The Aerospace Research Laboratory of the USAF (no longer in existence) examined supersonic cyclones having separation accelerations in excess of 100 million times gravity without achieving the sought-for high efficiencies [2,25–36]. We believe the proper approach is to enhance separation by the suppression of the g function in equation (13).

The reason why a rotating insert can be such a suppression technique has been discussed in earlier work [2–3]; the turbulence data reported [5–6] and some typical results are shown in Fig. 3. Our present data, efficiency as a function of rotation rate with all other independent variables fixed, primarily reflect the sensitivity of η to suppression in g via increased insert rotation. As our earlier hot-wire data showed, although the insert rotation also caused an increase in V_θ, the effect was surprisingly small; the most important effect was the uniformly lower turbulence-levels. Thus, rotation tends to increase the effective f function (because the relative conversion of inlet circulation to the circulation experienced in the annular region with the cyclone is increased by the insert's rotation) and to substantially increase the g function—two simultaneous, positive improvements which are reflected by the data showing dramatic increases in efficiency for relatively modest levels of rotation.

Experimental Facility and Procedure

A block diagram of the facility is shown in Fig. 4. The blower used is a squirrel cage type and has a capacity of 170 SCCM (6000 SCFM) at 3200 Pa (13 in. water). The outlet duct of the blower is 0.41 m (16 in.) dia. The flow rate was measured by the use of a calibrated pitot static probe within this round duct. A transition section was needed to convert this duct to the rectangular dimensions of the cyclone scroll (23 by 46 cm, or 9 by 18 in.). The particulate feeding system ingested the fly ash into the top of this rectangular duct.

The feeding system shown in Fig. 5 consisted of a rectangular hopper with steeply sloped sides providing a storage volume of approximately 57 liters (2 cu ft). A screw, in the form of a wire coil, within a pipe section at the bottom of the hopper was used to provide a controlled feed rate of particulate into the cyclone air supply. A variable speed motor was used to drive the screw to provide an approximately uniform particulate loading to the cyclone of 23 g/m^3 (10 grains/ft^3) throughout the testing time. The feed system was designed so that the operator was able to visually monitor the feed rate to assure that the natural tendency of fly ash to hang up within the hopper did not occur. Flow visualization within the rectangular duct revealed that the particulate was uniformly and rapidly dispersed into the air providing a typical cyclone inlet condition.

The experimental procedure began by sifting the fly ash through a 12 by 14 mesh screen by hand in order to break up large clumps that had accumulated. The ash sifted easily and did not reform into clumps during the experimental handling. The ash was mechanically separated to determine its size distribution. The method used was a series of decreasing sized sieves placed on a Ro-Tap machine for 15 min according to ASTM standards. The screen size ranged from 50 to 325 mesh (297 to 73 μm). The results are listed in Table 1. Note that almost all the particulate was smaller than the smallest screen or less than 43 μm (additional data are in the results section).

Table 2 presents the specifications of the coal used and a chemical analysis of the fly ash. The powder was weighted into 14 to 18 kg (30 to 40 lbm) quantities and put in the feeding hopper. The blower was then started and taken up to speed at a moderate rate until a steady reading was obtained at the pitot tube manometers. If rotation was to be used this would be done simultaneously with blower start-up as each mechanism affected the other. Insert speed was first checked by stroboscope. This proved to be inaccurate and difficult so a Hasler speed indicator was substituted.

Once the steady state was achieved at both the insert and pitot tube, the particulate feed motor was switched on. The dust concentration was calculated between 17 and 25 g/m^3 (7.4 and 10.9 grains cu ft). At first the vibrators seemed necessary to prevent bridging or arching in the ash hopper, but an occasional rap with a leather hammer proved sufficient to obtaining continuous feeding. Continued operation was maintained until the feeder completely emptied. This resulted in runs from 4 to 7 min. The blower and insert were allowed to continue for 2 to 3 min before they were turned off. The ash collected in the bag was then weighed to determine collection efficiency.

At high flow rates and insert speeds the partial vacuum usually present at the duct inlet was lost, causing the ash to puff back out. The lost dust was carefully collected and substracted from the input weight before calculating the efficiency. This problem was also solved by modifying the feeding system during later experimentation.

The cyclone exhaust was channeled through a 41 cm (16 in.) dia duct to an oil impregnated fiberglass filter. This filter was cylindrical with a solid top and bottom. The inlet was at the top and the dimensions were approximately 1.2 m tall (4 ft) and 0.9 m (3 ft) in diameter.

Table 1 Size distribution of fly ash used

Mesh Range	Size Range (micron)	Weight (gram)	Percent
50–100	297–147	0.65	0.5
100–150	147–104	2.25	1.8
150–200	104–74	0.13	0.1
200–325	74–43	20.38	16.0
+325	<43	103.96	81.6
			100.0

Table 2 Coal and fly ash analysis

Ash Analysis, percent	Typical	Range
Phosphorous pentoxide P_2O_5	0.28	0.08 to 0.36
Silica, SiO_2	26.49	23.53 to 40.76
Ferric oxide, Fe_2O_3	41.47	19.84 to 55.0
Alumina, Al_2O_3	21.56	14.35 to 24.17
Titania, TiO_2	0.98	0.60 to 1.12
Lime, CaO	3.53	0.80 to 9.13
Magnesia, MgO	0.85	0.15 to 2.98
Sulfur trioxide, SO_3	2.21	0.43 to 8.44
Potassium oxide, K_2O	0.84	0.84 to 2.20
Sodium oxide Na_2O	0.81	0.08 to 0.81
Undetermined	0.98	0.10 to 1.70
	100.00	

During early runs with the insert speeds ranging from 0 to 300 rpm, it was recognized that ash was holding up somewhere in the system. This was determined by observing that efficiencies initially dropped off contrary to expected results. When the blower was restarted anywhere from 1.5 to 4.5 kg (3 to 10 lbm) of powder was released into the collection bag. Since there was no accumulation in the feed duct, it was suspected that the powder was hanging up in the cone. Striking the cone side of the collector with a block of wood in a constant manner caused the dust to be released. This was done after every run after the blower and insert were turned off. All the data reported here were obtained by this method. Further, since all the runs were consecutive, any loss of collected mass from an earlier run (leading to a reduced η) would show up as an increased mass later (leading to a larger η). Thus, we believe that the data accurately characterize the separation potential of the cyclone.

This exact cause of dust hanging up is not presently known. The radial pressure gradient was observed to increase with rotation and was shown by the empty collection bag being pulled into the cyclone by a vacuum. Finally, for the case with no insert rotation the pressure at the collection bag was positive, as shown by the bag expanding like a balloon. Attempts at taking data with insert rotating in the unfavorable direction were unsuccessful as the torque required at the relatively high air flow rates used here exceeded the capacity of the belt/pulley system.

Results and Discussion

The separation data presented here were taken in two periods. The fly ash used was identical for all runs as given in Tables 1 and 2, and in approximately the same concentration (23 g/m^3) during each run and between runs. The flow rate for all these data was also constant at 110 m^3/min (3900 SCFM) which is at the upper end of the manufacturer's recommended operating range of 82 to 113 m^3/min (2900 to 4000 SCFM) for an unmodified cyclone. This flow rate corresponds to an inlet duct Reynolds number of 4.9×10^5 (based upon a 30.5 cm hydraulic diameter) and to a cyclone Reynolds number (defined as $Q/\nu D$) of 1.2×10^6. All geometrical variables were kept constant.

The only independent variable which has been examined to date is the rotation rate. During the first data period, the maximum allowable rotation rate was 300 rpm due to the onset of excessive vibration. After modification of the insert and cyclone support structure (which, we believe, did not affect the separation dynamics) we were able to attain rotation rates of 375 rpm.

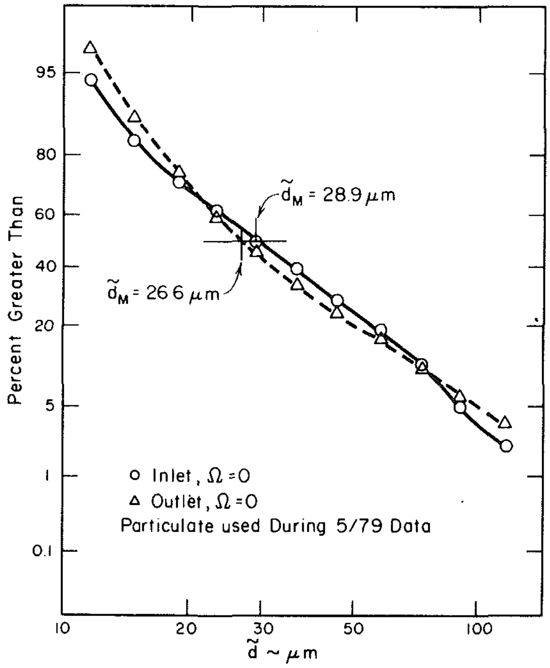

Fig. 6 Particulate distributions for no rotation

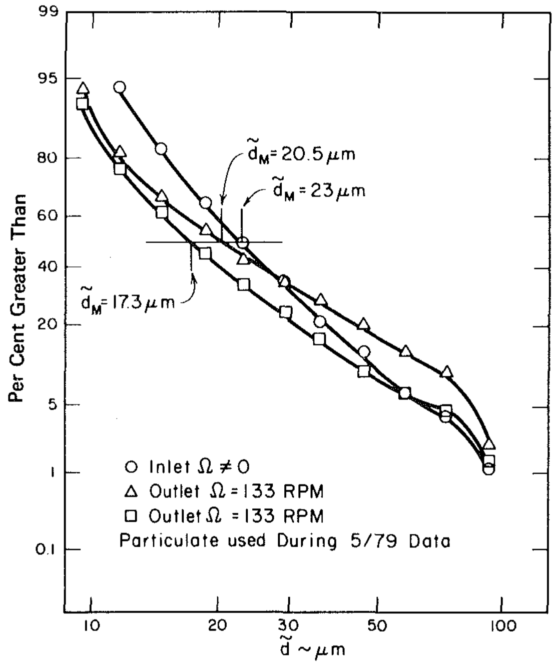

Fig. 7 Particulate distributions with rotation

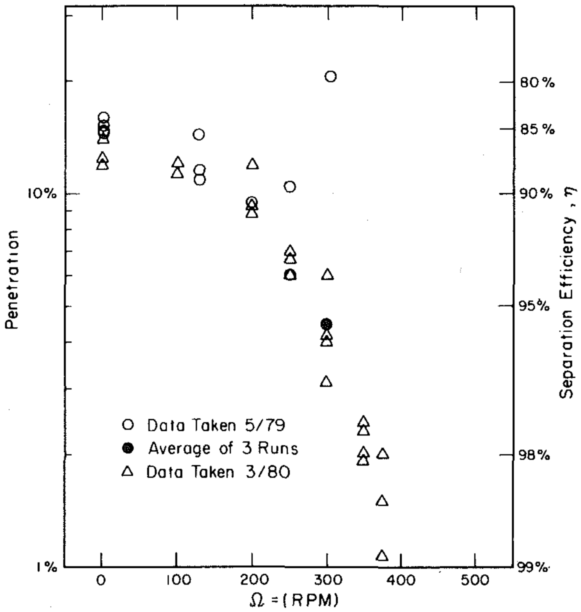

Fig. 8 Separated efficiency data

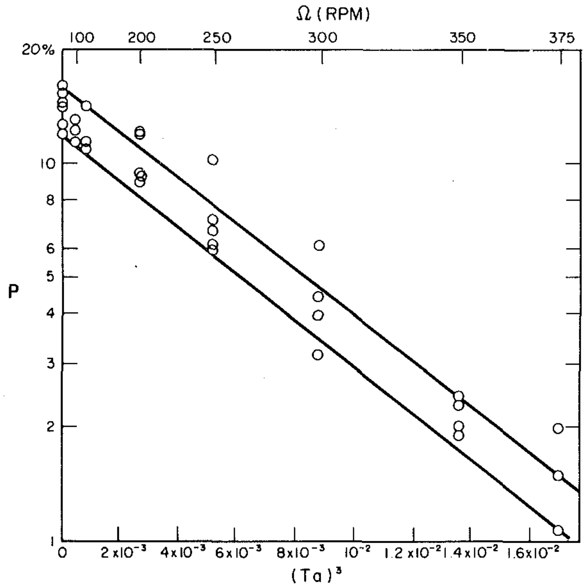

Fig. 9 Separation efficiency corrolation

During the first data period, a Coulter counter analysis was performed by an outside laboratory using a Model TA-II with Isoton II as the electrolyte counting more than 30,000 particles in 16 data channels from 4 to 161 μm. Two samples analyzed for the inlet and outlet distributions for the no-rotation case are shown in Fig. 6 using probability-logarithmic coordinates. The remaining three samples that were analyzed are shown in Fig. 7 and provide the inlet distribution and two outlet distributions for a rotation rate of 133 rpm. Comparing these two figures it may be seen that one of the apparent effects of rotation is to skew the size distribution curve, although the effect is not dramatic.

The penetration data, defined as 1-η, are shown in Fig. 8 for both periods of data as a function of rotation rate. One of the data points, shown as a solid circle, is highlighted to show some of the difficulties of the data-taking procedure. Because the fly ash escaping from the cyclone was collected on a large filter it was impractical to recover and complete the mass balance. During our preliminary runs, we observed that fly ash tended to hang up within the cyclone. This can be seen by examining the following three data runs which were taken consecutively on the same day under identical conditions:

Run	Input Mass (lbm)	Collected Mass (lbm)	η (percent)	P (percent)
1	26.0	25.1	97	3
2	28.3	24.1	85	15
3	32.8	34.1	104	−4

By simply adding the three input and output masses we believe a very good measure of efficiency, here 95.6 percent, can be obtained; this particular data point is shown by the solid circle on Fig. 8. After experimenting with various rapping procedures we were able, we believe, to eliminate this effect upon our data. Two further points should be noted: (1) Any hang-up of particulate *lowers* our claimed efficiency as that mass missing in the collection hopper is presumed lost out the top, and, (2) our more than 30 runs were sequential so if any hang-ups occured it would have shown up in some later run giving us efficiencies greater than 100 percent, which did not happen.

Since solid-body rotation systems are usually described in terms of a Taylor number, we have sought to develop a correlation between the rotation rate expressed as some form of the Taylor number and the separation efficiency. We are suggesting the following:

$$\tilde{T}a = (\Omega^2 D \tilde{d}^3/\nu^2)^{0.5} \tag{14}$$

which includes the effect of the separation field and the inlet particulate diameter (here, 23/μm). Since these data are only for variable rotation rate, the exact grouping of the Taylor number is not presently established. In Fig. 9 we have shown the efficiency data of Fig. 8 versus the cube of the above Taylor number. The straight lines drawn on this figure encompass 28 of the 35 data points (or 30 out of 37 if one counts the solid circle data point as 3 points). The wild point at 300 rpm in Fig. 8 has not been shown in Fig. 9.

Clearly there is a strong suggestion that the efficiency can be correlated in terms of the third power of $\tilde{T}a$ (or Ω). Using the above data, we find that

$$\eta = 1 - \exp\left[-f\left(\frac{\tau a V_i}{R}\right)(1 + 70\,\tilde{T}a^3)\right] \tag{15}$$

where, from our data,

$$f\left(\frac{\tau a V_i}{R}\right) \cong 2 \tag{16}$$

Thus, we are suggesting that the g function defined in equations (12) and (13) can, for this particular technique of turbulence-suppression, be expressed as given above.

If the above relationship holds for higher rotation rates than have been presently examined, and there is no suggestion from the data that it does not, then efficiencies of 99.9 percent could be attained at rotation rates as low as 480 rpm.

Acknowledgments

The authors wish to acknowledge the assistance of the United McGill Corp. which provided the cyclone that was modified for this experiment. Tomiyoshi Masuda, Robert Frank, and Prof. R. H. Essenhigh assisted in the construction of the test facility and the following students, in addition to Mr. Masuda, assisted in the first data-taking period: Steve Marek, Rebecca Kanner, and John Myers.

References

1 Razgaitis, R., and Holman, J. P., "A Survey of Heat Transfer in Confined Swirl Flows," *Future Energy Production Systems: Heat and Mass Transfer Processes*, Vol. II, Academic Press, 1976, pp. 831–866.

2 Razgaitis, R., "An Analysis of the High-Temperature Particulate Collection Problem," Argonne National Laboratory, ANL-77-14, Oct. 1977.

3 Deis, G. A., "A Turbulence-Dependent Model for Dust Separation in a Cyclone," M.Sc. Thesis, Ohio State University, 1977.

4 Razgaitis, R., and Deis, G. A., "The Efficiency Potential of Cyclone Separators," manuscript in preparation.

5 Bigler, M. L., "Turbulence Suppression in a Cyclone Separator by Means of a Rotating Insert," M.Sc. Thesis, Ohio State University, 1978.

6 Razgaitis, R., Guenther, D. A., and Bigler, M. L., "Turbulence Suppression in a Cyclone Separator by Means of a Rotation Insert," presented at Winter Annual Meeting ASME, New York, Paper No. 79-WA/APC-8, 1979.

7 Rosin, P., et al., *Zeitschrift des Vereins Deutscher Ingenieure*, Vol. 76, 1932, pp. 433–437.

8 Shepherd, C. H., and Lapple, C. E., "Flow Pattern and Pressure Drop in Cyclone Dust Collectors," *Industrial and Engineering Chemistry.*, Vol. 31, 1939, pp. 972–984.

9 Lapple, C. E., and Shepherd, C. B., "Calculation of Particle Trajectories", *Industrial and Engineering Chemistry*, Vol. 32, May 1940.

10 Davies, C. N., "The Separation of Airborne Dust and Particles," *Proc. Institution of Mechanical Engineers*, Vol. 166, No. 5, 1952, pp. 185–213.

11 Thompson, B. W. and Strauss, W., "The Application of Vortex Theory to the Design of Cyclone Collectors," *Chemical Engineering Society*, Vol. 26, 1971, pp. 125–31.

12 Hejma, I. J., "Influence of Turbulence on the Separation Process in a Cyclone," *Staub-Reinhaltuing der Luft*, Vol. 31, July 1971, pp. 22–28.

13 Beeckmans, J. M., "A Steady-State Model of the Reverse-Flow Cyclone," *Aerosol Science*, Vol. 3, 1972, pp. 491–500.

14 Leith, D., and Licht, W., "The Collection Efficiency of Cyclone—Type Particule Collectors—A New Theoretical Approach," *AIChE Symposium Series*, Vol. 68, No. 126, 1972, pp. 196–206.

15 Ciliberti, D. F., and Lancaster, B. W., "Fine Dust Collection in a Rotary Flow Cyclone," *Chemical Engineering Society*, Vol. 31, 1976, pp. 499–503.

16 Soo, S. L., *Fluid Dynamics of Multiphase Systems*, Blaisdell, 1967, p. 317.

17 Crawford, M., *Air Pollution Control Theory*, McGraw-Hill, 1976. p. 259.

18 Ter Linden, A. J., "Investigations in Cyclone Dust Collectors," *Institute of Mechanical Engineers Proceedings*, Vol. 160, 1949, pp. 233–240.

19 Stairmard, C. J., "The Design and Performance of Cyclone Separators," *Transactions Institute of Chemical Engineers*, Vol. 29, 1951, pp. 356–373.

20 Beeckmans, J. M., and Kim, C. J., "Analysis of the Efficiency of Reversed Flow Cyclone," *Canadian Journal Chemical Engineering*, Vol. 55 1977, pp. 640–643.

21 Soo, S. L., "Some Basic Aspects of Cyclone Separators," Particle Technology pro. First Intn. Conf. on Part. Tech., IITRI, 1973, pp. 9–18.

22 Bradshaw, P., "Effects of Streamline Curvature on Turbulent Flow," AGARD-AG-169, NATO, publication, 1973.

23 Brown, A., and Burton, R. C., "The Effects of Free-Stream Turbulence Intensity and Velocity Distribution on Heat Transfer to Curved Surfaces," ASME JOURNAL OF ENGINEERING FOR POWER, Vol. 100, 1978, pp. 159–165.

24 Ramaprian, B. R., and Shivaprasad, B. G., "Turbulent Boundary Layers Along Midly Curved Surfaces," *Journal Fluid Mechanics*, Vol. 85, Pt. 2, Mar. 21, 1978, pp. 273–303.

25 Hasinger, S. H., Mills, R. H., and von Ohain, H. J. P., Internal unpublished ARL report.

26 Pinchak, A. C., and Poplawski, R., "On the Attainment of Extremely High Rotational Velocities in a Confined Vortex Flow," AIAA Second Annual Meeting, San Francisco, Calif., Paper 65-200, July 26–29, 1965.

27 Poplawski, R., and Pinchak, A. C., "Aerodynamic Performance of Reversed Flow Vortex Chambers," ARL 65-219, Oct. 1965.

28 Fiorina, T. D., Jr. and Poplawski, R., *Experimental Optimization of the Reversed Flow Vortex Chambers*, ARL 65-66, Apr 1965.

29 Poplawski, R. and Pinchak, A. C., "Aerodynamic Effects of Secondary Flows in Confined Vortices," Res. Review, Office of Aerospace Research (OAR).

30 Miller, R. A., and Poplawski, R., "The Inertial Particle Separator for Military Turbine Powered Vehicles," *Proceedings of the Office of Aerospace Research (OAR) Research Applications Conference*, Washington, D.C., Apr 5, 1966, pp. 44–69.

31 Poplawski, R., "Potential Scope of Application of the ARL Separator for Turbine Powered Vehicles," *Proceedings of the Counter-Insurgency Research and Development Symposium*, Advanced Research Projects Agency, Washington, D.C.

32 Fletcher, E. C., Gyarmathy, G., and Hasinger, S., "Separation of Submicron Condensate Particles in a Vortex Chamber," ARL 66-0218, Nov. 1966.

33 Miller, Roger A., "Field Testing the ARL Dust Separator," Res. Rev. (Office Aerosp. Res.) *VI*(1), 1–6, Jan. 1967.

34 Pinchak, A. C., "A Review of the State of the Art of Cyclone-Type Separators," ARL 67-0047, Mar 1967.

35 Gyarmathy, G., "Optical Measurement of Radial Density Distributions in a High Speed Confined Vortex," ARL 67-0234, Dec. 1967.

36 Poplawski, R., and Miller, R. A., "Microscopic Particle Separation and Applications," ARL 68-0024, Feb. 1968.

F. L. Stasa
Assistant Professor,
Department of Mechanical Engineering,
Florida Institute of Technology,
Melbourne, Fla 32937,
Assoc. Mem. ASME

F. Osterle
Professor of Mechanical Engineering,
Carnegie-Mellon University,
Pittsburgh, Penna 15213
Mem. ASME

The Thermodynamic Performance of Two Combined Cycle Power Plants Integrated with Two Coal Gasification Systems

Thermodynamic models of both an adiabatic and an endothermic coal gasifier integrated with either a waste heat combined cycle or a supercharged boiler combined cycle are developed. The adiabatic gasification process requires air and steam, while the endothermic gasification process requires only steam. The combined cycle is composed of an open Brayton cycle and a superheated regenerative Rankine cycle without reheat. Certain components are added to each configuration in an effort to improve thermodynamic performance. From the results, it appears that with consideration of the pollution criteria, the station efficiencies for each configuration are within 1 percentage point of each other when flue gas recirculation is used as a means to control the nitric oxide. With a gas turbine inlet temperature of 2000°F, and with consideration of the pollution criteria, the configuration employing an adiabatic gasifier and a waste heat system is marginally the best with a station efficiency of only 37 percent.

Introduction

This paper presents an analytical study of the performance to be expected from four configurations into which two coal gasification systems and two combined cycle power generation systems can be arranged [1]. The coal gasification systems considered are an adiabatic gasifier "fired" with air and steam, and an endothermic gasifier "fired" with steam and heat. The power generation systems considered are the so-called waste heat and supercharged boiler combined steam/gas turbine cycles.

The last few years have seen a resurgence of interest in the use of coal-gas producers and related technology for the purpose of generating electricity. This interest stems from the hope that a clean, coal-derived, pressurized gaseous fuel can be obtained in this way and used in a combined steam/gas turbine cycle to generate electrical power at high efficiency [2]. Coal gasifiers can be distinguished by a number of characteristics. The flow (coal, air, steam) may be parallel or counter. The gasifier may operate at atmospheric or an elevated pressure. The coal may be gasified with air, air and steam, oxygen enriched air and steam, or steam and heat. The ash may be removed in a dry, slag, or agglomorated form. The bed may be fixed, fluidized, entrained, or molten. The gas cleanup may be hot (1000°F to 2500°F) or cold (100°F to 250°F). Details regarding these gasifier characteristics may be found in numerous references [3–12]. In our study we specify gasification with air and steam (adiabatic) or with steam and heat (endothermic), and take a "black box" view of the gasifier where the products exit in chemical equilibrium with each other, thus obviating the necessity for stipulating most of the other characteristics. Specification of this exit temperature (and pressure) fixes the coal, air, and steam flow ratios. We further indicate cold gas clean-up (e.g., the Benfield process) on grounds that cold cleanup is closer to commercial reality than hot cleanup at the present time. The most comprehensive study to date on electrical power generation from coal is the Energy Conversion Alternatives Study (ECAS) [13, 14] which, in fact, considers the adiabatic (but not the endothermic) gasifier/combined cycle concept. NASA has evaluated this study and summarized its findings [15]. However, ECAS covers such a large number of conversion processes that, at least in the above mentioned case, a full appreciation of the effect of configuration rearrangements and operating parameter adjustments on the performance of the conversion system cannot be gained from their presentation. In this paper we attempt to remedy this situation by providing a comprehensive treatment of certain gasifier/combined cycle systems. This study is a continuation of earlier work on the same subject [16, 17].

The Four Basic Configurations

Figures 1 to 4 show simplified schematics of the four basic configurations. These will be referred to as Configurations 1 to 4, respectively. In Figs. 1 and 3 it is seen that the path of the gas in the waste heat boiler is from the superheater section (SH), to the evaporator section (EV), and finally to the economizer section (EC). In contrast to this, in Figs. 2 and 4 the gas enters the evaporator and superheater sections, then is expanded in a gas turbine, and finally passes through the economizer section of the supercharged boiler. Note in Fig. 1 and 2 that coal is gasified with air and steam with no provisions for heat transfer, and in Fig. 3 and 4, coal is gasified with steam only but with a provision for heat transfer. In these two latter configurations, the combustor is used as the source of heat for the endothermic gasification. Since one of the goals is to determine the best configuration relative to the others, arbitrary but realistic values are assigned to the various specifiable cycle point parameters. In fact, where it was possible to do so, the same value is assigned to the same cycle point parameter in each configuration. Tables 1 and 2 give the assumed coal and air compositions, respectively. In the remainder of this section,

---

Contributed by The Power Division for publication in the JOURNAL OF ENGINEERING FOR POWER. Manuscript received at ASME Headquarters August 19, 1980.

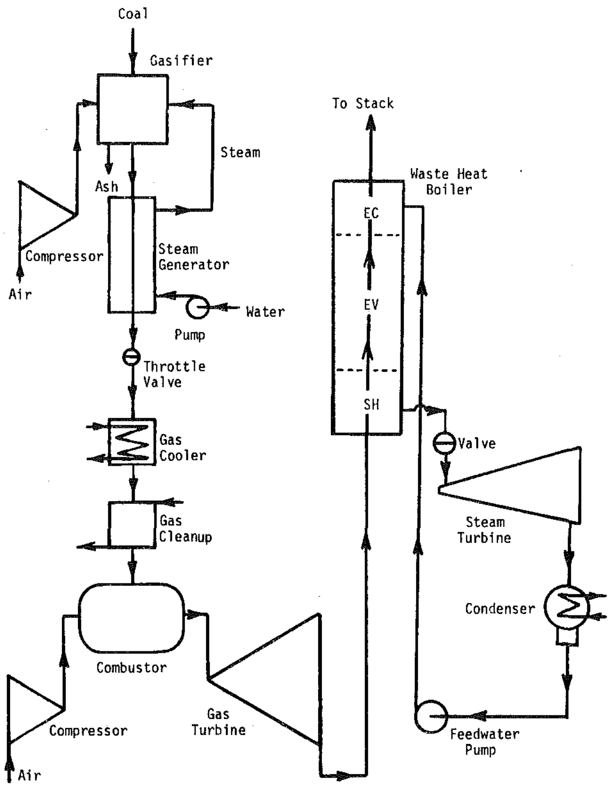

Fig. 1 **Simplified schematic of adiabatic gasifier intergrated with waste heat boiler combined cycle (Configuration 1)**

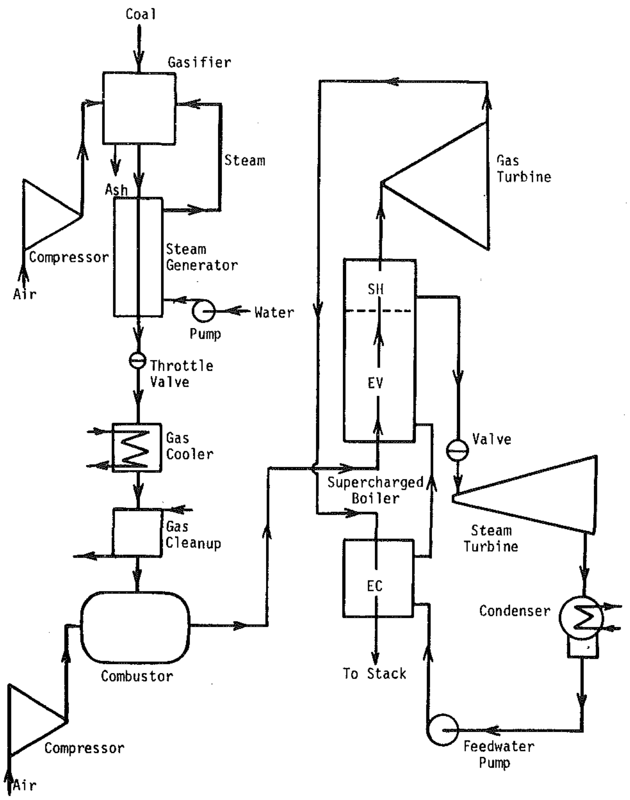

Fig. 2 **Simplified schematic of adiabatic gasifier intergrated with supercharged boiler combined cycle (Configuration 2)**

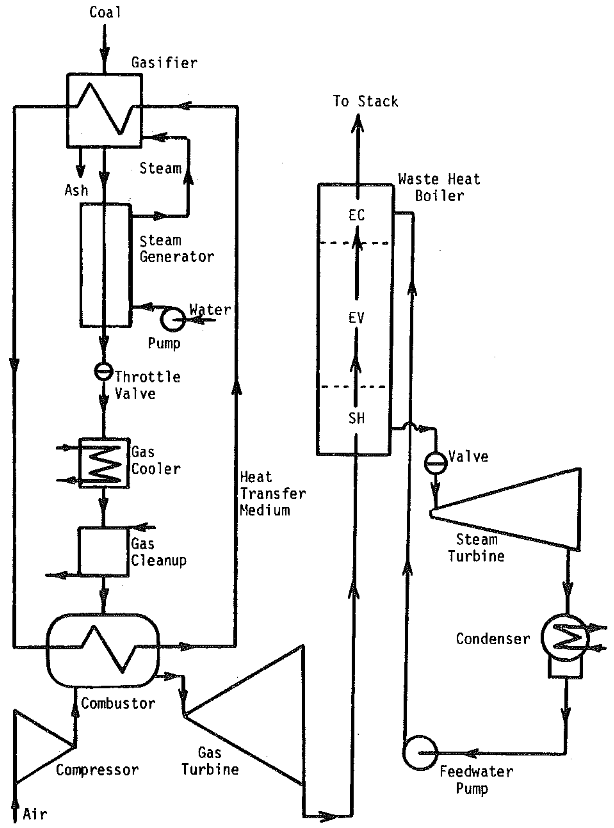

Fig. 3 **Simplified schematic of endothermic gasifier intergrated with waste heat boiler combined cycle (Configuration 3)**

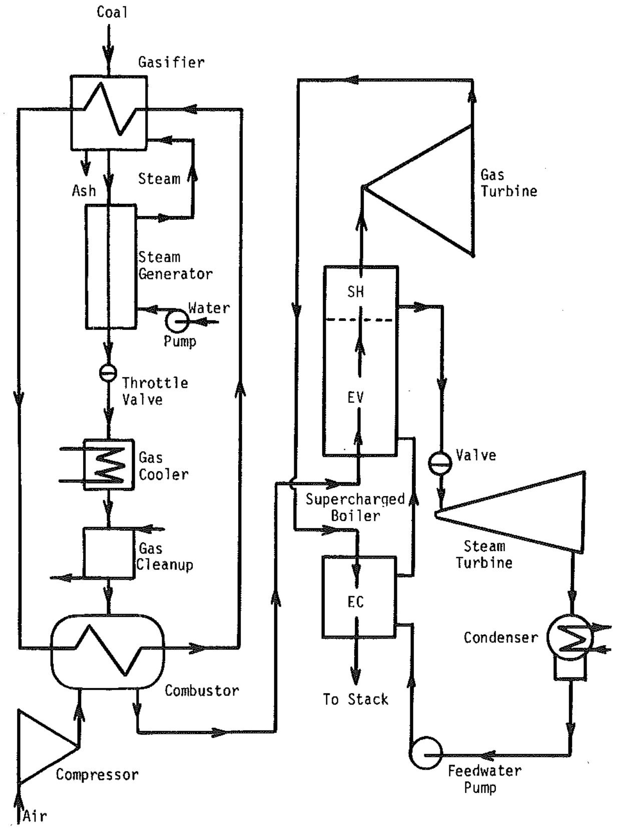

Fig. 4 **Simplified schematic of endothermic gasifier intergrated with supercharged boiler combined cycle (Configuration 4)**

all the assumed values will be summarized for Configuration 1, with only differences noted for the other configurations.

First, it is convenient to specify all the pressure-related data including all assumed pressure drops. It is emphasized that these are preliminary values, since later we will present the results from the optimization. The gasifier is assumed to operate at 11 atm, the combustor at 10 atm, the steam side of the boiler at 1600 psia, and the condenser at 1.75 psia. Ambient pressure is taken to be 14.7 psia. The following pressure drops are assumed in the gas cycle portion: none through the gasifier and combustor; a 10 psi drop through the steam-side of the steam generator and a total of 0.7 psi through the gas-side; a 0.1 psi drop through the gas cooler; and a 0.1 psi drop through the gas cleanup system. This implies a pressure drop of more than 10 psi in the gas throttle valve. In the steam-cycle portion, the following pressure drops are assumed: 0.04, 9.25, and 0.40 psi through the gas-side of the superheater, evaporator, and economizer sections of the boilers, respectively, and 10, 0, and 0.1 psi through the same sections of the steam-side; a 400 psi drop through the steam throttle valve; and none in the condenser.

Next the temperature-related input are specified. An ambient condition of 77°F is assumed for each air, coal, and water inlet to the system. The gasifier is assumed to operate at 2000°F with the same ash discharge temperature. The gas is assumed to be cooled to 200°F by the gas cooler. The gas turbine and the combustor are assumed to operate at 2000°F. Superheated steam at 960°F is assumed to be generated in the boiler with 7°F subcooling assumed at the evaporator inlet. The cooling water temperature is 70°F and is assumed to undergo a 5°F temperature rise. Finally, the pinch point temperature differences within the steam generator and boiler are specified to be equal to or greater than 40°F.

The following component efficiencies are assumed: 0.90 for the air compressors, 0.75 for the pump serving the steam generator, 0.85 for the gas turbine, 0.90 for the steam turbine, and 0.85 for the feed-water pump. In the gas cleanup system, 90 percent of the H_2S (by weight) is removed.

Having completed the specification of the cycle point parameters for Configuration 1, the pertinent changes are now indicated in the remaining configurations relative to Configuration 1. In Configurations 2 and 4, the combustor exit temperature is no longer 2000°F; instead, combustion with 10 percent excess air is assumed (since these two configurations use a supercharged boiler). Configurations 3 and 4 have no air compressor serving the gasifier and so the corresponding input conditions are no longer relevant. All other parameter specifications for these configurations remain the same. One other point should be made. In Configuration 3, the heat source for the endothermic gasifier is the combustor which also operates at 2000°F. This implies heat transfer through a zero temperature difference and consequently an infinite heat transfer area. For now let us accept this and reexamine this issue after the results of the optimization are presented.

The Base Case Station Efficiencies

Table 3 summarizes the station efficiencies for each configuration which were calculated from an extensive computer program [1] which made use of many of the property routines developed for the PSEF study [17]. In this program, ten chemical species are assumed to be formed in the gasifier and 15 in the combustor, including pollutants (NO_x, SO, SO_2, and SO_3). Typical gaseous molar compositions will be reported later after the optimization. Station efficiency is defined as the coal-pile to bus-bar efficiency minus an assumed 10 percent for station loads, which include station auxiliaries, lighting, generation losses, and so forth.

For completeness, Table 4 presents a summary of the miscellaneous results obtained for these same base cases. In Table 4, all flow rates, heat quantities, and work quantities are given with respect to one pound of coal. Furthermore, the lower heating value of the coal described in Table 1 is 12750 Btu per pound of coal. This provides a convenient reference value to which all heat and work quantities may be compared. The only exception is the heating values of the power gas, which are given in Btu/SCF—the usual units for gases. Recall that

Table 1 Ultimate analysis of coal (weight fraction)

Carbon	0.7304
Hydrogen	0.0528
Oxygen	0.0616
Nitrogen	0.0088
Sulfur	0.0264
Moisture	0.0300
Ash	0.0900

Table 2 Composition of air (weight fraction)

N_2	0.7546
O_2	0.2319
Ar	0.0135
$H_2O(g)$	0.0000

Table 3 Summary of station efficiencies for base cases

Configuration Number	Station Efficiency (percent)
1	34.6
2	29.9
3	38.6
4	32.7

Table 4 Summary of miscellaneous results for base cases

	Configuration			
	1	2	3	4
Flows (lbm)				
Gasifier				
Coal	1.000	1.000	1.000	1.000
Steam	0.022	0.022	0.997	0.997
Air	3.783	3.783	—	—
Dirty Gas	4.715	4.715	1.907	1.907
Ash	0.090	0.090	0.090	0.090
Gas Cleanup				
Dirty Gas	4.715	4.715	1.907	1.907
Water	0.285	0.285	0.179	0.179
Clean Gas	4.977	4.977	2.061	2.061
Waste	0.023	0.023	0.025	0.025
Combustor				
Fuel	4.977	4.977	2.061	2.061
Air	19.845	6.732	23.764	10.887
Products	24.822	11.709	25.825	12.948
Boiler				
Gas-side	24.822	11.709	25.825	12.948
Steam-side	3.920	5.649	4.258	5.568
Net Work (Btu)				
Gas Cycle	3018	1525	3432	1967
Steam Cycle	1878	2706	2039	2667
Total	4896	4231	5471	4634
Low Heating Val.				
Coal (Btu/lbm)	12747	12747	12747	12747
Gas (Btu/SCF)	135	135	288	288
Heat Trans. (Btu)				
To Gasifier from Comb.	0	0	5041	5041
To Steam Cyc.	5362	7727	5823	7615
Gas Cyc. Loss	4367	3495	3492	3165
From Steam Cycle	3484	5021	3784	4948
Excess Air to Comb. (percent)	224	10	140	10
Comb. Exit Temp (°F)	2000	3250	2000	3057
Stack Gas Temp (°F)	324	263	319	423
Gas Cooler Heat Loss (Btu)	2606	2606	623	623
Min. Temp. Dif. (°F)				
Steam Gen.	1380	1380	733	733
Boiler	40	140	40	300

natural gas has a heating value of about 1000 Btu/SCF, another convenient reference value. From these results, it should be noted that adiabatic gasification (with air and steam) produces a low-Btu gas (≤150 Btu/SCF) and endothermic gasification (with steam only) produces an intermediate-Btu gas (150 to 300 Btu/SCF).

It is important to note that the federal gaseous pollution criteria on sulfur dioxide and nitrogen oxides have been ignored for now. These are considered after the designs are optimized to more clearly show the effect of meeting pollution standards on thermodynamic performance.

Adding Components to the Basic Configurations

Each basic cycle was reviewed with respect to possible design changes that would improve the thermodynamic performance. These changes included the addition of regenerative feedwater heaters, an intercooled air compressor serving the combustor, and a regenerator within the gas cleanup system on all four configurations. In addition, for Configurations 1 and 2 which have air flow to the gasifier, two other components were added: a regenerator between the air and power gas streams and an intercooled air compressor serving the gasifier.

Effect of Adding Regenerative Feedwater Heaters. One closed feedwater heater and one open feedwater heater were added to the steam cycle in each of the four configurations. (See Figs. 5 to 8)

The next step was to assign reasonable values for the new specifiable parameters. The first extraction point was taken to be 30 psia and the second 6 psia. No additional pressure drops were assumed since a lumped loss of 400 psi was already taken. A terminal temperature difference of 3°F in the closed feedwater heater was assumed. The efficiency of each turbine stage was taken to be 0.90 and that of the condensate pump also 0.90. When the steam cycles of each of the basic configurations were modified using the above data, the station efficiency for each configuration decreased slightly as shown in Table 5. However, the steam cycle efficiency increased as expected. In each case, the increase in heat loss through the stack was greater than the savings in heat rejected from the steam cycle.

Although the above clearly shows that cycle performance deteriorated slightly when feedwater heating was employed, the heaters were kept in the cycles for the following reasons. Without feedwater heating, the final feedwater temperature was 123°F, and Configuration 4 would begin to condense some of the water vapor locally within the economizer. Clearly, all four configurations would probably have local condensation in the stack gas as the condenser pressure is reduced. This must be avoided because of the corrosive nature of the acid which would form. Another reason for keeping the feedwater heaters in the cycle was to provide a convenient location to deaerate the water. Finally, a higher stack gas temperature increases the so-called stack effect, and a smaller diameter stack could be used. For these reasons, the two feedwater heaters were kept in each configuration, and the loss of less than 0.5 percentage points in station efficiency was accepted.

Unless otherwise stated, all subsequent results are presented with the regenerative feedwater heaters in the steam cycle.

Effect of an Intercooled Compressor Serving the Combustor. Next the air compressor serving the combustor on each configuration was replaced with a two-stage intercooled compressor. The new data applicable to the modified portion of the cycles must be specified. It is easily shown that the optimum pressure ratio for each stage of the two stage compression process is equal to the square root of the product of the initial and final pressures. This results in the minimum amount of total compressor work being required. Therefore, the first-stage outlet pressure was taken to be 3.16 atmospheres. A 0.1 psi drop through the intercooler was further assumed. The temperature to which the air is cooled was assumed to be 50°F above ambient, or 127°F. Each stage of compression was assumed to have an efficiency of 0.9.

With these modifications, the station efficiencies did not improve for any configuration as shown in Table 6. Therefore, the replacement of the air compressor with an intercooled compressor serving the combustor was not warranted. Unless otherwise stated, all subsequent results are presented without these intercooled compressors in the cycles.

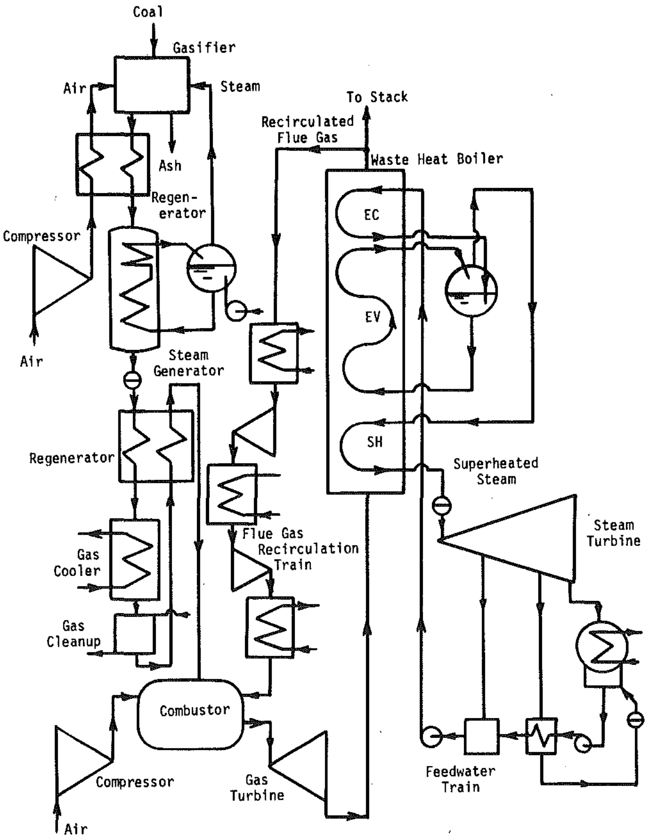

Fig. 5 Schematic of final version of Configuration 1

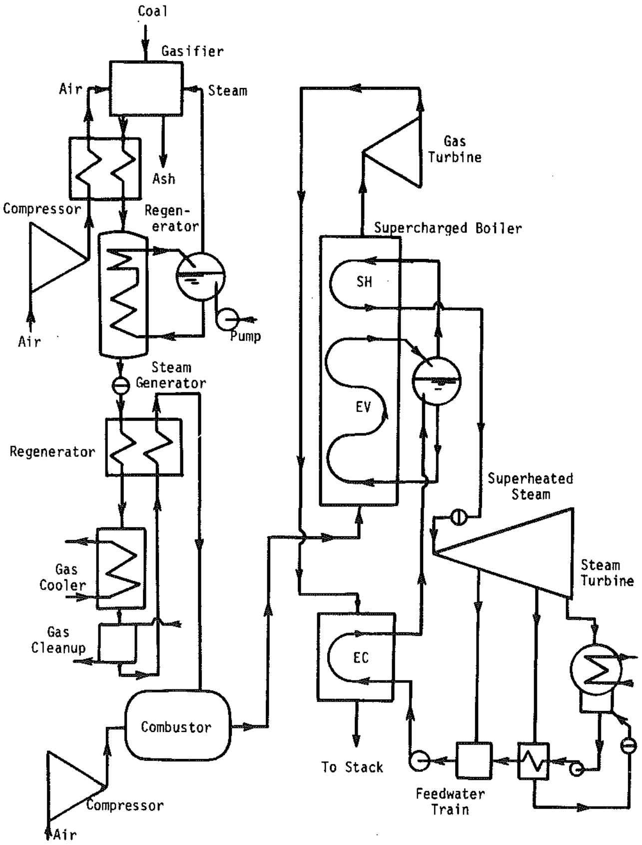

Fig. 6 Schematic of final version of Configuration 2

Effect of Adding a Regenerator within the Gas Cleanup System. A gas-to-gas counterflow heat exchanger (regenerator) between the "dirty" power gas entering the gas cleanup system and the "clean" gas leaving this system was added to reduce the heat lost in the gas coolers. (See Figs. 5 and 6) Use of a heat exchanger effectiveness sufficiently characterizes the heat exchanger and enables us to retain our thermodynamic approach. An effectiveness of 0.80 was assumed. A pressure drop of 0.1 psi was assumed for each side of the regenerator.

When this modification was made to the cycles, the results summarized in Table 7 were obtained. The improvement in cycle performance was dramatic, especially for Configurations 1 and 2. Without the regenerator in service, the configurations with an endothermic gasifier performed better than those with an adiabatic gasifier. This was not surprising since the higher steam demand for endothermic gasification resulted in less heat being lost in the gas cooler, as shown in Table 7 for the results without regeneration; but with the regenerators in service, the adiabatic configurations were superior to the endothermic configurations. Generating steam from 77°F water with 2000°F gas represented a large irreversibility compared to that associated with 80 percent effective gas-to-gas regeneration. Since endothermic gasification required much more steam than adiabatic, the former contribution to the total irreversibility was emphasized, thus de-emphasizing the contribution from the latter. Configuration 1 became the best performer. Note, however, that the two configurations utilizing a waste heat system were still superior to the two incorporating a supercharged boiler system. Unless otherwise stated, all subsequent results are presented with the regenerator in the gas cleanup system.

Effect of Adding a Regenerator between the Air Stream to the Gasifier and the Power Gas Stream. Since there was no air flow to the gasifier for Configurations 3 and 4, these two cycles were dismissed from further consideration in this section. The air inlet temperatures of the air to the gasifier are shown in Table 8 to be 651.9°F for Configurations 1 and 2 while the gasifier gas exit temperature is 2000°F. The large temperature clearance between these two fluid

Table 5 Results with feedwater heating

	1	2	3	4
Station Eff. (percent)				
Without	34.57	29.87	38.63	32.72
With	34.29	29.47	38.32	32.32
Steam Cycle Eff. (percent)				
Without	35.02	35.02	35.02	35.02
With	37.88	37.88	37.88	37.88
Increase in Stack Loss over Base Case(Btu)	510	732	553	724
Decrease in Steam Cyc. Heat Rej. over Base Case (Btu)	470	676	510	669
Final Feedwater Temp. (°F)				
Without	122.8	122.8	122.8	122.8
With	252.9	252.9	252.9	252.9
Stack Gas Temp. (°F)				
Without	324.1	262.8	319.1	422.8
With	405.7	502.9	402.0	622.9
Dew Point Temp. (°F)	93	119	116	141

Table 6 Results with intercooled compressor serving the combustor

	Configuration			
	1	2	3	4
Station Eff. (percent)				
Without	34.29	29.47	38.32	32.32
With	32.75	28.74	36.48	31.19
Air Temp to Comb (°F)				
Without	622.1	622.1	622.1	622.1
With	378.7	378.7	378.7	378.1
Air Flow to Comb. (lbm)				
Without	19.84	6.73	23.76	10.89
With	17.06	6.73	20.46	10.89
Comb. Outlet Temp (°F)				
Without	2000	3250	2000	3057
With	2000	3154	2000	2920
Heat to Steam Cycle				
Without	4852	4664	5270	6891
With	4375	6430	4699	6001
Gas Cyc. Net Work (Btu)				
Without	4856	4175	3432	1967
With	4638	4071	3387	2145

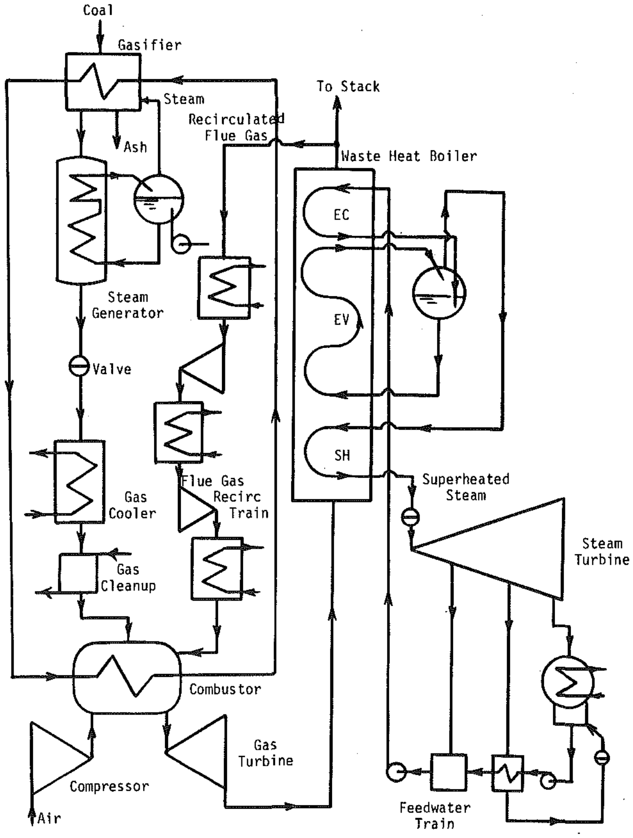

Fig. 7 Schematic of final version of Configuration 3

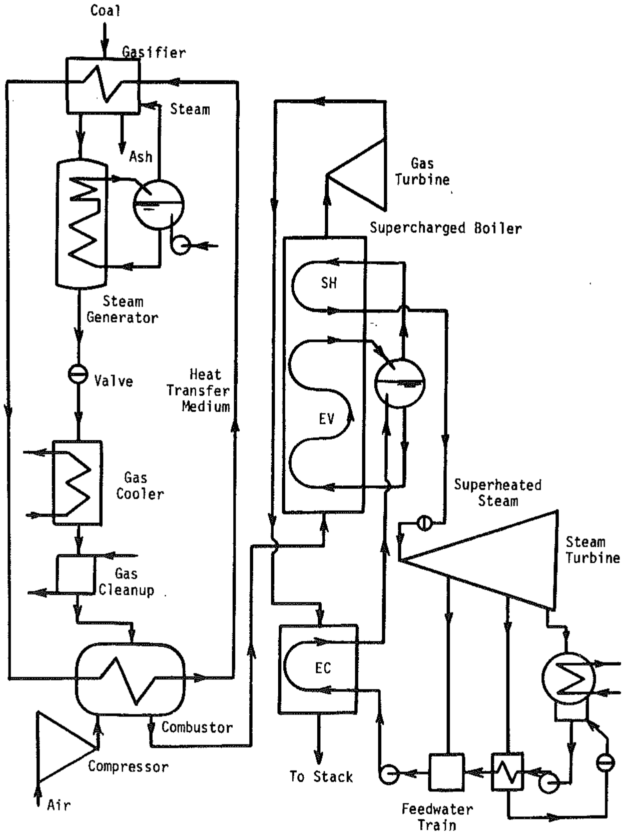

Fig. 8 Schematic of final version of Configuration 4

streams suggested that a regenerator could be incorporated into these configurations (see Figs. 5 and 6). Again the regenerator effectiveness was assumed to be 0.80. The pressure drops on each side of regenerator were assumed to be 0.1 psi. With this modification, the results shown in Table 8 were obtained.

It should be noted that the station efficiency improved only slightly. The reason for this is, of course, that the other regenerator was already effectively reducing the heat loss from the power gas flow stream. The required steam flow to the gasifier increased from 0.022 to 0.195 lbm. This resulted in more heat transfer in the steam generator helping to reduce the total gas cycle heat loss slightly. The hotter air into the gasifier resulted in less air demand but more total sensible heat was added to the gasification process from the air. Furthermore, the lower heating value of the power gas improved from 135 to 155 Btu/SCF. Admittedly, this regenerator improved the performance very little. As implied above, the gasification efficiency significantly improved (from 86.58 to 94.75 percent). Improving the gasification efficiency significantly does not necessarily result in a significant improvement in station efficiency. Although the incremental improvement in performance was small, this regenerator was kept in Configurations 1 and 2 for all subsequent calculations unless otherwise stated.

Effect of an Intercooled Compressor Serving the Gasifier. Finally, an intercooler was added to the compressor serving the gasifier in Configurations 1 and 2 with the hope that the station efficiency might be increased by reducing the work of compression. Note that this modification applied only to the two configurations incorporating an adiabatic gasifier.

The first-stage pressure ratio was taken to be equal to the square root of the product of the inlet pressure of the first stage and outlet pressure of the second stage; therefore the pressure at the outlet of the first stage was 3.317 atmospheres. Again it was assumed that a 0.1 psi pressure drop occurred through the gas cooler, that the gas was cooled to within 50°F of ambient (i.e., to 127°F), and that each compressor stage had an efficiency of 0.90. With this modification, the results shown in Table 9 were obtained. Note that the station efficiency of Configuration 1 decreased, but that of Configuration 2 remained just about the same. In Configuration 1 the small increase in the net gas cycle work was not enough to offset the even greater increase in the gas cycle heat loss. In Configuration 2 the larger amount of net gas cycle work was just about cancelled by the effect due to the greater gas cycle heat loss.

In summary, the addition of an intercooled compressor serving the gasifier was not warranted. Unless otherwise stated, all subsequent results are presented without an intercooled air compressor serving the gasifier.

Table 7 Results with 80 percent effective regenerator within gas cleanup system

	1	2	3	4
Station Eff. (percent)				
Without	34.29	29.47	38.32	32.32
With	41.53	36.04	40.04	34.17
Heat Loss in Gas C/r (Btu)				
Without	2606	2606	623	623
With	485	485	122	122

Table 8 Results with 80 percent effective regenerator between gasifier air and gas streams

	Configuration	
	1	2
Station Efficiency (percent)		
Without	41.52	36.04
With	41.80	36.62
Temp. of Air to Gasifier (°F)		
Without	651.9	651.9
With	1730.4	1730.4
Heat Transfer in Regenerator within Gas Cleanup Sys. (Btu)		
Without	2121	2121
With	1096	1096
Heat Trans. in Present Regenerator (Btu)		
Without	0	0
With	902	902
Steam Flow to Gasifier (lbm)		
Without	0.022	0.022
With	0.195	0.195
Heat Transfer in Steam Gen. (Btu)		
Without	28	28
With	252	252
Gas Cycle Heat Loss (Btu)		
Without	3240	1782
With	3192	1695
Air Flow to Gasifier (lbm)		
Without	3.783	3.783
With	3.121	3.121
Enthalpy of Air to Gasif. (Btu)		
Without	1017	1017
With	1740	1740
Heating Value of Gas (Btu/SCF)		
Without	135	135
With	155	155

Table 9 Results with intercooled compressor serving the gasifier

	Configuration	
	1	2
Station Efficiency (percent)		
Without	41.80	36.62
With	41.62	36.63
Gas Cycle Net Work (Btu)		
Without	3705	1609
With	3709	1662
Gas Cycle Heat Loss (Btu)		
Without	3192	1694
With	3265	1774

Results of the Optimization

The goal was to optimize each configuration by determining those operating conditions which maximize the station efficiency. It can be argued that the optimization needs to be done with respect to only three variables: the gasifier exit temperature, the combustor pressure, and the gasifier steam temperature. Increasing the steam cycle peak pressure would improve performance but the steam turbine exit quality was already near the practical lower limit of 88 percent and increasing the steam pressure would make the turbine exhaust even wetter. It was already shown that feedwater heating is not really desirable in a combined cycle. Clearly, the optimum steam extraction pressure is the limiting low pressure in the steam cycle, namely the condenser pressure. It was not necessary, therefore, to optimize with respect to these pressures. Obviously, increasing the gas turbine inlet temperature would result in improved station efficiency, but this parameter was fixed by present-day gas-turbine technology at 2000°F, similarly, the peak steam-cycle temperature was fixed at 960°F. For the supercharged boiler configurations, the excess air fraction was a specifiable parameter. However, when the excess air was increased from the current value of 10 percent, performance did not improve. Consequently this parameter too was not considered in the optimization. All other variables had obvious optimum values (like zero pressure drops) and were dismissed. The effect on performance of some of these parameters was considered in some parametric studies.

Before the optimization was executed, the steam turbines second- and third-stage efficiencies were changed to be more realistic, namely 0.825 and 0.75 respectively. The new base case station efficiencies became 41.26, 35.74, 39.52, and 33.47 percent for Configurations 1 to 4 respectively. The steam turbine exit quality was calculated to be 87.9 percent for each configuration, which was marginally acceptable.

For each configuration, the following optimization procedure was used. The data for each cycle as already described up to this point was used. Then, by varying only the temperature of the gas leaving the gasifier, the value which resulted in the highest station efficiency, was noted. With this new value for the gasifier exit gas temperature, the combustor pressure was then varied and the station efficiency calculated. The "optimum" value was noted. Finally, with the above two optimum values used, the temperature of the superheated steam entering the gasifier was varied, and the effect on station efficiency noted. Depending on the outcome, this procedure was repeated until no further changes in the optimum conditions occurred. This procedure was followed, of course, for all four configurations.

It should be noted, however, that the optimum pressure for the gasification system was not independent of that for the gas turbine cycle. Clearly, these two pressure levels should be as nearly the same as possible, since any difference between them tends to act as an effective gas cycle pressure drop in the throttle valve. In reality, the gasification pressure must be slightly higher than the gas turbine cycle pressure because there will be losses in the real system. We used a difference of 1 atmosphere. Considering the other pressure drops which have previously been specified, this was equivalent to assuming a 13.5 psi drop through the throttle valve after the steam generator.

Optimization of Configuration 1. Table 10 shows the final results of the optimization of Configuration 1. The optimum gasifier gas temperature of 2000°F and the optimum gas cycle pressure of 10 atm were used from the outset. The somewhat arbitrary gasifier steam temperature of 600°F was sufficiently close to the original value of 620°F that a new iteration was not necessary. Furthermore, station efficiency depended very little on this steam temperature.

We conclude, therefore, that the optimized cycle had a station efficiency of 41.26 percent. It should be emphasized that this included the assumed 10 percent station load. Pressure drops and component inefficiencies were also included. Without this 10 percent station load, the station efficiency would be 45.8 percent. It should be pointed out, however, that we have yet to consider the impact of meeting the federal gaseous emission requirements. These are considered in the next major section.

Optimization of Configuration 2. Table 11 shows the final results of the optimization. It is concluded that for Configuration 2 the optimum operating conditions are as follows: 1800°F gasification temperature, 10 atm gas cycle pressure, and 600°F gasifier steam temperature. While the last specification is not really optimal, the decrease in station efficiency from that at 1000°F is almost undetectable. The station efficiency for the optimized cycle is only 35.8 percent, which is significantly below that of Configuration 1.

Optimization of Configuration 3. The results are shown in Table 12. For Configuration 3, the optimal conditions are a gasification temperature of 1800°F, a combustor pressure of 10 atm, and a gasifier steam temperature of 1000°F. However, the station efficiency was a very weak function of the gasifier steam temperature. These condi-

Table 10 Final results of optimization of configuration 1 without consideration of gaseous pollution standards

Search for Optimum Gasifier Temperature	
Gas Temperature (°F)	Station Efficiency (percent)
1600	40.75
1800	41.17
2000	41.26
2200	41.25
2400	41.22
2600	41.19
Search for Optimum Gas Cycle Pressure	
Combustor Pressure (atm)	Station Efficiency (percent)
5	40.58
10	41.26
15	40.62
20	39.54
25	38.28
30	36.83
Search for Optimum Temperature of Steam to Gasifier	
Steam Temperature (°F)	Station Efficiency (percent)
400	41.25
500	41.25
600	41.26
700	41.26
800	41.26
900	41.26
1000	41.27

Table 11 Final results of optimization of configuration 2 without consideration of gaseous pollution standards

Search for Optimum Gasifier Temperature	
Gas Temperature (°F)	Station Efficiency (percent)
1600	35.42
1800	35.79
2000	35.74
2200	35.66
2400	35.59
2600	35.51
Search for Optimum Gas Cycle Pressure	
Combustor Pressure (atm)	Station Efficiency (percent)
5	32.20
10	35.79
15	35.60
20	35.28
25	34.89
30	34.50
Search for Optimum Temperature of Steam to Gasifier	
Steam Temperature (°F)	Station Efficiency
400	35.77
500	35.78
600	35.79
700	35.79
800	35.80
900	35.81
1000	35.82

Table 12 Final results of optimization of Configuration 3 without consideration of gaseous pollution standards

Search for Optimum Gasifier Temperature	
Gas Temperature (°F)	Station Efficiency (percent)
1600	39.18
1800	39.52
2000	39.52
2200	39.41
2400	39.27
2600	39.12
Search for Optimum Gas Cycle Pressure	
Combustor Pressure (atm)	Station Efficiency (percent)
5	38.53
10	39.52
15	39.12
20	38.26
25	37.20
30	36.00
Search for Optimum Temperature of Steam to Gasifier	
Steam Temperature (°F)	Station Efficiency (percent)
400	39.44
500	39.48
600	39.52
700	39.55
800	39.59
900	39.62
1000	39.66

Table 13 Final results of optimization of Configuration 4 without consideration of gaseous pollution standards

Search for Optimum Gasifier Temperature	
Gas Temperature (°F)	Station Efficiency (percent)
1600	33.12
1800	33.55
2000	33.47
2200	33.40
2400	33.21
2600	33.02
Search for Optimum Gas Cycle Pressure	
Combustor Pressure (atm)	Station Efficiency (percent)
5	39.00
10	33.55
15	35.29
20	35.81
25	35.54
30	35.23
Search for Optimum Temperature of Steam to Gasifier	
Steam Temperature (°F)	Station Efficiency (percent)
500	35.77
600	35.81
700	35.84
800	35.87
900	35.90
1000	35.93

tions are considered to be optimal and resulted in a station efficiency of 39.7 percent.

Optimization of Configuration 4. The results of the optimization are shown in Table 13. For Configuration 4 the optimum station efficiency is found to be 35.9 percent without consideration of gaseous pollution standards. The optimal gasification temperature, gas cycle pressure, and steam temperature were found to be 1800°F, 20 atm, and 1000°F, respectively. It should be pointed out that the gasification temperature has a very small effect on station efficiency for every configuration. The implication is that it would be possible to operate the gasifier at off-optimal temperatures if this became desirable for other reasons.

Consideration of the Gaseous Pollution Criteria

The computer program was capable of predicting the amount of sulfur oxides (SO_x) and nitrogen oxides (NO_x) that enter the atmosphere from the stack.

Through the EPA, the federal government has set limits on these two types of pollutants from power plants. These limits are summarized in Table 14 for the various fuel types. Note that the units used in this table are lbm (of pollutant) per million Btu (of fuel input based on the higher heating value of the fuel).

It should be noted that provisions were already made for reducing SO_x emissions via the gas cleanup system. Recall that it was assumed that 90 percent of the H_2S (by weight) was removed from the power gas before it was burned in the combustor. Since there was much free oxygen in the combustor, the sulfur in the remaining H_2S and all the COS ended up mostly in the form of SO_2 with smaller amounts in the form of SO and SO_3. The amounts of SO_x that would enter the atmosphere were calculated to be 0.60, 0.57, 0.50, and 0.49 lbm/10^6 Btu for the Configuration 1 to 4, respectively.

The NO producing reaction has been reported (20) to freeze at a temperature of about 2400°F. In other words, the NO producing reaction slows down markedly for temperatures below 2400°F. So it can be argued that even though combustion would take place at temperatures over 3000°F which would produce a larger amount of NO, the concentration of NO would decrease as the stack gas temperature is approached. However, because of the above mentioned freeze phenomenon, the concentration of NO never would go below its equilibrium value at 2400°F.

Table 15 shows the amount of NO_x formed with and without the freeze effect. When the NO producing reaction is assumed to freeze at 2400°F, the supercharged boiler configurations are acceptable. The waste heat boiler configurations, however, exceed the limit on NO_x by more than a factor of four.

Flue gas recirculation is sometimes used as a way to reduce NO_x. In essence some of the relatively cool flue gas is recirculated back into the combustor replacing some of the excess air as the diluent. This serves two purposes: one is to reduce the amount of gas that actually goes to the atmosphere, and the other is to reduce the amount of NO produced in the first place.

Flue gas recirculation was incorporated into the models of Configurations 1 and 3. Unless the flue gas enters the combustor at a reduced temperature the benefit of flue recirculation is lost. Also gas compressors are needed, since the flue gas is at atmospheric pressure and the combustor is operated at elevated pressures. The first gas cooler was added to reduce the work required by the first stage of compression. The intercooler helped to reduce the work required by the second stage of compression. Finally the second gas cooler was utilized to lower the temperature of the compressed flue gas before entering the combustor to maximize the effect of the flue gas recirculation. Additional data needed to be specified before the NO_x emission could be calculated. It was assumed that each of compressor stages had an efficiency of 0.9 and that the first gas cooler reduced the flue gas temperature to 250°F, the second to 300°F, and the third to 350°F. It was not possible to reduce these temperatures to within 50°F of ambient as before because the flue gas had a high volume fraction of water vapor. As the pressure is increased, the dew point temperature is increased. Condensation in the flue gas recirculation system was to be avoided for the same reasons it was to be avoided elsewhere in the system. A pressure drop of 0.1 psi was assumed in each gas cooler.

Table 14 Federal emission limits [18, 19]

Type of Fuel	Limit (lbm per 10^6 Btu) SO_x	NO_x
Coal	1.2	0.7
Oil	0.8	0.3
Gas	0.2	0.2

Table 15 NO_x Emissions with and without a freeze temperature of 2400°F (lbm/10^6 Btu)

	Configuration 1	2	3	4
Without Freeze	1.24	3.21	1.03	2.74
With Freeze	3.54	0.41	2.93	0.47

Table 16 Effect of flue gas recirculation on Configuration 1 and 3

Fraction of Flue Gas Recirculated	Configuration 1 Station Efficiency (percent)	NO_x (lbm/10^6Btu)
0.30	38.36	1.89
0.35	37.95	1.62
0.40	37.55	1.34
0.45	37.19	1.05
0.50	36.85	0.74
0.55	36.56	0.33
Fraction of Flue Gas Recirculated	Configuration 3 Station Efficiency (percent)	NO_x (lbm/10^6 Btu)
0.30	37.08	1.37
0.35	36.71	1.10
0.40	36.38	0.82
0.45	36.07	0.49

Table 17 Results without regenerator in service and elevated gasifier steam temperatures

Gasifier Steam Temp. (°F)	1280	1200
Station Efficiency (percent)		
Previous Optimum	36.07	35.93
Without Modifications	36.14	35.95
Steam Generator Gas Exit Temperature (°F)	211	222
Heat Removed by Gas Cooler (Btu)	11	22

With this modification to only Configurations 1 and 3, the results shown in Table 16 were obtained. Note the decrease in performance as the fraction of flue gas recirculation is increased. In order to ensure some margin, it appeared that about 53 percent recirculation was necessary for Configuration 1, while for Configuration 2 only 45 percent was needed. Unless otherwise stated, the fraction of recirculated flue gas was fixed at these values for all subsequent calculations. The NO_x shown in Table 16 was calculated assuming the 2400°F freeze temperature.

When Configurations 1 and 3 were checked to determine how flue gas recirculation might effect the previously calculated optimum conditions, no shift in these parameters occurred. That is, the configurations were still optimum for the previously determined operating conditions.

Review and Summary of Results

The optimizations of Configurations 3 and 4 with respect to the gasifier steam temperature demonstrate that it is possible to cool the dirty power gas to the level required by the Benfield cleanup process by increasing the steam temperature. This suggests that the regenerator could be removed from these endothermic configurations at the expense of making the steam generator superheater larger. When this regenerator was removed from these configurations and the temperature of the steam to the gasifier increased, the results shown in Table 17 were obtained. Only the results from the steam temperature which gave a steam generator gas exit temperature near 200°F are presented. Clearly, the gas cooled before the gas cleanup system could also be removed, since cleanup at both 211°F and 222°F is acceptable. This would result in even higher performance, but the improvement would be small.

It should be noted that the purpose of this modification was to eliminate the use of expensive equipment and not to improve the station efficiency by less than a tenth of a percentage point. By taking advantage of using a higher gasifier steam temperature, it was possible to eliminate an expensive piece of equipment, namely the regenerator, from Configurations 3 and 4. The gas cooler, however, was left in the cycles, but it should be kept in mind that this too could be eliminated if an actual plant were to be built. Figures 1 to 4 were modified to include the results up to this point. The modified configurations are shown schematically in Figs. 5 to 8 and represent the final versions of the original cycles presented earlier with consideration of gaseous emission criteria.

The key results for each optimized configuration are summarized in Table 18. From this table it is seen that all four configurations have practically the same station efficiency, although Configuration 1 is marginally the best. More importantly, Configuration 1 required less total steam than the other configurations. As expected, the endothermic configurations required much more steam than the adiabatic ones. Note the amount of heat rejected through the condenser for the waste heat configurations. For Configuration 1, only about 29 percent of the heat input to the cycle was actually rejected to the heat sink, probably a river, compared to about 63 percent for an equally efficient conventional fossil-fueled plant. This difference could be significant enough to eliminate the need for expensive cooling towers, which seem today to be almost standard equipment on new power plants. This benefit practically disappeared for the supercharged boiler configurations. Flue gas recirculation took its toll on station efficiency.

It is convenient at this point to present typical equilibrium compositions of the clean fuel gas and the combustor product gas. The former are summarized in Table 19 and the latter in Table 20. Note that the composition is given by mole (or volume) fraction.

Conclusions

Several conclusions may be drawn from the results presented. First and foremost is the result of the optimization with respect to both components and operating conditions with consideration of the emission criterion on nitric oxides. As summarized in Table 18, Configuration 1 resulted in the best station efficiency but only marginally. In fact, the difference between the highest and lowest station efficiencies is less than 1 percentage point. If the nitric oxide problem that exists in the configurations which utilize waste heat boilers could be solved without the use of flue gas recirculation, then these configurations could have higher station efficiencies by as much as five percentage points over those incorporating supercharged boilers. All of these comments depend, of course, on the validity of the 2400°F freeze temperature assumption for the NO producing reaction.

While Configuration 1 was marginally the best performer, it would require the most equipment. Further complicating the trade-offs which must be made concerning the search for the best configuration was the relatively small consumable water requirement for Configuration 1. In general, the configurations employing endothermic gasifiers require about twice as much total water as those incorporating adiabatic gasifiers. Finally, the waste heat configurations rejected a much smaller amount of heat from the steam cycle compared to that of the supercharged boiler configurations. This could result in substantial capital cost savings if cooling towers could be eliminated in the waste heat configurations.

It is instructive to compare these results with the station efficiency of a conventional coal-fired plant with stack gas scrubbers. Osterle, et al. [17] calculated the station efficiency of a coal-fired plant under assumptions very similar to those made in this work to be 37.5 percent, without consideration of the penalty from the stack gas scrubbers. Rubin [21] presented data which show that about 2½ percentage points should be subtracted from the above station efficiency to include the energy requirements of the scrubbers. Therefore, the station efficiency of 36.67 percent for Configuration 1 is slightly better than that of 35.0 percent for a conventional coal-fired plant. Configuration 1 appears to be significantly better than a nuclear plant, the station efficiency of which is usually given as 33 percent. In terms of heat rates, these station efficiencies correspond to 9307, 9750, and 10,300 Btu/kwhr for Configuration 1, the coal-fired plant, and the nuclear plant, respectively.

Table 18 Summary of results for final version of each configuration

	Configuration			
	1	2	3	4
Station Eff. (percent)	36.67	35.79	36.14	35.95
Comb. Cycle Eff. (percent)	43.01	41.83	42.08	44.86
Heat. Value of Gas (Btu/SCF)	155	157	288	290
Water Req. (lbm)				
Gasification	0.195	0.264	1.038	1.068
Gas Cleanup	0.268	0.243	0.123	0.000
Total	0.463	0.507	1.161	1.068
Heat Rej. (Btu)				
Gas Cycle	3861	1710	4114	2243
Steam Cycle	3692	5968	3515	5412
Ratio of Gas Cycle Work to Steam Cycle Work	1.44	0.47	1.53	0.63
Fraction of Flue Gas Recirculated	0.53	—	0.45	—
Pollution (lbm/10^6Btu)				
NO_x	0.52	0.41	0.50	0.47
SO_x	0.59	0.57	0.49	0.49
Station Eff. (percent) without Pollution Control	41.26	35.79	39.66	35.93

Table 19 Composition of clean fuel gas for final version of each configuration (mole fraction)

Species	1	2	3	4
H_2	0.1835	0.1933	0.4968	0.4950
CH_4	0.0021	0.0046	0.0299	0.0530
H_2O	0.0784	0.0784	0.0784	0.0392
CO	0.3017	0.2954	0.3771	0.3822
N_2	0.4256	0.4130	0.0022	0.0024
Ar	0.0053	0.0052	0.0000	0.0000
CO_2	0.0027	0.0094	0.0149	0.0274
H_2S	0.0004	0.0004	0.0006	0.0006
COS	0.0002	0.0002	0.0001	0.0002
NH_3	0.0001	0.0001	0.0000	0.0000

Table 20 Composition of combustor product gas for final version of each configuration (mole fraction)

Species	1	2	2	4
H_2	0.0000	0.0006	0.0000	0.0002
H_2O	0.1254	0.1327	0.1995	0.1865
CO	0.0000	0.0037	0.0000	0.0008
N_2	0.7025	0.6922	0.6430	0.6511
O_2	0.0185	0.0121	0.0165	0.0148
Ar	0.0088	0.0087	0.0081	0.0082
CO_2	0.1443	0.1441	0.1325	0.1343
NO	0.0002	0.0034	0.0002	0.0027
OH	0.0000	0.0020	0.0000	0.0012
H	0.0000	0.0001	0.0000	0.0000
O	0.0000	0.0001	0.0000	0.0000
NO_2	0.0000	0.0000	0.0000	0.0000
SO	0.0000	0.0000	0.0000	0.0000
SO_2	0.0003	0.0003	0.0002	0.0002
SO_3	0.0000	0.0000	0.0000	0.0000

Table 21

The following table of conversion factors from U.S. customary units to International System (SI) units is included as space limitations do not allow all of the results to be presented in duplicate.

1 °C = 1.8 °F
or
T (°C) = [T (°F) − 32] 5/9
1 Btu = 1.055 kilo-Joule
1 psi = 6.894 k PA
1 atm = 101.325 k PA
1 lbm = 0.4536 kg
1 ft^3 = 28.3168 liters

It appears that better performance can be expected when the amount of work produced by the gas cycle is a high fraction of the total work. This was a characteristic of the configurations employing a waste heat boiler. Unfortunately, these same configurations were unacceptable with respect to nitric oxide emissions. When flue gas recirculation was used as a means to reduce the amount of this effluent, the station efficiency decreased substantially to very nearly the values of station efficiency for the supercharged boiler configurations.

Regenerative feedwater heating in the steam cycle portion of a combined cycle resulted in a deterioration of plant performance. While the steam cycle efficiency improved, the station efficiency did not. The decrease in heat rejection from the steam cycle through the condenser was smaller than the increase in the gas cycle heat loss through the stack. Feedwater heating raises the final feedwater temperature. A higher stack gas temperature, of course, results in a higher sensible heat loss through the stack. It should be noted that this conclusion is a result of the concept of a combined cycle and does not apply to a conventional fossil-fueled power plant. In the latter, feedwater heating does improve the plant performance significantly. Several reasons have been identified, however, which make some feedwater heating desirable. In a combined cycle only a minimum number of feedwater heaters should be used.

For the configurations employing an adiabatic gasifier it appears that some kind of heat recovery system is necessary beyond that of the steam generator. A gas-to-gas counterflow heat exchanger between the gas streams to and from the cleanup process was seen to improve station efficiency more than 3 percentage points if the device is 80 percent effective. Increasing the temperature of the steam to the gasifier in the endothermic configurations allowed the elimination of this regenerator. In these configurations the steam generator was capable of reducing the gas temperature to the proper level required by the cleanup process. It should also be noted for the adiabatic configurations that the regenerator near the gas cleanup system was much more important than the one between the air and gas streams to and from the gasifier, respectively. In fact, with the former in service at an effectiveness of 0.80, the latter may be removed completely with the station efficiency decreasing less than 0.5 percentage points.

With the exception of Configuration 3, the effective gasification temperature may be chosen to be higher than that which results in the optimum station efficiency. The advantages of this are a faster reaction rate, a lower steam requirement, and conditions which are more conducive to attaining chemical equilibrium. Since the heat source for the endothermic gasification required by Configuration 3 was at 2000°F, the effective gasification temperature must necessarily be below this. The effect of gas cycle pressure on station efficiency was much larger than that of the effective gasification temperature. Although the temperature of the steam to the gasifier hardly affected the plant performance, proper specification of this parameter for the endothermic configurations could result in the saving of expensive equipment, namely a regenerator.

In all cases the use of intercooled air compressors did not appear to be justified. The station efficiencies either dropped slightly or remained the same when this modification was made to each configuration. Fortunately, it was also found through parametric studies not reported here that each configuration was fairly insensitive to different types of coal. When three other types of coal were used in the analysis, the station efficiency hardly changed. Boiler pinch point temperature differences, too, were unimportant. Halving the 40°F minimum pinch point temperature difference resulted in a relatively small improvement in station efficiency with the largest increase of slightly more than 0.5 percentage points occurring in Configuration 1. The inefficiencies associated with the cycle components, particularly the turbines and compressors, played a major role in reducing plant performance. For the hypothetical case of ideal components, the station efficiency was calculated to increase more than 6 percentage points. (The pressure drops apparently played a much smaller role in determining station efficiency.)

Finally, it was found that the real success of the combined cycle concept integrated with a coal gasifier depends on the attainment of higher gas turbine inlet temperature. It was shown in the original work [1] that for Configuration 1, an increase of almost exactly 5 percentage points would result, after consideration of the pollution criteria if the turbine inlet temperature could be raised to 2400°F. The use of flue gas recirculation to control the production of NO on the waste heat configurations resulted in decreasing the station efficiency about 3 percentage points.

References

1 Stasa, F. L., "The Thermodynamic Performance of Two Combined Cycle Power Plants Integrated with Two Coal Gasification Systems," Doctoral Dissertation, Carnegie-Mellon University, Pittsburgh, PA, 1978.

2 Ad Hoc Panel on Low-Btu Gasification of Coal of the Committee on Processing and Utilization of Fossil Fuels, "Assessment of Low- and Intermediate-Btu Gasification of Coal," Commission on Sociotechnical Systems of the National Research Council for the National Academy of Sciences, Wash, 1977.

3 Haslan, R. T., and Russel, R. P., *Fuels and Their Combustion,* McGraw-Hill, New York, 1926.

4 Rudolph, P. F. H., "The Lurgi Process for Coal Gasification," *Energy Technology Handbook,* D. M. Considine (ed.), McGraw Hill, New York, 1977, pp. 1-188 to 1-200.

5 Bodle, W. W., and Vyas, K. C., "Clean Fuels from Coal," *The Oil and Gas Journal,* Aug. 1974, pp. 73–88.

6 Ad Hoc Panel on the Evaluation of Coal Gasification Technology, "Evaluation of Coal Gasification Technology: Part II—Low- and Intermediate-Btu Fuel Gases," National Research Council for National Academy of Sciences, Wash. 1973.

7 Bodle, W. W., and Vyas, K. C., "Clean Fuels from Coal—Introduction to Modern Processes," *Clean Fuels from Coal Symposium,* Vol. II, Institute of Gas Technology, Chicago, pp. 11 to 25, 1975.

8 Hall, E. H., et al., "Fuel Technology: A State-of-the-Art Review," U.S. Environmental Protection Agency, Publication NTIS PB-24-535, National Technical Information Service, Springfield, VA, 1975.

9 Hebden, D., "High Pressure Gasification under Slagging Conditions," Paper presented at the Seventh Synthetic Pipeline Gas Symposium of the AGA, ERDA, and IGU, Chicago, 1975.

10 Von Fredersdorff, C. G., and Elliott, M. A., "Coal Gasification," *Chemistry of Coal Utilization—Supplementary Volume,* H. H. Lowry (ed.), John Wiley & Sons, New York, 1963.

11 Grace, R. T., "Bi-Gas Process for Production of High-Btu Pipeline Gas from Coal," *Energy Technology Handbook,* D. M. Considine (ed.), McGraw-Hill, New York, 1977, pp. 1-212 to 1-218.

12 Traenckner, K., "Pulverized-Coal Gasification Ruhrgas Processes," *Trans. ASME,* 1953.

13 Beecher, D. T., et al., "Energy Conversion Alternatives Study (ECAS), Westinghouse Phase II Final Report, NASA CR-134942, Vol. I to III, Cleveland, Nov, 1976.

14 Corman, J. C., et al., "Energy Conversion Alternatives Study (ECAS)" General Electric Phase II Final Report, NASA-CR 134949, Vol. I to III, Cleveland, Dec 1976.

15 "Evaluation of Phase 2 Conceptual Designs and Implementation Assessment Resulting from the Energy Conversion Alternatives Study (ECAS)," NASA Lewis Research Center, NASA TX-73515, Cleveland, Apr 1977.

16 Osterle, J. F., "Thermodynamic Considerations in the Use of Gasified Coal as a Fuel for Power Conversion Systems," *Proceedings of the Frontiers of Power Technology Conference,* Oklahoma State University, Carnegie-Mellon University, Pittsburgh, Oct 1974.

17 Osterle, J. F., Impink, A. J., Jr., Lipner, M. H., and Candris, A., "Pressurized Gasification Systems Coupled to Combined Steam-Gas Power Cycles for the Generation of Clean Electric Power from Pennsylvania Coal," Final Report Prepared for the Pennsylvania Science and Engineering Foundation under Agreement No. 241, Carnegie-Mellon University, Pittsburgh, July, 1975.

18 "Standards of Performance for New Stationary Sources," *Federal Register,* Vol. 36, No. 247, Dec 23, 1971.

19 Small, J. R. and Williamson, J. A., "Source Monitoring of NO_x and SO_2," *Energy Technology Handbook,* D. M. Considine (ed.), McGraw-Hill, New York, 1977, p. 9–374.

20 Hottel, H. C., et al., *Thermodynamic Charts for Combustion Processes,* John Wiley and Sons, New York, 1949.

21 Rubin, E. S., (Proj. Dir.), "Comparative Environmental Assessments of Coal Utilization Systems: Vol. I: Overview and Summary," Final Report prepared for Brookhaven National Lab (DOE), Middle Atlantic Power Research Committee, and Pennsylvania Science and Engineering Foundation by the Center for Energy and Environmental Studies, Carnegie-Mellon University, Pittsburgh, Mar 1978.

H. B. Urbach
J. G. Purnell
D. T. Knauss
David W. Taylor Naval Ship Research and Development Center,
Annapolis, MD 21402

Performance of a Multiphase Boiling MHD Generator

Adiabatic liquid metal-water MHD generators produce power during water boiling because both temperature and pressure drop throughout the phase change. Therefore, boiling MHD generators with boiling water, as distinguished from purely expansive steam-liquid metal MHD generators, may be useful energy-conversion devices. A generator, with a working fluid consisting of a liquid-metal eutectic of tin and bismuth, water, and steam, was analyzed in accordance with anticipated isentropic efficiencies. Real-gas-law data from steam tables were employed to integrate one-dimensional multiphase thermodynamic equations by using Simpson's rule. Consistency checks on the boiling section showed errors of about 1 percent. The contribution of the boiling section of the generator was computed to be about 20 percent greater per unit length and 360 percent greater per unit volume than the purely expansive section of the MHD generator for the studied inlet conditions.

Introduction

Liquid-metal MHD systems provide an alternate approach to MHD energy conversion where low-temperature energy sources are insufficient to produce ionized conducting gases. Such MHD generators employing combinations of liquid metals or alloys, with steam as a working fluid, have been studied in the U. S. [1] and abroad. However, the multiphase combination of MHD working fluid consisting of liquid metal, water and steam with boiling has only recently been suggested [2]. Water and liquid metal are used to provide a relatively efficient water-metal nozzle (as opposed to a steam-metal nozzle) to accelerate the fluid. On entry of the water-metal mixture into the MHD generator, water begins to boil.

A boiling MHD generator must transfer enthalpy from liquid metal to water while simultaneously sustaining transfer of free energy, in the form of electrical current, to an external load. Since the boiling process is simultaneous with the adiabatic expansion, the Clapeyron-Clausius equation relates temperature to pressure throughout the process.

Using real-gas data, the multiphase equations may be integrated by means of Simpson's rule to yield the thermodynamic state points and the energy transfer. The thermodynamic data permit design of an MHD generator with a boiler section which is contiguous with the usual purely expansive two-phase device. The methodology and the results of such a study are presented in the body of this report.

Thermodynamic Analysis of Multiphase Systems

Analysis of multiphase MHD systems has been treated extensively by Elliott and Weinberg [3], particularly for nozzles. The following analysis provides undiscussed details associated with MHD-generator working fluids undergoing a boiling transition.

The superficial appearance of the equations for multiphase thermodynamic systems is similar to that of single-phase systems. The combined first and second-law statement of the enthalpy for the j-th isolated phase is (see Nomenclature.)

$$dh_j = Tds_j + v_j dp \tag{1}$$

For multiple-component systems with interaction at equilibrium, the enthalpy statement becomes

$$\Sigma dh_j = \Sigma T ds_j + \Sigma v_j dp \tag{2}$$

To simplify the writing, the summation and subscript signs are dropped with the understanding that

$$dh = \Sigma dh_j, \tag{3}$$

etc. Then

$$dh = Tds + vdp. \tag{4}$$

Generally it is useful to express the enthalpy in terms of the temperature and pressure. Then

$$dh = C_p dT + (v - T\,\partial v/\partial T)dp, \tag{5}$$

where the partial derivative is at constant pressure.

For isentropic processes,

$$dh_s = vdp. \tag{6}$$

Regardless of the mechanisms of irreversibility, we can relate the degree of reversibility in an expansion process to a coefficient as follows:

$$dh = \eta dh_s. \tag{7}$$

By combining equations (5, 6) and (7), the result is

$$dT = [(\eta - 1)vdp + T(\partial v/\partial T)dp]/C_p \tag{8}$$

for an expansion process. To obtain the final pressure change in a process, equations (6) and (7) are combined to eliminate dh_s so that

$$dp = dh/\eta v. \tag{9}$$

The pressure changes calculated from equation (9) are used to solve for temperature changes in equation (8). However, in processes wherein phase changes occur, such as in freezing, melting, condensing or boiling, the pressure and temperature must be related through the Clapeyron-Clausius equation

---

Contributed by the Energetics Division for publication in the JOURNAL OF ENGINEERING FOR POWER. Manuscript received at ASME Headquarters September 2, 1980.

$$dT = (\upsilon_{fg}/s_{fg})\,dp, \tag{10}$$

where the subscripts represent volume or entropy changes in passing from the liquid to the gaseous phase. Combining equations (8) and (10), the resultant equation is

$$T(\partial \upsilon/\partial T) + (\eta - 1)\upsilon - C_p(\upsilon_{fg}/s_{fg}) = 0 \tag{11}$$

When the system is undergoing phase changes, υ and C_p must be functions of the quality. Thus,

$$\upsilon = x\upsilon_{fg} + \upsilon_f + r\upsilon_1, \tag{12}$$

where the subscript f represents the condensed gas phase (water in this study), the subscript 1 represents liquid metal or oil, and υ_{fg} is the volume change on vaporization. Likewise,

$$C_p = xC_{pfg} + C_{pf} + rC_{pl} \tag{13}$$

The solution of these equations for a boiling generator, by the use of Simpson's rule and finite elements, will now be described. It is assumed that steam-table data are available for rapid retrieval in a computer-program format for these calculations.

Now, from the tables, the local condition of the heat capacity of the gas is

$$C_{pg} = [(h_g)_{T+\Delta T/2} - (h_g)_{T-\Delta T/2}]/\Delta T, \tag{14}$$

where ΔT is a small temperature change and

$$C_{pfg} = C_{pg} - C_{pf} \tag{15}$$

We obtain an estimate of the effective specific-heat ratio from the expression

$$[n/n-1]_{est} = \log[T_{f(est)}/T_0]/\log[p_{f(est)}/p_0], \tag{16}$$

where the estimates of T_f and p_f are described below.

$$p_i = p_0 + i[p_{f(est)} - p_0]/2N, \quad i = 0 \text{ to } 2N \tag{17}$$

where $2N$ is the number of equally spaced pressure intervals. Then

$$T_i = T_0(p_i/p_0)^{n/(n-1)}. \tag{18}$$

Then at each local point, we have a matrix of thermodynamic values derived from steam tables, which may include p_i, T_i, υ_i, υ_{gi}, υ_{fi}, h_{gi}, h_{fi}, s_{gi}, s_{fi}, C_{pfi}, C_{pgi}, C_{pi} where

$$\upsilon_i = x_i\upsilon_{fg_i} + \upsilon_{f_i} + r\upsilon_1 \tag{19}$$

and

$$C_{p_i} = x_iC_{pfg_i} + C_{pf_i} + rC_{pl}, \tag{20}$$

which follows from equations (12) and (13).

Now Simpson's rule for integration [4] is

$$\int_{p_0}^{p_f} f(p, T, \ldots)dp = [(p_f - p_0)/6N][f(p_0, T_0 \ldots) + 4\sum_{j=1}^{N} f_{2j-1}(p, T, \ldots) + 2\sum_{j=2}^{N-1} f_{2j-2}(p, T, \ldots) + f(p_f, T_f, \ldots)]. \tag{21}$$

We may now solve equation (11) for a boiling MHD generator starting with a system of liquid metal and water and ending with liquid metal and steam. The partial derivative of the volume in equation (11) becomes (with all partial derivatives at constant pressure)

$$\partial\upsilon/\partial T = \upsilon_{fg}(\partial x/\partial T)\,\Delta T/|\Delta T| + x(\partial\upsilon_{fg}/\partial T) + (\partial\upsilon_f/\partial T) + r(\partial\upsilon_1/\partial T). \tag{22}$$

The derivative $\partial x/\partial T$ represents the change in quality with respect to change in temperature, whether or not the temperature increases or decreases (as occurs in boiling with energy extraction). The factor $\Delta T/|\Delta T|$ provides for this contingency.

Using finite-element analysis, Equation (22) may be written

$$\partial\upsilon/\partial T = 1/2\,[(\upsilon_{fg})_{T_i} + (\upsilon_{fg})_{T_{i-1}}][(x_i - x_{i-1})/|T_i - T_{i-1}|] + {} + 1/2\,[(\upsilon_{fg})_{T_i} - (\upsilon_{fg})_{T_{i-1}}][(x_i + x_{i-1})/(T_i - T_{i-1})] + {} + ((\upsilon_f)_{T_i} - (\upsilon_f)_{T_{i-1}})/(T_i - T_{i-1}) + r\,\partial\upsilon_1/\partial T \tag{23}$$

Moreover, defining thermodynamic values in an interval in terms of the end point values, we get

$$T = (T_i + T_{i-1})/2 = \overline{T}, \tag{24}$$

$$\Delta T = T_i - T_{i-1}, \tag{25}$$

$$\upsilon_{fg} = (\upsilon_{fg_i} + \upsilon_{fg_{i-1}})/2 = \overline{\upsilon}_{fg}, \tag{26}$$

$$\Delta\upsilon_{fg} = \upsilon_{fg_i} - \upsilon_{fg_{i-1}}, \tag{27}$$

$$C_p = (x_i + x_{i-1})C_{pfg}/2 + C_{pf} + rC_{pl}, \tag{28}$$

$$s_{fg} = (s_{fg_i} + s_{fg_{i-1}})/2 = \overline{s}_{fg} \tag{29}$$

Inserting equations (23–29) into equation (11), the finite element equation for the quality x_i becomes

$$x_i[(\overline{\upsilon}_{fg}/2)(\eta - 1) + \overline{T}\,\overline{\upsilon}_{fg}/|\Delta T| + (\overline{T}/2)\Delta\upsilon_{fg}/\Delta T - (C_{pfg}/2)\overline{\upsilon}_{fg}/\overline{s}_{fg}] + x_{i-1}\,[\overline{\upsilon}_{fg}(\eta - 1)/2 - \overline{T}\,\overline{\upsilon}_{fg}/|\Delta T| + \overline{T}\,\Delta\upsilon_{fg}/(2\Delta T) - (C_{pfg}/2)\,\overline{\upsilon}_{fg}/\overline{s}_{fg}] + [(\upsilon_f + r\upsilon_1)(\eta - 1) + \overline{T}(\Delta\overline{\upsilon}_f/\Delta T + r\partial\upsilon_1/\partial T) - (C_{pf} + rC_{p1})\,\overline{\upsilon}_{fg}/\overline{s}_{fg}] = 0 \tag{30}$$

Before equation (30) can be solved, an estimate of the final temper-

Nomenclature

A = cross-sectional area of flow
B = magnetic induction vector in the MHD generator
C_p = heat capacity at constant pressure
C_{pf} = heat capacity of water at constant pressure
C_{pfg} = heat capacity difference between steam and water at constant pressure
C_{pg} = heat capacity of steam at constant pressure
C_{pl} = heat capacity of the liquid metal at constant pressure
E = electric-intensity vector
f_c = a factor converting English pressure to S.I. units
h = enthalpy per unit mass
h_{fg} = enthalpy difference between steam and water per unit mass
h_g = enthalpy per units mass of gas
h_s = enthalpy value in an isentropic process
I = total electrical current
J = current density
ℓ = MHD-channel length
ℓ_m = magnetic length
m = mass flow rate
N = an index for numbering state points and intervals
n = effective specific-heat ratio in a two-phase system
P = power
p = pressure
r = mass ratio of liquid metal to water and steam in the flow
s = entropy per unit mass
s_f = entropy per unit mass of water
s_{fg} = entropy change during boiling of water
s_g = entropy per unit mass of steam
T = absolute temperature
V = velocity
V_0 = electrical potential
υ = volume per unit mass
$\dot{\upsilon}$ = volume flow
ν_f = volume per unit mass of water
υ_{fg} = volume difference between steam and water per unit mass
υ_g = volume per unit mass of steam
υ_1 = volume per unit mass of liquid metal
w = generator width or electrical length
x = quality
α = void fraction of liquid-metal alloy in the generator
η = efficiency of a process
η_{el} = electrical efficiency (load factor)
σ = electrical conductivity
χ = flow-length variable in the generator

ature, at which boiling is complete, is made from the relation

$$T_{f(set)} = T_0 - h_{fg0}/C_{p0} \tag{31}$$

Since at $T_{f(est)}$ the steam is saturated, the final pressure $P_{f(est)}$ is immediately known from the steam tables (incorporated into our computer program). Then each pressure p_i is known from equation (17) and each T_i is fixed by the tables. Since pressure and temperature are not independent in the two-phase region of water, equation (18) is not used.

Then all the thermodynamic values are known at each point, except for the quality x_i, which is now obtained from (30) by stepping from T_0 to $T_{f(est)}$. If, at $T_{f(est)}$, $x_{f(cal)}$ does not equal 1 ± error (0.001), a new $T_{f(est)}$ is calculated from $(T_{f(est)})_{\text{old}} \cdot (x_{f(cal)})^{0.2}$.

This is a purely empirical procedure which was contrived to obtain rapid convergence to a point on the saturation line. The new $T_{f(est)}$ is used to obtain a new $P_{f(est)}$ for the right-hand member of equation (17). This iterative technique is repeated until $x_{f(cal)}$ equals 1 ± error (0.001). All thermodynamic properties, including the quality, will then be known at each of the $2N + 1$ points.

Quantitites such as Δh are then obtained from expressions which include the quality; thus

$$\Delta h = \eta \int_{p_0}^{p_f} (x\, v_{fg} + v_f)dp + r v_1 (p_f - p_0), \tag{32}$$

where the integral is calculated by the use of Simpson's rule. A test of the internal consistency of the analysis is then obtained from a comparison with the Δh obtained from integration of equation (5).

Design of a Boiling MHD Generator

There are many two-phase liquid-metal MHD power-producing systems. The liquid-metal MHD generator of this study was preceded by a mixer and a nozzle. In the mixer, the liquid-metal alloy (43 percent tin and 57 percent bismuth) is assumed to mix uniformly with liquid water above the vaporization pressure. The alloy-water weight ratio (see Table 1) was chosen to be 680.9, which permitted a maximum void ratio of 0.85 at the exit pressure of 0.517 MPa (75 psia). In the nozzle just preceding the generator, sufficient enthalpy is converted to kinetic energy to provide an invariant generator velocity of 15.24 m/s (50 ft/s).

Precisely at the instant when the required nozzle velocity is attained, the working fluid enters the MHD generator and the water begins to boil. When the boiling phase transition has been completed, a contiguous purely expansive MHD-generator section begins. The end of the purely expansive section is the point at which the assumed void fraction of 0.85 has been attained.

Since the magnetic induction is maintained at high uniform values (1.0 to 3.6 Tesla), the Hartmann number is large (see below). In MHD generators with large Hartmann numbers, the ratio of viscous to ohmic dissipation is sufficiently small so that the viscous drag term may be neglected. Then only the Lorentz force and the pressure gradient constitute the significant elements of the momentum-balance equations.

Thus, considering steady-state flow conditions and perpendicular J and B fields, we have

$$\nabla p = \mathbf{J} \times \mathbf{B} = -JB\mathbf{i}. \tag{33}$$

Table 1 Thermodynamic and physical constraints in a boiling MHD generator

Constraints	Characteristic Value
Inlet pressure, boiler	40.08 bar (581.2 psia)
Inlet temperature, boiler	250.4 (482.8°F)
Isentropic efficiency	0.85
Load factor	0.94
Aspect ratio	2.55
Velocity	15.24 m/s (50 ft/s)
Exit void fraction	0.85
Exit pressure	0.517 MPa (75 psia)
Mass ratio	680.9
Steam rate	1.352 kg/s (2.981 lbm/s)
Magnetic induction	3 Tesla

Now the current density is given by

$$J = \sigma V B (1 - \eta_{el}). \tag{34}$$

Eliminating J from equations (33) and (34), the result is

$$dp = -\sigma(1 - \eta_{el}) V B^2 d\chi. \tag{35}$$

Now σ varies [2] as the void fraction, thus

$$\sigma = 2\sigma_0(1 - \alpha)/(2 + \alpha), \tag{36}$$

where the void fraction is given by

$$\alpha = [1 + r v_1/(x\, v_{fg} + v_f)]^{-1} \tag{37}$$

Combining equations (35) and (36) and integrating, the channel or flow length, l, becomes

$$\Delta\chi = \ell = [-f_c/(2\sigma_0(1 - \eta_{el})VB^2)] \int_{P_0}^{P_f} [(2 + \alpha)/(1 - \alpha)]dp, \tag{38}$$

where f_c converts pressure in psia to pascals when the data employed in the integral are in English units. The integral is solved by Simpson's rule as described above.

The relationship between electrical efficiency and generator aspect ratio (ratio of the flow length to the electrical length) is given in Fig. 1 (from reference [5]). Losses arise at the ends of the generator because the induced electric intensity falls off rapidly in the working fluid at the inlet and exit stations of the channel. As a consequence, the high-intensity fields in the generator discharge through the working fluid at the ends of the generator where low or zero electric-intensity fields exist. This discharge is an electrical short circuit. By employing long generators, the end losses become less significant, but in confined spaces, long generators are often impractical. Insulating vanes which are parallel to the flow may be placed in the end areas to reduce losses, and the results of analytical studies [5] predicting their effect are shown in Fig. 1.

The data of Fig. 1 may be used to calculate the isentropic generator efficiencies, which include all other losses such as hydrodynamic losses. Fig. 2 shows the computed relationships [6] for a Hartmann number of 750. From five-vane analyses similar to that of Fig. 2, isentropic efficiencies of 0.85 show that an electrical efficiency (load factor) of 0.90 is required. From Fig. 1, the interpolated five-vane data show that for an electrical efficiency of 0.90, an aspect ratio of about 5.5 would be required.

As described above, real-gas cycle analysis provides data on the thermodynamic state points at all stations of the flow, including the two-phase volumes of the fluid per unit weight of steam. Thus, the total volume rate is given by

$$\dot{v}(\chi) = v(\chi) m \tag{39}$$

at the inlet to the boiling section, at the end of the boiling section, and at the exit of the MHD generator. The total cross-sectional area of the generators, at any point, is given by

$$A(\chi) = \dot{v}(\chi)/V. \tag{40}$$

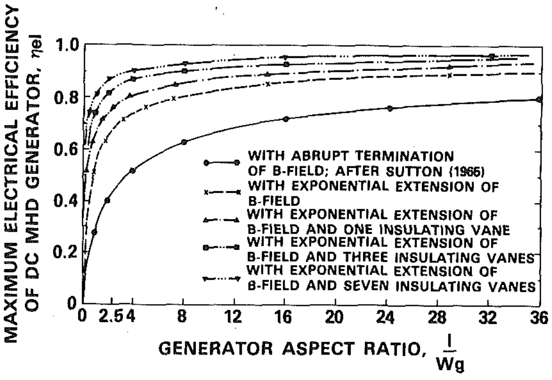

Fig. 1 Maximum electrical efficiency of an MHD generator (reference [5])

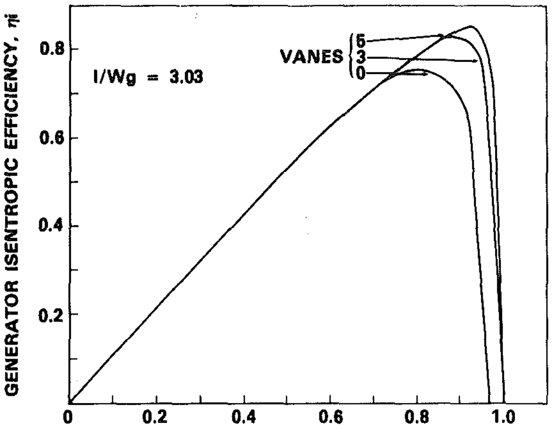

Fig. 2 Generator isentropic efficiency versus electrical efficiency (load factor) (reference [6])

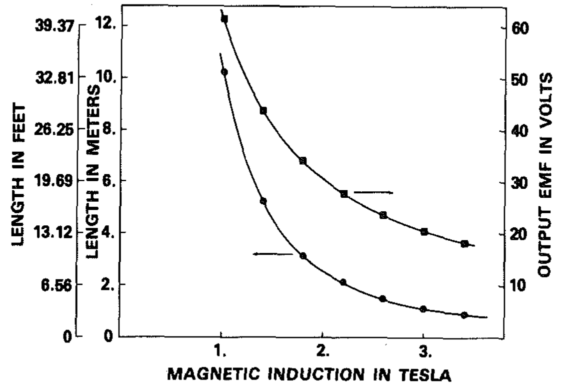

Fig. 3 *B*-field effect on MHD generator size and Emf

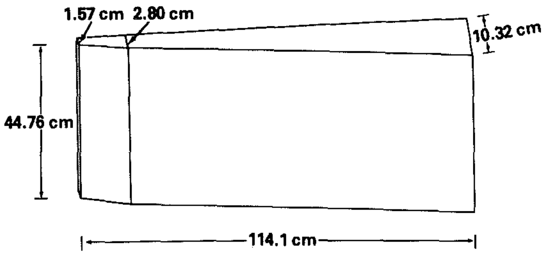

Fig. 4 Computed configuration of an MHD generator channel

Table 2 Computed thermodynamic and physical properties in a boiling MHD generator

Parameter	Characteristic Value
Exist pressure, boiler	31.59 bar (458.1 psia)
Exit temperature, boiler	236.7°C (458.1°F)
Exit pressure, expander	5.17 bar (75.0 psia)
Exit temperature, expander	233.2°C (451.8°F)
Boiler length	0.131 m (0.430 ft)
Expander length	1.011 m (3.32 ft)
Total generator length	1.141 m (3.74 ft)
Area, inlet	0.0070 m^2 (0.75 ft^2)
Area, boiler exit	0.0125 m^2 (0.135 ft^2)
Area, final exit	0.0462 m^2 (0.497 ft^2)
Magnetic length, inlet	0.0157 m (0.0515 ft)
Magnetic length, boiler exit	0.0280 m (0.919 ft)
Magnetic length, expander exit	0.1032 m (0.339 ft)
Electrical length	0.4476 m (1.469 ft)
Output potential	20.46 V
Boiler work	0.0217 kWh/kg steam (33.6 Btu/lb)
Expander work	0.1454 kWh/kg steam (225.2 Btu/lb)

The electric intensity is given by

$$E = \eta_{el} VB. \tag{41}$$

The aspect ratio (l/w) yields the generator electrical length

$$w = \ell/(\ell/w). \tag{42}$$

The output potential is the product of the electric intensity and length; thus,

$$V_o = Ew. \tag{43}$$

The magnetic length is a variable given by

$$\ell_m = A/w = \ell_m(\chi). \tag{44}$$

Since the generator area will be largest at the exit station, the magnetic gap is determined by the value of l_m at the exit or

$$\text{magnetic gap} = \ell_m(\ell). \tag{45}$$

The magnetic induction field must be uniform throughout the channel.

The current density at any point of the channel will be a function of the void fraction α at that point and is given by

$$J(\chi) = 2\sigma[(1 - \alpha(\chi))/(2 + \alpha(\chi))](1 - \eta_{el})\eta_{el} VB. \tag{46}$$

The total generator current is given by

$$I = \int_0^{\ell_m} J(\chi)\, \ell_m(\chi)\, d\chi. \tag{47}$$

The gross total MHD output power is

$$P = V_0 I. \tag{48}$$

Results and Discussion

The thermodynamic constraints listed in Table 1 provided the computer results listed in Table 2. As mentioned, a check of the internal consistency of the boiling analysis was based upon a comparison of enthalpy results from equations (5) and (32). Convergence limits on the computer program were based on the quality, which is unity when boiling is complete. With quality constraints fixed by $0.999 < x < 1.001$, the enthalpy discrepancy was about 1 percent for a series of boilers with varying mass ratios. With narrowed tolerance in x the enthalpy discrepancy is reduced.

Figure 3 represents the effect of the magnetic induction field on the generator size and output potential as calculated by use of a computer program employing the above analysis. High B fields are preferred because the size of the generator channel is inversely proportional to B^2. Unfortunately, the output potential is inversely proportional to B because the induced electric intensity is only linear in B. Since high output potential is desirable to obtain high inverter efficiency and low currents, a trade-off decision between output emf and length is required.

The listing (Table 2) of computer-calculated generator-channel properties is based on a three-Tesla field. The average Hartmann number, which varies with position in the generator channel, is approximately 10,000.

The channel length of 1.41 m (3.74 ft) does not include provision for the additional length required for the insulating vanes. With allowance for an additional half electrical length for the vanes at each end, a design length of 1.59 m (5.21 ft) is obtained. The maximum magnetic gap is 10.32 cm (4.06 in.). Figure 4 illustrates the configuration of the channel without the insulating vanes.

From Table 2 it may be calculated that the boiler section represents 11.5 percent of the channel length and 3.6 percent of the channel volume. From the thermodynamic analysis, the boiling section contributes 13.1 percent of the output so that the boiling expansion is approximately 20 percent more effective in producing work per unit length. On a volume basis, it is about 360 percent more effective. This high effectiveness may be attributed largely to the low void fraction in the boiler and partly to the peculiarly large heat of vaporization of water.

The assumption of one-dimensional flow in the generator should be examined. For the given magnetic and flow lengths, the channel half angles are 2.68 and 2.13 deg for the boiler and expander sections, respectively. Considering the large Reynolds number (3.3×10^7), the one-dimensional assumption appears reasonable.

Since the working fluid of the two-phase nozzle which precedes the MHD generator consists of liquid metal and very small quantities of liquid water, the efficiency of the device is higher [2] than that of a liquid-metal, steam nozzle (0.95 versus 0.87). Thus, the boiling MHD-generator section, which would be anticipated to succeed such a nozzle, would appear to be a compact and useful device in liquid-metal power conversion systems.

Conclusions

Multiphase thermodynamic analysis of liquid-alloy and boiling water MHD generators may be effected by consideration of the Clapeyron-Clausius equation. Simpson-rule integration of multi-phase finite-element thermodynamic equations yields consistent results with discrepancies proportional to tolerance limits.

Comparison of the performance of boiling, as opposed to purely expansive, MHD generators shows that the boiling section contributes 20 percent more energy per unit length and 360 percent more energy per unit volume. The higher effectiveness is attributed to the low void fraction prevailing in the boiler and to the large heat of vaporization peculiar to water.

Acknowledgment

The authors are pleased to acknowledge detailed discussions with Drs. E. S. Pierson and C. B. Reed of Argonne National Laboratory who suggested the study of the boiling MHD generator problem.

References

1 *Proceedings of the Rand Corporation Conference on Liquid-Metal MHD Power Generation,* Edited by R. V. Pei and S. W. Purnell R-2290-DOE, 1978.

2 Pierson, E. S., and Reed, C. B., Argonne National Laboratory, Argonne, Ill, Private Communication. Mar 1978.

3 Elliott, D. G., and Weinberg, E., "Acceleration of Liquids in Two-Phase Nozzles," NASA Technical Report 32-987.

4 Kaplan, W., *Advanced Calculus,* Addison-Wesley, New York, 1952.

5 Fabris, G., "Mixers and Surfactants," in *Proceedings of the Rand Corporation Conference on Liquid Metal MHD Power Generation,* Edited by R. V. Pei and S. W. Purnell, R-2290-DOE 1978.

6 Reed, C. B., Argonne National Laboratory, Private Communication, June 7, 1978.

Chung-Hsiung Li[1]
Specialist,
Engineering Mechanics Division,
Sargent and Lundy Engineers,
Chicago, Ill

The Effect of Bevel Angle on Safety Valve Vent-Pipe Systems

I Introduction

Theoretical study of vent-pipe systems is well documented, but no one has discussed the effect of a bevel angle on the vent-pipe as cited in the *Power Piping Code* [1]. The basic purpose of this investigation is to find the effect of bevel angle on vent-pipe discharge. For subsonic flow, the bevel angle will not affect the one-dimensional vertical flow, but for choked flow, the exit reaction force will act at an angle (ϕ) with the axis of the vent-pipe discharge. This reaction force direction (ϕ) is a function of bevel angle (θ), and the relationship is based on the ratio of momentum head to static pressure head at the vent-pipe exit. The detailed effect of a bevel angle on one-dimensional flow at the exit of a vent-pipe discharge will be analyzed in this paper.

II Analysis

The one-dimensional compressible flow in a discharge pipe is considered with the flow being choked at the discharge pipe exit. From the geometry at Fig. 1, the projected area of the ellipse plane in the x-direction is

$$A_x = \pi a^2 \cot\theta; \quad 0 < \theta \leq \frac{\pi}{2}, \tag{1}$$

where a is the radius of the discharge pipe, and in the y-direction

$$A_y = \pi a^2. \tag{2}$$

Consequently the force component in the x-direction will be

$$F_H = (P - P_a)\,\pi a^2 \cot\theta, \tag{3}$$

and in the y-direction,

$$F_V = \left(P - P_a + \frac{\rho V^2}{g_c}\right)\pi a^2, \tag{4}$$

where P, V and ρ are the mean pressure, mean velocity, and mean density of one-dimensional flow at the exit of the discharge pipe, respectively. P_a is the ambient pressure, and g_c (= 32.174 lbm-ft/lb$_f$ − s^2) is the inertia proportionality factor.

The projected area and force component in the x-direction are functions of (θ) as shown in equations (1) and (3). When (θ) is decreased, the projected area will increase, but the mean pressure at vent-pipe exit will decrease. Hence the horizontal force component will depend both on the projected area in the x-direction, and on the mean pressure.

The magnitude of the total reaction force at the exit plane of bevel discharge pipe can be expressed as

$$\begin{cases} \dfrac{F_R}{(P-P_a)\pi a^2} = \sqrt{\csc^2\theta + 2\left[\dfrac{\rho V^2}{(P-P_a)g_c}\right] + \left[\dfrac{\rho V^2}{(P-P_a)g_c}\right]^2}, & P > P_a, \ (5a) \\ F_R = \left(\dfrac{\rho V^2}{g_c}\right)\pi a^2, & P = P_a, \ (5b) \end{cases}$$

and the direction of reaction force with respect to the axis of the discharge pipe is

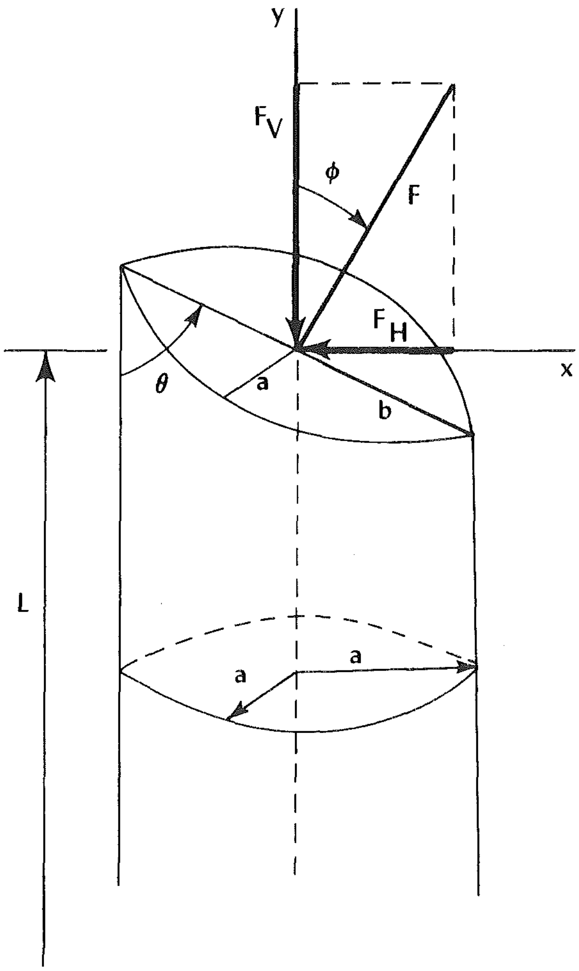

Fig. 1 Beveled vent-pipe exit

---

[1] Present Address: C-E Air Preheater Company, Andover Road, Wellsville, NY 14895.

Contributed by the Power Division for publication in the JOURNAL OF ENGINEERING FOR POWER. Manuscript received at ASME Headquarters September 11, 1980.

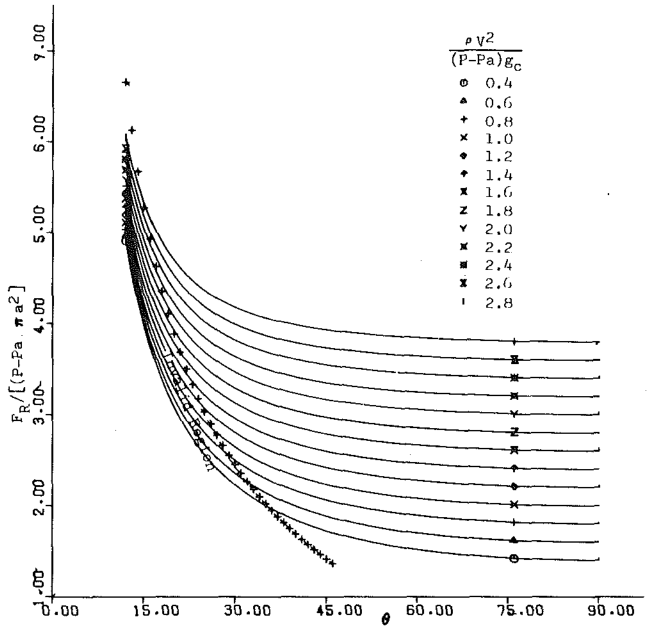

Fig. 2 Bevel angle effect on steady reaction force.

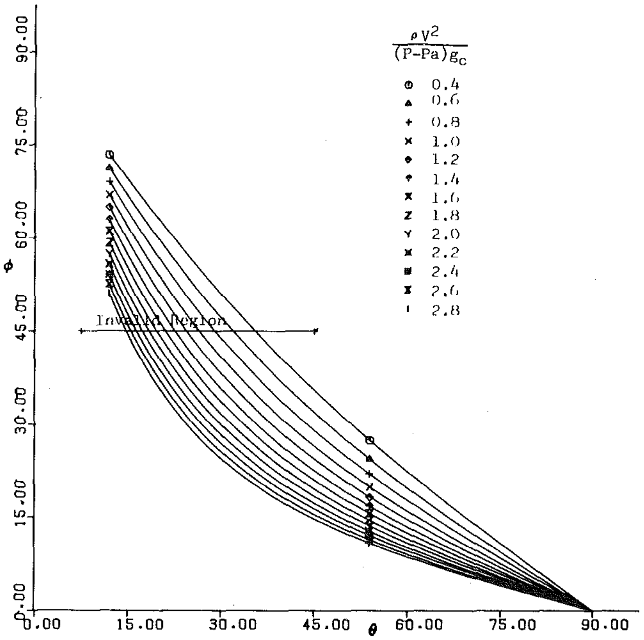

Fig. 3 Bevel angle effect on reaction force direction

$$\begin{cases} \phi = \tan^{-1}\dfrac{F_H}{F_V} = \tan^{-1}\left\{\dfrac{1}{\left[1+\dfrac{\rho V^2}{(P-P_a)g_c}\right]\tan\theta}\right\}, P > P_a, & (6a) \\ \phi = 0, \qquad\qquad P = P_a. & (6b) \end{cases}$$

The solutions of equations (5a) and (6a) are expressed in Figs. 2 and 3.

The mean pressure, mean velocity, and mean density are substituted in equations (3) and (4) with one-dimensional flow at the exit of the discharge pipe. Both force components in equations (3) and (4) will be the upper limits, i.e., exit turbulence or flow distortion are ignored. From momentum balance, the horizontal reaction force cannot be greater than the vertical reaction force, i.e., $F_H < F_V$. Equations (6a) and (6b) lead to the following constraints:

$$45 \text{ deg} > \phi \geq 0 \tag{7}$$

$$\tan^{-1}\left\{1/\left[1+\frac{\rho V^2}{(P-P_a)\,g_c}\right]\right\} < \theta \leq 90 \text{ deg}. \tag{8}$$

The limiting values of equations (7) and (8) are shown in Figs. 2 and 3; any attempt to increase the projected area in the x-direction beyond these limits results in an invalid force component in the x-direction.

III Conclusion

Compressible flow discharge through the bevel exit of a vent-pipe has been analyzed with a one-dimensional flow approach. The proposed analysis provides a simple and conservative method to compute the reaction force and its direction at the bevel angle exit of the vent-pipe. Note that equal signs do not appear in the left side of constraint equations (7) and (8). That is, the constraint equations cannot be applied at the upper bound, $F_H = F_V$. $F_V \gg F_H$ will be the optimum condition for application. The analysis of the bevel angle effect is useful in the design of vent-pipe anchors which must be capable of withstanding the moment generated by the horizontal and vertical components of the force in a beveled vent-pipe. The method of this paper leads to a conservative estimate of the magnitude of the unbalanced forces in the vertical and horizontal direction.

Reference

1 ASME, ANSI B31.1, *Power Piping*, American National Standard Code for Pressure Piping, 1977.

APPENDIX

In Fig. 7-1 on page 164 of the *Power Piping Code* [1] the pressure, velocity and flow rate at the exit of the vent-pipe have been computed assuming one-dimensional gas-dynamics; the data are

$$P = 51.4 \text{ psia},$$

$$V = 2116 \text{ ft/s},$$

$$W = 116.38 \text{ lbm/s (mass flow rate)}.$$

The bevel angle θ is 30 deg and the cross-sectional area of the vent pipe is 114.80 in^2.

Below is a comparison of the forces obtained from the same data using both methods.

	Code [1] method	Proposed method
The direction of reaction force (ϕ)	30 deg (by assumption)	31.59 deg (by calculation)
The horizontal force component	5931 lb$_f$	7297.41 lb$_f$
The vertical force component	10272 lb$_f$	11867.17 lb$_f$
Total reaction force	11861 lb$_f$	13931.33 lb$_f$

Note that the figures obtained by the proposed method are more than those obtained in the Code's [1] example.

Y. Hishinuma
Senior Researcher.

H. Akimoto
Researcher.

S. Azuhata
Researcher.

F. Nakajima
Department Manager.

S. Matsuda
Senior Researcher,
Hitachi Research Laboratory.

Y. Uchiyama
Senior Researcher,
Mechanical Engineering Research Laboratory.

R. Oshima
Assistant Chief Engineer,
Hitachi Works,
Hitachi Research Laboratory,
Hitachi, Ltd.,
3-1-1, Saiwai-cho,
Hitachi-shi,
Ibaraki-ken, Japan

M. Kato
General Group Manager,
Power Generation and Transmission Group,
Hitachi, Ltd.,
Nippon Bldg. 6-2, 2-chome,
Outemachi, Chiyoda-ku,
Tokyo, Japan

NOx Removal Process by Injection of NH_3 and H_2O_2 in Gas Turbine Exhaust Gas

For the removal of NOx in a gas turbine exhaust gas, the reduction of NO_x with NH_3 and H_2O_2 was studied. It was found that the addition of H_2O_2 very effectively lowered the reduction temperature of NO with NH_3 and that more than 90 percent NOx reduction could be attained at 550°C in the absence of O_2. However, the NOx reduction rate decreased with increases in the concentration of O_2, and NOx reduction was about 40 to 60 percent under gas turbine exhaust gas condition (15 percent O_2). In order to attain a high rate of reduction of NOx, a combined reduction process, which consisted of the homogeneous gas phase and the catalytic heterogeneous reactions, was also developed. The efficiency of the new process was proved in a pilot plant using half a size model of a 25-MW gas turbine combustor.

Introduction

Present day emission standards for nitrogen oxides (NOx) are strict and NOx emissions from gas turbines, as well as from other combustion devices, must be reduced. The conventional technologies which have been developed to decrease NOx emissions from gas turbines consist mainly of combustion modifications, e.g., fuel lean combustion [1], water or steam injection [1–5], two-stage combustion [1], *etc.* Water or steam injection is the most common method used, however, with this method, thermal efficiency decreases because of the heat lost in the form of steam from the stack. It is difficult to meet the present strict emission requirements in Japan, which are in some cases below 10 ppm, with combustion modification technology alone.

Gas turbine exhaust gas has features which distinguish it from the exhaust gases of other combustion devices such as boilers. The amount of excess air which is admixed in a turbine combustor is about three times as much as that which is admixed in a boiler of the same output power, and this causes the gas turbine to produce large amounts of exhaust gas. The oxygen concentration in the gas turbine exhaust gas is 14 to 16 percent and the temperature of the gas is 400 to 600°C.

Two NOx reduction methods which use NH_3 have already been developed for boilers, the homogeneous gas phase reduction and the heterogeneous catalytic reduction methods. The catalyst for treating the boiler flue gas, which is used in the temperature range of 300 to 400°C, is not suitable for the treatment of the gas turbine exhaust gas because of its high temperature. In addition, the catalytic reduction method is uneconomical when applied to gas turbines because of the large volume of the exhaust gases. On the other hand, the gas phase reduction method using NH_3, which was developed by Exxon Research and Engineering Company [6, 7] is economical, because of its simplicity. However, this method is highly temperature sensitive and is effective only within a narrow temperature range, 800 to 1050°C. It has also been reported by Exxon that the addition of H_2 lowers the reaction temperature to about 700°C, but, even so, performance would be poor under the 400 to 600°C conditions of gas turbine exhaust gases.

Therefore, efforts have been made to reduce NOx with NH_3 at lower temperatures without catalyst and to develop a catalyst with a high temperature reactivity.

Contributed by the Gas Turbine Division for publication in the JOURNAL OF ENGINEERING FOR POWER. Manuscript received at ASME Headquarters September 29, 1980.

This paper describes the lowering of the temperature of the gas phase reduction of NOx with NH_3 to about 500°C by adding H_2O_2 and a catalyst which was developed to reduce NOx in the 400 to 600°C temperature range. Both laboratory scale and pilot plant (1000 Nm^3/hr) tests were carried out.

Experimental Apparatus and Procedures

Laboratory Scale Test. The homogeneous gas phase reactions were studied in the flow system shown in Fig. 1. A 1 m long Pyrex tube with an inner diameter of 40 mm was used as a reactor vessel, except for the experiments of high temperature reaction of NO with NH_3, in which a quartz tube of the same dimensions was used. Reactants were passed through the electrically heated reactor. A gas mixture, consisting of NO, NH_3, O_2 and N_2, was preheated and aqueous solution of H_2O_2 was sprayed into the N_2 stream and injected into the reactor. The amount of H_2O_2 injected was controlled by changing the concentration of the H_2O_2 solution. Calibrated rotameters were used to control the flow rate of each reactant and to set the total flow rate at 100 Nml/s.

The NOx concentration was measured by a chemiluminesence monitor and NH_3 and H_2O_2 concentrations were determined by chemical analyses.

The experimental conditions were varied over a wide range to study the characteristics of the reactions.

Catalyst activity on the reaction of NO with NH_3 was studied in an apparatus similar to the one mentioned above. A Pyrex tube with an inner diameter of 20 mm was heated to 350° to 600°C by an electrical furnace. The reactor contained a 7 ml catalyst bed of 7 to 8 mesh size catalyst. A simulated exhaust gas was passed through the catalyst bed at a rate of 50 Nml/s, producing a space velocity of 25,000 hr^{-1}.

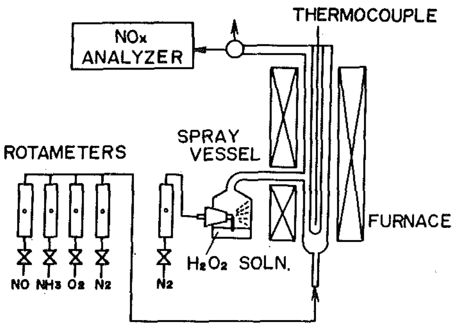

Fig. 1 Experimental apparatus for Laboratory test

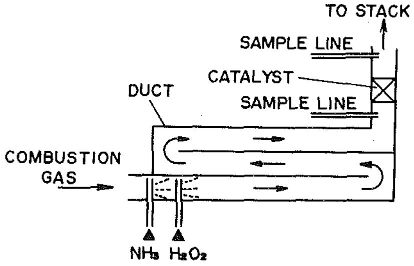

Fig. 2 1000 Nm^3/hr test schematic

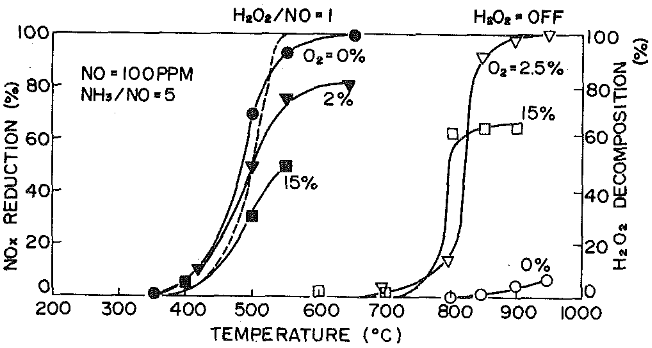

Fig. 3 Relationship of NOx reduction and temperature on NO-NH_3-O_2 and NO-NH_3-H_2O_2-O_2 reactions

1000 Nm^3/hr Pilot Plant Test. The pilot plant, which is shown in Fig. 2, consisted of a stainless steel duct with a square cross section and a catalyst bed, was used to verify the laboratory tests. The duct was 300 × 300 mm in cross section and 15 m long. An exhaust gas flow of 1000 Nm^3/hr from a half size model of one combustor of a 25 MW gas turbine, comprising of ten combustors, was introduced into the duct, and NH_3 and H_2O_2 were injected at the duct inlet. The composition of the exhaust gas was 40 to 200 ppm NO_x, 15 to 16 percent O_2, 4 percent CO_2, 4 percent H_2O and the remainder N_2, to which NH_3 and H_2O_2 were injected in an NH_3/NOx mole ratio of 1 to 5 and H_2O_2/NOx in a ratio of 0 to 1. The concentration of NOx in the exhaust gas was controlled by combustion modification. A special high temperature catalyst which was developed by Hitachi was placed in the duct. The volume of catalyst (4 to 6 mm spheres) supplied was 59, 38 and 16 l, producing a space velocity of 17,000, 26,000 and 63,000 hr^{-1}, respectively.

Results and Discussion

Effect of H_2O_2 Addition on Reaction of NO with NH_3. The composition of exhaust gas of a modern gas turbine is 40 to 200 ppm NO and 14 to 16 percent O_2, and the temperature is 400 to 600°C. The conditions vary widely, depending on the kind of fuel used, combustion modifications, application of water and/or steam injection, load conditions, etc. Taking these facts into consideration, NOx reduction studies were conducted over a wide range of conditions with the laboratory scale apparatus.

Figure 3 shows the effect of H_2O_2 addition on the reduction of NO with NH_3. The NOx reduction with or without H_2O_2 is shown as a function of temperature and O_2 concentration. In the absence of H_2O_2, the NOx reduction rate proceeded in the presence of excess O_2 at temperatures above 800°C. This is in agreement with the results obtained by Lyon [6]. However, the temperature at which the reaction proceeded was lowered by about 300°C by adding H_2O_2, and the NOx reduction occurred even at 500°C.

In Fig. 3, the broken line shows the decomposition rate of H_2O_2 to hydroxyl radicals, which was calculated from Baulch's kinetic data [8].

$$H_2O_2 + M \rightarrow \cdot OH + \cdot OH + M$$

$$k = 1.2 \times 10^{17} \exp\left(-\frac{2290}{T}\right) \text{cm}^3\,\text{mole}^{-1}\,\text{s}^{-1}$$

$$(M = N_2) \qquad (1)$$

The coincidence of the temperature of H_2O_2 decomposition with that of NOx reduction is consistent with the assumption that both the reaction of NH_3 with hydroxyl radicals to produce amino radicals and the reaction of the amino radicals with NO are very fast. This will be discussed later in detail.

When H_2O_2 was added in the absence of O_2, the NOx reduction proceeded at a higher rate. However, the NOx reduction rate decreased with an increase in concentration of O_2. This suggests that the amino radicals produced by the hydrogen abstraction reaction from NH_3 are oxidized by O_2 to form NO and NO_2, as is explained later in this paper.

Effects of the Amount of H_2O_2 and NH_3 on NOx Reduction. The dependence of the NOx reduction rate on the amount of H_2O_2 was studied using a gas mixture which contained 100 ppm NO, 500 ppm NH_3, 0, 2, or 15 percent O_2, and 0 to 500 ppm H_2O_2

In addition to the NOx reduction to N_2, an oxidation reaction to NO_2 was also observed in the NO-NH_3-H_2O_2-O_2 reaction system. Figure 4 shows the relation of the NOx reduction and the NO_2 production to the molar ratio of H_2O_2/NO. When O_2 was not present, the NOx reduction rate increased linearly with the increase in H_2O_2, and NO_2 was not observed to form. In the presence of O_2, the NOx reduction rate reached a maximum value when H_2O_2/NO was about unity. In this case, the rate of formation of NO_2 increased with the increase in H_2O_2. Considering that NO_2 did not form in the absence of O_2, it seems that NO_2 is formed by the reaction of the amino radical with O_2. This reaction was reported by Bull [9] who studied the oxidation of NH_3 using a shock tube.

The effect of the amount of NH_3 on the NOx reduction was studied using a gas mixture which contained 100 ppm NO, 15 percent O_2, 200, 300, or 500 ppm NH_3, and 20 to 140 ppm H_2O_2 at 550°C. The NOx reduction and the NO_2 formation are shown as a function of the H_2O_2/NO ratio at a constant NH_3/NO ratio in Fig. 5. It can be seen that as the NH_3/NO ratio increases, the NOx reduction increases, while the NO_2 formation decreases. When the H_2O_2/NOx ratio was small, the NOx reduction was little affected by the NH_3/NO ratio. This fact suggests that NH_3 is oxidized by H_2O_2 to form NO and NO_2.

Effect of Inlet NO Concentration on NOx Reduction. The NOx reduction with NH_3 in the presence of H_2O_2 was studied in the range of inlet NO concentrations of from 40 to 200 ppm, at $NH_3/NO = 3$, $H_2O_2/NO = 1$, 15 percent O_2 and at a temperature of 550°C. The results are given in Fig. 6. It was found that the NOx reduction rate increased regularly as the inlet NO concentration increased. The NOx reduction rate is approximately proportional to the 0.43 power of the inlet NO concentration.

Pathway of Homogeneous Reaction of NO with H_2O_2 and NH_3. The reaction mechanism of the homogeneous reaction of NO with NH_3 in the presence of H_2O_2 can be formulated, as illustrated in Fig. 7.

If the experimental results obtained in the present study are combined with those obtained by others, then the following elementary reactions can be obtained for the homogeneous reduction of NO:

$$H_2O_2 + M \rightarrow \cdot OH + \cdot OH + M \qquad (1)$$

$$NH_3 + \cdot OH \rightarrow \cdot NH_2 + H_2O \qquad (2)$$

$$\cdot NH_2 + NO \rightarrow N_2 + H_2O \qquad (3)$$

$$\cdot NH_2 + \cdot OH \rightarrow \cdot NH + H_2O \qquad (4)$$

$$\cdot NH + NO \rightarrow N_2 + \cdot OH \qquad (5)$$

The decomposition of H_2O_2 into the hydroxyl radicals shown in equation (1) [10, 11] can be assumed to be the rate determining reaction. The hydroxyl radicals produced abstract hydrogen from NH_3 in reaction (2) [12, 13], and then the amino radicals, which are very reactive with NO [14], reduce NO to nitrogen and water in reactions (3–5).

Two side reactions, which interrupt the NO reduction reaction, can also be assumed. One of them is the oxidation of the amino radicals with oxygen. Though it is well known that amino radicals are more reactive with NO than O_2, the oxidation of amino radicals proceeds in the presence of high concentrations of O_2 because the concentration of O_2 (15 percent), relative to that of NO (100 ppm), is extremely high in this experiment. The following scheme, which was proposed by Bull [9], explains the formation of NO_2.

$$\cdot NH_2 + O_2 \rightarrow HNO + \cdot OH \qquad (6)$$

$$HNO + \cdot OH \rightarrow NO + H_2O \qquad (7)$$

$$HNO + O_2 \rightarrow NO_2 + \cdot OH \qquad (8)$$

The other side reaction is the oxidation of NO by H_2O_2. In the decomposition of H_2O_2, other intermediate radicals, such as oxygen atoms and HO_2 radicals, which are active oxidizing agents, are also formed. The following NO oxidation reactions with these radicals have already been reported [8, 15].

$$NO + \cdot O + M \rightarrow NO_2 + M \qquad (9)$$

$$NO + \cdot HO_2 \rightarrow NO_2 + \cdot OH \qquad (10)$$

Therefore, these oxidation reactions would proceed at a high rate in the presence of excess H_2O_2.

If the above reaction mechanism is assumed to be correct, then the experimental results that were obtained can be explained qualitatively. A decrease in NOx reduction with increasing concentration of O_2 is caused by the side reactions shown in equations (6–8), and a decrease with excess H_2O_2 is caused by the side reactions shown in equations (9) and (10).

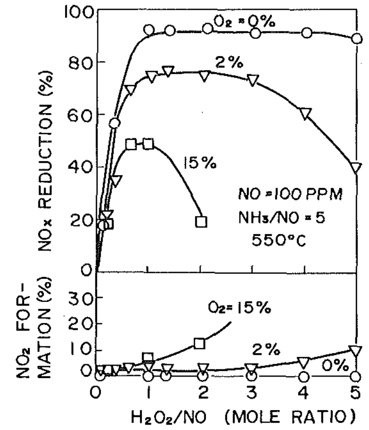

Fig. 4 Effects of H_2O_2 and O_2 concentrations on $NO\text{-}NH_3\text{-}H_2O_2\text{-}O_2$ reaction

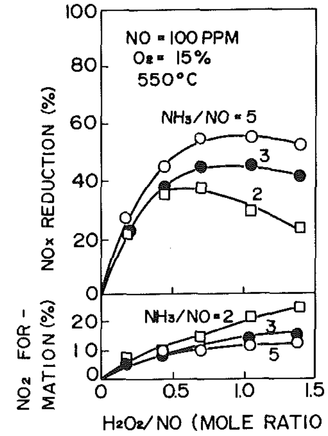

Fig. 5 Effects of H_2O_2 and NH_3 concentration on $NO\text{-}NH_3\text{-}H_2O_2\text{-}O_2$ reaction

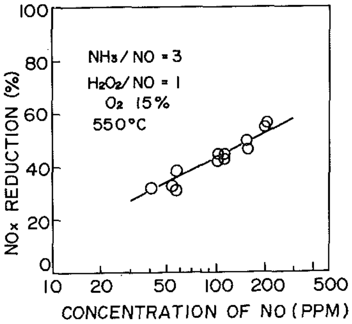

Fig. 6 Effect of inlet NO concentrations on $NO\text{-}NH_3\text{-}H_2O_2\text{-}O_2$ reaction

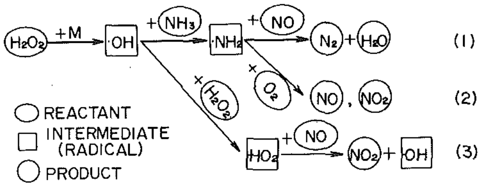

Fig. 7 Mechanism of $NO\text{-}NH_3\text{-}H_2O_2\text{-}O_2$ reaction

Activity of Newly Developed Catalyst. The catalyst which has been developed to treat gas turbine exhaust gas is composed of a refractory metal oxide of group IV element (about 90 atom percent) and transition metal oxides. In Fig. 8, the activity of this catalyst is shown as the NOx reduction versus temperature. The catalyst is highly active over the wide temperature range of 400 to 600°C. Since this temperature range covers the temperature of gas turbine exhaust gas, this catalyst is suitable for NOx reduction with NH_3 in gas turbines.

1000 Nm^3/hr Pilot Plant Test. A pilot plant test was carried out in a large scale reactor using a combustion exhaust gas to verify the laboratory data. Figure 9 shows the dependence of NH_3 concentration on NOx reduction at various initial NOx concentrations. As in the laboratory scale tests, the NOx reduction depended on the amount of NH_3 and the inlet NOx concentration. The NOx reduction efficiency was 40 to 60 percent, depending on the inlet NOx concentration. This homogeneous gas phase reduction is very simple and is as effective as steam or water injection. However, when NOx reduction requirements become stricter, the homogeneous gas phase and the catalytic reduction are also necessary.

The catalyst activities on the reduction of NOx with NH_3 in the presence and in the absence of H_2O_2 were measured at a space velocity of 67,000 hr^{-1} (Fig. 10). It can be seen from the figure that the performance of the combined process, consisted of the gas phase and the catalytic reduction components, is better than that of the catalytic reduction alone. The percentage of NOx reduction of the combined process was higher than the percentage of reduction that was calculated for either gas phase or catalytic reduction alone. This demonstrates that H_2O_2 injection is also very effective in catalytic reduction.

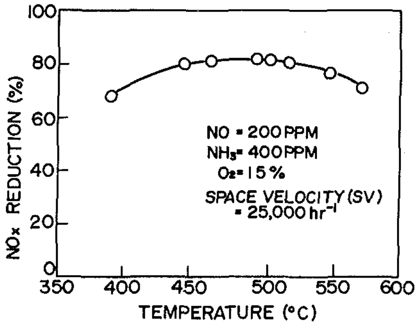

Fig. 8 Activity of catalyst on NO-NH_3-O_2 reaction

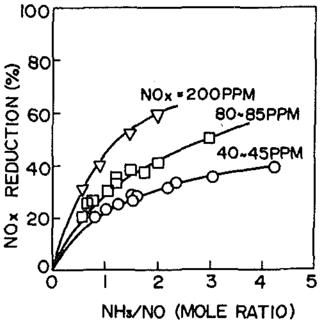

Fig. 9 Gas phase NOx reduction without catalyst (Pilot test)—Gas mixture: 40 to 200 ppm NOx(2 to 4 ppm NO_2), 15 percent O_2, $H_2O_2/NO = 0.75$, Temperature: 520 to 550°C

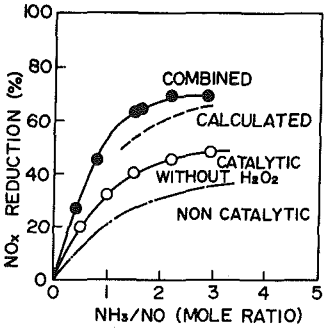

Fig. 10 Catalytic NOx reduction with or without H_2O_2(Pilot test)—Gas mixture:40 to 45 ppm NOx(2 ppm NO_2), 15 percent O_2, 30 ppm H_2O_2, 60 to 120 ppm NH_3, Space velocity: 63,000 hr^{-1}, Temperature: 520 to 550°C

The net reduction of the combined process at various space velocities is shown in Fig. 11. In this process, high rates of NOx reduction can be achieved by selecting the amount of the catalyst.

Proposal of a NOx Removal Process for Gas Turbines. Based on the results of this investigation, the process shown in Fig. 12 was proposed for the treatment of NOx from gas turbine exhaust gas. NH_3 and H_2O_2 are injected into the exhaust gas at a temperature of about 550°C. The process essentially consists of two parts, a homogeneous gas phase reaction zone and a catalyst bed.

When 40 to 60 percent NOx removal is required, the catalyst bed is not needed. In order to attain a higher reduction of NOx, a catalyst bed must be installed. However, the volume of the catalyst bed in this process is much smaller than that of the one which is used in the catalytic reduction process.

Conclusion

A gas phase homogeneous reduction process and a combined process which consisted of the gas phase homogeneous reduction plus the catalytic reduction were developed to remove NOx in gas turbine exhaust gases. Using the combined process and combustion modification, high NOx reduction would be achieved.

Also, in order to test and further refine this new NOx reduction process, a demonstration plant of 50,000 Nm^3/hr, which is now under operation, was constructed.

References

1 White, D. J., Roberts, P. B., and Compton, W. A., "Low NOx Emission Combustor for Automobile Gas Turbine Engines," EPA Contract No. 68-04-0016, Feb. 1973.

2 Ingebo, R. D., and Norgen, C. T., "Effect of Primary-Zone Water Injection on Pollutants from a Combustor Burning Liquid ASTM A-1 and Vaporized Propane Fuels," NASA TN D-7293, May 1973.

3 Markowski, S. J., Lohmann, R. P., and Reilly, R. S., "The Vortex Burner—A New Approach to Gas Turbine Combustor," ASME Paper No. 75-GT-20.

4 Rossbach, R. J., "Development of Low Emission Porous-Plate Combustor for Automobile Gas Turbine and Rankine Cycle Engines," EPA Contract No. 68-01-0461, Sep. 1973.

5 Dowson, D. W., Hanson, K. A., and Holder, R. C., "Low NOx Emission Combustor Development for Automobile Gas Turbine Engines," EPA Contract No. 68-04-0014, Feb. 1973.

6 Lyon, R. K., "Method for Reducing of the Concentration of NO in Combustion Effluents Using Ammonia," US Patent 3,900,554, Aug 19, 1975.

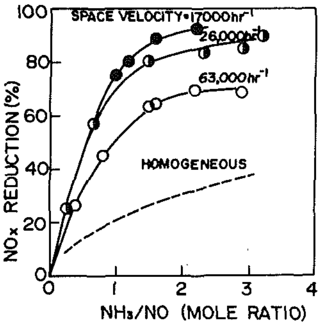

Fig. 11 NOx reduction by combined gas phase and catalytic reduction (Pilot test)—Gas mixture: 40 to 45 ppm NOx (2 ppm NO_2), 15 percent O_2, 30 ppm H_2O_2, Temperature: 520 to 550°C

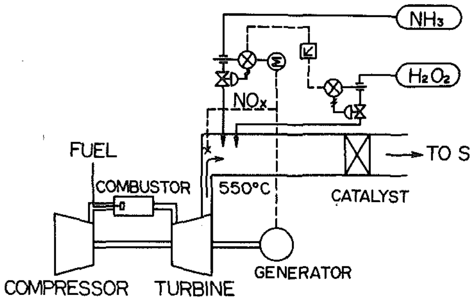

Fig. 12 Proposed process for the reduction of NOx from gas turbine exhaust gas by NH_3 and H_2O_2 injection

7 Bartok, W., "Noncatalytic Reduction of NOx with NH_3," *Proceedings of the 2nd Stationary Source Combustion Symposium,* Vol. II, EPA Report No. EPA-600/7-77-0736, July 1977, pp. 145–157.

8 Baulch, D. L. et al., *Evaluated Kinetic Data for High Temperature Reactions,* 1st ed., Vol. 1, Butterworth, London, 1972, pp. 365–375.

9 Bull, D. C., "A Shock Tube Study of the Oxidation of Ammonia," *Combustion and Flame,* Vol. 12, Dec. 1968, pp. 603–610.

10 Baldwin, R. R. and Brattan, D., "Homogeneous Gas-Phase Decomposition of Hydrogen Peroxide," *8th Symposium on Combustion,* The Combustion Institute, 1960, pp. 110–119.

11 Meyer, E., Olschewski, H. A., Troe, J., and Wagner, H. Gg., "Investigation of N_2H_4 and H_2O_2 Decomposition in Low and High Pressure Schock Waves," *12th Symposium on Combustion,* The Combustion Institute, 1968, pp. 345–355.

12 Wolfhard, H. G., and Parker, W. G., "A New Technique for the Spectroscopic Examination of Flames at Normal Pressures," *The Proceedings of the Physical Society,* Section A, Vol. 62, Part 11, Nov. 1949, pp. 722–730.

13 Perry, R. A., Atkinson, R., and Pitts, J. N. Jr., "Rate Constants for the Reactions $OH + H_2S$ $H_2O + SH$ and $OH + NH_3$ $H_2O + NH_2$ over the Temperature Range 297 − 427°K," *The Journal of Chemical Physics,* Vol. 64, No. 8, Apr. 15, 1976, pp. 3237–3239.

14 Gesser, H., "The Photolysis of Ammonia in the Presence of Propane and Oxygen," *Journal of the American Chemical Society,* Vol. 77, May 1955, pp. 2626–2629.

15 Cox, R. A., and Derment, R. G., "Kinetics of the Reaction of HO with Nitric Oxide and Nitrogen Dioxide," *Journal of Photochemistry,* Vol. 4, 1975, pp. 139–153.

A. R. Giaquinta
Institute of Hydraulic Research
The University of Iowa
Iowa City, Iowa 52242
Mem. ASME

Once-Through Cooling Potential of the Middle and Lower Mississippi River During Low Flow Conditions

The once-through cooling potential of the Middle and Lower Mississippi River has been computed for the seven-day, ten-year low flow by the steady-state Iowa Thermal Regime Model. Longitudinal temperature distributions are shown with existing power plants and future power plants proposed through 1995. Permissible future plant additions based on current thermal standards also are determined. It is shown that even if thermal standards were based on low flow conditions, no existing or proposed future power plants will violate present thermal standards, and the total permissible future fossil-fueled power plant capacity along the study reach ranges from about 70,000 to 90,000 MW depending on the temperature base used. It also is shown that the total consumptive water use for existing and proposed future plants should cause no problems even during periods of low flow.

Introduction

The public demand for cheap electrical power tends to encourage utility companies to seek low-cost methods of generating electricity. On the other hand, the public also demands that air and water pollution be minimized and conservation of natural resources be maximized. Unfortunately, these demands oppose each other, since low cost fuels and low cost techniques of power generation usually lead to increased air and water pollution, and cleaner methods of power generation are costlier and usually involve consumption of more fuel and water.

Consideration of these points in light of an expanding power industry is but one indication of the need for long range planning of the siting and sizing of future power plant installations. Of particular interest in the present study is the effect of discharging large amounts of heated water from power plants using once-through condenser cooling systems to the Middle and Lower Mississippi River (downstream from the southern Iowa border) during low flow conditions.

Once-through cooling is known to be one of the most effective methods for condenser cooling. This technique is efficient economically, generally involving the lowest capital and operating costs of all cooling systems, and it is efficient thermodynamically, generally allowing lower condenser temperatures and, hence, higher steam-cycle efficiencies. Of all the condenser cooling systems in current use, except for dry cooling towers, evaporative water losses are lowest with once-through cooling. Of course, once-through cooling suffers from the disadvantage of discharging large amounts of heat to natural waterbodies, which may be detrimental ecologically. The current need of our nation to generate as well as conserve energy demands the optimum (including ecological protection) allocation of natural resources which requires knowledge of the assimilative capacity of major rivers.

There are several large steam-electric power plants which utilize once-through condenser cooling systems located along the Middle and Lower Mississippi River. Within the next two decades, more once-through-cooled power plants are proposed for installation along this river reach. It is important to consider the cumulative effects of the existing as well as the future power-plant discharges to determine the future once-through cooling potential of the river. It is also necessary to consider the availability of water for use in once-through cooling and the amount of evaporative water loss.

The steady-state version of the Iowa Thermal Regime Model (ITRM), a numerical model for the calculation of streamwise temperature distributions in rivers, was used to determine the existing and future thermal regimes of the Middle and Lower Mississippi River. The computational model is basically a heat balance equation relating the rate of convective heat transfer, the rate of surface heat exchange between the river and the atmosphere, and the rates of heat input from power plants or other artificial (unnatural) heat sources and tributary inflows. The major processes of heat transfer between the water surface and the atmosphere include short- and long-wave radiation, evaporation, and conduction. The computational model is briefly presented in the Appendix.

Thermal regimes of the Middle and Lower Mississippi River are determined for the extreme (seven-day, ten-year low flow) hydrological condition and average meteorological conditions with existing power plants and proposed future plants (through 1995). Permissible future plant additions based on current thermal standards also are determined.

It is shown that even if the thermal standards are based on low flow conditions, no existing or proposed future power plants will violate the present thermal standards. The total capacity of additional future plants which are permissible along the study reach according to present thermal standards ranges from 71,300 to 90,200 MW for fossil-fueled plants (49,400 to 63,400 MW for nuclear-fueled plants) depending on the temperature base being used. These new plants must be properly spaced to avoid the cumulative effects of upstream heat loads.

It is not suggested that all of the permissible power plants be constructed since there are obviously several other ecological hazards that must be considered. This study simply indicates the potential once-through cooling capacity of the river based on current regulations of thermal discharges.

Contributed by the Power Division and presented at the Winter Annual Meeting, 1978. Revised manuscript received for publication in the JOURNAL OF ENGINEERING FOR POWER Oct. 2, 1980.

Description of the Middle and Lower Mississippi River

The Upper Mississippi River extends from the source to the mouth of the Ohio River for a distance of about 1370 mi, and the Lower Mississippi River is from the mouth of the Ohio River to the Gulf of Mexico, a distance of about 980 mi. The reach of interest is shown in Fig. 1. Locations along the Upper Mississippi are identified by river miles measured along the channel upstream from the intersection of the thalwegs of the Ohio and Mississippi Rivers. Along the Lower Mississippi, distances are measured in river miles upstream from Head of Passes, La. When it is necessary for clarification, distances above the Ohio River are labeled AOR and those along the Lower Mississippi, AHP (above Head of Passes).

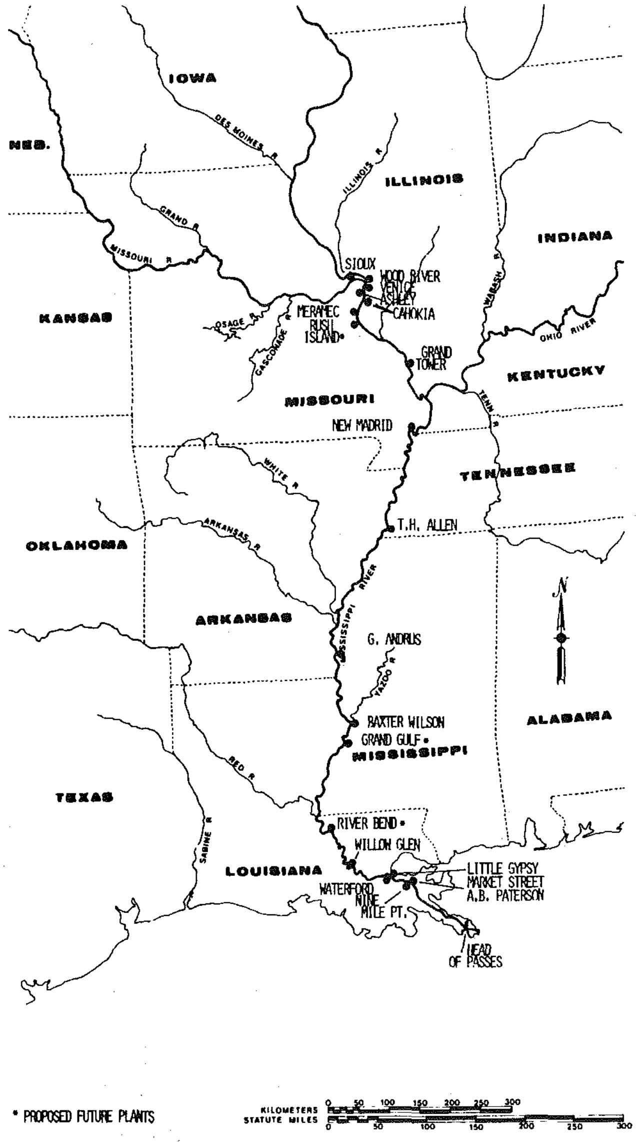

Fig. 1 Middle and lower Mississippi River showing locations of existing and proposed future thermal power plants

The present study is concerned with the river reach from about Keokuk, Iowa (mile 361 AOR), to Head of Passes (mile 0 AHP), a distance of about 1320 mi. The short reach of the Upper Mississippi included in this study is referred to herein as the Middle Mississippi to avoid confusion with the major portion of the Upper Mississippi.

The climatic conditions along the river are represented by data from seven class A weather stations located along or close to the Mississippi River. Monthly mean values of daily weather data for the 20-year period from 1954 to 1973 were used in the analysis. The locations of the stations and tables of data are given by Giaquinta and Keng [1].

The lowest average flow for a period of seven consecutive days which may occur once in ten years (seven-day, ten-year low flow) is commonly used to determine water supply potential for power plant use. Table 1 shows the seven-day, ten-year low flow values at eleven gaging stations which are used to establish the "worst case" conditions in the thermal regime study. These data were obtained from references [2] and [3].

The thermal standards for states along the Mississippi River are given in reference [1]. The maximum allowable temperature rise resulting from thermal discharges into the river is 5°F (2.78°C) at the edge of the mixing zone along the length of the Mississippi River considered in the present study. The standards also include a maximum allowable water temperature, but the allowable temperature increase is the governing standard in all cases.

There are 18 existing once-through cooled power plants (as of Jan. 1975) with a total of 58 units located along the Mississippi River downstream from the southern Iowa border, as shown in Fig. 1. The loading and cooling system characteristics of these power plants are listed in Tables 2 and 3.

The total installed plant capacity using once-through cooling is about 14,000 MW. All existing power plants employ fossil fuel. The total plant capacity using once-through cooling proposed for installation along the study reach through 1995 is about 3600 MW. Information describing these future plants is listed in Table 4. Because of delays in the availability of pertinent data related to this study, certain power plants which were proposed when the study was made may now be existing. (Data for the year ended Dec. 31, 1974 were not published until Sept. 1978.) Several other power plants are proposed for con-

Table 1 Summary of 7-Day, 10-Year Low Flows

Gaging Station	River Mile	Period	Flow Rate (cfs)
Keokuk	364.2 AOR	1880–73	10,950
Alton	202.7 AOR	1934–67	20,860
St. Louis	180.0 AOR	1934–69	37,800
Chester	109.9 AOR	1934–67	41,800
Thebes	43.7 AOR	1934–67	43,800
Hickman	922.0 AHP	1945–70	111,000
Memphis	734.8 AHP	1945–70	115,000
Helena	663.3 AHP	1945–70	118,000
Arkansas City	554.1 AHP	1929–70	120,000
Vicksburg	430.4 AHP	1933–67	121,000
Tarbert Landing	306.3 AHP	1938–70	103,000

Nomenclature

A = river cross-sectional area
B = river top width
c_p = specific heat of water
E = longitudinal dispersion coefficient
P = power plant capacity
Q = river discharge
Q_c = condenser flow rate
T = river temperature
t = time
TI = rate of heat input from power plants and tributary inflows per unit length along the stream
x = distance along channel
ΔT_c = condenser temperature rise
ΔT_R = allowable river temperature rise
Δx = mesh width
η_I = in-plant losses
η_p = overall thermal efficiency
ρ = density of water
ϕ^* = surface heat-exchange rate
ϕ_B = net long-wave radiation leaving the waterbody
ϕ_E = heat loss by evaporation
ϕ_H = heat loss by conduction
ϕ_R = net short-wave radiation entering the waterbody
ϕ_S = heat loss by melting of snow

struction before 1995, but they are planned for closed-cycle cooling systems and are not included in this study. Major thermal discharges from industries (other than power plants and municipalities) along the river also are considered in the calculation of river temperature. However, most of these heat loads are very small compared with those from power plants and have little effect, as determined from National Pollutant Discharge Elimination System (NPDES) permit applications supplied by EPA. A description of the computational model utilized for the present study is given in the Appendix.

Thermal Regimes

The steady-state ITRM, equation (3), was used to determine the temperature distribution along the Mississippi River for the hydrological condition of the seven-day, ten-year low flow during the months of August and November, taken as the worst case condition because of meteorological effects on the surface heat exchange. River top widths were determined corresponding to the flow rates for the study months using stage-discharge relationships and hydrographic survey maps obtained from the U.S. Geological Survey and the U.S. Army Corps of Engineers. Several assumptions related to the interpretation and use of the available data and the presentation of the results are listed as follows: (1) The upstream boundary condition temperatures near Keokuk, Iowa (mile 361 AOR), were obtained from Paily, et al. [3]; (2) The thermal discharges included only those from steam-electric power plants using once-through cooling systems with capacities greater than 50 MW; thermal effluents from industries and municipalities located along the main stem of the river were found, from National Pollutant Discharge Elimination System (NPDES) permit applications supplied by the EPA, to be negligible; (3) The thermal impacts of tributary streams were neglected except for the Ohio and Missouri Rivers. Treatment of the thermal inputs of these tributaries is discussed under assumptions 8 and 9; (4) River discharges, climatological variables, and channel top widths were assumed to vary linearly between measuring stations with two exceptions: (i) the main stem flow rate downstream from Tarbert Landing, Mississippi, was assumed to be constant and equal to the value at Tarbert Landing [1]; (ii) solar radiation and cloud cover downstream from New Orleans, La. were assumed to be constant and equal to the value at New Orleans; (5) All existing, future proposed, and future permissible power plants were assumed to be operating at full load, and load capacity factors were not considered; (6) Site selection of future permissible plants was based only on the maximum heat uptake capacity of the river, and physical, geological, or socio-economical factors were not considered; (7) The mixing zone of thermal discharges was assumed to be immediately downstream of the outfall structures and to occupy the full width of the river cross section. In other words, complete mixing of the effluent with the entire river flow was assumed. This assumption seems rather restrictive, but the model was shown to yield very good results in verification studies [3, 5]; (8) The natural and existing temperatures of the Missouri River downstream from the southern Iowa border have been computed by Giaquinta and Keng [1]. For the determination of the future permissible plants, it was assumed that the Missouri River would have its maximum thermal effect at the confluence with the Mississippi River. The temperature of the Missouri River at its mouth was, therefore, assumed to be 5°F (2.78 °C) above the natural or existing temperature depending on the base being considered. The thermal input to the Mississippi River then may be simply included in an analysis; (9) Computation of the natural temperature of the Ohio River is beyond the scope of the present study. Since the existing temperature of the Mississippi and Ohio Rivers is known, it was assumed that the natural and future temperature differences are equal to the known existing temperature difference. This assumption seems reasonable because experience with the Missouri and Mississippi Rivers shows that these temperature differences are quite close to each other.

Table 2 Existing* Power Plants Along the Middle Mississippi River

Power Plant	River Mile (AOR)	Rated Capacity MW_e	Condenser flow rate cfs	Temp rise °F
Sioux	209.5	1100	876	20.9
Wood River	199.6			
#1–3		150	453	6
#4		112.5	148	13
#5		387	311	23
Venice	182.4			
#1,2		80	184	17.5
#3,4		196	364	16
#5,6		198	342	17
Ashley	179.7	70	285	20
Cahokia	178.2	300	857	20
Meramec	161.7			
#1,2		275	356	15.5
#3		289	258	22.3
#4		359	314	21.2
Grand Tower	82			
#3		76	196	8.6
#4		110	140	15.2

* The term "existing" implies data which were available at the time of the study and includes the period up to Jan. 1, 1975.

Table 3 Existing* Power Plants Along the Lower Mississippi River

Power Plant	River Mile (AHP)	Rated Capacity MW_e	Condenser flow rate cfs	Temp Rise °F
New Madrid #1	884.5	650	713	24
Thomas H. Allen	725.7	990	768.6	20
R. E. Ritchie	661.2			
#1		359	312	25
#2		545	373	30
Gerald Andrus	537	750	425.5	35
Baxter Wilson	436			
#1		544.6	374	28
#2		783	522	28.3
Willow Glen	201.5			
#1		163.2	169	20
#2		239.4	212	20
#3		591.8	512	20
#4		591.8	512.5	22.3
Waterford, #1,2	129.6	860	975	19
Little Gypsy	128.8			
#1		247.8	321	25
#2		420.8	477	22
#3		582.3	595	19
Ninemile Point	103.9			
#1		69	109	17
#2		112.5	147	16.9
#3		169.8	170	20.6
#4		783	897	16
#5		783	897	16.5
Market St.	96.5			
#11		30	84.6	11.7
#12		37.5	84.6	12.0
#13		28.8	78.1	10.9
A. B. Paterson	92.7	224	334.3	17.8

* The term "existing" implies data which were available at the time of the study and includes the period up to Jan. 1, 1975.

Table 4 Future Proposed* Once-Through-Cooled Power Plants Along the Middle and Lower Mississippi River

Power Plant	River Mile	Rated Capacity MW_e	Condenser flow rate cfs	Temp Rise °F	Scheduled in-service date
Rush Island	140 AOR				
#1		621	615	20	2/76
#2		621	615	20	/77
New Madrid #2	884.5 AHP	600	713	24	6/77
Willow Glen #5	201.5 AHP	580	572.9	20	4/76
Waterford #3	129.4 AHP	1165	2172.3	16	1/81

* The term "future proposed" implies power plants proposed for construction after Jan. 1, 1975. Some of the proposed power plants may be presently existing.

Four temperature profiles for each study month were predicted as explained below. Thermal regimes were computed under ambient conditions of the seven-day, ten-year low flows at all gaging stations along the river, combined with average weather conditions for the months of August and November.

1 **Natural Thermal Regime.** The natural thermal regime is the temperature distribution that would exist if all the unnatural heat loads were absent. It is a function only of the hydrological, meteorological, and natural inflow and outflow conditions. Surface heat exchange with the atmosphere and the convective transport of heat are the most important factors controlling the natural thermal regime. The natural thermal regime must be known to identify the effects of thermal effluents on the natural conditions of a river; it also serves as a base to predict the thermal regime of future permissible plants.

2 **Temperature Distribution with Existing Heat Loads.** This temperature profile combines the natural river temperature and existing heat loads which include power plants and major thermal discharges from industries and municipalities. Existing power plants are those in operation before Jan. 1975; they are listed in Tables 2 and 3.

3 **Temperature Distribution with Existing and Future Proposed Power Plants.** Analysis is made including the combined effects of heat loads from existing plus proposed new power plants assuming these proposed plants operate at full capacity. Details of these future plants are given in Table 4. If the present temperature standards are violated, the future plants are assumed to operate with some fraction of closed-cycle cooling.

4 **Temperature Distribution with Permissible New Plants According to Existing Thermal Standards.** In addition to the existing and future proposed heat loads, the most desirable sites for future plants in terms of maximum heat assimilation capacity of the river were chosen, and capacities of these future permissible once-through-cooled plants were computed. Obviously, heat assimilation capacity is only one of several environmental criteria used for power plant site selection. Therefore, it is not suggested that all of the permissible power plants can be installed. Each power plant would have to be considered from the basis of all the governing regulations. Existing thermal standards were used to determine the permissible heat assimilation capacity of the river for the low flow conditions. However, when applying the criterion of the "allowable temperature rise," i.e., 5°F (2.78°C), there is some uncertainty concerning which temperature base (either natural or existing), should be used. Thus, the thermal regime analysis was carried out using each base to determine the sites and capacities of future permissible plants. It is obvious that the natural-temperature base would produce more conservative results than the existing-temperature base which will permit the addition of more heat loads to the river eventually limited by maximum temperature standard.

The local remaining cooling capacity of the river at any location is related to the heat rejected through the condenser which is a function of the condenser flow rate, Q_c, and temperature rise, ΔT_c, by

$$Q\Delta T_R = Q_c \Delta T_c \qquad (1)$$

in which Q = river flow rate and ΔT_R = allowable temperature rise of the river. The condenser parameters are related to the power plant capacity, P, overall thermal efficiency, η_p, and in-plant losses, η_I, by

$$Q_c = 15.194\,(P/\Delta T_c)[(1 - \eta_I)/\eta_p - 1] \qquad (2)$$

in which Q_c is computed in cfs, P is given in MW, and ΔT_c is in °F. The permissible capacity of the plant may be calculated from equation (2) after the condenser flow rate is determined from equation (1) for a known condenser temperature rise. It is assumed herein that η_p = 36 percent, η_I = 15 percent, ΔT_c = 18°F for fossil-fueled plants.

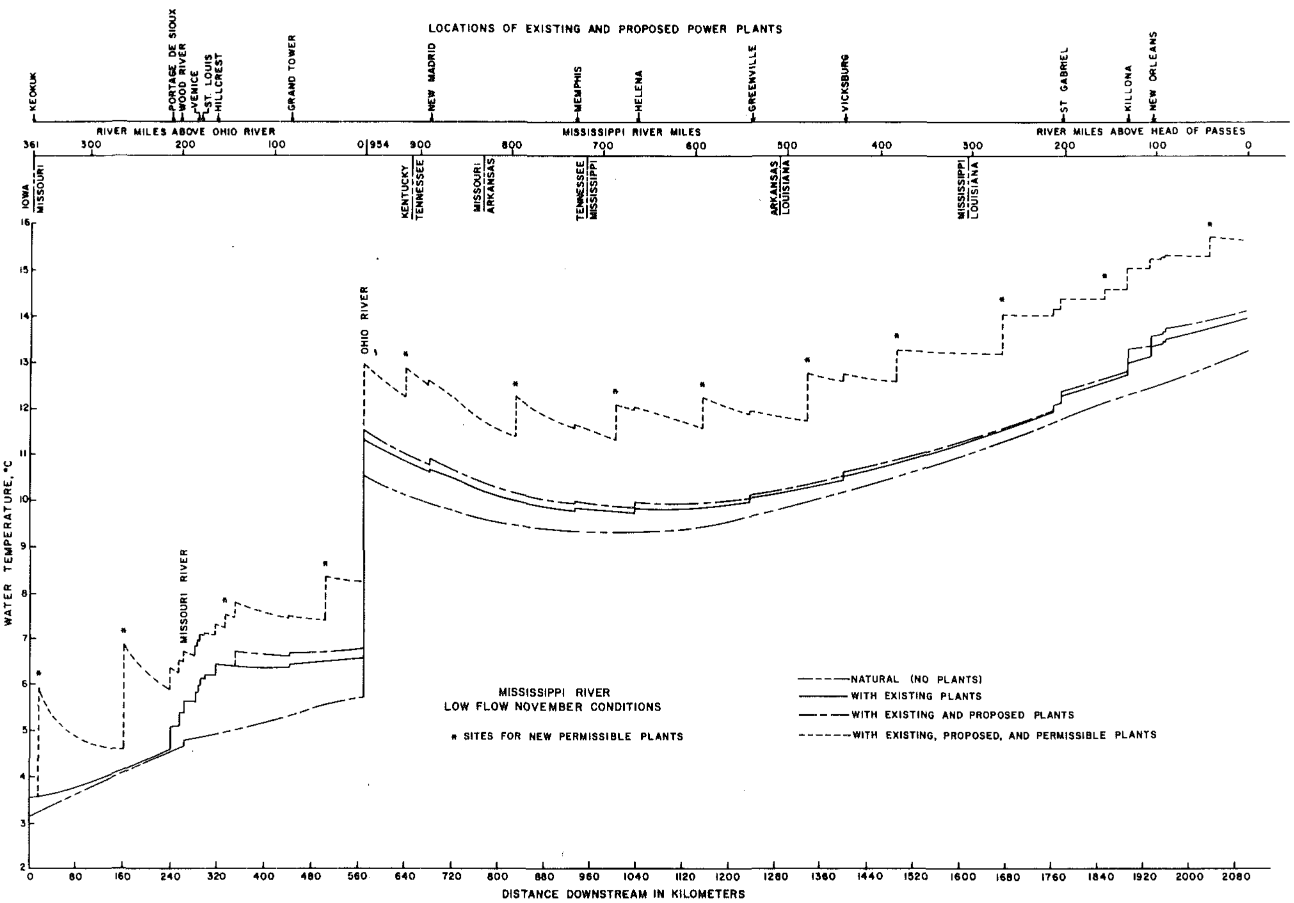

Fig. 2 Temperature distributions for low flow conditions with permissible new plants determined from the natural-temperature base

Cooling Water Requirements and Consumptive Use

In using natural waterbodies for once-through condenser cooling, it is important to consider the availability of water and the consumptive water use. The amount of cooling water required by a power plant depends on the overall plant efficiency, type of cooling system and the temperature rise across the condenser. The temperature rise varies with cooling water discharge and plant heat rate. Also ambient water temperature and water quality requirements influence the magnitude of the allowable temperature rise.

As shown in Tables 2–4, existing and future proposed steam-electric power plants having total capacities of several thousand megawatts are located or planned for future installation along the Middle and Lower Mississippi River. It is important to make accurate estimates of the cooling water requirements of future power plants to aid in decision-making and planning. Condenser cooling water flow rate for a power plant may be calculated from equation (2), if the plant capacity, condenser temperature rise, overall thermal efficiency, and in-plant losses are known. The condenser design and efficiencies of future plants usually are not known and must be estimated. As mentioned, reasonable values of power plant efficiencies and condenser temperature rises can be assumed, and condenser flow rates can be calculated. By assuming that the heat dissipated by evaporation is 50 percent of the heat rejected in the condenser, the Federal Energy Regulatory Commission [7] has shown that the water consumption of power plants using once-through cooling is about one percent of the condenser flow rate. The condenser flow rates of existing power plants along the study reach total about 15,100 cfs, and the condenser flow rates of future proposed plants which will employ once-through cooling is about 4700 cfs. There are also some existing and proposed power plants using closed-cycle cooling systems which take make-up water from the Mississippi River. The consumptive use of these power plants roughly may be estimated as one percent of the condenser flow rate which totals about 1100 cfs for existing plants and about 5200 cfs for proposed future plants [1]. The total consumptive water use for existing and future plants proposed for construction through 1995 will be about 260 cfs. Consideration of the seven-day, ten-year low flow for the Mississippi River indicates that the future consumptive water use should cause no problems.

Presentation and Discussion of Results

Figures describing the thermal regimes of the Middle and Lower Mississippi River for the conditions previously discussed are given in this section. As mentioned, the allowable temperature rise of 5°F (2.78°C) was the limiting criterion for the entire study reach. Application of this temperature criterion verified that no heat loads from existing and future proposed power plants would violate existing standards, so closed-cycle cooling systems are not required.

Locations and capacities of permissible future power plants based on river temperature standards depend on the remaining allowable heat assimilation capacity of the river. The plant sites are chosen arbitrarily, with proper consideration of existing or proposed heat loads, and are spaced approximately 100 miles apart. After a location is chosen, the maximum permissible capacity of the plant may be calculated by using equations (1) and (2).

The thermal regimes at the extreme hydrological conditions of the seven-day, ten-year low flow combined with average weather conditions for the months of August and November were computed. It was found that the November conditions were more critical, and the temperature distributions for that month are shown in Fig. 2 for existing, proposed, and permissible new plants referred to the natural-temperature base. Table 5 summarizes the locations and capacities of the future permissible plants. If capacities and locations of permissible new plants are determined from the existing-temperature base, the temperature distributions are shown in Fig. 3, and the details

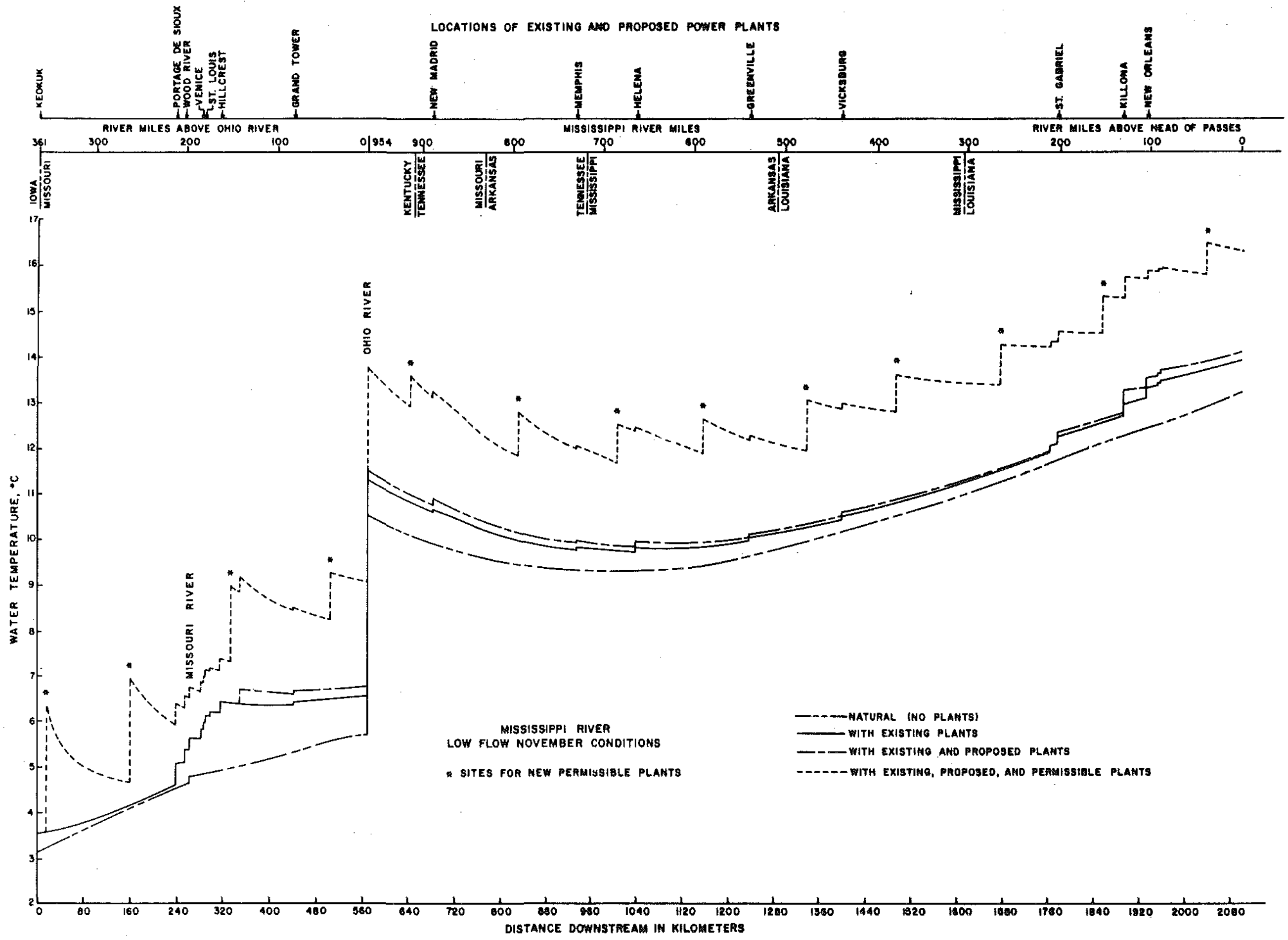

Fig. 3 Temperature distributions for low flow conditions with permissible new plants determined from the existing-temperature base

are summarized in Table 5. It is seen that there are no power plants operating at full load which will violate the temperature standards. It should be noted that the Ohio and Missouri Rivers cause a temperature increase of the main stem Mississippi. Also, the increased main stem flow rate, particularly downstream from the Ohio River, diminishes the thermal effects of heated effluents, and the thermal behavior of the main stem is very similar to the natural behavior with the temperature magnitude raised by the thermal input of the Ohio River. For the natural-temperature base, 13 future power plants are permissible with a total capacity of 71,300 MW for fossil-fueled plants. For the existing-temperature base, thirteen new plants also are allowable, with a total capacity of about 90,200 MW for fossil-fueled plants. If any nuclear-fueled plants were installed, permissible capacities would be about 31 percent lower.

For the purpose of comparison, Fig. 4 shows the temperature distributions corresponding to average flow and weather conditions for the month of November. Thermal regimes based on these ambient conditions for the months of February, May, August, and November (representing the four seasons of a year) are given by Giaquinta and Keng [1]. A summary of the capacities and locations of permissible future plants for the natural-temperature base is given in Table 6. Of course, multiple unit installations are implied in some cases. The average river flows for the month of November also are given to aid in the interpretation of Fig. 4. It is seen that if thermal standards were based on average river flows, there are 11 additional locations available for new once-through-cooled plants. The allowable capacity of each new plant is given in Table 6. A total capacity of about 80,300 MW for fossil plants is possible along the study reach. Of course, if the existing-temperature base were considered with average flow conditions, the total permissible future capacity would be higher as given in reference [1].

In comparing Fig. 2 with Fig. 4, it is interesting to note the sharp difference in the rate of temperature decay. For the low flow case, the temperature increase due to each thermal discharge is greater than that for the average flow case. However, the temperature decay rate is higher for the low flow allowing two more sites for new plants than the average flow case allows. The capacities of most of the permissible new plants are higher for the average flow case, but for the power plants located at mile 41.7 AOR, mile 264.8 AHP, and mile 40.2 AHP, the permissible capacities are higher for the low flow case. This apparent anomaly occurs because the rapid temperature decay in the low flow case eliminates some of the problems caused by the cumulative effects of upstream plants.

The seven-day, ten-year low flow may occur only rarely, but it is applied by some states in assessing environmental impacts of power plants. The present paper, therefore, emphasizes this extreme hydrological condition. However, the flow rate of the lower Mississippi River is so large (even at the seven-day, ten-year low flow) that the

Table 5 Locations and Capacities of Permissible Power Plants at Low Flow

River Mile	River Flow Q(cfs)	Permissible Plant Capacity**-MW Natural Base	Permissible Plant Capacity**-MW Existing Base
351.2*	11,700	2497	2836
258.9*	17,400	3245	3436
149.9*	39,500	994	5931
41.7*	45,100	3772	4093
907.9	111,300	6547	6847
789.5	113,800	8882	9771
681.4	117,200	7906	8703
588.2	119,400	6423	7263
475.4	120,600	10,470	11,204
378.5	121,400	7530	8674
264.8	103,000	7522	7679
154.8	103,000	1596	7221
40.2	103,000	3931	6548

* River Mile above Ohio River; all others are River Mile above Head of Passes.

** Fossil-fueled plant capacities, nuclear-fueled capacities would be about 31 percent lower.

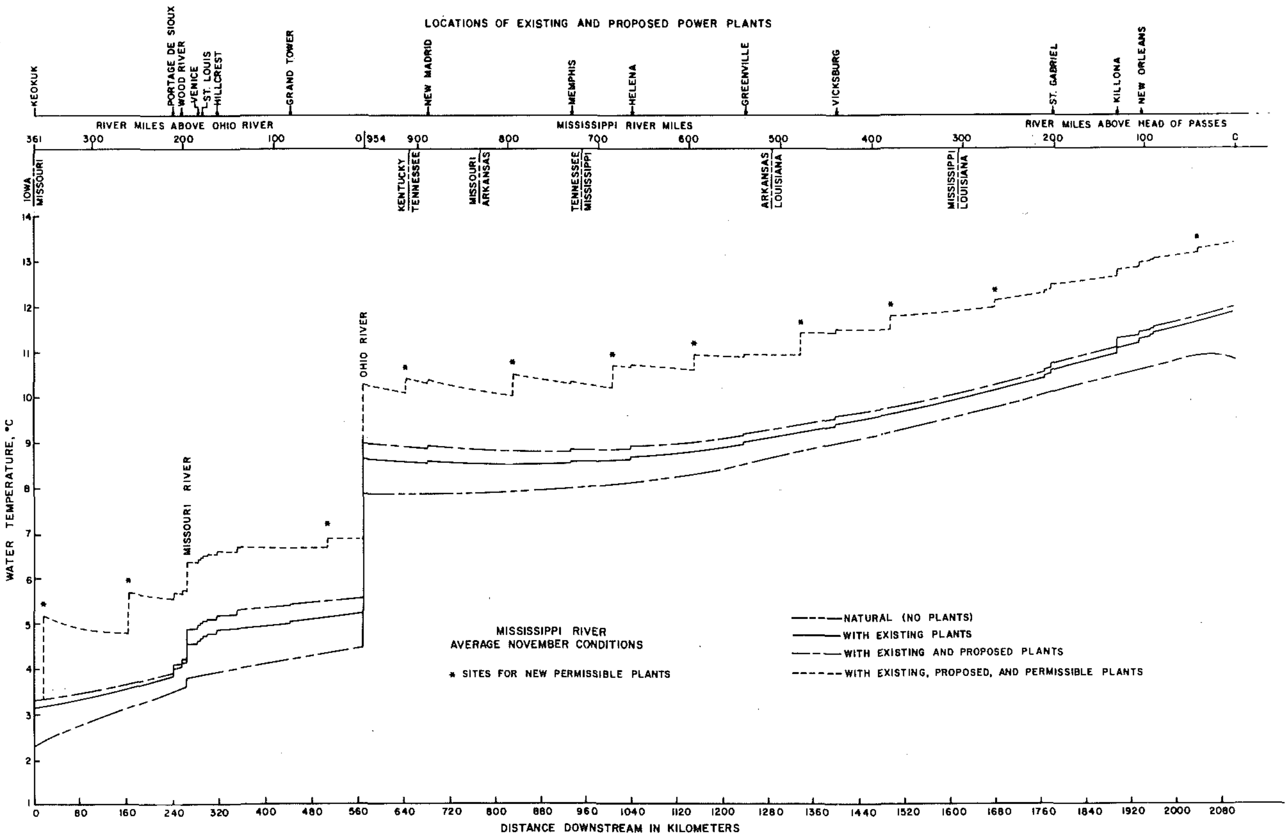

Fig. 4 Temperature distributions for average flow conditions with permissible new plants determined from the natural-temperature base

Table 6 Locations and Capacities of Permissible Power Plants Based on Predicted Natural Temperatures at Average Flow

River Mile	Nov. River Flow Q(cfs)	Permissible Plant Capacity** (MW)
351.2*	49,916	8110
258.9*	62,382	4785
41.7*	141,383	2372
907.9	262,691	7436
789.5	277,385	11,189
681.4	270,002	11,262
588.2	280,715	7869
475.4	317,075	13,512
378.5	353,296	8494
264.8	239,000	3504
40.2	239,000	1766

* River Mile above Ohio River; all others are River Mile above Head of Passes.
** Fossil-fueled plant capacities, nuclear-fueled capacities would be about 31 percent lower.

total permissible capacity of future power plants at the low flow condition is only about 10 to 25 percent (depending on the temperature base) lower than the allowable capacity determined from average flow conditions.

The validity of the numerical results was tested against field measurements reported by Dragnich, et al. [8] showing observed temperature distributions along reaches of the Lower Mississippi River for 1972. Average observed river temperatures for the months of February, May, August, and November at several stations were taken from these curves. The ITRM was used to calculate the average river temperatures at the same locations. The upstream boundary condition chosen for the calculation was the observed temperature at Canton, Mo. (mile 343 AOR). Meteorological and hydrological data for the four study months of 1972 were used, and the average river temperatures were computed. The results of the computations downstream from mile 800 AHP together with the observed average temperatures are shown in Fig. 5.

The computed results are seen to agree fairly well with the observed temperatures (a difference of less than 1°C) except for the stations downstream from mile 250 during the months of February and August. This discrepancy is due most likely to the assumption that the solar radiation and cloud cover downstream from New Orleans are constant and equal to the New Orleans values. Uncertainties about flow rate data at locations close to the Gulf of Mexico also may lead to computational errors. In general, the comparison is seen to be quite acceptable, and it enhances the confidence in using ITRM for thermal regime calculations of large rivers.

Conclusions

An analysis of the thermal regimes of the Mississippi River downstream from the southern Iowa border during the seven-day, ten-year low flow condition is presented. The results show that under present thermal regulations, the river has adequate heat transfer and assimilation capacities to handle all of the waste heat from power plants planned for installation through 1995. In addition it is shown that the total capacity of additional future power plants which may use once-through cooling ranges from 71,300 MW to 90,200 MW for fossil-fueled plants depending on the temperature base which is employed. If thermal standards were based on average flow conditions, the permissible future capacity would be about 10 to 25 percent greater.

The total condenser cooling water requirement for existing and future once-through-cooled power plants proposed for installation along the study reach through 1995 is about 19,800 cfs. The consumptive water use of these plants plus that of existing and proposed future plants employing closed-cycle cooling systems is estimated to be about 260 cfs.

It is thus seen that the Middle and Lower Mississippi River has tremendous capacity for future once-through-cooled power plants. However, to take full advantage of this capacity careful planning related to siting new plants and proper design of cooling water discharge structures will be necessary.

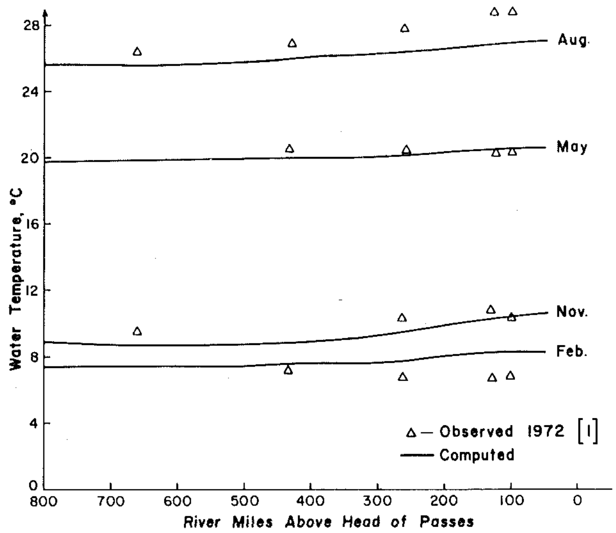

Fig. 5 Comparison of computed and observed temperatures

Acknowledgment

This project was financed in part by a grant from the U.S. Department of the Interior, Office of Water Research and Technology under Public Law 88-379 as amended, and made available through the Iowa State Water Resources Research Institute. During the data gathering phase of the project, several state and federal agencies, utility companies, and electric reliability councils supplied needed information. Special acknowledgment is due to the Federal Power Commission, U.S. Environmental Protection Agency, U.S. Geological Survey, U.S. Army Corps of Engineers, and several power companies and utilities located along the river. Grateful acknowledgment is due to Mr. T. C. Keng who carried out the computations leading to the results presented herein. Funds for computer time were provided by the Graduate College of The University of Iowa.

References

1 Giaquinta, A. R., and Keng, T. T. C., "Thermal Regimes of the Mississippi and Missouri Rivers Downstream from the Southern Iowa Border," IIHR Report No. 211, Jan. 1978, Iowa Institute of Hydraulic Research, The University of Iowa, Iowa City.

2 Lower Mississippi Region Comprehensive Study Coordinating Committee, "Lower Mississippi Region Comprehensive Study," Appendix C, Vol. 1, Regional Climatology Hydrology & Geology, 1974.

3 Paily, P. P., Su, T.-Y., Giaquinta, A. R., and Kennedy, J. F., "The Thermal Regimes of the Upper Mississippi and Missouri Rivers," IIHR Report No. 182, Oct. 1976, Institute of Hydraulic Research, The University of Iowa, Iowa City.

4 Paily, P. P., and Kennedy, J. F., "A Computational Model for Predicting the Thermal Regimes of Rivers," IIHR Report No. 169, Nov. 1974, Institute of Hydraulic Research, The University of Iowa, Iowa City.

5 Paily, P. P., and Kennedy, J. F., "Evaluation of River Thermal Regime Models," *Advances in Water Resources*, Vol. 1, No. 4, 1978.

6 Paily, P. P., Macagno, E. O., and Kennedy, J. F., "Winter-Regime Surface Heat Loss from Heated Streams," IIHR Report No. 155, Mar. 1974, Institute of Hydraulic Research, The University of Iowa, Iowa City.

7 Federal Energy Regulatory Commission, "Steam-Electric Plant Air and Water Quality Control Data," (for the year ended Dec. 31, 1974 based on FPC Form No. 67) Summary Report, DOE/FERC-0018, Sept. 1978, Federal Energy Regulatory Commission, Washington, D.C.

8 Dragnich, D. W., Myhres, A. S., and Jaske, R.T., "Assessment of Lower Mississippi River Thermal Capacity Phase I," Oct. 1974, Battelle Pacific Northwest Laboratories, Richland, Washington.

APPENDIX

Computational Model

Governing Equation and Numerical Technique. The general differential equation that describes the conservation of heat in an elemental volume of water in a river is three-dimensional and unsteady. However, in most streams large temperature gradients in the transverse and vertical directions occur only in the near-field regions of sites where thermal loads are imposed. In considering the overall thermal regime of a river, the zones of the three-dimensional effects usually are small compared to the lengths of the river reaches, and, therefore, a one-dimensional formulation may be employed.

The one-dimensional, unsteady, convection-diffusion equation expressing the conservation of thermal energy in a free surface flow may be expressed as

$$\frac{\partial T}{\partial t} + \frac{Q}{A}\frac{\partial T}{\partial x} - \frac{1}{A}\frac{\partial}{\partial x}\left(AE\frac{\partial T}{\partial x}\right) = \frac{B}{A}\frac{\phi^*(T)}{\rho c_p} + \frac{TI}{A\rho c_p} \qquad (3)$$

in which T = cross-sectional average temperature, t = time, x = streamwise distance along the channel, Q = river discharge, A = cross-sectional area of flow, E = longitudinal dispersion coefficient, B = top width of the river flow section, ϕ^* = rate of surface heat exchange between the water and the atmosphere, TI = rate of heat input from power plants and tributary inflows per unit length along the stream, ρ = density of water, and c_p = specific heat of water. The first four terms of the equation represent four different mechanisms of heat transport in the river, namely, the local rate of change of temperature, the heat advected by the current, the heat dispersed by turbulent transport processes, and the heat transferred by the air-water interfacial transport processes, respectively. The last term of the equation includes the rate of artificial heat input and the rate of tributary heat inflow.

In examining the thermal regime of a river, it frequently suffices to determine the steady-state temperature distributions corresponding to average meteorological, hydrological, and thermal loading conditions, implying that the local temperature change with respect to time is zero. Also, since longitudinal dispersion makes only a very small contribution to the energy-balance equation, it may be neglected. So for steady-state conditions, equation (3) may be written

$$\frac{dT}{dx} = \frac{B}{Q}\frac{\phi^*(T)}{\rho c_p} + \frac{TI}{Q\rho c_p} \qquad (4)$$

This equation can be solved to obtain the steady-state longitudinal distribution of temperature in a river.

A computational technique to solve equation (3), the Iowa Thermal Regime Model (ITRM), was developed by Paily and Kennedy [4]. The steady-state version of ITRM was employed to study the thermal regimes of the Upper Mississippi and Missouri Rivers [3] and was validated in that study by comparing numerical results with measured field temperature data along both rivers [5]. The steady-state ITRM also is used to predict the temperature distributions in the present study. To compute the temperature distribution along a river from equation (4) the total river length is divided into a convenient number of reaches. Each reach is subdivided into a finite-difference grid defined by a number of meshpoints, and the solutions for adjacent reaches are linked by the common conditions at the junction node points connecting them.

If the temperature at any meshpoint, x_i, is T_i, the temperature at the next meshpoint, x_{i+1}, which is at a distance Δx downstream is given by

$$T_{i+1} = T_i + (\Delta x)\left[\frac{(B_{i+1}+B_i)/2}{(Q_{i+1}+Q_i)/2}\right]\frac{\phi^*_{i+1/2}}{\rho c_p} + \frac{1}{(Q_{i+1}+Q_i)/2} \times \left[\frac{(TI)_{i+1}}{\rho c_p}\right] \qquad (5)$$

in which $\phi^*_{i+1/2}$ is the surface heat exchange rate corresponding to $T_{i+1/2}$, the temperature at the middle of the mesh space, Δx. With a proper adjustment of the mesh space from Δx to $\Delta x/2$, this equation may be used to compute $T_{i+1/2}$ (in terms of ϕ^*_i) which is needed to calculate $\phi^*_{i+1/2}$. So if the temperature at the upstream boundary (i = 1) is known, equation (5) can be used to calculate the temperature at downstream meshpoints $i = 2, 3 \ldots N$, where N is the total number of meshpoints for the entire length of the reach under consideration.

In the above equations the rate of surface heat exchange, $\phi^*(T)$, the principal factor influencing the thermal regimes of rivers, depends upon several climatic factors, including solar radiation, air temperature, wind speed, relative humidity, atmospheric pressure, and cloud cover. The most important processes included in the mechanism of heat transfer between the water surface and the atmosphere are the net short-wave radiation entering the waterbody, ϕ_R ;the net long-wave radiation leaving the waterbody, ϕ_B; evaporation, ϕ_E; conduction, ϕ_H; and the melting of snow, ϕ_S. The heat transfer process is expressed as

$$\phi^* = \phi_R - \phi_B - \phi_E - \phi_H - \phi_S \qquad (6)$$

Equations for computing the components of surface heat exchange are given elsewhere [1, 3].

The input data required for the model include (1) river mile at the upstream boundary; (2) river temperature at the upstream boundary; (3) number and spacing of meshpoints in each reach; (4) top widths of the river at selected stations along the river; (5) main stem river flow rates at selected locations and tributary inflows; (6) weather conditions at suitable locations along or close to the stream including air temperature, wind speed, relative humidity, cloud cover, cloud height, visibility, atmospheric pressure, and solar radiation; and (7) thermal discharges into the river from power plants and other sources. It was assumed that flow rates, climatological data, and top widths varied linearly between measuring stations, and linear interpolation was used to distribute these variables from the measuring stations to each meshpoint.

Journal of Engineering for Power

Discussion

An Experimental Study of Endwall and Airfoil Surface Heat Transfer in a Large Scale Turbine Blade Cascade[1]

S. V. Horn.[2] The authors have made a remarkable contribution to heat transfer measurement in a large scale turbine cascade. Their measurement of the Stanton number distribution not only reflects the heat loads to the turbine passage, but also, according to Reynolds analogy, the skin friction coefficient distribution over the blade.

Since the cascade design without the boundary layer control can be understood as the design with a suitable skin friction coefficient distribution, the released data of the Stanton number distribution indicate a slight possibility of the more efficient cascade design. For the given turbine flow conditions, the mentioned design would apply small deceleration before the maximum curvature region in order to achieve near-to-separation state of boundary layer (skin friction coefficient and Stanton number closer to zero). It would also result in lower heat load in this region.

Author's Closure

While it is true that a near-to-separation state of the boundary layer could result in lower heat transfer coefficients in this region, designs of earlier stage turbine airfoils are strongly dependent on the trade off between aerodynamic and heat transfer performance. The airfoil used in the referenced test reflects the geometry most suitable for satisfying the operating characteristics for a specific gas turbine engine.

A near-to-separation state of the boundary layer and a corresponding reduction in heat transfer coefficient in this region could, in principle, be achieved by a redesign of the airfoil. However, for a prescribed load coefficient the redesigned airfoil may not necessarily result in a more efficient cascade design. A near separating boundary layer on the suction surface of the airfoil, obtained through a local curvature change or increased diffusion, will result in a higher shape factor in the trailing edge region of the airfoil. This condition will most likely give higher losses for the redesigned airfoil. Near-to-separation airfoils, which result from controlled diffusion design concepts,[3] are more suitable for compressor applications because such airfoils have relatively higher diffusion than turbine airfoils.

---

[1] By R. A. Graziani, M. F. Blair, J. R. Taylor, and R. E. Mayle, published in the April issue of the ASME JOURNAL OF ENGINEERING FOR POWER, Vol. 102, No. 2, 1980, pp. 257–267.

[2] Research and Advanced Product Development, Transamerica Delaval Inc., P.O. Box 8788, Trenton, NJ 08650.

[3] Liebeck, R. H., "On the Design of Subsonic Airfoils for High Lift," AIAA Paper No. 76-406, presented at AIAA 9th Fluid and Plasma Dynamics Conference, San Diego, CA, 1976.

Application of Abrasive Coatings to Clearance Control in the Gas Turbine[1]

E. F. Finkin.[2] Thank you for inviting my discussion of this paper. As a wear authority, it has long been my contention that much good would come from the coordination of this field with practical application areas such as gas turbines [1–3].

The authors have developed a meaningful and seemingly reliable test method for this type of problem. This development is extremely valuable in its own right.

Plasma spraying, aluminum oxide, chromium carbide, tungsten carbide, silicon carbide, and chromium oxide, with or without the binders nickel-aluminide, cobalt and nickel-chromium, have been virtually studied to death over the last 20 years in the development of gas bearings. In a gas bearing you want wear resistance, noncatastrophic failure in a rub plus integrity aspects (e.g., adherence, thermal stability).

Vogan and Stetson have looked at these same materials systems from a different point of view—their ability to abrade contacting surfaces rather than their ability to resist being worn by contacting surfaces. Essentially, what they found is that what makes these materials systems good bearing surfaces also unfortunately makes them poor choices for use in abrading vane tips.

The paper creates some confusion in presenting the data which the authors must clear up. The text contains the phrase "as evident in Table 1, the baseline abrasive was aluminum oxide," although Table 1 contains no mention of aluminum oxide. The authors' discussion in referring to Table 1 lists seven tested materials systems, the latter two being NiCr bonded chromium carbide and NiAl bonded chromium carbide, but the table lists only six tests. A table is needed specifically listing the test material and its binder for each test in Table 1.

The paper concludes that coating RC-1, a proprietary composition of Solar which contains a low temperature inorganic binder, is best for this application. Earlier in the paper it is stated that RC-1 contains an epoxy binder. Well, which is it? It seems to me that successful long term clearance control in operation would necessitate use of a high-temperature inorganic bonder (say, a silicate). A coating containing an organic or low-temperature binder would chemically degrade or soften at high temperature, leading to coating failure which would increase the clearance by the width of the missing coating.

Additional References

1 Finkin, E., "Abrasive Wear," *Evaluation of Wear Testing*, ASTM STP 446, The American Society for Testing and Materials, 1969, pp. 55–90.

2 Finkin, E., "Wear—A Critical Review," *Journal of Japan Society of Lubrication Engineers*, Vol. 24, 1979, pp. 13–24.

3 Finkin, E., "Adhesive Wear," *Materials in Engineering Applications*, 1979, pp. 154–161.

---

[1] By J. W. Vogan and A. R. Stetson, published in the January 1980 issue of the ASME JOURNAL OF ENGINEERING FOR POWER, Vol. 102, pp. 113–119.

[2] Vice President, Allegheny Ludlum Industries, Inc., 2 Olive Plaza, Pittsburgh, Penn. 15222

Author's Closure

The first question refers to the data in Table 1. Unfortunately, during review of the paper a data table from another paper became interchanged with the one intended for this paper. A copy of the correct Table 1 is shown here. It lists nine material systems rather than seven. Four of these (including RC-1) are based on the use of aluminum oxide as the abrasive ceramic phase. The corrected Table 1 also indicates the binder used where applicable.

Mr. Finkin is correct in assuming that an organic based binder, such as epoxy, is unsuitable for the intended application. No tests were performed using epoxy materials as a binder for abrasive retention. The referenced use of epoxy adhesive was for determination of coating-substrate bond strength. Unfortunately, the test procedure callout is incomplete. It should be:

ASTM C-633, Adhesive or Cohesive Strength of Flame Sprayed Coatings—Test for

In this test the coating to be tested is applied to two test specimens. The two specimens are then joined using an epoxy adhesive to form a single tensile specimen. The specimen is then tested in the conventional manner per the referenced ASTM procedure.

Table 1 Initial Screening Test Results for Rotor Abrasive Coatings Applied to an AISI 410 Base

				Adherence		
Abrasive System	Ease of Application	Surface Roughness (μ metre–μ in.)	Microstructure Appearance	Bend Test (% Material Lost)	Tensile Bond Strength (MPa–psi)	Abrasive Grain Appearance
Nickel Aluminide Bonded Aluminum Oxide	Difficult	4.4–175	Laminar with approximately 10 percent abrasive	30	29–4200	Rounded edges
Plasma Sprayed Aluminum Oxide (53 > 15 microns)	Moderate	5.0–200	Laminar with discontinuous voids	20	47–6800	Flat with rounded corners
Flame Sprayed Aluminum Oxide (75 > 30 microns)	Difficult to control thickness	5.7–225	Similar to plasma sprayed with larger voids	15	52–7500	Ovoid
RC-1	Easily applied to required thickness	10.6–425	Projecting abrasive grains bonded to substrate	5	N/A	Sharp blocky grains
Cobalt Bonded Tungsten Carbide (43 > 30 microns)	Moderate	4.5–180	Fine uniformly dispersed abrasive grains in metal matrix	5	52–7600	Metallic coating on abrasive
Cobalt Bonded Tungsten Carbide (53 > 30 microns)	Moderate	8.8–350	Uniform structure with evenly dispersed grains	10	45–6600	Rounded abrasive grains
Cobalt Bonded Tungsten Carbide (74 > 30 microns)	Easily applied to finish dimension	14.4–575	Open structure with approximately 20 percent voids	10	58–8400	Large rounded grains
Nickel-Chromium Bonded Chromium Carbide	Moderate	6.3–250	Fine fused appearance	90	64–9300	Fine grains dispersed in metal matrix
Nickel Aluminide Bonded Chromium Carbide	Moderate	4.4–175	Laminar structure with discontinuous voids	10	30–4300	Fine rounded grains

Axial—Flow Compressor Turning Angle and Loss by Inviscid-Viscous Interaction Blade—to—Blade Computation[1]

Ramakant B. Deshpande.[2] The paper by E. C. Hansen, et al. makes interesting reading because of their inclusion of inviscid-viscous interaction in blade-to-blade computations to predict turning angles and loss. The theoretical treatment is quite elegant and the experimentally obtained comparisons with the theory are very impressive. But what is not understood is that when blade angles are calculated from air angles the cascade data used are for a maximum Mach number of 0.1. If the test data based on a Mach number of 0.1 are considered adequate, I would imagine that any of the methods of Katnasis for blade-to-blade computations in which the effect of inviscid-viscous flow interaction has not been taken into consideration should suffice. The computer program used by the author is capable of calculating laminar, transitional, and turbulent boundary layers and I would imagine it will take considerable amount of computer time compared to inviscid solutions. In light of the above, I would like to know whether such an elegant and expensive method should be preferred for predicting fluid angles and total pressure loss when the cascade data used are incorrect.

Author's Closure

I would like to thank Ramakant B. Deshpande for the discussion concerning the use of inviscid—viscous interaction techniques. We

---

[1] By E. C. Hansen, G. K. Serovy, and P. M. Sockol, published in the January issue of the ASME JOURNAL OF ENGINEERING FOR POWER Vol. 102, No. 1, 1980, pp. 28-34.

[2] Director, Research Development and Engineering Centre, M/s. K. G. Khosla Compressors Ltd., Faridabad—121 003, India.

compared the theoretical calculations with the low speed cascade data of Herrig, et al. (reference [23]) which we feel to be technically accurate. Because an inviscid solution alone produces a basically linear relationship of $\Delta\beta$ with α, an inviscid solution for blade-to-blade flow can not produce the experimentally measured drop in turning at high angles of attack as shown in Fig. 3 of the paper. The drop off of $\Delta\beta$ is a result of visicous effects, which are a result of large surface pressure gradients at high angles of attack not necessarily high Mach numbers. At high angles of attack inviscid methods alone are not adequate to calculate turning angles and can not calculate losses.

Computation of Supercritical Compressor and Turbine Cascades with a Design Method for Transonic Flows[1]

Ramakant B. Deshpande.[2] I would like to congratulate Dr. Schmidt for a very interesting paper on design method for a compressor and turbine cascades for transonic flows. His method seems to be the first to appear since the method devized by Stanitz who, however, had not taken into consideration the viscous terms in his calculations. Although the present method is quite capable of predicting combined subsonic supersonic flow beccause of center difference and up wind difference schemes, the basic problem with the method seems to be how does one prescribe a velocity distribution theoretically to arrive at a blade shape which will give correct pressure increase and pressure drop for compressors and turbines. Most of the examples given in the paper are based on experimentally available velocity profiles. What one really needs is a theoretical approach which will once and for all give a velocity distribution, and will guarantee a blade shape which will not turn out to be a figure eight. Can the author throw some light on his method of prescribing velocity distribution?

Author's Closure

The author wishes to thank Ramakant B. Deshpande for his comments. A generally valid theoretical solution for the prescription of velocity distributions for transonic cascade flow avoiding contour overlapping does not exist to our knowledge. As a necessary condition, the velocity density integral in the pitchwise direction at any longitudinal position of the flow channel must not fall below the value of the upstream velocity density value; i.e.

$$\Omega(s) = \frac{\int_0^t \rho(s,n)\mathrm{La}(s,n)\,\sin\beta(s,n)dt}{\rho_1 \mathrm{La}_1 \sin\beta_1 t} \geq 1.$$

This condition, however, is exactly examinable only after solving the velocity field and the flow direction field. But approximations for the prescription of velocity distributions due to this condition are available by specifically adapted mean value considerations basing on stream tube theory, and considering the different character of each part of the flow field.

In these considerations, the velocity distributions are presumed to be chosen so that they produce the turning of the flow required by the continuity condition (equation (11) of [1]). The turning, however, is only precisely determinable after solving the velocity field (see block diagram, Fig. 2 of [1]). But if the ratio of the arc lengths of the suction and pressure side is well known in advance, as in the case of compressor cascades, the velocity distribution for a required turning can be rather exactly predetermined by comparison of the circulation from the up and downstream values (equation (12)) with the circulation from the integration around the blade contour (equation (16)). In the subsequent computation some iteration cycles with self controlling variation of the velocity distribution yield the correct turning (iteration number depending on accuracy demands). The pressure increase or pressure drop of the potential flow is fixed by the isentropic equations since up and downstream velocities are prescribed. Whether this pressure change can be realized in viscous flow is investigated by boundary layer calculations, the results of which are also required for correcting the computed potential flow contour.

---

[1] By E. Schmidt, published in the January issue of the ASME JOURNAL OF ENGINEERING FOR POWER Vol. 102, No. 1, 1980 pp. 68–74.

[2] Director, Research Development and Engineering Centre, M/s. K.G. Khosla Compressors Ltd., Faridabad-121 003, India.

compared the theoretical calculations with the low speed cascade data of Herrig, et al. (reference [23]) which we feel to be technically accurate. Because an inviscid solution alone produces a basically linear relationship of $\Delta\beta$ with α, an inviscid solution for blade-to-blade flow can not produce the experimentally measured drop in turning at high angles of attack as shown in Fig. 3 of the paper. The drop off of $\Delta\beta$ is a result of visicous effects, which are a result of large surface pressure gradients at high angles of attack not necessarily high Mach numbers. At high angles of attack inviscid methods alone are not adequate to calculate turning angles and can not calculate losses.

Computation of Supercritical Compressor and Turbine Cascades with a Design Method for Transonic Flows[1]

Ramakant B. Deshpande.[2] I would like to congratulate Dr. Schmidt for a very interesting paper on design method for a compressor and turbine cascades for transonic flows. His method seems to be the first to appear since the method devized by Stanitz who, however, had not taken into consideration the viscous terms in his calculations. Although the present method is quite capable of predicting combined subsonic supersonic flow beccause of center difference and up wind difference schemes, the basic problem with the method seems to be how does one prescribe a velocity distribution theoretically to arrive at a blade shape which will give correct pressure increase and pressure drop for compressors and turbines. Most of the examples given in the paper are based on experimentally available velocity profiles. What one really needs is a theoretical approach which will once and for all give a velocity distribution, and will guarantee a blade shape which will not turn out to be a figure eight. Can the author throw some light on his method of prescribing velocity distribution?

Author's Closure

The author wishes to thank Ramakant B. Deshpande for his comments. A generally valid theoretical solution for the prescription of velocity distributions for transonic cascade flow avoiding contour overlapping does not exist to our knowledge. As a necessary condition, the velocity density integral in the pitchwise direction at any longitudinal position of the flow channel must not fall below the value of the upstream velocity density value; i.e.

$$\Omega(s) = \frac{\int_0^t \rho(s,n)\mathrm{La}(s,n) \sin \beta(s,n)dt}{\rho_1\mathrm{La}_1 \sin \beta_1 t} \geq 1.$$

This condition, however, is exactly examinable only after solving the velocity field and the flow direction field. But approximations for the prescription of velocity distributions due to this condition are available by specifically adapted mean value considerations basing on stream tube theory, and considering the different character of each part of the flow field.

In these considerations, the velocity distributions are presumed to be chosen so that they produce the turning of the flow required by the continuity condition (equation (11) of [1]). The turning, however, is only precisely determinable after solving the velocity field (see block diagram, Fig. 2 of [1]). But if the ratio of the arc lengths of the suction and pressure side is well known in advance, as in the case of compressor cascades, the velocity distribution for a required turning can be rather exactly predetermined by comparison of the circulation from the up and downstream values (equation (12)) with the circulation from the integration around the blade contour (equation (16)). In the subsequent computation some iteration cycles with self controlling variation of the velocity distribution yield the correct turning (iteration number depending on accuracy demands). The pressure increase or pressure drop of the potential flow is fixed by the isentropic equations since up and downstream velocities are prescribed. Whether this pressure change can be realized in viscous flow is investigated by boundary layer calculations, the results of which are also required for correcting the computed potential flow contour.

---

[1] By E. Schmidt, published in the January issue of the ASME JOURNAL OF ENGINEERING FOR POWER Vol. 102, No. 1, 1980 pp. 68–74.

[2] Director, Research Development and Engineering Centre, M/s. K.G. Khosla Compressors Ltd., Faridabad-121 003, India.